

LOUGHBOROUGH
UNIVERSITY OF TECHNOLOGY
LIBRARY

AUTHOR

WILLIAMS, G J

COPY NO.

006287/02

VOL NO.

CLASS MARK

ARCHIVED COPY
FOR REFERENCE ONLY

THE INFLUENCE OF INLET CONDITIONS ON
THE BOUNDARY LAYER GROWTH AND OVERALL
PERFORMANCE OF ANNULAR DIFFUSERS

by

G. J. WILLIAMS B. Tech.

Supervisor: S. J. Stevens Ph.D.

Submitted for the Degree of Doctor of Philosophy
of Loughborough University of Technology

August 1972

Longborough University	
Of Test. City 12/1	
Date	Dec 72
Class	
Acct. No.	006287/02

SUMMARY

An experimental investigation of the flow behaviour in, and overall performance of, the straight-core annular diffuser under naturally and artificially generated inflow conditions is described. For naturally developed near uniform inflow diffuser overall performance, and stability limits, are theoretically predicted.

In the first part of the research program the diffusers were tested over a range of naturally developed inflow velocity profiles from near-uniform to fully developed flow. The diffuser pressure recovery was observed to fall with initial thickening of the inlet boundary layers and subsequently improved as the flow became fully developed. Downstream of the diffuser exit pressure recovery continued for some two hydraulic diameters into the settling length. The measured levels of diffuser performance compared well with relevant published data but similar stability limits were not found. This was attributed to the varying inflow conditions for the published data.

Detailed investigations of the boundary layer growth in the test diffusers showed that the flow development was dominated by pressure forces and that the asymmetric boundary layer growth on the inner and outer walls was attributable to the distorting effect of the diffuser outer wall inlet bend. Tests with artificially generated flow mixing at inlet showed that velocity profile distortion in the diffuser was reduced by increasing the level of flow mixing near the wall at diffuser inlet; attendant improvements in static pressure recovery and exit flow stability were also noted.

For naturally developed near uniform inflow the diffuser overall performance, and stability limits indicated by test results were successfully predicted using integral methods based on the physics of boundary layer entrainment.

ACKNOWLEDGEMENTS

The work described in this thesis was carried out at Loughborough University of Technology, Department of Transport Technology under the overall direction of Professor K.L.C. Legg whose guidance the author gratefully acknowledges. The research was sponsored by the Science Research Council and the author was financially supported initially by the Science Research Council and later by Loughborough University of Technology, and the author wishes to thank both sources for the opportunity to carry out this research.

The work was supervised by Dr. S. J. Stevens whose help, personal example, and encouragement at every stage of the work have been greatly appreciated. Thanks are also due to staff at several other Universities and Industrial establishments for useful discussions, in particular the author wishes to thank and acknowledge Dr. M.R. Head of the Engineering Department of Cambridge University for several helpful discussions and suggestions on theoretical aspects of the work.

Much help was given by the technical staff of the Department of Transport Technology and, in particular, the author wishes to thank Mr. G. Bowler and Mr. W. Brooks for their excellent rig work. Also Mrs. I Gay is thanked for her careful typing of this thesis, and the generosity of the G.E.C. Mechanical Engineering Laboratory in making available photocopying facilities is acknowledged.

Finally the author wishes to thank his wife whose help and patience during the period this work was carried out have been a constant support.

C O N T E N T S

	<u>PAGE</u>
Summary	i
Acknowledgements	ii
Contents	iii
List of Figures	viii
Nomenclature	xvi
 <u>CHAPTER 1</u>	
<u>1.0 INTRODUCTION</u>	1
1.1 The Diffuser - its uses and problems	1
1.2 Diffuser Geometry	1
1.3 Evaluation of Diffuser Performance	3
1.3.1 Flow Stability	3
1.3.2 Performance Parameters	4
1.4 A Review of Recent Investigations of Diffusers	6
1.4.1 Diffusers Operating with Naturally Developed Inlet Conditions.	13
1.4.2 Diffusers Operating with Artificially Generated Inlet Conditions	16
1.5 Prediction of Diffuser Performance	18
1.6 Scope and Aims of Present Work	19
 <u>CHAPTER 2</u>	
<u>2.0 EXPERIMENTAL TEST FACILITY AND INSTRUMENTATION</u>	
2.1 Choice of Test Diffuser Geometries	22
2.2 Rig Design	23
2.3 Artificially Generated Inlet Conditions	24
2.4 Instrumentation	25

	<u>PAGE</u>
2.4.1 Measurement of Static Pressure and Mean Velocity	25
2.4.2 Measurement of Turbulence Parameters	26
 <u>CHAPTER 3</u>	
3.0 <u>EXPERIMENTAL WORK</u>	28
3.1 Test Series	28
3.1.1 Naturally Developed Inlet Conditions	28
3.1.2 Artificially Generated Inlet Conditions	30
3.2 Experimental Technique	31
3.3 Data Reduction	32
3.3.1 Mean Velocity Profile Data	32
3.3.2 Turbulence Data	33
3.4 Accuracy	33
3.4.1 Experimental Accuracy	33
3.4.2 Accuracy of Calculated Parameters	34
3.5 Preliminary Tests and Calibrations	36
3.5.1 Preliminary Tests	36
3.5.2 Calibrations	37
 <u>CHAPTER 4</u>	
4.0 <u>PRESENTATION AND DISCUSSION OF EXPERIMENTAL TEST RESULTS</u>	39
4.1 Naturally Developed Inlet Conditions	39
4.1.1 Diffuser Inlet Conditions	39
4.1.2 Outlet Conditions and Flow Stability	40
4.1.3 Static Pressure Recovery	42
4.1.4 Overall Performance	42
4.1.5 Comparison With Published Data	44
4.1.6 Effect of Downstream Settling Length	47
4.1.7 Internal Boundary Layer Development and Flow Stability	48
4.1.8 Shear Stress and Turbulence Intensity	50

	<u>PAGE</u>
4.1.9 Law of the Wall - Estimation of Skin Friction	55
4.1.10 Mixing Length and Eddy Viscosity	58
4.1.11 Balance of Momentum	62
4.2 Flow Mixing at Inlet Generated by a Flow Spoiler on the Outer Wall	63
4.2.1 Optimisation of Wall Spoiler Upstream Position	63
4.2.1.1 Diffuser Inlet Conditions	64
4.2.1.2 Outlet Conditions and Flow Stability	65
4.2.1.3 Static Pressure Recovery	66
4.2.1.4 Overall Performance	67
4.2.1.5 Comparison with Published Data	68
4.2.1.6 Effect of Downstream Settling Length	70
4.2.2 Internal Flow Development for Optimum Spoiler Position	70
4.2.2.1 Internal Boundary Layer Development	70
4.2.2.2 Shear Stress and Turbulence Intensity	71
4.2.2.3 Law of the Wall - Estimation of Skin Friction	73
4.2.2.4 Mixing Length and Eddy Viscosity	73
4.2.2.5 Balance of Momentum	74
4.3 Inlet Flow Mixing Generated by Coarse Gauze	75
4.3.1 Diffuser Inlet Conditions	75
4.3.2 Outlet Conditions and Flow Stability	76
4.3.3 Static Pressure Recovery	77
4.3.4 Overall Performance	78
4.3.5 Effect of Downstream Settling Length	78

CHAPTER 5

5.0 <u>THE APPLICATION OF INTEGRAL METHODS TO THE PREDICTION OF DIFFUSER PERFORMANCE AND STABILITY</u>	80
5.1 Introduction	80

5.2	Integral Methods	<u>PAGE</u> 81
5.2.1	Continuity - Mean Velocity Profile	82
5.2.2	Wall Shear Stress	87
5.2.3	Separation Criterion	88
5.2.4	The Auxiliary Equation	88
5.3	Entrainment Model due to Head (26)	89
5.3.1	Physical Basis	89
5.3.2	Application to Two-Dimensional Internal Flow	90
5.3.3	Application to Axi-Symmetric Internal Flow	92
5.4	Entrainment Model due to Thompson (71)	96
5.4.1	Physical Basis	96
5.4.2	Application of Thompson's Method Using the Concept of 'Equivalent Two-Dimensional Flow'	98
<u>CHAPTER 6</u>		
6.0	<u>COMPARISON OF THEORY WITH EXPERIMENT</u>	100
6.1	The Effect of the Mean Velocity Profile Form on the Evaluation of Diffuser Quantity Flow	100
6.2	Internal Flow Development	102
6.2.1	Head's Prediction Method	102
6.2.2	Thompson's Prediction Method	105
6.3	Prediction of Overall Performance and Stability Limits	106
6.4	Finite Difference Methods	107
<u>CHAPTER 7</u>		
7.0	<u>CONCLUSIONS AND RECOMMENDATION FOR FUTURE WORK</u>	108
7.1	Experimental Tests	108
7.1.1	Naturally Developed Inflow	108
7.1.2	Artificially Generated Inflow	109
7.2	Theoretical Methods	111
7.3	Future Work	112

	<u>PAGE</u>
<u>APPENDIX 1</u> <u>ARTIFICIALLY GENERATED PROFILES</u>	113
<u>APPENDIX 2</u> <u>MEAN VELOCITY MEASUREMENTS</u>	115
A.2.1 Mean Velocity Data Analysis	115
A.2.2 Accuracy of Velocity Measurement	117
<u>APPENDIX 3</u> <u>TURBULENCE MEASUREMENTS</u>	119
A.3.1 Operation of Hot-Wire Anemometer at Constant Temperature	120
A.3.2 Turbulence Data Analysis	123
A.3.3 Accuracy of Turbulence Measurements	124
A.3.4 Asymmetry and Verification of King's Law Checks	127
<u>APPENDIX 4</u> <u>MOMENTUM INTEGRAL EQUATION IN THE AXI-SYMMETRIC CO-ORDINATE SYSTEM</u>	128
<u>APPENDIX 5</u> <u>HEAD'S ENTRAINMENT METHOD</u>	133
A.5.1 Application of Head's Entrainment Method to Internal Axi-Symmetric Flows	133
A.5.2 Theoretical Predictions	137
<u>APPENDIX 6</u> <u>THOMPSON'S ENTRAINMENT METHOD</u>	138
A.6.1 Application of Thompson's Entrainment Method to Internal Axi-Symmetric Flow	138
A.6.2 Theoretical Predictions	141
<u>APPENDIX 7</u> <u>DIFFUSER INTERNAL FLOW DEVELOPMENT UNDER NATURALLY DEVELOPED INFLOW CONDITIONS</u>	
<u>APPENDIX 8</u> <u>DIFFUSER PERFORMANCE OVER A RANGE OF NATURALLY DEVELOPED INLET VELOCITY PROFILES</u>	
<u>APPENDIX 9</u> <u>DIFFUSER INTERNAL FLOW DEVELOPMENT AT OPTIMUM SPOILER POSITION</u>	
<u>APPENDIX 10</u> <u>DIFFUSER PERFORMANCE WITH GRID GENERATED INLET TURBULENCE</u>	
<u>APPENDIX 11</u> <u>MOMENTUM EQUATION BALANCE</u>	142
REFERENCES	144

LIST OF FIGURES

CHAPTER 1

- Figure 1.1 Straight Wall Diffuser - Basic Geometries.
- Figure 1.2 Two-Dimensional Diffuser Performance and Stability Limits.
- Figure 1.3 Effect of Inlet Velocity Profile.
- Figure 1.4 Performance Chart for Conical Diffusers
- Figure 1.5 Annular Diffuser Performance and Stability Limits.
- Figure 1.6 Performance Chart for Annular Diffusers.
- Figure 1.7 Typical Inlet Velocity Profiles - Artificially Generated.

CHAPTER 2

- Figure 2.1 Survey of Annular Diffusers Used in Turbomachinery Applications.
- Figure 2.2 Experimental Test Facility.
- Figure 2.3 Experimental Test Facility.
- Figure 2.4 Artificially Generated Inflows.
- Figure 2.5 Traversing Equipment.
- Figure 2.6 Diffuser Traverse Stations and Symbols.
- Figure 2.7 Hot-Wire Anemometer.
- Figure 2.8 Turbulent Shear Stress Measurement.
- Figure 2.9 Hot-Wire Probe and Carrier.

CHAPTER 3

- Figure 3.1 Data Presentation in Terms of Blocked Area Fraction
- Figure 3.2 Effect of Diffuser Inlet Bend.
- Figure 3.3 Fully Developed Inflow - Mean Velocity Profile.
- Figure 3.4 Fully Developed Inflow - Turbulent Shear Stress.

CHAPTER 4

- Figure 4.1 Range of Naturally Developed Inflow Velocity Profiles.
- Figure 4.2 Growth of Boundary Layer Along Approach Lengths.
- Figure 4.3 Inflow Velocity Profiles in Clauser Plot Form.
- Figure 4.4 Development of Inflow Turbulence.
- Figure 4.5 Flow Regions.
- Figure 4.6 Static Pressure Recovery in Diffuser.
- Figure 4.7 Variation of Static Pressure in Diffuser Inlet Region.
- Figure 4.8 Exit Velocity Profile Comparison.
- Figure 4.9 Effectiveness Loss in Annular Diffusers.
- Figure 4.10 Loss Factor in Annular Diffusers.
- Figure 4.11 Annular Diffuser Performance and Stability Limits.
- Figure 4.12 Annular Diffuser Performance and Stability Limits.
- Figure 4.13 Pressure Recovery in Settling Length.
- Figure 4.14 Behaviour of Velocity Profile Parameters in Settling Length.
- Figures 4.15
- Mean Velocity Profile Development.
4.26
- Figure 4.27 Flow Asymmetry Analysis.
- Figure 4.28 Boundary Layer Development in Test Diffusers.
- Figure 4.29 Boundary Layer Development in Test Diffusers.
- Figure 4.30 Diffuser Performance Improvement Through Inlet Suction.
- Figure 4.31 Comparison of Test Data with Turbulent Flow Separation Correlation.
- Figure 4.32 Turbulent Shear Stress Distribution.
- Figure 4.33 Turbulent Shear Stress Distribution.
- Figure 4.34 Comparison With Equilibrium Boundary Layer.
- Figure 4.35 Comparison with Transitory Stall Criterion.
- Figure 4.36 Determination of Skin Friction Coefficient.

- Figure 4.37 Variation of Skin Friction Coefficient in Test Diffusers.
- Figure 4.38 Effect of Pressure Gradient on the Law of the Wall.
- Figure 4.39 Effect of Pressure Gradient on the Law of the Wall.
- Figure 4.40 Mixing Length Distribution.
- Figure 4.41 Mixing Length Distribution.
- Figure 4.42 Eddy Viscosity Distribution.
- Figure 4.43 Eddy Viscosity Distribution.
- Figure 4.44 Momentum Integral Equation Balance.
- Figure 4.45 Momentum Integral Equation Balance.
- Figure 4.46 Methods Employed for the Generation of Highly Turbulent Inlet Profiles.
- Figure 4.47 Optimisation of Flow Spoiler Position - Inlet Velocity Profiles.
- Figure 4.48 Typical Inlet Velocity Profiles.
- Figure 4.49 Optimisation of Flow Spoiler Position - Inlet Turbulence Intensity.
- Figure 4.50 Optimisation of Flow Spoiler Position - Inlet Turbulent Shear Stress.
- Figure 4.51 Optimisation of Flow Spoiler Position - Exit Mean Velocity Profiles.
- Figure 4.52 Optimisation of Flow Spoiler Position - Static Pressure Recovery.
- Figure 4.53 Optimisation of Flow Spoiler Position - Variation of Static Pressure in Diffuser Inlet Region.
- Figure 4.54 Comparison of Inlet Conditions.
- Figure 4.55 Comparison With Compressor Exit Turbulence Intensity.
- Figure 4.56 Static Pressure Recovery in Settling Length.
- Figure 4.57 Optimum Spoiler Position - Mean Velocity Profile Integral Parameters in Settling Length.

- Figures 4.58-9 Mean Velocity Profile Development.
- Figure 4.60 Optimum Spoiler Position - Boundary Layer Development.
- Figure 4.61 Diffuser Exit Velocity Profile Comparison.
- Figure 4.62 Turbulent Shear Stress Distribution.
- Figure 4.63 Diffuser Exit Shear Stress Comparison.
- Figure 4.64 Mixing Length Distribution.
- Figure 4.65 Eddy Viscosity Distribution.
- Figure 4.66 Momentum Equation Balance.
- Figure 4.67 Comparison of Inflow Conditions Generated With a Coarse Grid.
- Figure 4.68 Diffuser Exit Velocity Profile Comparison.
- Figure 4.69 Static Pressure Recovery - Diffuser.
- Figure 4.70 Static Pressure Recovery in Settling Length.

CHAPTER 5

- Figure 5.1 Power-Law Mean Velocity Profile Formulation.
- Figure 5.2 Comparison of Power-Law Profile with Experiment.
- Figure 5.3 Sarnecki's Intermittency Correlation.
- Figure 5.4 Contours of (y/θ) for $u/U = 0.30$.
- Figure 5.5 Two-Part Velocity Profile, Comparison with Experiment.
- Figure 5.6 Turbulent Separation Correlation.
- Figure 5.7 Typical Comparisons with Experimental Data - Head's Prediction Method.
- Figure 5.8 Two-Dimensional Flow (Text).
- Figure 5.9 Head's Method - Shape Factor and Entrainment Functions.
- Figure 5.10 Head's Method - Solution Procedure.
- Figure 5.11 Entrainment Front (Text).
- Figure 5.12 Effective Centre of Intermittency.
- Figure 5.13 Straight-core Diffuser Geometry.
- Figure 5.14 Head's Method Functions - Axi-Symmetric Form.

- Figure 5.15 Head's Method - Solution Procedure in Axi-Symmetric Flow.
 Figure 5.16 Computer Program - Effect of Tolerance.
 Figure 5.17 Thompson's Method - Explanation of Terms.
 Figure 5.18 Equivalent Diffuser Concept.
 Figure 5.19 Thompson's Method - Solution Procedure.

CHAPTER 6

- Figure 6.1 Power-Law Velocity Profile.
 Figure 6.2 Power-Law Velocity Profile.
 Figure 6.3 Head's Method - $\bar{L}/\Delta R_1 = 10.0$, $B_1 = 0.028$.
 Figure 6.4 7.5.
 Figure 6.5 5.0.
 Figure 6.6 Location of Predicted Separation Point.
 Figure 6.7 Head's Method (Downstream Start) - $\bar{L}/\Delta R_1 = 10.0$, $B_1 = 0.028$.
 Figure 6.8 7.5.
 Figure 6.9 5.0.
 Figure 6.10 Head's Method (Single Function) - $\bar{L}/\Delta R_1 = 10.0$, $B_1 = 0.028$.
 Figure 6.11 7.5.
 Figure 6.12 5.0.
 Figure 6.13 Head's Method - Comparison with Conical Diffuser Data.
 Figure 6.14 Thompson's Method - $\bar{L}/\Delta R_1 = 10.0$, $B_1 = 0.028$.
 Figure 6.15 7.5.
 Figure 6.16 5.0.
 Figure 6.17 Conical Diffuser Performance Map.
 Figure 6.18 Annular Diffuser Performance Map.

APPENDIX 1

- Figure A.1.1 Two-Dimensional Gauze Grid System.
 Figure A.1.2 Peaked Velocity Profile Generator.
 Figure A.1.3 Gauze and Screen Ring Generators.

APPENDIX 2

Figure A.2.1 Trapezoidal Velocity Profile Analysis (Text).

Figure A.2.2 Mean Velocity Profile - Analysis Procedure.

APPENDIX 3

Figure A.3.1 Normal Hot-Wire Operation (Text).

Figure A.3.2 45° Slant Hot-Wire Operation (Text).

Figure A.3.3 Turbulence Data - Analysis Procedure.

Figure A.3.4 Illustration of Degree of Turbulent Shear Stress Asymmetry.

Figure A.3.5 Illustration of 'King's Law' from Test Results.

Figure A.3.6 Degree of Scatter in 'Raw' Turbulence Data.

APPENDIX 5

Figure A.5.1 Diagram of Flow in a Straight-Core Annular Diffuser.

APPENDIX 6

Figure A.6.1 Contours of (y/θ) for $u/U = 0.5$.

Figure A.6.2 Contours of (H) for $u/U = 0.5$.

Figure A.6.3 (t/θ) and $(\Delta u/U)$ vs. $\log R_\theta$ Relationships.

APPENDIX 7

Figure A.7.1 Mean Velocity Profile Development, $\bar{L}/AR_1 = 10.0$, $B_1 = 0.028$.

Figure A.7.2 Law of the Wall - Outer Wall "

Figure A.7.3 Law of the Wall - Inner Wall "

Figure A.7.4 Shear Stress Development "

Figure A.7.5 Turbulence Intensity Development "

Figure A.7.6 Mean Velocity Profile Development, $\bar{L}/AR_1 = 10.0$, $B_1 = 0.090$.

Figure A.7.7 Law of the Wall - Outer Wall "

Figure A.7.8 Law of the Wall - Inner Wall "

Figure A.7.9 Mean Velocity Profile Development, $\bar{L}/AR_1 = 7.5$, $B_1 = 0.028$.

Figure A.7.10	Law of the Wall - Outer Wall	, $\bar{L}/\Delta R_1 = 7.5$, $B_1 = 0.028$.
Figure A.7.11	Law of the Wall, Inner Wall	"
Figure A.7.12	Shear Stress Development	"
Figure A.7.13	Turbulence Intensity Development	"
Figure A.7.14	Mean Velocity Profile Development,	$\bar{L}/\Delta R_1 = 7.5$, $B_1 = 0.090$.
Figure A.7.15	Law of the Wall - Outer Wall	"
Figure A.7.16	Law of the Wall - Inner Wall	"
Figure A.7.17	Mean Velocity Profile Development,	$\bar{L}/\Delta R_1 = 5.0$, $B_1 = 0.028$.
Figure A.7.18	Law of the Wall - Outer Wall	"
Figure A.7.19	Law of the Wall - Inner Wall	"
Figure A.7.20	Mean Velocity Profile Development,	$\bar{L}/\Delta R_1 = 5.0$, $B_1 = 0.090$.
Figure A.7.21	Law of the Wall - Outer Wall	"
Figure A.7.22	Law of the Wall - Inner Wall	"

APPENDIX 8

Figure A.8.1	Exit Velocity Profiles, $\bar{L}/\Delta R_1 = 10.0$.
	Exit Velocity Profiles, $\bar{L}/\Delta R_1 = 7.5$.
	Exit Velocity Profiles, $\bar{L}/\Delta R_1 = 5.0$.

APPENDIX 9

Figure A.9.1	Mean Velocity Profile Development,	$\bar{L}/\Delta R_1 = 5.0$, $B_1 = 0.117$.
Figure A.9.2	Law of the Wall - Outer Wall	"
Figure A.9.3	Law of the Wall - Inner Wall	"
Figure A.9.4	Shear Stress Development - Outer Wall	"
Figure A.9.5	Shear Stress Development - Inner Wall	"
Figure A.9.6	Turbulence Intensity Development - Outer Wall	"
Figure A.9.7	Turbulence Intensity Development - Inner Wall	"

APPENDIX 11

Figure A.11.1 Momentum Balance - Outer Wall, $\bar{L}/\Delta R_1 = 10.0$, $B_1 = 0.028$.

Figure A.11.2 Momentum Balance - Inner Wall, "

Figure A.11.3 Momentum Balance - Outer Wall, $\bar{L}/\Delta R_1 = 7.5$, $B_1 = 0.028$.

Figure A.11.4 Momentum Balance - Inner Wall, "

Figure A.11.5 Momentum Balance - Outer Wall, $\bar{L}/\Delta R_1 = 5.0$, $B_1 = 0.028$.

Figure A.11.6 Momentum Balance - Inner Wall, "

Figure A.11.7 Momentum Balance - Outer Wall, $\bar{L}/\Delta R_1 = 5.0$, $B_1 = 0.117$.

Figure A.11.8 Momentum Balance - Inner Wall, "

NOMENCLATURE

The following nomenclature applies unless otherwise defined in the text:

A	Area of cross-section
AR	Area ratio
B	Blocked area fraction $1 - \frac{1}{A} \int_A \frac{u}{U} dA$
c_f	Local skin friction coefficient $\tau_w / \frac{1}{2} \rho U^2$
$\overline{C_p}$	Static pressure recovery coefficient based on mean inlet dynamic head, $\Delta p / \frac{1}{2} \rho u_1^2$
D	Diameter of cross-section
D_h	Hydraulic mean diameter, $D_o - D_i$
\mathcal{D}	Shear work integral, $\frac{2}{\rho U^3} \int_0^\delta \tau \frac{du}{dR} dR$
H	Shape parameter, δ^* / θ
\overline{H}	Shape parameter, δ^{**} / θ
$H_{\delta-\delta^*}$	Shape parameter, $(\delta - \delta^*) / \theta$
\overline{L}	Diffuser average wall length
L_e	Length of approach pipe upstream of diffuser
L_s	Distance to upstream flow spoiler
ℓ	Prandtl mixing length, $\left\{ - \overline{u'v'} / \frac{du}{dR} \left \frac{du}{dR} \right \right\}^{\frac{1}{2}}$
N	Diffuser axial length
p	Static pressure
P	Total pressure
R	Radius

R_{eff}	Radius, effective centre of entrainment
ΔR	Annulus height, $R_o - R_i$
R_e	Reynolds number, UD_h/ν
R_θ	Reynolds number, $U\theta/\nu$
u	Local axial velocity
\bar{u}	Mass average velocity
u_τ	Friction velocity
u^+	u/u_τ
$\sqrt{u'^2}$	r.m.s. fluctuation velocity in X-direction
$\overline{u'v'}$	Reynolds shear stress
U	Maximum velocity at cross-section.
$\sqrt{v'^2}$	r.m.s. fluctuation velocity in R-direction
X	Axial distance from diffuser inlet
X_d	Axial distance into settling length
y	$(R_o - R), (R - R_i)$
y^+	$\frac{yu_\tau}{\nu}$
α	Velocity profile energy coefficient, $\frac{1}{A} \int^A \left(\frac{u}{U}\right)^3 dA$
β	Velocity profile momentum coefficient, $\frac{1}{A} \int^A \left(\frac{u}{U}\right)^2 dA$
γ	Intermittency factor
δ_o^*	Displacement thickness of boundary layer on outer wall $\int_{R_\delta}^{R_o} \left(1 - \frac{u}{U}\right) \frac{R}{R_o} dR$

δ_i^* Displacement thickness of boundary layer on inner wall

$$\int_{R_i}^{R_\delta} \left(1 - \frac{u}{U}\right) \frac{R}{R_i} dR$$

δ_o^{**} Energy thickness of boundary layer on outer wall

$$\int_{R_\delta}^{R_o} \left(1 - \left(\frac{u}{U}\right)^2\right) \frac{u}{U} \frac{R}{R_o} dR$$

δ_i^{**} Energy thickness of boundary layer on inner wall

$$\int_{R_i}^{R_\delta} \left(1 - \left(\frac{u}{U}\right)^2\right) \frac{u}{U} \frac{R}{R_i} dR$$

θ_o Momentum thickness of boundary layer on outer wall,

$$\int_{R_\delta}^{R_o} \left(1 - \frac{u}{U}\right) \frac{u}{U} \frac{R}{R_o} dR$$

θ_i Momentum thickness of boundary layer on inner wall,

$$\int_{R_i}^{R_\delta} \left(1 - \frac{u}{U}\right) \frac{u}{U} \frac{R}{R_i} dR$$

ε Eddy viscosity

λ Loss coefficient

ν Fluid kinematic viscosity

ρ Fluid density

τ Shear stress

ϕ Diffuser wall angle

ζ Diffuser effectiveness

SUBSCRIPTS

1 Diffuser datum inlet station

2 Diffuser outlet
 o Outer wall
 i Inner wall
 w General wall value
 δ Limit of boundary layer.
 t Turbulent flow
 p Potential flow
 2-D Two-dimensional parameter value

NOTE

--At the time this work was commenced Imperial Units were still in
 general use and thus values are quoted in terms of these units. However
 as the vast majority of the experimental data is presented in non-dimensional
 terms this only has a minimal effect. The following conversion factors are
 included to assist in relating to the S.I. units where required:

Unit	Unit Symbol	S.I. Equivalent
inch	1 in	2.54×10^{-2} metre
ft/sec	f/s	3.048×10^{-1} metre/sec

CHAPTER 1

1.0 INTRODUCTION

1.1 The Diffuser - its uses and problems

The diffuser is a fluid flow device consisting of a passage of increasing cross-sectional area through which fluid is decelerated with an accompanying pressure rise. Whether velocity reduction or pressure rise is the primary objective depends on the particular application.

A diffuser is often used to minimise fluid energy losses in, and hence power requirements of, ducting systems. The reduction of flow velocity gives a lower dynamic head, and consequently a reduction in the losses in downstream components. A typical example of this application is found in the closed circuit wind tunnel. Gas turbines also employ a diffuser, to decelerate the compressor exit flow; in this case the purpose is to ensure stable combustion and a sufficient supply of dilution air. Uses of the pressure rise capability of the diffuser include reduction of back pressure on turbines, thereby increasing their work output, and the reduction of back pressure in exhaust systems to provide better scavenging of exhaust products.

Whatever the application, the pressure rise in a diffuser results in an adverse pressure gradient which can cause unstable separated exit flow conditions so impairing the performance of the diffuser and adjacent components. Thus the designer must, within whatever practical constraints may apply, specify a diffuser geometry capable of achieving the desired velocity reduction and/or pressure rise with stable unseparated outlet flow conditions.

1.2 Diffuser Geometry

A diffuser in a flow system may have any of an infinite variety of

cross-sections and wall shapes. For engineering purposes many diffuser geometries are used; such as curved diffusers connecting inlet and outlet ducts at right-angles, or diffusers connecting ducts of different cross-section. Owing to the problems these types present, both in manufacture and use, straight-wall diffusers of simple geometry are used wherever possible.

Simple straight-wall diffusers can be sub-divided into the following basic geometries:

- (i) two-dimensional diffusers
- (ii) conical diffusers
- (iii) annular diffusers.

Figure 1.1 shows these geometries together with the nomenclature adopted; types (i) and (ii) are special cases of the annular geometry.

For a symmetrical two-dimensional diffuser the wall length (L), area ratio (AR_{1-2}), and the divergence angle (2ϕ) are related as follows:

$$AR_{1-2} = 1 + 2 \frac{L}{W_1} \sin \phi \quad 1.1$$

while for an asymmetric diffuser with one divergent wall, of divergence angle ϕ ,

$$AR_{1-2} = 1 + \frac{L}{W_1} \sin \phi \quad 1.2$$

In view of this relationship between the basic diffuser geometry parameters it has become common practice to present two-dimensional diffuser data in terms of area ratio (AR_{1-2}) or divergence angle (ϕ), and non-dimensional length (L/W_1 or N/W_1).

Conical diffusers exhibit another three parameter group, where:

$$AR_{1-2} = 1 + 2 \frac{L}{R_1} \sin \phi + \left[\frac{L}{R_1} \sin \phi \right]^2 \quad 1.3$$

hence in this case data may be presented in terms of AR_{1-2} or ϕ , and L/R_1 .

For an equiangular annular diffuser the expression is similar in form to that for two-dimensional diffusers, being:

$$AR_{1-2} = 1 + 2 \frac{L}{\Delta R_1} \sin \phi \quad 1.4$$

However, when both cone angles vary the expression is much more complex:

$$AR_{1-2} = \frac{1 + 2 \frac{L}{\Delta R_1} \left[\sin \phi_o + \frac{R_i}{R_o} \sin \phi_i \left[\frac{\cos \phi_o}{\cos \phi_i} \right] \right]}{\left[1 + \frac{R_i}{R_o} \right]} + \frac{\frac{L^2}{\Delta R_1^2} \left[1 - \frac{R_i}{R_o} \right] \left[\sin^2 \phi_o - \sin^2 \phi_i \left[\frac{\cos \phi_o}{\cos \phi_i} \right]^2 \right]}{\left[1 + \frac{R_i}{R_o} \right]} \quad 1.5$$

It can be seen that while the two-dimensional and conical geometry relationships involve three parameters, the general annular diffuser case has five variables. Thus by the very nature of its geometry any general experimental investigation of the annular diffuser must consider a much wider range of test geometries.

1.3 Evaluation of Diffuser Performance

For any of the straight-wall diffusers described in section 1.2, operating with low-speed incompressible naturally developed inlet flow, it is possible to predict the diffuser flow behaviour by theoretical methods, provided the pressure gradients are moderate. These conditions are not usually encountered in engineering practice, and systematic experimental tests are needed to establish diffuser performance and stability limits. This experimental data must be suitably evaluated and presented to ensure its general applicability.

1.3.1 Flow Stability

It is important that flow separation does not occur in a diffuser since this gives rise to unstable flow conditions with insufficient

diffusion and increased energy losses.

A correlation of flow stability limits in terms of the two-dimensional diffuser geometry was obtained by Fox and Kline* (23) for diffusers with low speed incompressible flow and thin inlet boundary layers. Four flow regimes were defined from flow visualisation studies:

- (i) Steady flow with no appreciable stall.
- (ii) Unsteady flow with strong transitory stall.
- (iii) Steady, fully developed, two-dimensional stall.
- (iv) Steady jet flow.

The demarcation between conditions (i) and (ii) was denoted the 'line of first stall', see Figure 1.2(a), and represents the limit of diffuser stability. Similar presentations of stability limits may be made for conical and annular diffusers.

1.3.2 Performance Parameters

It is necessary to quantify diffuser performance and losses by representative parameters. For many designs a specific velocity reduction is required; however, since the velocity varies across a diffuser cross-section, and can be difficult to measure accurately, its use as a parameter is impracticable.

In the absence of appreciable flow swirl or streamline curvature, the static pressure is essentially constant over a diffuser cross-section and can be measured with confidence. In view of this a performance parameter often used is the pressure recovery coefficient, defined for the general compressible spatially non-uniform flow by Livesey (36), and here defined in its form for incompressible, uniform, inflow:

* Numbers in parentheses denote references detailed at rear.

$$\overline{Cp}_{1-2} = \frac{\Delta p_{1-2}}{\frac{1}{2}\rho u_1^2} \quad 1.6$$

being the measured static pressure rise between stations 1 (inlet) and 2 (outlet) expressed as a fraction of the pressure rise in a diffuser of infinite area ratio. A measure of the diffuser effectiveness (ζ_{1-2}) is often expressed by comparing the actual static pressure recovery coefficient with the ideal value attained in a diffuser of the same geometry with inviscid, one-dimensional flow, at the same flow rate. For these conditions:

$$\overline{Cp}_{1-2}^{\text{ideal}} = 1 - \frac{1}{AR_{1-2}^2} \quad 1.7$$

and

$$\zeta_{1-2} = \overline{Cp}_{1-2} / \overline{Cp}_{1-2}^{\text{ideal}} \quad 1.8$$

For many practical applications a knowledge of the energy loss in the diffuser is required. If the energy equation for incompressible flow is written as:

$$\alpha_1 \frac{1}{2} \rho \bar{u}_1^2 + p_1 = \alpha_2 \frac{1}{2} \rho \bar{u}_2^2 + p_2 + \lambda_{1-2} \frac{1}{2} \rho \bar{u}_1^2 \quad 1.9$$

where

$$\alpha = \frac{\int_A u^3 dA}{\bar{u}^3 A}$$

and is the kinetic energy flux coefficient of the mean velocity profile, and the overall loss coefficient λ_{1-2} is expressed as a fraction of the inlet mean dynamic head, then re-arranging equation 1.9 gives:

$$\overline{Cp}_{1-2} = \left[\alpha_1 - \frac{\alpha_2}{AR_{1-2}^2} \right] - \lambda_{1-2} \quad 1.10$$

Equation 1.10 shows that good pressure recovery is dependent on a low energy loss in the diffuser coupled with an exit velocity profile having a low degree of distortion with a correspondingly low value of α_2 . The evaluation of α_2 and λ_{1-2} involves measuring both static pressure recovery

and the inlet and outlet mean velocity profiles. While the static pressure and inlet velocity profile can be determined accurately, the exit velocity profile is often difficult to measure because of unsteady flow conditions and asymmetry. For this reason values of λ_{1-2} and α_2 are not often available from experimental data.

1.4 A Review of Recent Investigations of Diffusers

A detailed literature review on subsonic diffuser flow has been given by Cockrell and King (17) and from this and other sources the following comments may be made:

Experimental investigation of diffuser flow has tended to focus on two main areas:

- (i) gross geometry effects
- (ii) effects of adjacent flow conditions.

The above effects are usually evaluated in terms of diffuser performance and flow stability.

A limited number of detailed studies of diffuser internal flow have been carried out on various diffuser geometries for development and evaluation of theoretical prediction methods. However these tests form a small part of the total effort up to the present time.

Among the most systematic recent investigations of gross geometry effect are those due to Kline and others at Stanford University. The majority of their tests were carried out on straight-wall diffusers with subsonic incompressible flow, as a large proportion of all diffuser investigations have been, and these limitations will be assumed for the remainder of this chapter, unless specifically stated otherwise. Fox and Kline (23) and Reneau et al (54) presented flow regime and performance maps respectively in terms of the two-dimensional symmetrical diffuser

geometry. These are shown in Figures 1.2(a), (b). It is seen that the gross diffuser geometry has a major effect on flow regime and performance, and that presentation of experimental data in these terms is a very powerful design aid. However the designer can inadvertently assume that diffusers designed from these maps will always give good results; this is not true since adjacent flow conditions can also have marked effects on diffuser stability and performance.

Some of the inlet flow parameters/conditions which can influence diffuser flow are:

- (i) Mean velocity profile
- (ii) Flow mixing/turbulence
- (iii) Swirl
- (iv) Reynolds number.
- (v) Mach number.

(i) Mean Velocity Profile

For a given pressure gradient it can be shown that for any streamline, neglecting energy losses, the local deceleration is inversely proportional to the local mean velocity. Hence the thicker the inlet boundary layer to any diffuser the lower the mean velocity at any fixed distance from the wall, and the greater the tendency of the mean velocity profile to distortion with a high α_2 and an attendant performance penalty, as shown by equation 1.10. Waitman et al (79), Cockrell and Markland (18), and Stevens and Markland (68), working on two-dimensional, conical, and annular diffusers respectively, have all noted this reduction in diffuser performance with initial thickening of the inlet boundary layer, and correlate the performance with some characteristic boundary layer thickness or blockage parameter.

Sovran and Klomp (62) show that diffuser performance is in fact largely

governed by the distortion of the exit mean velocity profile. Considering equation 1.10 and dividing by $\overline{Cp}_{1-2}^{\text{ideal}}$, they show that the effectiveness ζ_{1-2} :

$$\zeta_{1-2} = \frac{\alpha_1 \left[1 - \frac{\alpha_2/\alpha_1}{AR_{1-2}^2} \right]}{\left[1 - \frac{1}{AR_{1-2}^2} \right]} - \frac{\lambda_{1-2}}{\left[1 - \frac{1}{AR_{1-2}^2} \right]} \quad 1.11$$

In the first term above $\alpha_2 > 1$ represents the excess kinetic energy flux of the exit velocity profile. A high value of α_2 indicates insufficient diffusion which results in a reduction of diffuser effectiveness. The second term represents the reduction in effectiveness due to energy losses; however, the expression gives no indication of the relative importance of these two terms.

Considering the maximum velocity streamline, denoted m , and assuming constant static pressure over a cross-section, we have, for incompressible flow:

$$P_m = p + \frac{1}{2}\rho U^2 \quad 1.12$$

thus

$$P_2 - P_1 = \frac{1}{2}\rho(U_1^2 - U_2^2) - \lambda_{1-2} \bar{q}_1 \quad 1.13$$

where

$$\lambda_{1-2} = \frac{P_{m1} - P_{m2}}{\bar{q}_1} \quad 1.14$$

and the effectiveness ζ_{1-2} may thus be expressed as

$$\zeta_{1-2} = \left[\frac{U_1}{\bar{U}_1} \right]^2 \left[\frac{1 - \left[\frac{U_2}{U_1} \right]^2}{1 - \frac{1}{AR_{1-2}^2}} \right] - \frac{\lambda_{1-2}}{1 - \frac{1}{AR_{1-2}^2}} \quad 1.15$$

Now at any station the effective area (A_E) is by definition

$$A_E U = \int_A u \cdot dA \quad 1.16$$

and the blocked area fraction

$$A_B = A - A_E \quad 1.17$$

These are non-dimensionalised as follows:

$$E \text{ (effective area fraction)} = A_E/A \quad 1.18$$

$$B \text{ (blocked area fraction)} = A_B/A \quad 1.19$$

By continuity the quantity flow (Q) is equal at all stations, thus:

$$\begin{aligned} Q &= \int_A u dA = A_{E_1} U_1 = A_{E_2} U_2 \\ &= A_1 E_1 U_1 = A_2 E_2 U_2 \end{aligned}$$

giving

$$\frac{U_2}{U_1} = \left[\frac{A_1}{A_2} \right] \left[\frac{E_1}{E_2} \right] \quad 1.20$$

and re-writing equation 1.15 gives

$$\zeta_{1-2} = \frac{1}{E_1^2} \left[\frac{1 - \left[\frac{E_1}{E_2} \right]^2 / AR_{1-2}^2}{1 - \frac{1}{AR_{1-2}^2}} \right] - \frac{\lambda_{1-2_m}}{1 - \frac{1}{AR_{1-2}^2}} \quad 1.21$$

If a potential core exists throughout the length of the diffuser then $\lambda_{1-2_m} = 0$, and even when this is not the case λ_{1-2_m} is often small compared with the exit profile distortion term. Thus it may be concluded that an effectiveness value of less than 100% is largely due to distortion of the outlet profile. Sovran and Klomp point out that the exit profile distortion will be determined by the inlet profile and the distortion it undergoes during diffusion. For diffusers on the $^+C_p^*$ optimum line pressure forces predominate over viscous forces and the exit velocity profile distortion is essentially governed by these pressure forces, which are in turn determined by the diffuser area ratio. Thus Sovran and Klomp were able to correlate exit

* The locus of maximum pressure recovery coefficient at prescribed non-dimensional length.

velocity profile distortion as denoted by E_2 for Cp^* diffusers in terms of the following empirical parameter involving inlet blockage fraction (B_1) and diffuser area ratio (AR_{1-2}):

$$AR_{1-2}(B_1)^{\frac{1}{4}} \quad 1.22$$

This correlation is shown in Fig. 1.3(a).

The definition of blockage area

$$A_B = A - \int \frac{u}{U} dA$$

takes the following form for axi-symmetric pipe flow:

$$\begin{aligned} A_B &= \int_0^R 2\pi r dr - \int_0^R \frac{u}{U} 2\pi r dr \\ &= 2\pi R \int_0^R \left(1 - \frac{u}{U}\right) \frac{r}{R} dr \end{aligned}$$

and hence

$$A_B = 2\pi R \delta^* \quad 1.23$$

where δ^* is the axi-symmetric boundary layer displacement thickness.

Now the inlet blocked area fraction (B_1) can be related to δ^* as follows:

$$B_1 = \frac{A_{B1}}{A_1} = \frac{2\pi R_1 \delta^*}{\pi R_1^2} = \frac{2\delta^*}{R_1} \quad 1.24$$

Thus the inlet blocked area fraction is directly proportional to the inlet boundary layer displacement thickness. This explains the success of previous correlations which, for a specific diffuser geometry with naturally developed inlet flow, relate diffuser performance to some inlet boundary layer thickness or blockage fraction.

(ii) Flow Mixing

Current boundary layer thinking indicates that a high level of flow

mixing near the wall in the diffuser inlet flow will have a beneficial effect on performance and flow stability, tending to re-energise the wall flow in the diffuser and to delay the onset of separation, thus avoiding the severe performance penalty caused by blockage of the outlet flow by the separated boundary layer.

Livesey and Turner (38) have studied the effect of high decay rate inlet velocity profiles generated by wall flow spoilers at inlet to two-dimensional diffusers. Values for diffuser effectiveness of greater than 100% were measured and, while this is mainly attributable to the failure of the accepted definition of diffuser effectiveness to take account of the kinetic energy flux of the inlet velocity profile, it still represents a 10% improvement over the effectiveness with naturally developed inflow.

For wide angle two-dimensional diffusers of 20° included angle Migai (43) eliminated flow separation by introducing flow mixing using coarse grids upstream of diffuser inlet. He also noted an optimum increase in pressure recovery from $\bar{C}_{p_{1-2}} = 30\%$, with naturally developed inlet flow, to 60% with flow mixing; however part of this increase is again probably attributable to the definition of $\bar{C}_{p_{1-2}}$.

Changes in the turbulence structure of naturally developed flows can also affect diffuser performance. Bradshaw (3), commenting on the conical diffuser test data of Cockrell and Markland (18), has suggested that fully developed inlet flow can give rise to an increase in pressure recovery coefficient, compared to that for a thin inlet boundary layer, due to the higher level of radial momentum transfer in a fully developed flow. This hypothesis has been verified in the recent work of Stevens and Williams (69).

These examples show that a high degree of flow mixing in the wall region can improve diffuser performance and current designs of mixed com-

pression intakes illustrate the use of vortex generators to improve subsonic diffuser performance. Thus where a high degree of radial momentum transfer is inherent, as it is in many engineering flows, then diffuser designs based on data from tests carried out with naturally developed inlet flows could be unnecessarily conservative.

(iii) Swirl

There have been relatively few recent published investigations on the effect of inlet flow swirl; earlier tests were made by Peters (50) and Schwartz (61) working on conical and converging-core annular diffusers respectively. Peters found that diffuser effectiveness improved with large (20°) inlet swirl components, while Schwartz noted that a similar degree of swirl caused separation from the inner cone of the annular diffuser, while a low degree of swirl was tolerated with little effect on pressure recovery.

Recent work reported by Hoadley (29) from tests on straight-core annular diffusers shows casing stall for zero inlet swirl and hub stall at large swirl angles. At intermediate conditions both walls are unstalled.

Therefore, the influence of inlet flow swirl can vary with both the degree of swirl and the diffuser geometry.

(iv), (v) Reynolds Number and Mach Number

The effects of Reynolds number and Mach number overlap to a certain degree. Initial increase in inlet Reynolds number, for a given profile generation length, causes changes in the velocity profile and turbulence structure, which will probably affect diffuser performance. At some critical Mach number, in the high subsonic range, local shock systems are formed around the inlet bend with detrimental effects on performance which intensify up to the attainment of choking flow.

Squire (65) has shown, for a suitable velocity range below the critical Mach number, that the performance of a range of conical diffusers (up to the

C_p^* optimum geometry at $AR_{1-2} = 4$) was only very weakly dependent on Reynolds number, with no clear trend being apparent. It is probable that this is also true for other diffuser geometries.

Again working with conical diffusers, Livesey and Hugh (37) investigated Mach number effects on diffusers of area ratio up to 16 and included angles 5° , 8° and 12° . Above a certain critical Mach number there is a sudden increase in losses. The critical Mach number is not constant but tends to decrease with increasing diffuser included angle. This is probably due to more marked pre-entry flow acceleration at the higher angles causing the formation of local shock systems around the inlet bend at a lower inlet Mach number.

Finally it should be noted that downstream flow conditions can modify diffuser performance; for instance, flow separation in a downstream component can cause disturbances to propagate upstream to the diffuser. However virtually no systematic experimental data is available in this field.

1.4.1 Diffusers Operating with Naturally Developed Inlet Conditions

The majority of diffuser investigations have been carried out under naturally developed inflow conditions. The work of Reneau et al (54) on symmetrical two-dimensional diffusers has previously been referred to, but some further comment is relevant at this stage. It is noted that diffuser pressure recovery is affected much more by inlet conditions than is the flow regime. Peak pressure recovery correlates as a single line on the AR_{1-2}^{-L/W_1} plot for the range of thin to thick inlet boundary layers tested. However, the region over which this correlation is valid reduces with increasing boundary layer thickness and this would suggest that the same limitations apply to the 'line of first stall'.

Earlier tests by Reid (53) on the two-dimensional diffuser geometry showed that asymmetric diffusers were prone to worse stall than the equivalent

(same L/W_1 , AR_{1-2}) symmetrical diffuser geometry but no adverse effect on optimum performance was apparent, for the geometries tested.

Cockrell and Markland (18) reported on a comprehensive series of tests carried out on a range of conical diffusers operating with thin inlet boundary layers to fully developed inflow. This data was re-analysed by Sovran and Klomp (62) and presented as a performance map in terms of the conical diffuser geometry, shown in Fig. 1.4. Two optimum lines Cp^* and Cp^{**} were defined, where:

Cp^* - is the locus of points which define the diffuser area ratio producing maximum pressure recovery in a prescribed non-dimensional length.

Cp^{**} - is the locus of points which define the diffuser non-dimensional length producing maximum pressure recovery at a prescribed area ratio

The Cp^* optimum line was shown to be reasonably independent of inlet boundary layer thickness for the range tested; however, the same reservation will apply to its use for all inlet conditions as previously stated for the two-dimensional diffuser geometry.

Several variations of the basic annular diffuser geometry occur in turbomachines, emphasising the practical importance of this type. However, due to its complex geometry it has been the subject of comparatively few systematic experimental investigations.

Ainley (1) measured the performance of a range of equiangular annular diffusers of area ratio 3.20, with thin inlet boundary layers. Diffusers with included angles from 6.5° to 19° were tested; a maximum diffuser effectiveness of 86% was measured for an 8.5° diffuser.

More recently Howard et al (30) presented performance and 'line of first stall' maps for equi-angular and straight-core annular diffusers with

fully developed inflow, see Fig. 1.5. The 'line of first stall' for equi-angular diffusers comes below that for two-dimensional diffusers given by Fox and Kline (23), while that for straight-core diffusers is for the most part above the two-dimensional diffuser line. Since a blown rig was used for these tests, while the inlet mean velocity profile is shown to compare with that of Brighton and Jones (9), it is unlikely that the turbulence structure was that of a naturally developed flow. It has been shown that the degree of flow mixing can have a marked effect on diffuser pressure recovery and to a lesser extent, flow regime, so this must be borne in mind in the interpretation of these results. Indeed the measured values of pressure recovery for the equi-angular geometry are shown to correlate with those of Johnston (31), who tested Ainley's range of diffusers with inlet profiles distorted by wire screens placed some three hydraulic diameters upstream of diffuser inlet. Further Ainley's diffusers with angles 6.5° and 8.5° and non-dimensional lengths 19.2 and 14.4 respectively fall in the 'region of appreciable stall' on the flow regime map. Yet no flow instability was noted by Ainley and the measured outlet velocity profiles show no evidence of separation or near-separation. Hence the equi-angular 'line of first stall' must be regarded with some reservation. Howard et al note in their report that there is a step at the outer-tube cone junction; this may have affected the diffuser flow regime and explain the noted lack of correlation.

Stevens and Markland (68), as part of a more detailed investigation, give performance measurements for two equi-angular annular diffusers of area ratio 4.0 with included angles of 5° and 10° . Their tests were carried out for naturally developed inlet conditions from thin inlet boundary layer to a fully developed flow. The effect of artificially thickening the inlet boundary layers with wire screen rings, placed some twenty hydraulic diameters upstream of inlet in order to minimise flow mixing effects, was also investi-

gated. They found that diffuser effectiveness steadily decreases with increasing blockage fraction, including that due to the artificially thickened profiles. A maximum effectiveness of 95% was noted for the 5° included angle diffuser, both diffusers exhibiting asymmetry of flow over a large proportion of their length.

By far the most comprehensive investigation of the annular diffuser geometry is that of Sovran and Klomp (62), who tested over one hundred diffuser geometries, most of which had diverging centre-bodies. The tests were carried out for a thin inlet boundary layer condition ($B_1 \approx 0.02$). The results, in the form of a performance map, are shown in Fig. 1.6. The tests indicated that the C_p^* optimum diffuser occurred at an area ratio that was reasonably independent of the combination of wall angles and radius ratio employed. The effect of inlet blockage fraction on the performance of the C_p^* optimum diffuser was predicted using the previously described $E_2 - AR_{1-2}(B_1)^{\frac{1}{4}}$ correlation. The line for this correlation was taken from a 'best fit' of all available diffuser data for all geometries.

1.4.2 Diffusers Operating with Artificially Generated Inlet Conditions

Many diffusers have been tested with 'blown' inlet conditions, which are nominally considered to be naturally developed, but may have a modified turbulence structure. Here 'artificially generated' is taken to mean an inlet profile generated by flow spoilers, screens, or similar means.

The widest range of inlet conditions has been investigated by Wolf and Johnston (83) who tested symmetrical two-dimensional diffusers for wake, jet, step-shear, and uniform shear flow inlet conditions, see Fig. 1.7. For the latter three inlet profiles, with low velocity near the wall, a general deterioration in performance and flow stability was observed, whereas with wake flow at inlet the performance increased above that obtained with naturally developed inflow. Since grids comprised of small diameter wires were used to produce the inlet conditions, it is thought that a relatively

low level of turbulent mixing was introduced into the flow, and that the improvement in performance with wake flow is due primarily to the higher velocity near the wall. Peak pressure recovery performance was shown in terms of the Sovran and Klomp correlation and is over-plotted in Fig. 1.3(b). The data correlates well; however, Wolf and Johnston show that prediction of performance from this correlations is inaccurate for inlet blockage fractions in excess of 0.05.

For annular diffusers Johnston (31) tested Ainley's range of diffusers with distorted inlet profiles generated by means of upstream annular screens, mounted three hydraulic diameters upstream of diffuser inlet. The inlet profiles may be broadly classified as of the jet and step-shear types. With screens close to the diffuser inlet, some beneficial flow mixing effects were to be expected; however performance was poorer in most cases in comparison with Ainley's tests. Only in the case of one profile having a high velocity region near the outer wall was performance improved. The absence of flow mixing effects is probably due in part to the acceleration of flow downstream of the gauze prior to the diffuser inlet plane.

Tyler and Williamson (76) reported on a series of tests on a range of conical and annular diffusers for inlet blockage fractions up to 0.6. The inlet conditions are thought to be non-uniform, being produced by mounting the rig air intake section in the cross-flow of a wind tunnel. So far as is understood, inlet and outlet velocity profiles were only measured across one diameter so inlet flow asymmetry would not have been detected. For conical diffusers the static pressure recovery is shown to improve with increasing inlet blockage, which suggests a highly peaked inlet velocity profile. The performance data for annular diffusers exhibits the reverse trend and it is felt that a degree of separation must be present in the inlet annulus at blockage fractions in excess of 0.1. An example of the correlation

of the experimental data for conical diffusers at peak pressure recovery is shown over-plotted on Sovran and Klomp's $E_2 - AR(B_1)^{\frac{1}{4}}$ correlation in Fig. 1.3(c). Agreement is poor for an inlet blockage fraction in excess of 0.16. For annular diffusers deviation occurs for inlet blockages greater than 0.05. This suggests that Sovran and Klomp's correlation does not hold for highly asymmetric inlet velocity profiles of this type.

1.5 Prediction of Diffuser Performance

The basic problem in theoretical prediction of diffuser performance is to predict the growth of an internal boundary layer where, in this situation, the adverse pressure gradient is determined by the development of the boundary layer itself.

For naturally developed inlet conditions, predictions of diffuser performance have been made by a number of authors using 'integral' methods, where the variation of the boundary layer shape parameter (H) is given by some form of auxiliary equation. Examples are Cocanower et al (16), Carmichael and Pustintsev (11), and Stevens (67), who for two-dimensional, conical, and annular diffusers respectively show reasonable prediction of performance up to flow separation as compared with experimental data. Separation could not be predicted accurately because, as noted by Sovran (66), there is no reliable separation criterion.

In critical examination of the integral approach both Thompson (72) and Rotta (55) state that its range of application is severely limited unless the auxiliary equation has some physical basis, as for example in Head's entrainment equation. Thus many of the integral methods have now been superseded by the application of differential methods based on the mean flow equations with a suitable representation of the turbulence structure. These include those due to Spalding and Patankar (63) and Bradshaw et al (6), and were reviewed at the 1968 Stanford University Conference (66).

The disadvantage of these methods is that, while they should give better predictions of internal boundary layer behaviour in diffusers, they require detailed experimental data both for comparison and for turbulence models. Such detailed data on the development of mean velocity profile and turbulence structure along the diffuser is very sparse. Recourse therefore has to be made to general flat plate external boundary layer data which is invariably taken at low pressure gradients (e.g. Ludweig and Tillmann (40)) and is not representative of typical diffuser flow conditions.

However, a limited amount of diffuser-based data is available. For example, early tests by Uram (77) show the development of the mean velocity profile along a 7.5° included angle conical diffuser with a thin inlet boundary layer. Recent work of Trupp et al (74) gives the development of both mean velocity profile and turbulence structure in an 8° included angle conical diffuser of area ratio 4:1 with a thick inlet boundary layer.

For two equi-angular annular diffusers of area ratio 4:1 and 5° and 10° included angle, operating over a range of naturally developed inlet conditions, Stevens and Markland (68) show detailed measurements of velocity profile development. Traverses were taken at three circumferential positions and marked flow asymmetry was detected in both diffusers.

As can be seen from this brief review of published data the information at present available is insufficient; further more systematic investigations are required and should include the measurement of turbulence parameters.

1.6 Scope and Aims of Present Work

A comprehensive survey of diffuser literature, such as that carried out by Cockrell and King (17), shows a preponderance of work on the two-dimensional and conical geometries. The annular diffuser, while of great engineering importance, especially so in turbomachinery applications, has

been the subject of considerably less investigation. This is due in large part to the complexity of the annular geometry which prevents the simple correlation of experimental data.

Thus in view of its practical importance and the relative scarcity of data the annular diffuser was chosen as the subject of investigation, the annular geometry giving the added advantage of a flow free of 'side-wall' effects. The bulk of previous annular diffuser tests had been carried out on the 'jet pipe' geometry, broadly classified as a constant diameter outer body enclosing a conical inner body. Accordingly, so as to increase the scope of knowledge, the 'compressor exit' annular diffuser geometry was chosen, the asymmetric form with a conical outer body and constant diameter inner body being assumed so as to isolate any local effects due to the inlet bend. The objectives of the investigation were as follows:

- (i) To evaluate the overall performance of the 'compressor exit' type of annular diffuser, with incompressible flow, in terms of pressure recovery, energy losses, and flow stability over a wide range of inlet conditions.
- (ii) For certain of these inlet conditions to measure in detail the internal boundary layer growth in terms of the mean velocity and turbulence structure.
- (iii) To investigate the effect of the diffuser downstream settling length.
- (iv) In parallel with the test series, to evaluate integral prediction methods using physically based 'auxiliary equations' with a view to developing a reliable method of internal boundary layer growth prediction.

Chapters 2 and 3 describe the selection of the test diffuser geometries, the experimental facility, and the test techniques employed

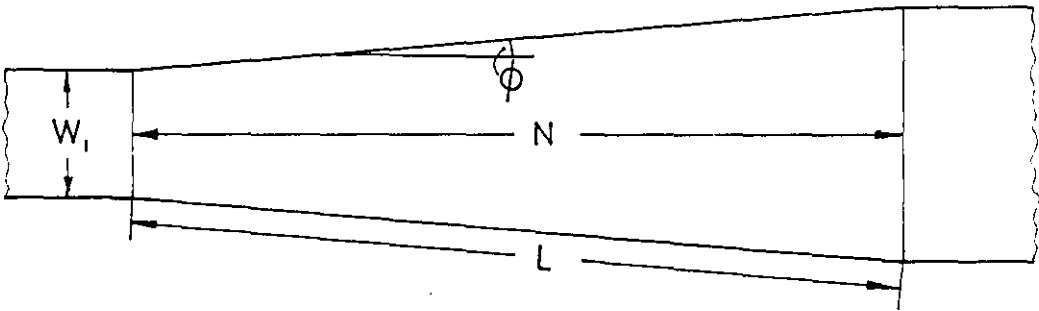
while Chapter 4 gives details of the experimental test results.

The theoretical prediction technique employed is given in Chapter 5 and results from this are compared with experimental data in Chapter 6; conclusions relevant to the whole investigation are drawn in Chapter 7.

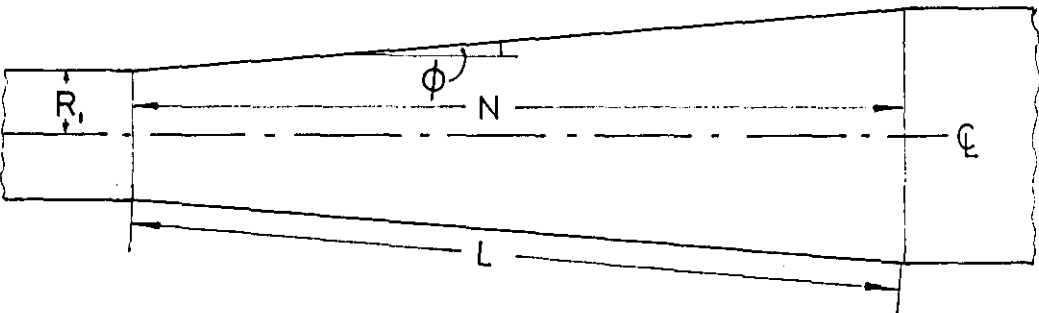
FIGURE 1.1

STRAIGHT WALL DIFFUSER—BASIC GEOMETRIES.

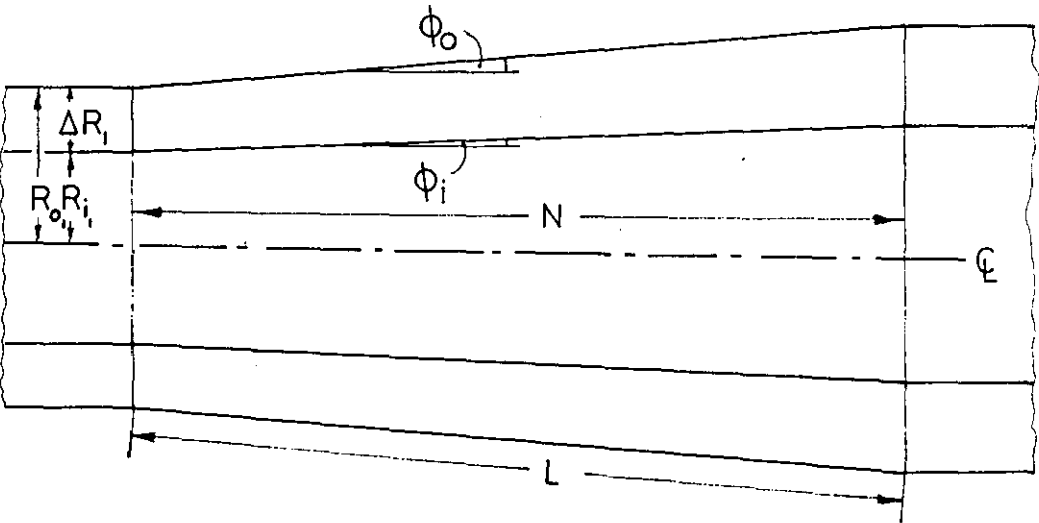
TWO-DIMENSIONAL



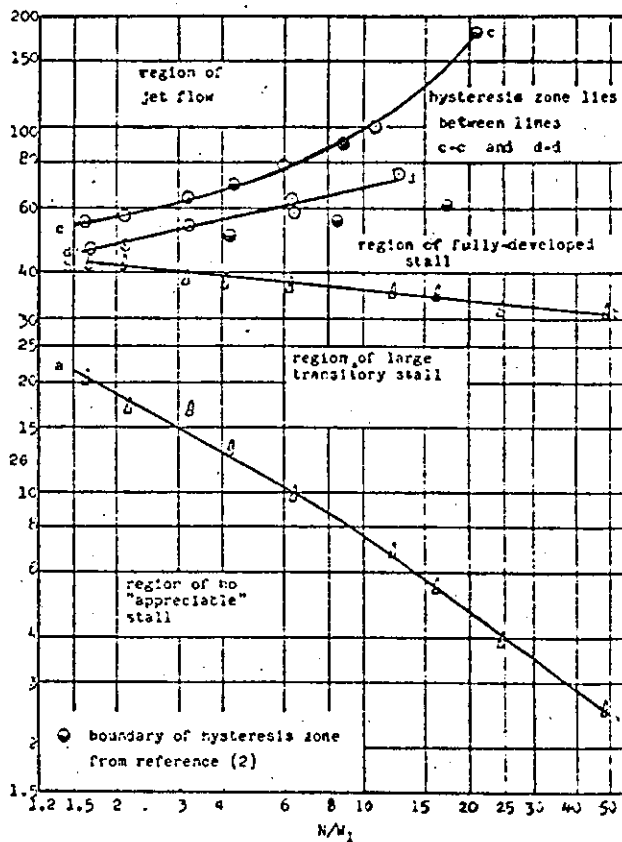
CONICAL



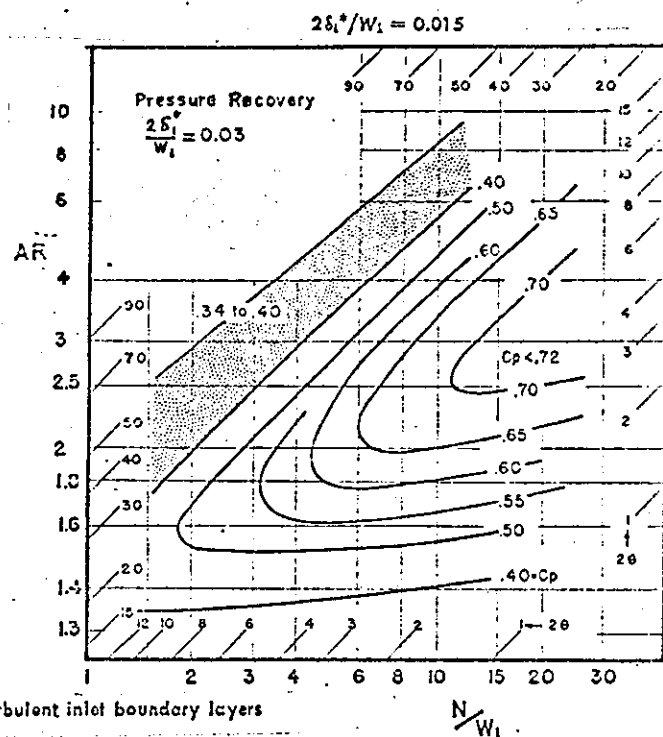
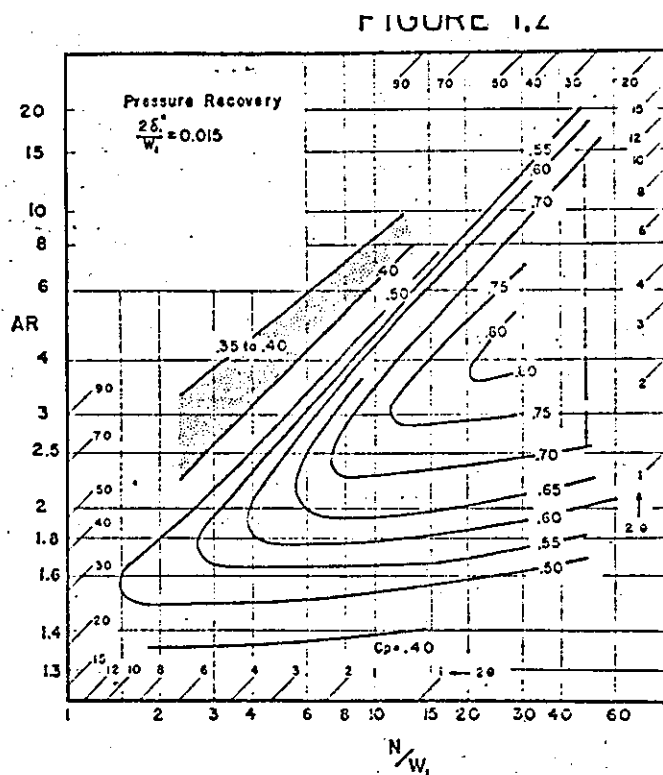
ANNULAR



TWO-DIMENSIONAL DIFFUSER PERFORMANCE & STABILITY LIMITS.

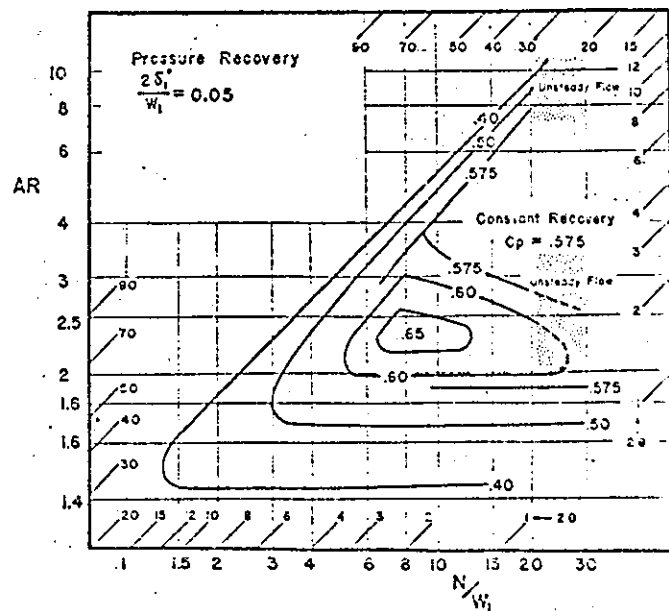
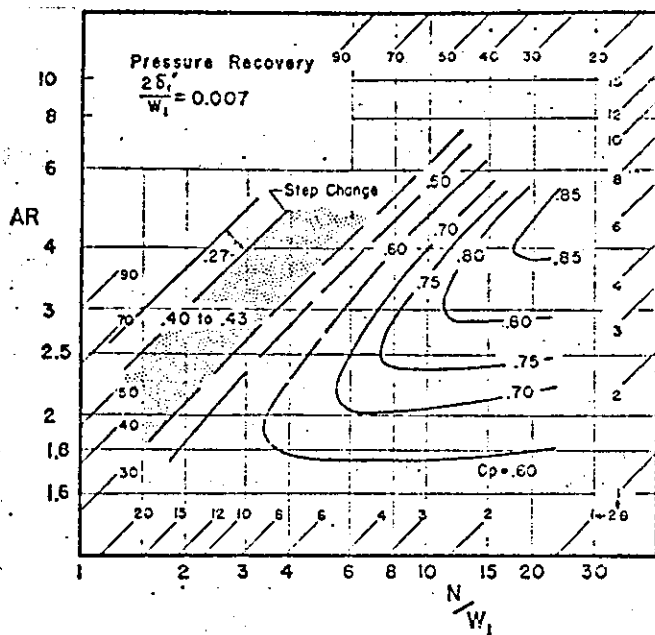


12(a) Flow regimes in two-dimensional, straight-walled diffusers
FOX & KLINE (23)

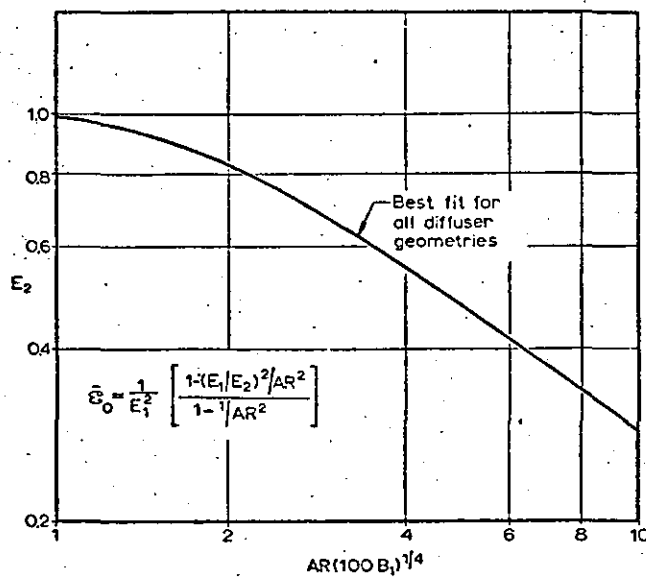


12(b) Pressure recovery of two-dimensional diffusers with turbulent inlet boundary layers

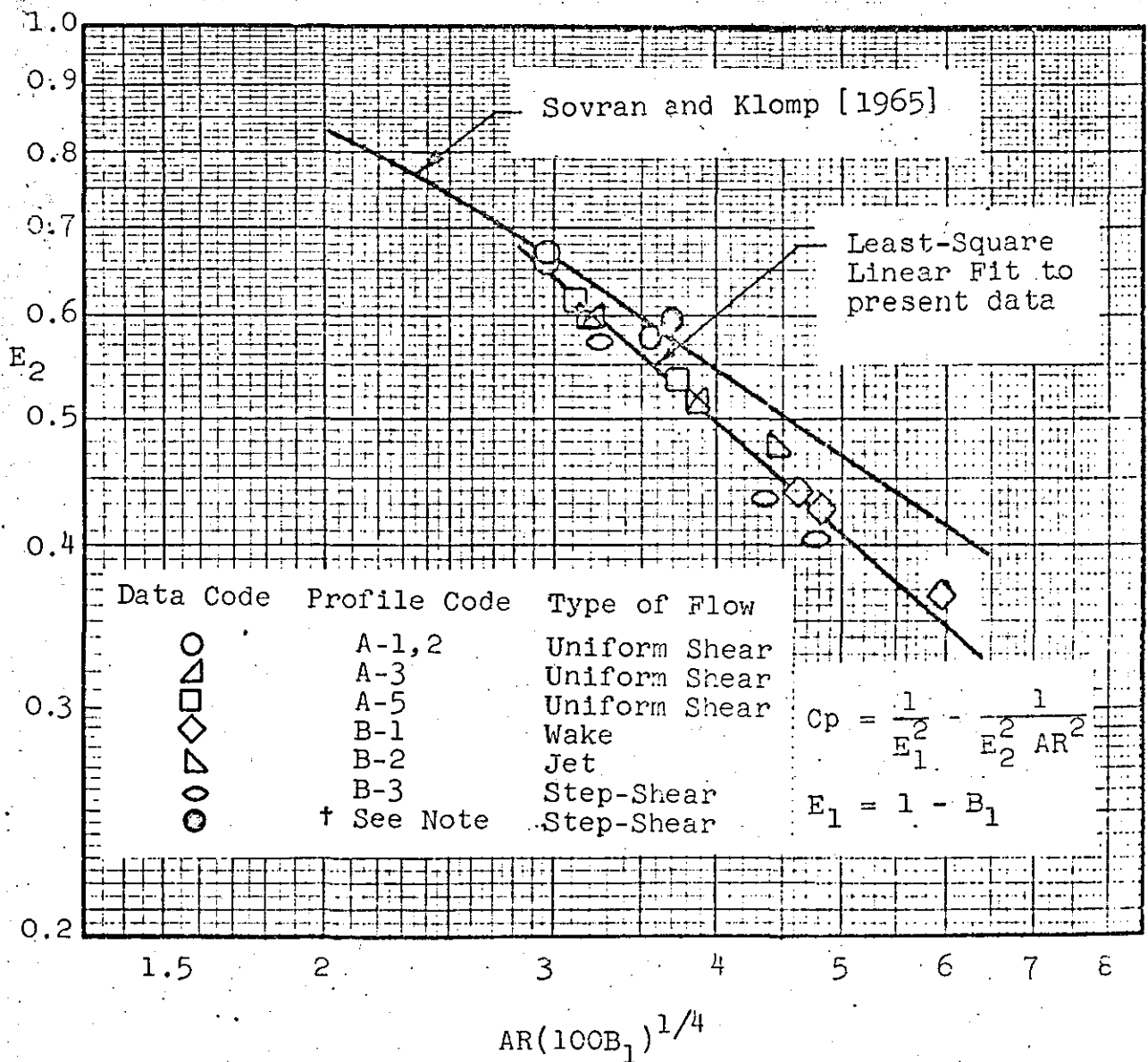
RENEAU et al (54) $\frac{2\delta_1^*}{W_1} = 0.03$



$\frac{2\delta_1^*}{W_1} = 0.007$

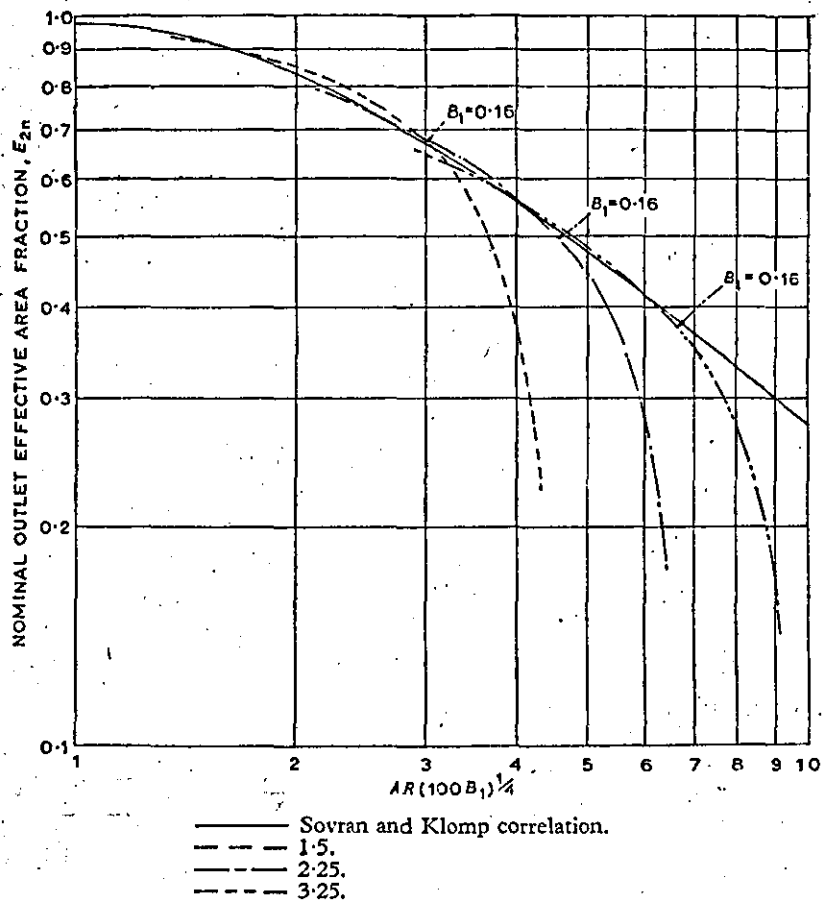


1.3(a) Effect of inlet-boundary-layer blockage on the performance of diffusers on C_p^* and near SOVRAN& KLOMP(62)



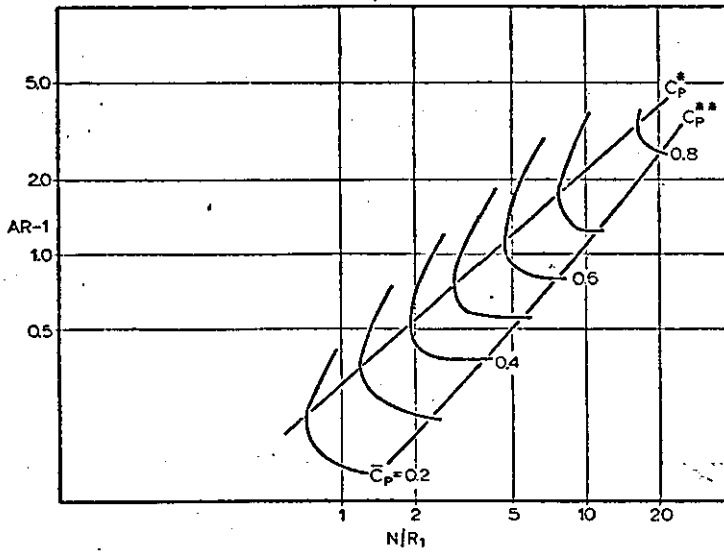
1.3(b) Correlation for peak pressure recovery at constant N/W_1 , E_2 as a function of $AR(100B_1)^{1/4}$

FIGURE 1.3(cont.)



1.3(c) TYLER & WILLIAMSON(76) — CONICAL

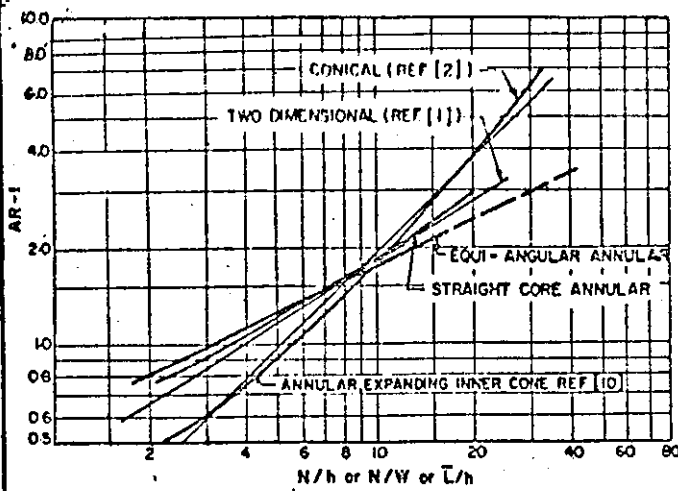
FIGURE 1.4



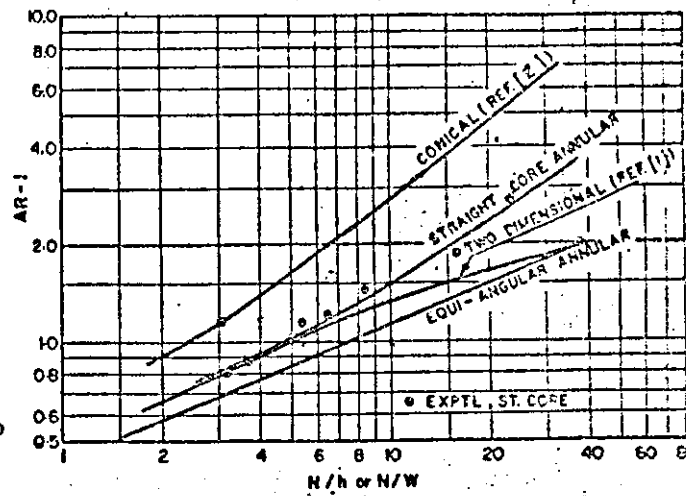
Performance chart for conical diffusers, $B_1 \approx .20$ (based on data from Cockrell & Markland).

SOVRAN & KLOMP (62)

FIGURE 1.5



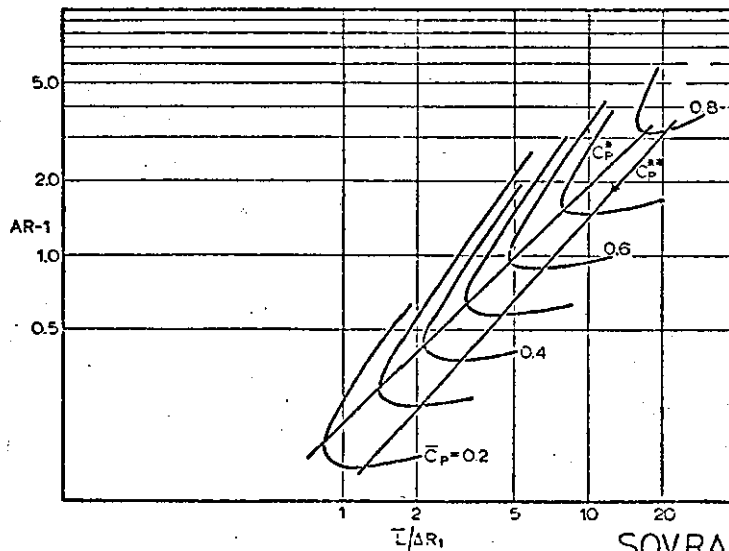
Optimum performance at constant-length ratio [data from (10) plotted against mean passage length L/h]



Lines of first stall

HOWARD et al (30)

FIGURE 1.6

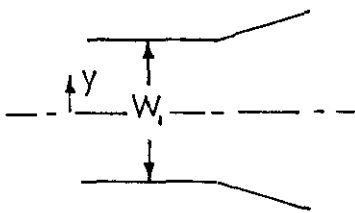
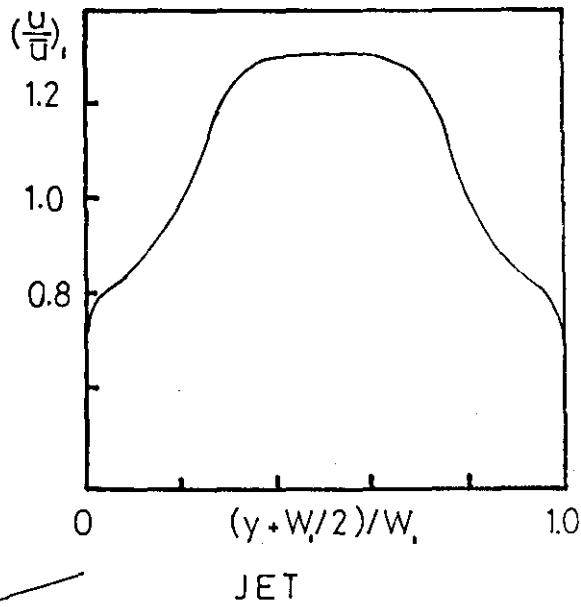
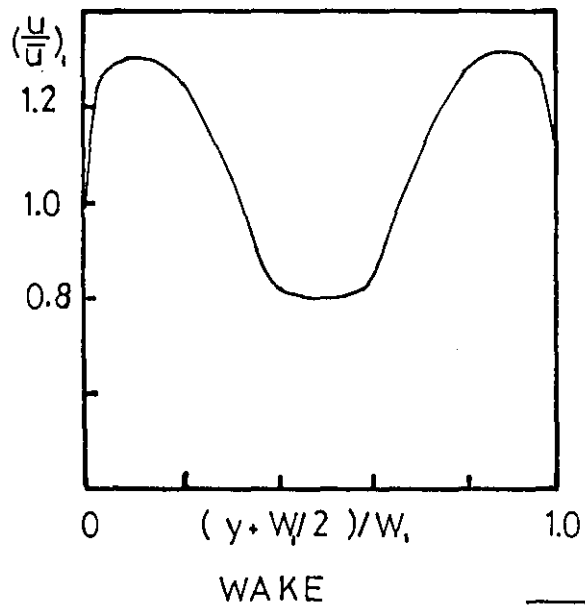
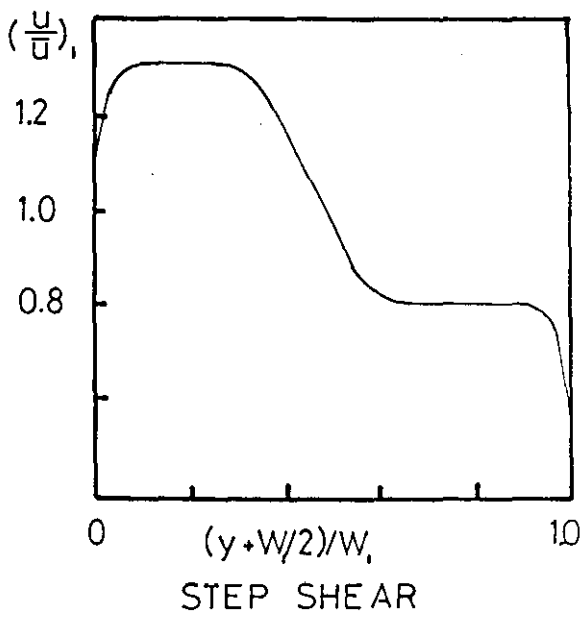
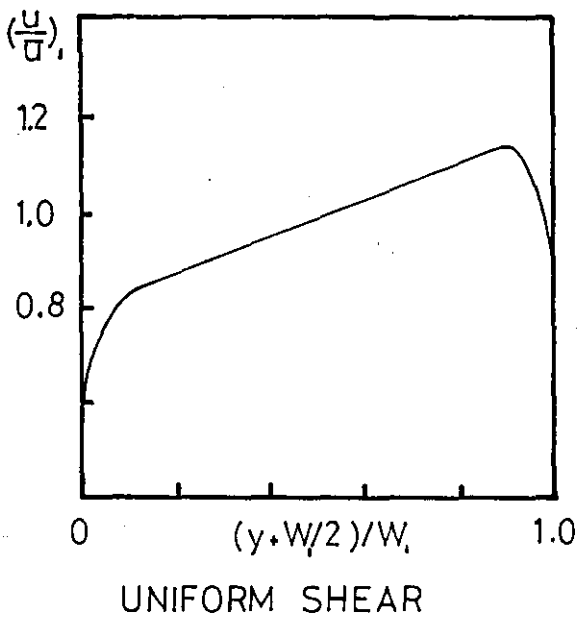


Annular-diffuser performance chart, $B_1 \approx .02$.

SOVRAN & KLOMP (62)

FIGURE 1.7

TYPICAL INLET VELOCITY PROFILES WOLF & JOHNSTON (83)



2.0 EXPERIMENTAL TEST FACILITY AND INSTRUMENTATION

2.1 Choice of Test Diffuser Geometries

Various sources were consulted in deciding on the range of test geometries. The correlation of a number of industrial gas-turbine diffuser geometries by Sovran and Klomp (62), shown in Fig. 2.1, indicates a preponderance of diffusers having an area ratio (AR_{1-2}) in the region of 2.0; however there is no clear indication of a 'typical' inlet radius ratio (R_1/R_0). Consultation with industrial sources confirmed that the area ratio of 2.0 was representative of engineering applications, and with a radius ratio of 0.85 - 0.90 this would give a typical compressor exit configuration. As this range of radius ratio also represented a useful extension to Sovran's range of test geometries it was chosen for the present test series. Due to manufacturing limitations, the figure of 0.833 was the highest obtainable but it was not felt that this represented a significant reduction.

The range of diffuser geometries was selected with a view to checking the annular diffuser stability limits indicated by Sovran and Klomp in their performance map, shown in Fig. 1.6, and ensuring that detailed data on internal flow development was taken at representative overall pressure gradients. Three geometries were chosen to make up the test range, the Cp^* and Cp^{**} optimum geometries, and a third with a more moderate pressure gradient for calibration purposes. Details of the overall geometry of these diffusers are given in Table 2.1.

TABLE 2.1
DIFFUSER GEOMETRIES

DESIGNATION	ENTRY DIA.		WALL ANGLES		AREA RATIO	N/ ΔR_1	$\left[\frac{R_i}{R_o}\right]_1$
	OUTER (in.)	INNER (in.)	OUTER ($^\circ$)	INNER ($^\circ$)			
Moderate Pressure Gradient	12.00	10.00	5.00	0.0	2.00	10.00	0.833
Cp**	12.00	10.00	6.65	0.0	2.00	7.50	0.833
Cp*	12.00	10.00	10.00	0.0	2.00	5.00	0.833

2.2 Rig Design

The diffusers were to be tested over a range of naturally and artificially developed inlet conditions and, in view of the uncertainty regarding the inlet turbulence structure presented by a 'blown' rig, a suction rig was chosen.

The general layout of the test rig is shown in Figs. 2.2 and 2.3. The choice of a vertical rig layout reduced the number of inlet support struts needed and ensured that strut interference effects were minimised. Further, eccentricity due to possible centre-body sag in the inlet length was avoided. Concentricity of the inner and outer tubes was ensured by a flanged and spigotted construction method and by manufacturing tolerances of 10.000 ± 0.002 in.

The majority of the rig flow components were fabricated from perspex allowing ease of flow visualisation and facilitating the 'setting up' of instrumentation. The path of the air flow through the rig was as follows:

Ambient air was drawn via a filter into an integral flare and bullet section (incorporating the inlet support struts), leading into an annular entry pipe of variable length, thus giving a naturally developed diffuser

inlet velocity profile ranging from near uniform flow ($L_e/D_{h_1} = 2.0$) to fully developed flow ($L_e/D_{h_1} = 50.0$). Stable transition to turbulent flow was ensured by mounting trip wires in the bell-mouth throat. After passing through the diffuser the flow entered a settling length and was discharged via a honeycomb flow straightener into a plenum box.

The plenum box was evacuated by a Keith Blackman 2513S centrifugal fan and the waste air ejected into the laboratory at a station remote from inlet so as to prevent flow recirculation. The maximum mean inlet velocity attainable under fully developed inlet flow conditions was 250ft/sec., giving a maximum inlet Reynolds number $Re_{D_{h_1}} = 2.7 \times 10^5$.

2.3 Artificially Generated Inlet Conditions

Some of the methods which can be used to generate non-uniform conditions at diffuser inlet are reviewed in Appendix 1; most of these are normally employed for the production of specific velocity distributions and take no account of the turbulence structure. It was felt that the effects of turbulent mixing should be isolated. Thus these methods were adapted to give an increased level of turbulent mixing to velocity profiles closely approximating particular naturally developed profiles.

The investigation was undertaken with the aim of quantifying the effect of increased inlet turbulent mixing on the test diffuser geometries. The two methods used were necessarily simple due to the manufacturing difficulties imposed by the combination of wall curvature and small annulus height.

These methods were:

(i) Flow Spoiler

In the diffuser used for this test the outer wall boundary layer deteriorated to a transitory stall condition under naturally developed flow conditions. The effect of a local increase in turbulent mixing at the outer wall was investigated by placing a continuous annular flow spoiler, a

selected distance upstream of the diffuser inlet plane, as shown in Fig. 2.4. In the settling distance allowed the velocity profile exhibited a low decay rate while retaining a relatively high local level of turbulent mixing.

(ii) Coarse Gauze

The objective of this method was to produce an overall increase in the level of turbulent mixing presented to the test diffusers. The inlet velocity profile selected was a near-uniform flow with thin boundary layers. Turbulence was introduced by means of a coarse gauze placed across the face of the inlet flare, as shown in Fig. 2.4; this configuration involved the minimum of additional flow energy losses. Some decay of the turbulence was expected as a result of acceleration to the flare throat, nonetheless the residual turbulence levels proved to be well in excess of the naturally developed values.

2.4 Instrumentation

The test program called for the measurement of overall performance and internal flow development for diffusers operating with incompressible flow. These were quantified in terms of the following:

- (i) wall static pressure
- (ii) mean velocity profile
- (iii) distribution of turbulence intensity
and shearing stress across the boundary
layer.

2.4.1 Measurement of Static Pressure and Mean Velocity

Static pressure measurements were made upstream of the diffuser inlet, and along the diffuser and downstream settling length. At each position three tappings 0.030in. in diameter were drilled equally spaced around the circumference of the inner and outer walls. Three radial total pressure traverses were also taken at selected stations both to allow measurement of

the mean velocity profile and to attempt to check the symmetry of flow. Details of the measuring stations, for the range of diffusers tested, are as follows:

The experimental layout and equipment for pressure and velocity measurement are shown in Figs. 2.5(a), (b) and the measuring stations detailed in Figs. 2.6(a), (b), (c). All pressure measurements were taken on a Betz micromanometer; to prevent contamination by ingested dust all tappings were blanked off when not in use.

The mounting of the pitot-tube traverse head is shown in Fig. 2.5(a) with detail of the traversing head given in Fig. 2.5(b). Traverses were taken normal to the wall, static pressure being assumed constant across the annulus and equal to the adjacent wall value. The pitot probes were slightly displaced to one side of the static tapping to prevent interference with 'near wall' measurements. These probes were made from stainless steel hypodermic tubing flattened at the end (0.047 x 0.023in.) to give an effective wall displacement of 0.015in. Different probe configurations were necessary for near inner and outer wall measurements, the probe heads being angled to ensure contact with the walls in each case.

2.4.2 Measurement of Turbulence Parameters

Turbulence measurements were taken with a D.I.S.A. 55A01 constant temperature hot wire anemometer with a mean bridge volts readout on a digital volt meter, as shown in Fig. 2.7. No suitable X-probe was available and so straight (55A53) and 45° slant (55A54) D.I.S.A. probe elements were used adopting the method used by Lee (35) as illustrated in Fig. 2.8 and fully described in Appendix 3, A.3.1. The slant wire was presented at an angle of 45° to the direction of the mean flow and could be rotated through 360° in 90° intervals by means of a square sectioned element carrier. This facility, in combination with the straight wire readings, allowed the

measurement of turbulence parameters $\overline{u'}$, $\overline{v'}$, $\overline{w'}$, $\overline{u'v'}$, $\overline{u'w'}$. The probe and carrier are shown in Fig. 2.9. They were designed to be inserted at the total pressure traverse stations, and traversed in the same manner as the pitot tubes.

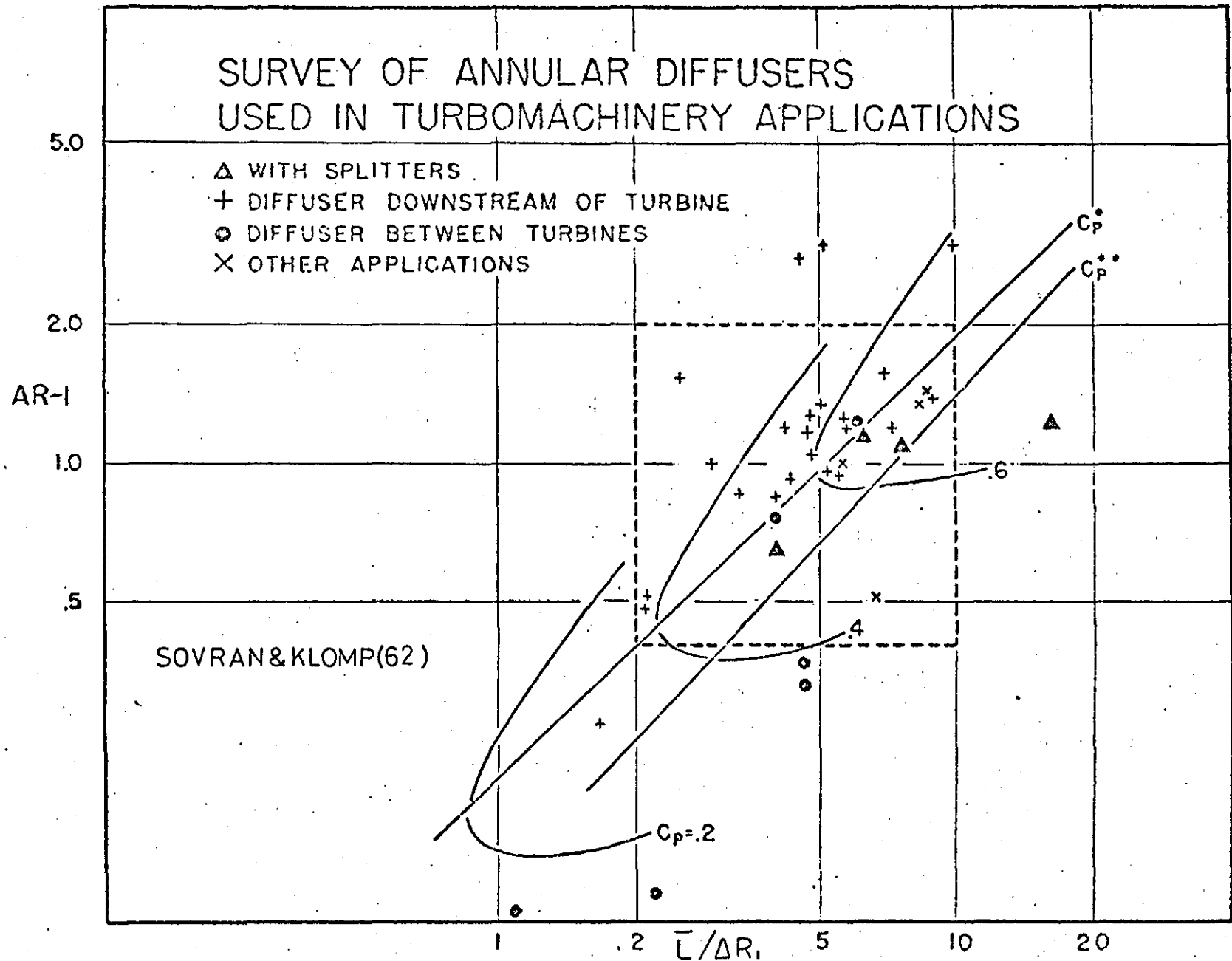


FIGURE 2.1

FIGURE 2.2

EXPERIMENTAL TEST FACILITY.

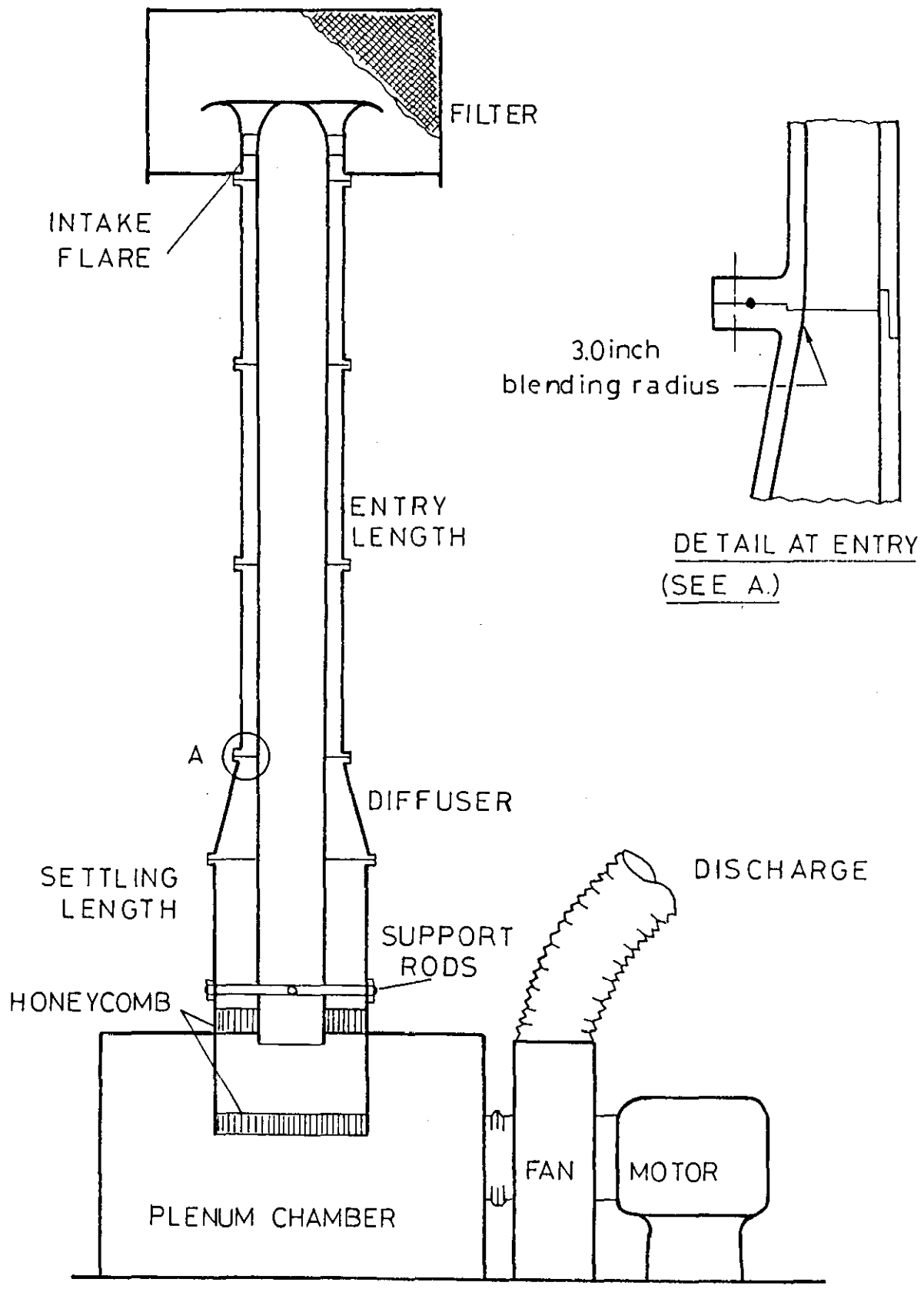


FIGURE 2.3 TEST FACILITY

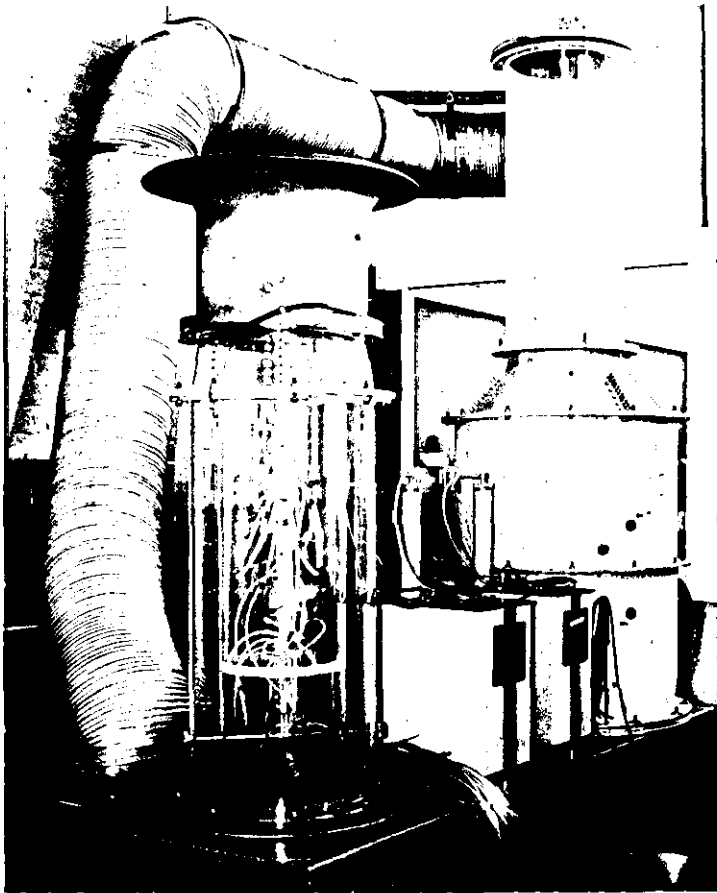


FIGURE 2.5(a) TRAVERSING EQUIPMENT

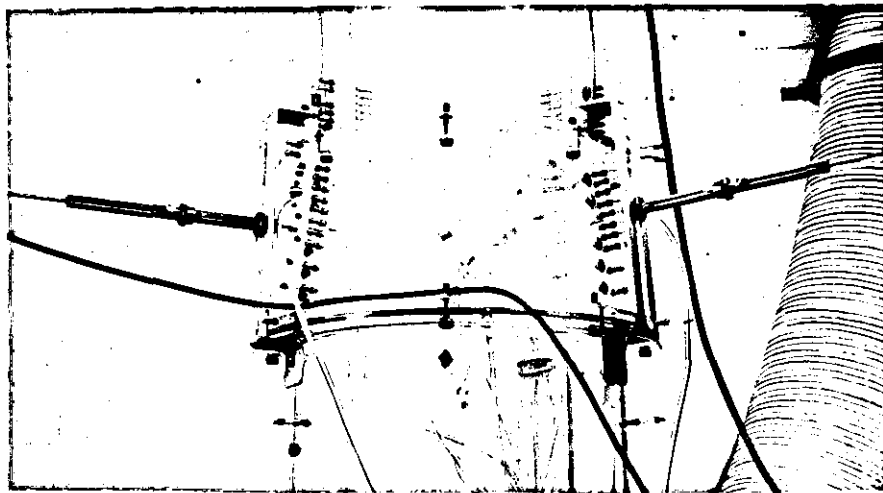


FIGURE 2.5(b) TRAVERSE HEAD

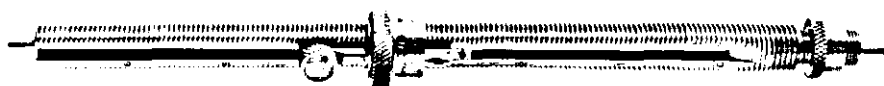


FIGURE 2.4

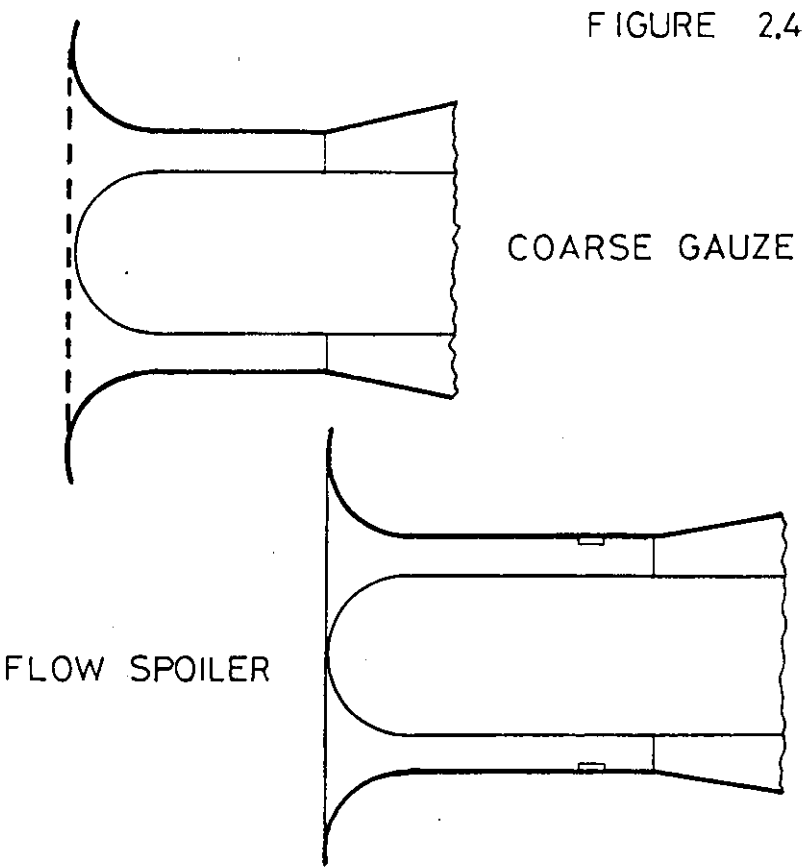
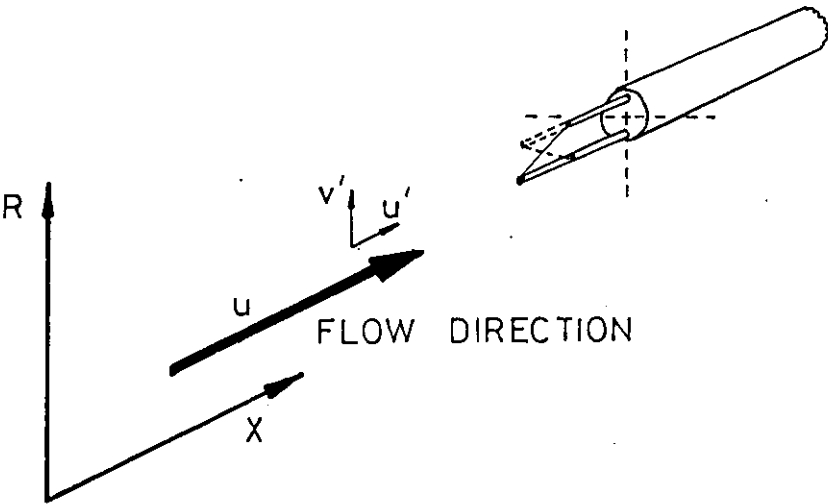


FIGURE 2.8

TURBULENT SHEAR STRESS MEASUREMENT
USING A 45° SLANT HOT-WIRE PROBE

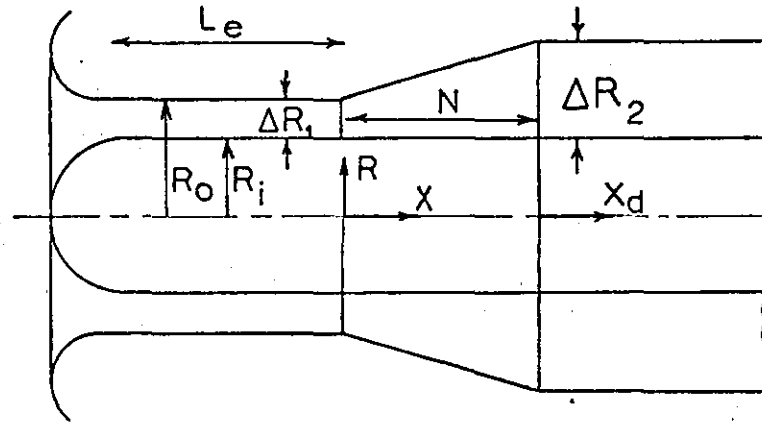


$$\bar{L}/\Delta R_1 = 10.0$$

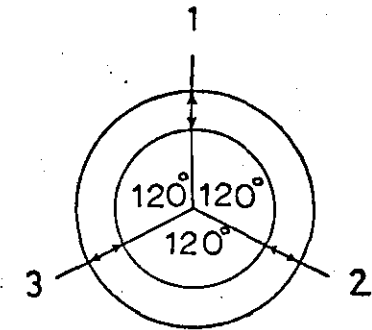
$$AR_{1-2} = 2.0$$

$$[R_i/R_o]_1 = 0.833$$

TRAVERSE STATIONS		
X/N	SYMBOL	STN
0.315	●	1
0.030	○	2
0.075	▲	3
0.145	△	4
0.215	X	5
0.270	●	6
0.370	▽	7
0.470	▼	8
0.590	⊗	9
0.770	●	10
0.985	∅	11
$x_d/\Delta R_2 = 1$	-	S1
2	-	S2
3	-	S3



GEOMETRY.	
$\phi_o = 5.0^\circ$	$N = 10.0$ IN.
$R_{o_1} = 6.0$ IN.	$R_{i_1} = 5.0$ IN.
$R_{o_2} = 6.875$ IN.	$R_{i_2} = 5.0$ IN.



TRAVERSE POSITIONS.

symbols as noted unless otherwise indicated

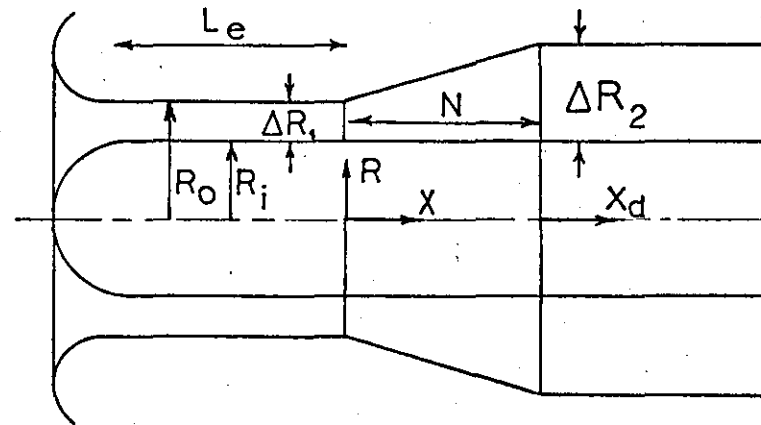
FIGURE 2.6(a)

$$\bar{L}/\Delta R_1 = 7.5$$

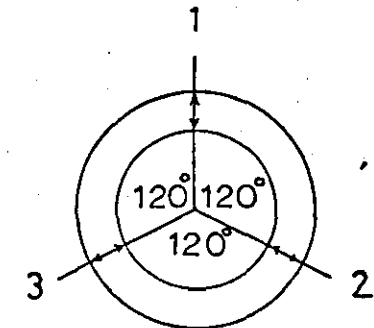
$$AR_{1-2} = 2.0$$

$$[R_i/R_o]_1 = 0.833$$

TRAVERSE STATIONS		
X/N	SYMBOL	STN
0.420	●	1
0.040	○	2
0.100	▲	3
0.167	Δ	4
0.293	X	5
0.420	⊙	6
0.547	▽	7
0.673	▼	8
0.800	⊗	9
0.963	⊙	10
$x_d/\Delta R_1 = 1$	-	S1
2	-	S2
3	-	S3



GEOMETRY.	
$\phi_o = 6.65^\circ$	$N = 7.5 \text{ IN.}$
$R_{o_1} = 6.0 \text{ IN.}$	$R_{i_1} = 5.0 \text{ IN.}$
$R_{o_2} = 6.875 \text{ IN.}$	$R_{i_2} = 5.0 \text{ IN.}$



TRAVERSE POSITIONS.

symbols as noted unless otherwise indicated

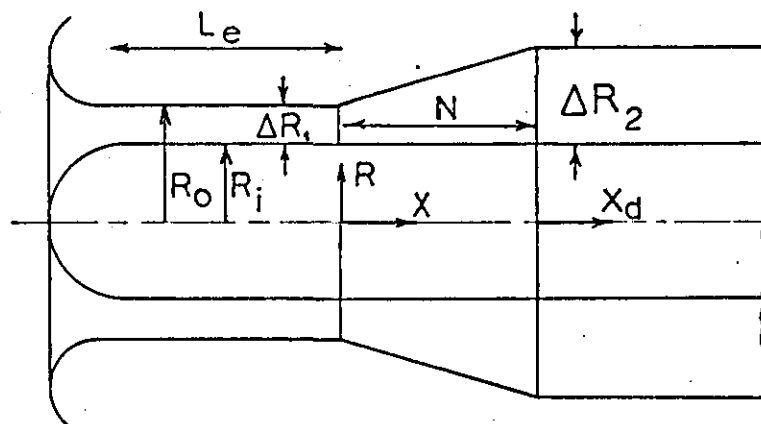
FIGURE 2.6(b)

$$\bar{L}/\Delta R_1 = 5.0$$

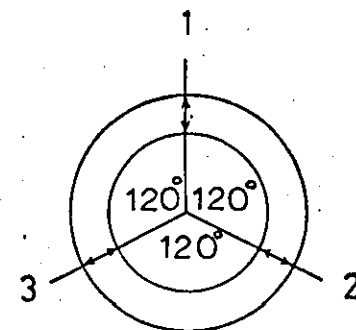
$$AR_{1-2} = 2.0$$

$$[R_i/R_o]_1 = 0.833$$

TRAVERSE STATIONS		
X/N	SYMBOL	STN
0.630	●	1
0.60	○	2
0.150	▲	3
0.270	△	4
0.390	X	5
0.510	⊙	6
0.630	▽	7
0.750	▼	8
0.856	⊗	9
0.963	⊙	10
$x_d/\Delta R_2 = 1$	-	S1
2	-	S2
3	-	S3



GEOMETRY.	
$\phi_o = 10.0^\circ$	$N = 4.96 \text{ IN.}$
$R_{o1} = 6.0 \text{ IN.}$	$R_{i1} = 5.0 \text{ IN.}$
$R_{o2} = 6.875 \text{ IN.}$	$R_{i2} = 5.0 \text{ IN.}$



TRAVERSE POSITIONS.

symbols as noted unless otherwise indicated

FIGURE 2.6(c)

CHAPTER 3

3.0 EXPERIMENTAL WORK

3.1 Test Series

The objectives of the experimental investigation were sub-divided as follows:

- (i) To evaluate the overall performance of the straight core annular diffuser over a representative range of naturally developed and artificially generated axial inflow conditions.
- (ii) To investigate in detail the diffuser internal flow development for selected inlet conditions.

3.1.1 Naturally Developed Inlet Conditions

Naturally developed inlet velocity profiles were generated by a series of inlet pipe lengths. The range of inlet lengths was initially chosen by reference to the work of Stevens and Markland (68), where the inlet velocity profile for a range of inlet lengths is characterised by blocked area fraction (B_1), as shown in Fig. 3.1. Using this data inlet lengths were chosen to give a range of inlet profiles from near uniform flow (low blockage) to fully developed flow conditions. Later in the test series the range of inlet lengths was augmented to give better coverage in the low blockage region and the final variation is shown in Table 3.1, where the velocity profiles are expressed in terms of the blocked area fraction (B_1).

TABLE 3.1

INLET LENGTH VARIATION

L_e/D_{h_1}	B_1	COMMENT
2.0	0.028	near uniform flow
4.5	0.053	
9.5	0.090	
12.0	0.109	
39.5	0.101	
50.0	0.105	fully developed flow

The range of tests carried out under naturally developed inlet conditions is summarised in Table 3.2, where the following convention has been adopted to indicate the scope of each test:

- F - measurement of the development of the internal boundary layer flows along the diffuser and settling length, measurement of inner/outer wall static pressure along the diffuser and settling length.
- T - measurement of turbulence parameters ($\overline{u'}$, $\overline{v'}$, $\overline{w'}$, $\overline{u'v'}$, $\overline{u'w'}$) in the internal boundary layer flows along the diffuser.
- S - measurement of diffuser inlet/outlet velocity profiles and inner/outer wall static pressure along the diffuser and settling length.

TABLE 3.2
TESTS WITH NATURALLY DEVELOPED INFLOW

$\frac{L/\Delta R_1}{L_e/D_{h1}}$	5.0	7.5	10.0
2.0	F	F,T	F,T
4.5	S	S	S
9.5	F	F	F
12.0	S	S	S
39.5	S	S	S

$$Re_{D_{h1}} \approx 1.7 \times 10^5$$

Together with the work of Stevens (67) for fully developed inflow the tests undertaken gave detailed data on internal mean flow development for a comprehensive range of naturally developed inlet conditions.

In view of the time available it was only possible to take detailed turbulence data for one inlet condition and it was felt that the thin inlet boundary layer case ($L_e/D_{h1} = 2.0$) merited first consideration since it

formed a logical comparison with the work of Stevens (67) regarding the universality of mixing length, eddy viscosity values, etc. for widely differing naturally developed inlet conditions.

3.1.2 Artificially Generated Inlet Conditions

Flow Spoiler

The range of diffuser tests carried out with an outer wall flow spoiler in the inlet length is given in Table 3.3. The objective of these tests was to investigate possible performance improvement for the $\bar{L}/\Delta R_1 = 5.0$ diffuser geometry having an increased level of turbulent mixing at the outer wall, as compared with naturally developed inflow, of approximately the same blockage fraction, and was undertaken in two stages:

- (i) To optimise the position of the wall flow spoiler upstream of diffuser inlet to give maximum improvement in diffuser performance in terms of pressure recovery.
- (ii) At the optimum condition to investigate fully the internal flow development along the diffuser.

TABLE 3.3

WALL FLOW SPOILER TESTS

L_e/D_{h1}	L_s/D_{h1}	TEST
9.5	2.0	*S
↓	3.0	S
	4.0	S
	5.0	S
	6.0	S
	*7.0	S, F, T
	8.0	S

$$\bar{L}/\Delta R_1 = 5.0$$

$$Re_{D_{h1}} \approx 1.6 \times 10^5$$

* Optimum geometry

+ Here denotes measurement of inlet turbulence parameters also

Coarse Gauze

The full range of diffuser geometries was tested with an increased level of inlet turbulence generated by a coarse gauze at inlet, applied to a near uniform inlet flow to allow comparison, in terms of overall performance, with tests having a near uniform naturally developed inflow. The details of these tests are given in Table 3.4 below.

TABLE 3.4

TURBULENCE GRID TESTS

\bar{L}/R_1	L_e/D_{h1}	TEST
5.0	2.0	S
7.5	2.0	S
10.0	2.0	S

$$Re_{Dh} \approx 1.6 \times 10^5$$

3.2 Experimental Technique

Before each diffuser test, prior to any measurements being taken all manometers, piping, and pitot probes were thoroughly checked for leaks and blockage. The fan was then started and allowed to run at high speed for some 30 minutes to warm up. The running point was set by adjusting the fan speed to give the required depression in the intake flare and a final period allowed for speed stabilisation.

Each diffuser test was carried out in up to four stages in the following order:

Flow behaviour

Observations were made of exit flow behaviour as indicated by wool tufts on the inner and outer walls.

Static pressure variation

Static pressure was recorded from the three circumferential tappings on the inner and outer walls for the measuring stations along the diffuser and settling length.

Mean velocity profile development

Measurements of the dynamic head, and hence velocity, variation across the diffuser annulus were made by traversing a pitot probe referenced to the adjacent wall static tapping, from the outer wall inwards to the point, or region, of maximum velocity, and similarly outwards from the inner wall. This procedure was carried out simultaneously for each of the three circumferential traverse positions at each measuring station.

Turbulence

At each of the measuring stations along the diffuser, for one circumferential position, a 45° slant hot-wire probe was traversed across the diffuser annulus in four 90° opposed configurations; this technique is fully described in Appendix 3, A.3.1. The readings from these traverses together with data from a straight-wire traverse gave the following values:

$$\sqrt{u'^2}, \sqrt{v'^2}, \sqrt{w'^2}, \overline{u'v'}, \overline{u'w'}$$

At appropriate stations asymmetry checks were carried out and as a precautionary measure the hot-wires were inspected under a microscope after each traverse to check for deformation or contamination and rejected or cleaned with Freon as necessary.

3.3 Data Reduction

3.3.1 Mean Velocity Profile Data

The boundary layer velocity profile data for the three circumferential traverse positions at the inner and outer walls respectively was non-dimensionalised in terms of the maximum velocity ($\frac{u}{U}$), and plotted in terms of distance from each respective wall. In general the symmetry of the data was such as to allow a mean line to be drawn as representative of the respective wall boundary layer velocity profiles.

These mean lines were then encoded onto punch cards for analysis by computer program. The program used a trapezoidal numerical integration

technique to generate the inner and outer wall boundary layer axi-symmetric integral parameters and, by combining both inner and outer wall profiles, the integral parameters of the annulus velocity profile.

The method of data preparation and analysis is given in detail in Appendix 2, A.2.1.

3.3.2 Turbulence Data

The raw data from hot-wire traverses in each configuration was plotted, mean lines drawn, and these lines encoded onto punch cards together with mean velocity data from the pitot-static measurements.

The computer program employed initially calculated at required intervals, in terms of distance from the respective wall, the boundary layer turbulence parameters:

$$\sqrt{\overline{u'^2}}, \sqrt{\overline{v'^2}}, \sqrt{\overline{w'^2}}, \overline{u'v'}, \overline{u'u'}, \ell, \epsilon$$

These values were then stored in the program and used in further analysis to give the turbulence integral parameters viz. the shear work integral (\mathcal{D}) and the Reynolds normal stress terms ($\int_0^\delta \overline{u'^2}, dR$, $\int_0^\delta \overline{v'^2}, dR$). Appendix 3, A.3.2 describes this analysis in full.

3.4 Accuracy

3.4.1 Experimental Accuracy

The limits of accuracy of the experimental instrumentation used are discussed in detail in Appendix 2, A.2.2 and Appendix 3, A.3.3. The following Table 3.5 summarises the main conclusions of these discussions; in each case the most pessimistic estimate is given.

TABLE 3.5
EXPERIMENTAL ACCURACY

PARAMETER	ACCURACY	
	EARLY STAGES IN DIFFUSION	LATTER STAGES OF DIFFUSION
Static pressure	.01in. water	.01in. water
Mean Velocity	2.0% (near wall region only)	20.0% (near wall region only)
Turbulence $\sqrt{u'^2}$ $\sqrt{v'^2}$ $\frac{u'v'}{u}$	5.0% 30.0% 10.0%	$\left. \begin{array}{l} 10.0-15.0\% \\ 60.0\% \\ 40\% \end{array} \right\} \text{ where } \sqrt{\frac{u'^2}{u}} > 0.20$

3.4.2 Accuracy of Calculated Parameters

The calculated parameters are liable to inaccuracy for two reasons:

- (i) The accuracy limits of the numerical integration techniques employed.
- (ii) Inaccuracy arising from errors in the basic measured data.

Of these the effect of the first is minimal since the numerical integration techniques were shown (see Appendix 2, A.2.1) to have an accuracy at least equal to that of integration by the planimeter method.

The effects of measured data errors may be summarised under the following headings:

Overall performance parameters

The use of Betz manometers resulted in accurate measurement of static pressure and it is estimated that the value of \overline{Cp}_{1-x} (general x station) is correct within 1%. However considering equation 1.10, in terms of the general x station:

$$\overline{Cp}_{1-x} = \left[\alpha_1 - \frac{\alpha_x}{AR_{1-x}^2} \right] - \lambda_{1-x} \quad 1.10$$

it is found that this error combined with possible inaccuracy in α_x , notably in the latter stages of diffusion, can give rise to errors of the order 30% in λ_{1-x} .

Boundary layer velocity profile parameters

Bearing in mind the possible errors in the determination of velocity, given in Table 3.5, it is estimated that the boundary layer integral parameters are accurate to within 3% in the early stages of diffusion and may be up to 10% inaccurate in the latter stages, where separation is imminent.

Turbulence parameters

For the purpose of clarity the possible errors in the calculated turbulence parameters attributable to errors in the measured data are given in Table 3.6. Where appropriate, allowance has been made for possible inaccuracy in the determination of the slope of the velocity profile ($\frac{du}{dR}$) as detailed in Appendix 3, A.3.3.

TABLE 3.6

INACCURACY OF CALCULATED TURBULENCE PARAMETERS

PARAMETER	ACCURACY	
	EARLY STAGES OF DIFFUSION	LATTER STAGES OF DIFFUSION
ℓ	10%	20%
ϵ	15%	30%
$\int_0^\delta \overline{u'^2} dR$	10%	20%
$\int_0^\delta \overline{v'^2} dR$	50%	100%
$D = \frac{2}{\rho U^3} \int_0^\delta \tau \frac{du}{dR} dR$	15%	30%

3.5 Preliminary Tests and Calibrations

Prior to the test series preliminary rig and instrumentation checks and calibrations were carried out.

3.5.1 Preliminary Tests

Size checks showed that all rig dimensions were within the stipulated general tolerance of 10.0in. \pm 0.002in.

Testing with the $\bar{L}/4R_1 = 10.0$ diffuser and a short inlet length ($L_e/D_{h_1} = 9.5$), the following measurements and observations were made:

Pressure variation

No appreciable circumferential pressure gradient was observed at any measuring station.

Symmetry of flow

Velocity profile measurements at the diffuser upstream measuring station showed excellent symmetry of flow at the three circumferential traverse positions with a boundary layer shape factor of 1.35, typical of the values found by Okiishi and Serovy (48) from their tests with turbulent flow at a similar Reynolds number in an annular pipe.

Flow Swirl

Wall tufts on the inner and outer walls at exit from the diffuser confirmed the absence of any appreciable degree of swirl in the diffuser.

Pre-entry static pressure variation

Measurement of the static pressure upstream of diffuser entry confirmed that the upstream datum measuring station was not in the region of influence of the outer wall inlet bend, noted by Stevens and Markland (68), as shown in Fig. 3.2.

Filter effect

The inlet filter was found to cause marked flow asymmetry and was thus not used during the test series. Subsequent tests showed that the noted

asymmetry of flow was not present when running with extremely long inlet lengths ($L_e/D_{h_1} \approx 50$).

Hot-wire operation in unfiltered flow

With the rejection of the inlet filter it became necessary to consider the possible contamination of the hot-wires by dust and other airborne impurities. This was studied by noting the probe behaviour during a prolonged exposure to the rig airflow. A marked deterioration in response was noted for periods in excess of 20 minutes and subsequent inspection under a microscope showed particles adhering to the wire; however, thorough cleaning of the wire restored the probe to its original operating condition. In the light of these findings a routine of inspecting and cleaning the probe after each traverse was adopted.

3.5.2 Calibrations

Following the preliminary tests described in Section 3.5.1 necessary rig and instrumentation calibrations were carried out.

Inlet calibration

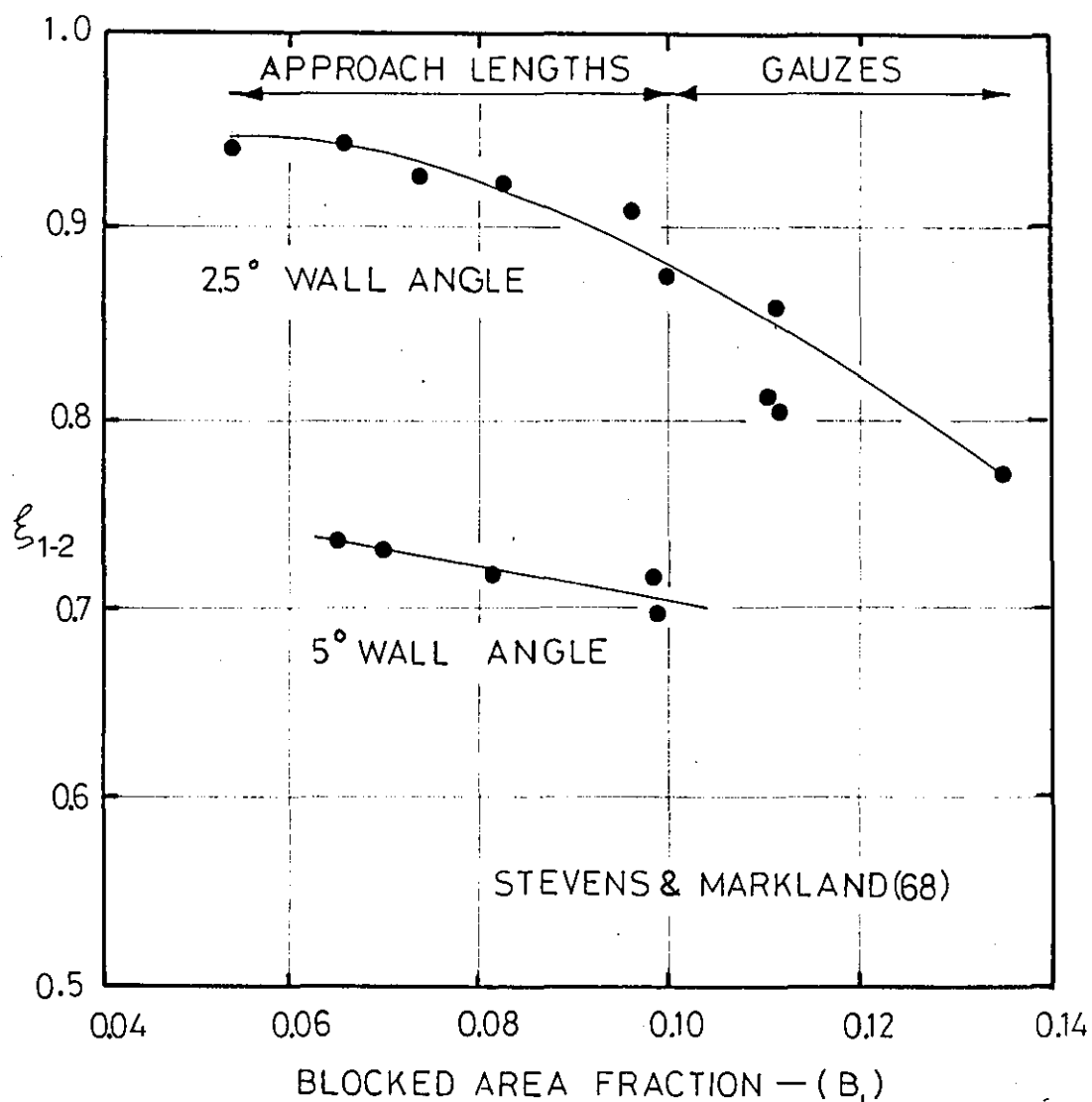
In view of the good symmetry of flow at inlet it was decided to calibrate the inlet flare/bullet to give a datum airflow for comparison purposes. This calibration gave a discharge coefficient of $C_D = 0.972$ with no observable variation over the attainable Reynolds number range.

Hot-wire calibration in fully developed flow

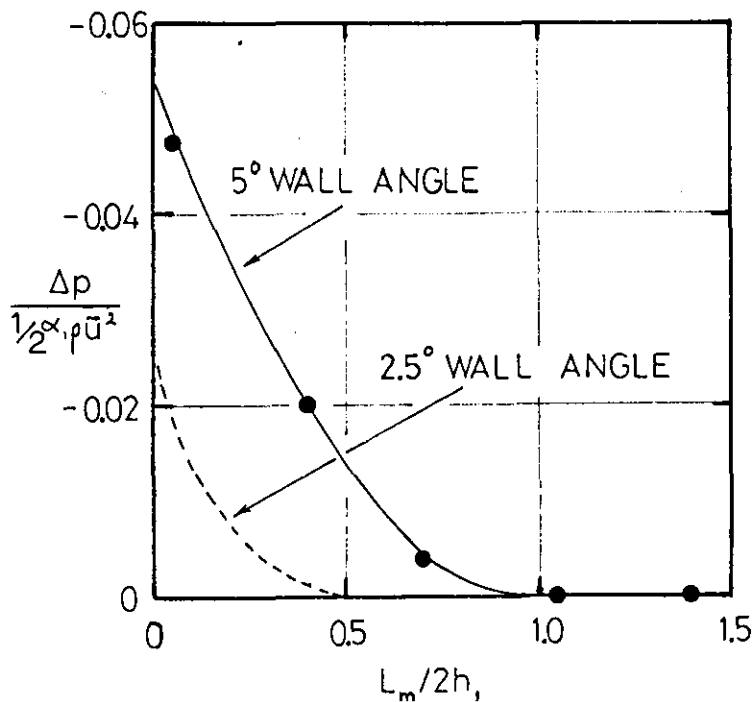
The measurement of shear stress by the slant wire technique was checked by traversing the hot-wire probe in a fully developed annular pipe ($L_e/D_{h_1} \approx 50$) calibration flow compared with the fully developed flow of Brighton and Jones (9) in Fig. 3.3. In this type of flow the turbulent stress τ is given by the relation:

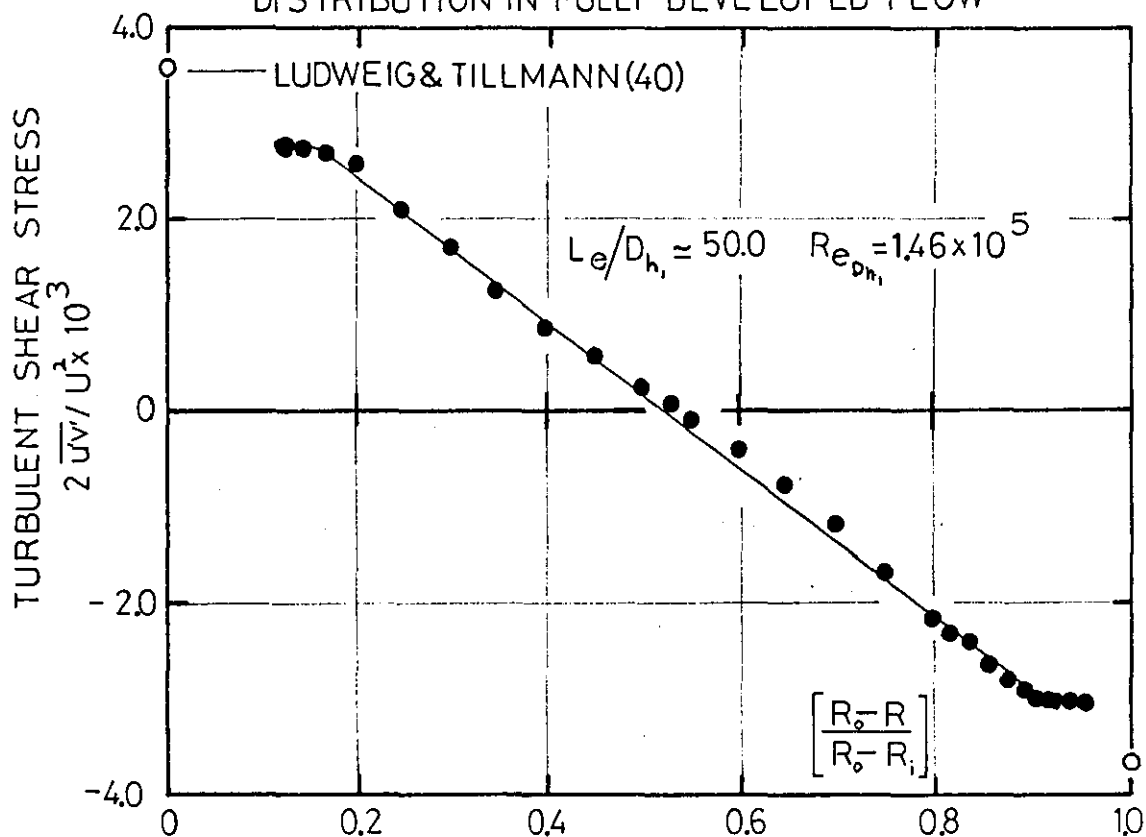
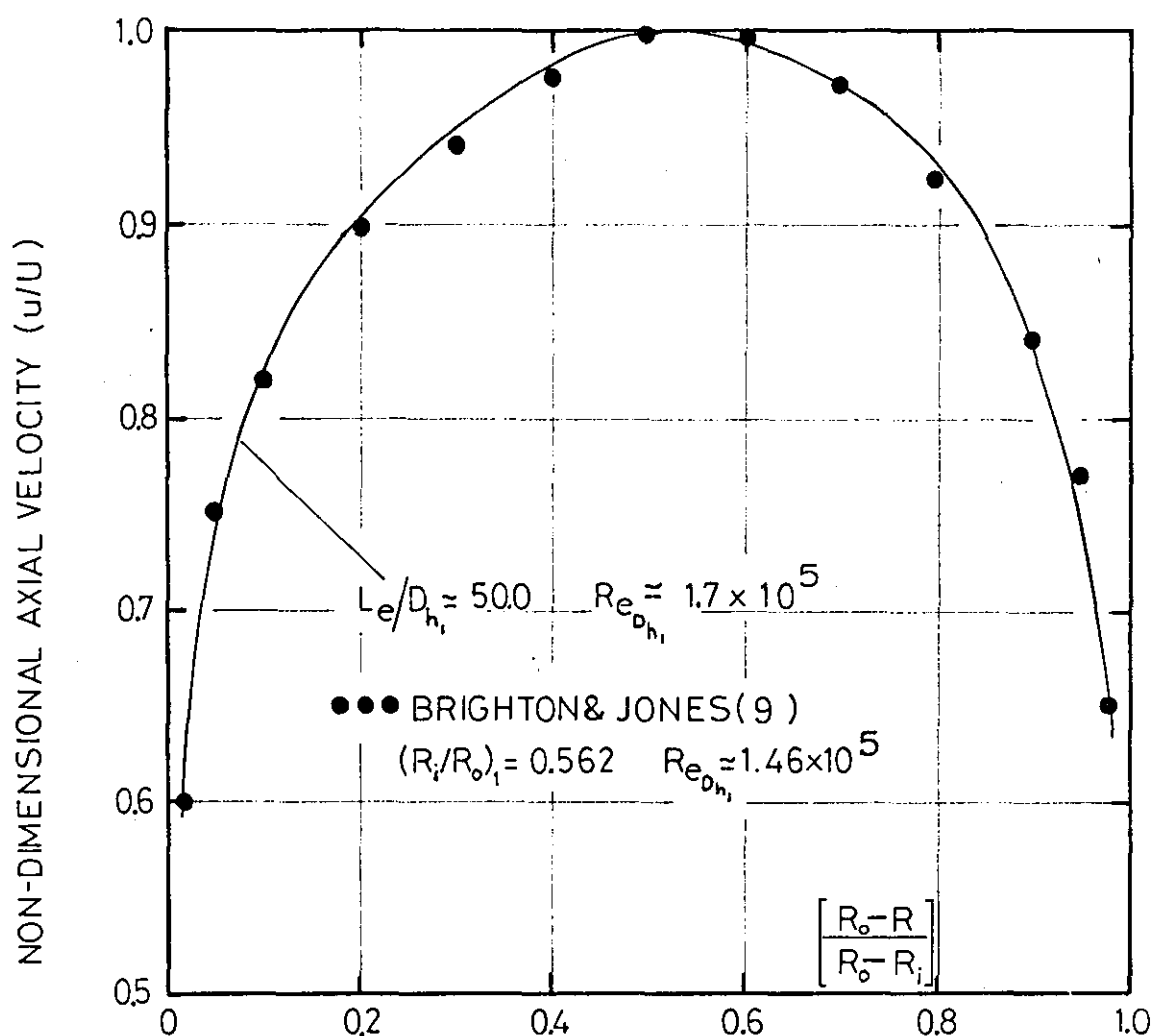
$$\tau = -\rho \overline{u'v'} = -\frac{R}{2} \frac{dP}{dx} \quad 3.1$$

hence the shear stress varies linearly with R , and measured values of shear stress for this flow should exhibit this variation. Fig. 3.4 shows shear stress measurements taken using the 45° reversed slant wire technique at the diffuser upstream measuring station in fully developed flow. The shear stress radial variation is seen to be linear and, when extrapolated to the wall, agreement with the skin friction coefficient of Ludweig and Tillmann (40) is excellent.



EFFECT OF DIFFUSER INLET BEND FIGURE 3.2
STEVENS & MARKLAND(68)





CHAPTER 4

4.0 PRESENTATION AND DISCUSSION OF EXPERIMENTAL TEST RESULTS

To clarify presentation the test results have been grouped under the general heading of 'type of inlet condition'. The bulk of graphical presentation of a repetitive nature, e.g. boundary layer velocity profiles, has been removed to the Appendices and representative examples given where pertinent to the text.

4.1 Naturally Developed Inlet Conditions

4.1.1 Diffuser Inlet Conditions

Throughout the test series an axial incompressible inflow was maintained with Reynolds number $Re_{D_{h_1}} \approx 1.75 \times 10^5$. Fig. 4.1 shows the inlet velocity profiles obtained using a range of inlet lengths. In view of the symmetry of the inlet flow, these profiles are shown as solid lines.

Table 4.1 shows the range of inlet velocity profile parameters.

TABLE 4.1

INLET VELOCITY PROFILE PARAMETERS

L_e/D_{h_1}	$\left[\frac{\delta_o^*}{\Delta R}\right]_1$	$\left[\frac{\delta_i^*}{\Delta R}\right]_1$	H_{o_1}	H_{i_1}	B_1	α_1	β_1
2.0	0.0142	0.0133	1.38	1.37	0.028	1.019	1.007
4.5	0.0253	0.0280	1.35	1.37	0.053	1.033	1.012
9.5	0.0450	0.0456	1.35	1.35	0.090	1.051	1.019
12.0	0.0523	0.0571	1.35	1.35	0.109	1.059	1.021
17.0	0.0565	0.0560	-	-	-	-	-
24.5	0.0570	0.0555	-	-	-	-	-
32.0	0.0520	0.0495	-	-	-	-	-
39.5	0.0520	0.0486	1.28	1.28	0.101	1.042	1.015
50.0	0.0545	0.0510	-	-	-	-	-

Reynolds number ($Re_{D_{h_1}}$) $\approx 1.75 \times 10^5$

The growth of boundary layer displacement thickness on the inner and outer walls is compared, in Fig. 4.2, with the data of Okiishi and Serovy (48)

from tests in an annulus for a similar Reynolds number and radius ratio, and shows good overall agreement. Over the inlet length range $L_e/D_{h_1} = 10.0 \rightarrow 50.0$, as Fig. 4.2 shows, an oscillation in the boundary layer displacement thickness on both walls is apparent, similar to that noted by Lee (35) from work on two-dimensional ducts. The extreme oscillatory behaviour of the outer wall displacement thickness noted by Okiishi and Serovy is not confirmed however, and examination of their results shows a marked degree of circumferential variation which suggests a high level of inlet flow asymmetry, probably modifying any oscillatory behaviour.

Presentation of the inlet mean velocity profiles in the form of Clauser plots for the outer and inner walls, in Figs. 4.3(a) and 4.3(b) respectively, shows that the profiles exhibit a linear form of the semi-logarithmic 'law of the wall' blending into a wake region. The thinnest inlet boundary layers ($L_e/D_{h_1} = 2.0$) are dominated by the wall and only a minor wake region is apparent.

The growth of the inlet turbulence structure, for selected inlet lengths, is illustrated in Figs. 4.4(a) and 4.4(b), in terms of the axial turbulence intensity $\frac{\sqrt{u'^2}}{U}$ and turbulent shear stress $\frac{\overline{u'v'}}{U^2}$ respectively. For the case of fully developed flow ($L_e/D_{h_1} = 39.5$) agreement with the shear stress data of Brighton and Jones (9), for a similar radius ratio and Reynolds number, is good. Further, the value of skin friction (c_f) obtained by extrapolating the shear stress distribution to the wall compares well with that given by Lüdweig and Tillmann (40).

4.1.2 Outlet Conditions and Flow Stability

From Table 4.1 a range of inlet lengths was chosen which would give a

* Fully described in Section 4.1.9

wide variation of inlet blockage fraction (B_1). For each of these blockage fractions the diffuser exit profiles were measured, and the flow state noted, for each of the test diffusers. The raw velocity profile data, together with tabulated velocity profile data, is presented in Appendix 8.

The state of the exit flow was observed using wool tufts on the inner and outer walls of the diffusers. Adopting the definitions of tuft behaviour given by Carlson and Johnston (10) as shown in Fig. 4.5, comments on the state of the exit flow, together with the accompanying velocity profile integral parameters, are given in Table 4.2; where flow asymmetry was present the worst case has been quoted.

The transitory stall which occurred in the $\bar{L}/AR_1 = 5.0$ diffuser was confined to patches on the outer wall over the region $\frac{X}{N} = 0.70 \rightarrow 1.0$.

TABLE 4.2

EXIT FLOW STATE AND VELOCITY PROFILE PARAMETERS

See page 41a

TABLE 4.2

EXIT FLOW STATE AND VELOCITY PROFILE PARAMETERS

$L_e/D_{h_1} = 2.0$ $B_1 = 0.028$								
$\bar{L}/\Delta R_1$	B_2	α_2	β_2	θ_{o_2} (in.)	θ_{i_2} (in.)	H_{o_2}	H_{i_2}	FLOW STATE
10.0	0.247	1.292	1.104	0.1195	0.1160	2.00	1.86	OUTER- S INNER- S
7.5	0.261	1.381	1.139	0.1114	0.1050	2.45	1.92	OUTER- U INNER- S
5.0	0.297	1.586	1.224	0.1047	0.0710	3.65	1.79	OUTER-IT INNER- U
$L_e/D_{h_1} = 4.5$ $B_1 = 0.053$								
$\bar{L}/\Delta R_1$	B_2	α_2	β_2	θ_{o_2} (in.)	θ_{i_2} (in.)	H_{o_2}	H_{i_2}	FLOW STATE
10.0	0.303	1.379	1.133	0.1350	0.1387	2.25	1.82	OUTER- S INNER- S
7.5	0.323	1.494	1.177	0.1310	0.1240	2.65	1.91	OUTER-TI INNER- S
5.0	0.378	1.808	1.300	0.1275	0.0867	3.89	1.73	OUTER-IT INNER- U
$L_e/D_{h_1} = 9.5$ $B_1 = 0.090$								
$\bar{L}/\Delta R_1$	B_2	α_2	β_2	θ_{o_2} (in.)	θ_{i_2} (in.)	H_{o_2}	H_{i_2}	FLOW STATE
10.0	0.320	1.378	1.130	0.1513	0.1513	2.18	1.82	OUTER- S INNER- S
7.5	0.347	1.519	1.182	0.1453	0.1296	2.64	1.85	OUTER-TI INNER- S
5.0	0.390	1.807	1.293	0.1366	0.0949	3.69	1.71	OUTER-IT INNER- U
$L_e/D_{h_1} = 12.0$ $B_1 = 0.109$								
$\bar{L}/\Delta R_1$	B_2	α_2	β_2	θ_{o_2} (in.)	θ_{i_2} (in.)	H_{o_2}	H_{i_2}	FLOW STATE
10.0	0.362	1.434	1.148	0.1566	0.1619	2.33	1.85	OUTER- S INNER- S
7.5	0.364	1.543	1.191	0.1511	0.1332	2.71	1.81	OUTER-TI INNER- S
5.0	0.406	1.833	1.297	0.1380	0.1098	3.71	1.72	OUTER-IT INNER- U
$L_e/D_{h_1} = 39.5$ $B_1 = 0.101$								
$\bar{L}/\Delta R_1$	B_2	α_2	β_2	θ_{o_2} (in.)	θ_{i_2} (in.)	H_{o_2}	H_{i_2}	FLOW STATE
10.0	0.297	1.292	1.101	0.1519	0.1426	2.03	1.64	OUTER- S INNER- S
7.5	0.331	1.406	1.142	0.1520	0.1410	2.35	1.71	OUTER- U INNER- S
5.0	0.369	1.657	1.237	0.1405	0.1107	3.24	1.67	OUTER-TI INNER- U

Reynolds number ($Re_{D_{h_1}}$) $\approx 1.75 \times 10^5$

4.1.3 Static Pressure Recovery

The static pressure recovery for each diffuser - blockage combination is given in Figs. 4.6(a), (b), (c), which show the static pressure variation in the diffuser, and Fig. 4.7, which details the local static pressure variation in the diffuser inlet plane. The data is presented in the form of pressure recovery coefficient $\overline{Cp}_{1-x} = \frac{\Delta p_{1-x}}{\frac{1}{2} \rho u_1^2}$, where the suffix (1-x) refers to the general axial x-station in the diffuser, taking the inlet station (1) as a datum.

In all cases the static pressure measured along the inner and outer walls of the diffuser and settling length showed good circumferential symmetry. Minimal radial pressure gradients are indicated save in the immediate region of the diffuser inlet plane; Fig. 4.7 illustrates the high local radial pressure gradient.

4.1.4 Overall Performance

The combination of pressure recovery data from Section 4.1.3 with that for outlet conditions from Section 4.1.2 allows evaluation of diffuser overall performance in terms of static pressure recovery and energy loss by using the relationship given in equation 1.10:

$$\overline{Cp}_{1-2} = \left[\alpha_1 - \frac{\alpha_2^2}{AR_{1-2}^2} \right] - \lambda_{1-2} \quad 1.10$$

Thus the details of diffuser overall performance were calculated and are given in Table 4.3 below. The value of pressure recovery coefficient (\overline{Cp}_{SK}) from the work of Sovran and Klomp (62) has been included for purposes of comparison.

TABLE 4.3

OVERALL PERFORMANCE

\bar{L}/R_1	B_1	\overline{Cp}_{1-2}	\overline{Cp}_{SK}	λ_{1-2}	B_2	α_2
10.0	0.028	0.615	0.610	0.085	0.247	1.292
10.0	0.053	0.610	-	0.085	0.303	1.379
10.0	0.090	0.615	-	0.090	0.320	1.378
10.0	0.109	0.600	-	0.115	0.362	1.434
10.0	0.101	0.630	-	0.090	0.297	1.292
7.5	0.028	0.605	0.620	0.080	0.261	1.381
7.5	0.057	0.575	-	0.090	0.323	1.494
7.5	0.089	0.570	-	0.110	0.347	1.519
7.5	0.109	0.575	-	0.090	0.364	1.543
7.5	0.101	0.620	-	0.075	0.331	1.406
5.0	0.027	0.515	0.610	0.120	0.297	1.586
5.0	0.053	0.455	0.550	0.130	0.378	1.808
5.0	0.090	0.470	0.515	0.125	0.390	1.807
5.0	0.109	0.470	0.535	0.130	0.406	1.833
5.0	0.102	0.540	0.525	0.085	0.369	1.657

Reynolds number ($Re_{D_h} \approx 1.75 \times 10^5$)

With initial increase in the inlet blockage fraction B_1 and attendant reduction in the 'near wall' velocities there is a decrease in static pressure recovery coefficient. With further increase of inlet length, and blockage, as the fully developed condition is approached an appreciable increase in pressure recovery coefficient is evident. This effect was first noted by Bradshaw (3), commenting on the conical diffuser work of Cockrell and Markland (17). He attributed this effect to the higher level of turbulent mixing in the 'near wall' region with fully developed flow. This increase in mixing may be seen by comparing the respective levels of turbulent shear stress at the diffuser inlet station in Fig. 4.4(b) for the $L_e/D_{h_1} = 9.5$ and 39.5 inlet lengths which have an approximately equal blocked area fraction. The higher level of radial mixing, with substantially the same inlet velocity profile, leads to a more uniform exit profile with a lower blockage and kinetic energy flux. This is graphically

illustrated for the $\bar{L}/\Delta R_1 = 5.0$ diffuser by comparison of the exit velocity profiles, for these two inlet conditions, shown in Fig. 4.8.

The prediction of the effect of inlet blockage given by Sovran and Klomp (62) for the C_p^* diffuser where pressure forces predominate, has been included in Table 4.3. This does not indicate the increase in \overline{Cp}_{1-2} when approaching fully developed flow as it is essentially velocity profile based and makes no allowance for the effects of turbulent mixing. However the conclusion drawn by Sovran and Klomp that exit flow blockage and not energy loss has the major influence on pressure recovery is clearly illustrated in Table 4.4. In this table the reduction in pressure recovery (\overline{Cp}_{1-2}) that occurs when the non-dimensional length ($\bar{L}/\Delta R_1$) of the diffuser is reduced from 10.0 to 5.0 is indicated. Using the suffix 10→5 to indicate this change, it is seen that at worst $(\Delta \lambda_{1-2})_{10 \rightarrow 5} = 0.3(\Delta \overline{Cp}_{1-2})_{10 \rightarrow 5}$ in the case of a near uniform inlet profile; while with fully developed inflow there is, within experimental error, no change in energy loss, and all of the reduction in pressure recovery must be attributed to increased exit blockage.

TABLE 4.4
PERFORMANCE PENALTIES DUE TO EXIT BLOCKAGE AND ENERGY LOSSES

$\bar{L}/\Delta R_1$	B_1	B_2	\overline{Cp}_{1-2}	λ_{1-2}
10.0	0.028	0.247	0.615	0.085
5.0	0.028	0.297	0.515	0.120
10.0	0.053	0.303	0.610	0.085
5.0	0.053	0.378	0.455	0.130
10.0	0.090	0.320	0.615	0.090
5.0	0.090	0.390	0.470	0.125
10.0	0.109	0.362	0.600	0.115
5.0	0.109	0.406	0.470	0.130
10.0	0.101	0.297	0.630	0.090
5.0	0.102	0.369	0.540	0.085

4.1.5 Comparison With Published Data

Published data of a comprehensive nature on the performance and losses

in an annular diffuser is sparse. An early series of tests by Wood et al (84) concentrated on the 'exhaust jet' type of annular diffuser with some form of inlet flow control, while the 'compressor exit' type of geometry was studied by Ainley (1) and Johnston (31). Much of this work is summarised in the N.A.C.A. publication:

'A summary of subsonic diffuser data (27)'.

More recently, interest has focussed mainly on the 'compressor exit' type of geometry and, for a limited range of geometries, the behaviour of the internal flow in this type of diffuser has been investigated by Stevens and Markland (68). However the area ratio employed ($AR_{1-2} = 4.0$) was high and makes this work unsuitable for the present comparison. Later work by Stevens and Williams (69), (70), was carried out on this type of diffuser at a more relevant area ratio ($AR_{1-2} = 2.0$).

Concentrating on overall performance and diffuser stability limits, wider studies were carried out by Sovran and Klomp (62) and Howard et al (30) respectively.

Comparison with the earlier data is shown in Figs. 4.9 and 4.10 in terms of static pressure recovery and flow energy loss respectively. It should be noted that, for the purposes of this comparison only, the following definitions apply:

$$\eta = \frac{\Delta P_{1-2} \sqrt{q_1}}{\left[\frac{AR_{1-2}^{-1}}{AR_{1-2}} \right]^2} = 4\lambda_{1-2}$$

Bearing in mind the wide spread of geometries and inlet conditions the broad comparison of data is reasonable, notably with the nearest geometrically equivalent diffusers tested by Ainley (1) and Nelson and Popp (47).

The results of Howard et al (30) from tests on the straight-core and symmetrical annular diffuser geometry are summarised in Fig. 4.11. Inter-

polating from these results for diffuser performance at the present test geometries we find the comparison given in Table 4.5 below.

TABLE 4.5

DIFFUSER PERFORMANCE - PRESENT WORK COMPARED WITH THE DATA OF
HOWARD ET AL FOR FULLY DEVELOPED INFLOW

$\bar{L}/\Delta R_1$	AR_{1-2}	$(R_1/R_o)_1$	$(R_1/R_o)_1$ HOWARD et al	$(\overline{Cp}_{1-2})_{F.D}$	$^*(\overline{Cp}_{1-2})$ HOWARD et al
10.0	2.0	0.833	0.78	0.63	0.61
7.5	2.0	0.833	0.78	0.62	0.58
5.0	2.0	0.833	0.78	0.54	0.53

* includes pressure recovery in settling length.

The performance quoted by Howard et al is at a somewhat lower level than has been found from the present tests and, although considering the possible experimental error, this difference is not large, since the static pressure recovery quoted by Howard et al must contain an additive element due to the effect of the settling length downstream (see Fig. 4.11), this does, in fact, represent quite an appreciable discrepancy. Further, when the stability limit indicated in Table 4.2 is compared with the 'line of first stall' given by Howard et al in Fig. 4.11 it would again appear that the state of the exit flow for the present tests is better. Also the 'first stall' line quoted for the equi-angular annular diffuser is in very poor agreement with the test data of Stevens and Markland (68). This suggests that the inlet turbulence structure in the rig used by Howard et al was not that of a fully developed flow.

The range of tests carried out by Sovran and Klomp (62) for a number of expanding inner cone diffusers with near uniform inlet conditions is indicated in Fig. 4.12 together with details of their test facility. Comparison of the diffuser performance with data from the present tests for near uniform inflow has been included in Table 4.3, where it is seen that

agreement is excellent save in the case of the $\bar{L}/\Delta R_1 = 5.0$ diffuser which was selected as a C_p^* optimum geometry from the performance map given by Sovran and Klomp. Table 4.2 shows that for the present tests the exit flow in this diffuser was in a transitory stall condition, while the value of pressure recovery quoted by Sovran and Klomp would seem to indicate an unstalled exit flow. This is probably attributable to a 'favourable' inlet turbulence structure in the test facility used by Sovran and Klomp, partly due to the fact that a 'blown' rig was used, and partly inherent in the design of the inlet section.

This $\bar{L}/\Delta R_1 = 5.0$ geometry merits further comment since it exhibits, in contrast to the other test diffusers, a wide variation in performance and flow behaviour over a relatively limited range of naturally developed inflow profiles. Thus the statement made by Sovran and Klomp that: 'Optimum geometry was seen to be relatively independent of inlet conditions' is not borne out and this fact must be considered when designing a C_p^* diffuser geometry for use in industrial flow conditions.

4.1.6 Effect of Downstream Settling Length

For all the diffuser - inlet blockage combinations tested, radial momentum transfer in the settling length led to a more uniform velocity profile with an attendant improvement in static pressure recovery, as shown in Figs. 4.13 and 4.14.

Fig. 4.14 shows the decrease in shape parameter and energy and momentum flux coefficients along the settling length, indicating progress towards a more uniform profile, this being reflected in the improved static pressure recoveries shown in Fig. 4.13. This improvement is seen to be substantially complete within $2.0(D_{h2})$ of diffuser exit, and for the $\bar{L}/\Delta R_1 = 10.0, 7.5$ geometries \overline{Cp}_{1-x} improves to a final value in the region 0.65 - 0.67 irrespective of the inlet blockage.

For the $\bar{L}/\Delta R_1 = 5.0$ diffuser the effect of the settling length is blockage dependent, having less effect ($\overline{Cp}_{1-x} = 0.63$) in the medium blockage range, $B_1 = 0.05 \rightarrow 0.09$ ($L_e/D_{h_1} = 4.0 \rightarrow 10.0$). This is no doubt due to the poor state of the exit flow at these inlet blockage fractions (see Table 4.2), while for the uniform flow ($B_1 = 0.028$) and fully developed inlet flow cases the improved state of the exit flow allows the settling length to again exert its full effect with improvements in \overline{Cp}_{1-x} up to 0.67.

4.1.7 Internal Boundary Layer Development and Flow Stability

A detailed investigation of internal flow development in the test diffusers was made for two 'potential core' inlet conditions. These were (as noted in Section 3.1.1) for $L_e/D_{h_1} = 2.0$ and 9.5, giving a near uniform flow ($B_1 = 0.028$) and a thick inlet boundary layer flow ($B_1 = 0.09$) respectively.

The 'raw' velocity profile data is given in Appendix 7 with tabulated values of the integral parameters, while plots showing the development of the mean velocity profile (mean of three circumferential traverse positions) are given in Figs. 4.15 \rightarrow 4.26. The accuracy limits of these measurements have been quoted in Section 3.4 and are substantiated by the fact that the integrated quantity flows at the traverse stations along each diffuser agree to within $\pm 1.5\%$ of the inlet datum flow.

While the diffuser tests with fully developed inflow indicated excellent symmetry of flow at all measuring stations (see Appendix 8 and Stevens (67)), for the tests carried out under 'potential core' inlet conditions a degree of exit flow asymmetry was present and in evaluating this the $\bar{L}/\Delta R_1 = 7.5$ diffuser was fully analysed, in that where any asymmetry was apparent a full circumferential analysis was carried out at that station. The results of this analysis are illustrated in Fig. 4.27 in terms of shape parameter (H) and momentum thickness (θ), and it is seen that even with apparent marked

asymmetry ($\bar{L}/AR_1 = 7.5$, $B_1 = 0.028$, EXIT STATION) the circumferential variation of the boundary layer integral parameters (H, θ) is not excessive.

Thus in Figs. 4.28, 4.29 mean curves are given showing the development of shape factor and momentum thickness along the test diffusers for the chosen inlet conditions. The most notable feature of these two figures is the marked disparity between the growth of the shape parameters along the inner and outer walls. This may be explained as follows.

In the absence of widely differing energy losses the velocity reduction along a streamline is, for any given pressure gradient, inversely proportional to the local velocity i.e. $du \propto \frac{1}{u}$. Thus for a symmetric inlet velocity profile having the same boundary layer profile on the inner and outer walls, with each boundary layer experiencing the same pressure gradient, we may reasonably expect, ignoring minor transverse curvature effects, that the boundary layer distortion in the diffuser will be the same on the inner and outer walls. However for the test diffuser geometries, as noted in Section 4.1.3 (see Fig. 4.7), the curvature around the outer wall inlet bend gives rise to a more adverse pressure gradient in the outer wall region at diffuser inlet, as compared to the inner wall, and this local adverse pressure gradient in turn causes a local distortion of the outer wall boundary layer and leads to asymmetric boundary layer growth in the diffuser. The effect of the local adverse pressure gradient is modified to a certain extent by the diffuser inlet velocity profile as inspection of Figs. 4.28 and 4.29 illustrates.

Thus for the $\bar{L}/AR_1 = 10.0$ diffuser where the inlet bend is moderate ($\phi_0 = 5^\circ$), and the inlet profile uniform, the boundary layer growth is nearly equal on both walls, while with the thicker inlet velocity profile ($B_1 = 0.090$) a marked difference in growth is apparent. For the $\bar{L}/AR_1 = 7.5$ diffuser these observations still hold true but for the $\bar{L}/AR_1 = 5.0$ geometry

the adverse effect of the more severe bend ($\phi_0 = 10^\circ$) extends to both inlet profiles.

These comments on the critical effect of the diffuser inlet bend are borne out by a recent J.S.M.E. paper by Furuya et al (24) where symmetric two-dimensional diffusers of high aspect ratio and a large included angle up to 45° , which normally produce a very low static pressure recovery, were dramatically improved by the addition of boundary layer suction slots just downstream of the inlet bend with a maximum off-take of only 3% of the total inlet flow. The improvements in recovery gained through the use of this technique are shown in Fig. 4.30.

As noted in Table 4.2 varying degrees of transitory stall were observed in the exit region of the $\bar{L}/AR_1 = 5.0$ diffuser, being dependent on the inlet condition. Unfortunately, as noted by Sovran (66), there is no completely reliable stall criterion and so in the present case the correlation of a wide range of experimental data for turbulent boundary layer stall due to Sandborn and Kline (56) has been employed. Data from the $\bar{L}/AR_1 = 5.0$ diffuser, at both inlet blockages, is compared with the Sandborn and Kline correlation in Fig. 4.31 and, as seen, transitory stall is indicated in both cases for $\frac{X}{N} > 0.70$, which agrees well with visual observations; certainly for the present tests the Sandborn and Kline correlation would seem to give a reliable indication of transitory stall.

4.1.8 Shear Stress and Turbulence Intensity

The development of the turbulence structure in the diffuser boundary layers in terms of turbulent shear stress and turbulence intensity was measured for the $\bar{L}/AR_1 = 10.0$ and 7.5 diffusers with a near uniform ($B_1 = 0.028$) inlet velocity profile. The $\bar{L}/AR_1 = 5.0$ diffuser geometry, for this inlet condition, exhibited transitory stall and the resulting unstable flow conditions rendered it impossible to obtain reliable turbulence data.

The data is presented in Appendix 7 where the turbulent shear stress is given in the form $2 \frac{\overline{u'v'}}{U^2}$ which, on extrapolation to the wall, allows comparison with the wall skin friction coefficient (c_f) given by the Ludweig and Tillmann (40) relationship:

$$c_f = 0.246(R_0)^{-0.268}(10)^{-0.678H} \quad 4.1$$

The variation of the axial turbulence intensity is presented in terms of $\frac{\sqrt{\overline{u'^2}}}{U}$, where the practice of non-dimensionalising using the local maximum velocity has been adopted throughout, the velocity measured by the pitot-static system being employed.

The turbulent shearing stress data is summarised in terms of carpet plots in Figs. 4.32 and 4.33.

Checks for flow asymmetry, and for the validity of King's Law, were carried out in selected cases and these are included in Appendix 3, A.3.4.

The values of turbulent shearing stress ($2\frac{\overline{u'v'}}{U^2}$) across the boundary layers in both diffusers exhibit a maximum which increases and moves away from the wall region as the flow proceeds downstream. This would suggest that though there are quite high levels of turbulence in the wall region they are uncorrelated, and thus not attributable to the local velocity gradient, perhaps being due to turbulence convected from upstream.

In axi-symmetric flow the mean flow equation takes the form:

$$u \frac{\partial u}{\partial x} + v \frac{\partial u}{\partial R} = - \frac{1}{\rho} \frac{dp}{dx} - \frac{\partial}{\partial x} (\overline{u'^2}) + \frac{1}{\rho R} \frac{d}{dR} (\tau R) \quad 4.2$$

for $R \gg \tau$, and ignoring the Reynolds normal stress gradient term, we have near the wall:

$$\frac{dp}{dx} = \frac{1}{R} \frac{d}{dR} (\tau R) \approx \frac{d\tau}{dR} \quad 4.3$$

being the force required to balance the pressure gradient ($\frac{dp}{dx}$). Thus, in view of the adverse pressure gradients in the test diffusers, we may expect a steep gradient of shear stress in the wall region, which inspection of

the shear stress data given in Appendix 7 shows is indeed the case.
 Table 4.6 below shows a typical comparison taken from this data.

TABLE 4.6
GRADIENT OF SHEAR STRESS AT WALL

$\bar{L}/\Delta R_1 = 10.0, B_1 = 0.028$			$\bar{L}/\Delta R_1 = 7.5, B_1 = 0.028$		
X/N	$\frac{dp/dx}{\rho U^2}$	$\left[\frac{d\tau/dR}{\rho U^2} \right]_{R=R_0}$	X/N	$\frac{dp/dx}{\rho U^2}$	$\left[\frac{d\tau/dR}{\rho U^2} \right]_{R=R_0}$
0.545	0.44	0.39	0.547	0.69	0.50
0.725	0.35	0.30	0.673	0.56	0.54
			0.800	0.43	0.42

This evidence is limited to the latter stages of diffusion, because only here were enough data points available near the wall to establish a reliable value of $\left[\frac{d\tau}{dR} \right]_{R=R_0}$. Within this limitation the relationship $\frac{d\tau}{dR} \approx \frac{dp}{dx}$ in the near wall region, for the diffuser geometries and inlet conditions tested, is confirmed.

In a general investigation of a near separating boundary layer, Spangenberg et al (64) could not verify the relationship $\frac{d\tau}{dR} \approx \frac{dp}{dx}$ near the wall but found that typically $\frac{d\tau}{dR} \approx 0.0-0.2 \frac{dp}{dx}$ with the Reynolds normal stress gradient $\left(\frac{du'^2}{dx} \right)$ providing most of the remaining force necessary to balance the pressure gradient. Further, Stevens (67) in an investigation of straight-core annular diffusers with fully developed inflow showed that $\frac{d\tau}{dR} \approx 0.5 \frac{dp}{dx}$ as the flow approached separation and again concluded that Reynolds normal stress gradient and other terms in the mean flow equation made a contribution.

Thus, from this experimental evidence, it would appear that as the flow approaches separation the gradient of Reynolds normal stresses provides part of the force required to overcome the pressure gradient. However it must be stated that under these conditions the other terms in the mean flow

equation should also be taken into account.

Where the boundary layer is proceeding against an adverse pressure gradient the shear stress structure tends to lag behind the mean flow development. A useful datum for comparison is the equilibrium boundary layer where the pressure and skin friction forces are in balance and the boundary layer has a given shape independent of Reynolds number. In representing the equilibrium boundary layer over a range of pressure gradient Nash (45) has given an empirical curve representing a correlation of experimental and theoretical data, viz:

$$G = 6.1(\pi + 1.81)^{\frac{1}{2}} - 1.7 \quad 4.4$$

where

$$\pi = \frac{\delta^*}{\tau_w} \frac{dp}{dx} - \text{'pressure gradient' parameter}$$

$$G = \left[\frac{2}{c_f} \right]^{\frac{1}{2}} \left[1 - \frac{1}{H} \right] - \text{'shape' parameter}.$$

This curve is presented in Fig. 4.34 with overplotted comparison for the test diffusers; the $\bar{L}/\Delta R_1 = 10.0$, 7.5 data indicate a condition of 'local equilibrium' in that while G and π do not remain constant, G as a function of π follows the equilibrium curve. As noted by Nash this does not mean that the shear stress distribution remains that of an equilibrium layer, and this is reflected in the comparison, given in Table 4.7, of the dissipation coefficient (\mathcal{D}) calculated from the test data with the equivalent \mathcal{D} equilibrium given by Walz (80),

$$\mathcal{D}_{\text{equilibrium}} = \frac{0.00962 + 0.1644 (\bar{H} - 1.5)^{4.81}}{R_0 (0.2317\bar{H} - 0.2644)} \quad 4.5$$

TABLE 4.7

COMPARISON WITH EQUILIBRIUM DISSIPATION COEFFICIENT

$\bar{L}/\Delta R_1 = 10.0, B_1 = 0.028, \text{ OUTER WALL}$			$\bar{L}/\Delta R_1 = 7.5, B_1 = 0.028, \text{ OUTER WALL}$		
X/N	ϕ Experiment	ϕ Equilibrium	X/N	ϕ Experiment	ϕ Equilibrium
0.030	0.00099	0.00351	0.040	0.00110	0.00350
0.100	0.00110	0.00352	0.167	0.00118	0.00360
0.225	0.00141	0.00365	0.293	0.00278	0.00374
0.325	0.00158	0.00380	0.420	0.00370	0.00389
0.425	0.00206	0.00390	0.547	0.00400	0.00399
0.545	0.00283	0.00399	0.673	0.00426	0.00405
0.725	0.00360	0.00405	0.800	0.00580	0.00410

Given the possible experimental inaccuracies (see Section 3.4), comparison of these values illustrates the degree of shear lag in the test diffusers, indicating an initial departure from an equilibrium shear stress distribution tending back towards equilibrium in the latter stages of diffusion.

All three components of the Reynolds normal stress were measured ($\overline{u'^2}$, $\overline{v'^2}$, $\overline{w'^2}$); however only the directly measured axial component has been presented since, as shown in Appendix 3, A.3.3, and also noted by Lee (35), the values of $\overline{v'^2}$ and $\overline{w'^2}$ measured using the slant wire technique are prone to inaccuracy. However, the $\overline{v'^2}$ values have been used in an attempt to make some estimate of the Reynolds normal stress contribution to the Momentum Integral Equation, discussed later in this section.

Spangenberg et al (64) note that a turbulence intensity, based on the local mean velocity, of $\frac{\sqrt{\overline{u'^2}}}{u} > 0.30$ is indicative of transitory stall, and Fig. 4.35 shows the development of this parameter at exit from the test diffusers; pitot-static measurements of the local mean velocity have been used in non-dimensionalising. The indications from this figure are that the $\bar{L}/\Delta R_1 = 10.0$ geometry should not exhibit transitory stall while the $\bar{L}/\Delta R_1 = 7.5$ diffuser should suffer a local transitory stall for $X/N > 0.70$.

Wall tuft observations confirm the former statement but not the latter.

While marked flow unsteadiness was noted in the outer wall exit region of the $\bar{L}/\Delta R_1 = 7.5$ geometry any transitory stall, if present, was extremely slight and did not reverse the wool tufts. However, on the basis of the present observations it would seem that the criterion $\frac{\sqrt{u'^2}}{u} \approx 0.30$ is a reasonable guide to the imminence of transitory stall.

4.1.9 Law of the Wall - Estimation of Skin Friction

The wall skin friction may be evaluated experimentally by such devices as the Preston or Stanton tube or a sublayer fence, however these instruments rely on the existence of a universal logarithmic velocity profile near the wall. Unfortunately, as noted by Thompson (73), in severe adverse pressure gradient the validity of the universal law of the wall is open to question, and may cause such devices to be inaccurate. The most satisfactory method of evaluating wall shear stress is by direct measurement, but the physical limitations of the test rig and the experimental complexity involved precluded its use in the present test series.

In view of these points it was decided to plot the 'law of the wall' after the method of Clauser (15), serving the dual purpose of:

- (i) investigating the validity of the law of the wall under conditions of severe adverse pressure gradient.
- (ii) obtaining an approximate value of the wall skin friction.

The law of the wall may be written:

$$\frac{u}{u_\tau} = A + B \log \left[\frac{yu_\tau}{\nu} \right] \quad 4.6$$

where in the present case $y = (R_o - R)$ or $(R - R_i)$ on the respective diffuser walls.

Noting that $\frac{u_\tau}{U} = \sqrt{\frac{c_f}{2}}$, for any given value of c_f we may write:

$$\frac{u}{U} = A' + B' \log \left[\frac{(R_o - R)U}{\nu} \right] \quad 4.7$$

On this basis a 'Clauser plot' is formed by generating a family of lines for a range of c_f values. The Clauser plots for all three test diffuser geometries with near uniform ($B_1 = 0.028$) and thick inlet boundary layer ($B_1 = 0.090$) inlet conditions are given in Appendix 7, where the following values of A and B, given by Thompson (73) as representing a wide range of experimental data, have been assumed:

$$A = 5.4$$

$$B = 5.5$$

A typical plot is given in Fig. 4.36.

The values of c_f estimated from these plots are shown for the $\bar{L}/AR_1 = 10.0, 7.5, 5.0$ diffuser geometries in Fig. 4.37. However the most notable feature of the Clauser plots is that in most cases the experimental profiles deviate from the linear law of the wall relationship before the point $y^+ = 100$, which means that forming a reliable estimation of c_f is very difficult. This deviation may be explained by again referring to equation 4.6, the law of the wall:

$$\frac{u}{u_\tau} = A + B \log \left[\frac{yu_\tau}{\nu} \right] \quad 4.6$$

This formulation is based on the assumption that there is no shear stress variation in a direction normal to the wall in the near wall region, i.e. in the present case $\frac{d\tau}{dR} \approx 0$ (near the wall).

Now as Section 4.1.8 shows, there is a large gradient of shear stress normal to the wall where $\left[\frac{d\tau}{dR} \right]_{R=R_0} \approx \frac{dp}{dx}$, thus a basic assumption made in generating the law of the wall is violated.

The simplest improvement which can be made to the 'law of the wall' to take account of the shear stress gradient at the wall may be effected by considering the relationship in the near wall region:

$$\frac{dp}{dx} = \frac{d\tau}{dR}$$

and assuming $\tau = \tau_w$ at the wall we may write

$$\tau = \tau_w + \frac{dp}{dx} y \quad 4.8$$

A more rigorous treatment is given by MacDonald (41) where a linear dependence of shear stress upon y is assumed, but this is allowed to extrapolate to a wall value τ_0 where $\tau_0 \neq \tau_w$. This approach gives:

$$u^+ = \frac{A^{\frac{1}{2}}}{k} \log_e \left[\frac{4A}{\alpha} \left[\frac{(\alpha y^+ + A)^{\frac{1}{2}} - A^{\frac{1}{2}}}{(\alpha y^+ + A)^{\frac{1}{2}} + A^{\frac{1}{2}}} \right] \right] + \frac{2}{k} \left[(\alpha y^+ + A)^{\frac{1}{2}} - A^{\frac{1}{2}} \right] + B^+ \quad 4.9$$

where

$$\tau = \alpha y + \tau_0$$

$$\alpha = a / \rho u_\tau^3$$

$$A = \tau_0 / \tau_w$$

$$k = 0.41$$

$$B^+ = \frac{B}{u_\tau} - \frac{A^{\frac{1}{2}}}{k} \log_e \left| \frac{4A}{\alpha} \right| + \frac{2A^{\frac{1}{2}}}{k}$$

If $\tau_0 = \tau_w$ then equation 4.9 simplifies to

$$u^+ = \frac{2}{k} \left[(\alpha y^+ + 1)^{\frac{1}{2}} - 1 \right] + \frac{1}{k} \log_e \left[\frac{4}{\alpha} \frac{(\alpha y^+ + 1)^{\frac{1}{2}} - 1}{(\alpha y^+ + 1)^{\frac{1}{2}} + 1} \right] + B^+ \quad 4.10$$

where $B^+ = 5.0$ for the present experimental pressure gradients. Thus in this form the law of the wall is seen to depend on the parameter α and, if $\tau = \tau_w + \frac{dp}{dx} y$, then $\alpha = \frac{v}{\rho u_\tau^3} \frac{dp}{dx}$ i.e. the ratio of the pressure to the viscous forces.

Following the work of, among others, Ludwig and Tillmann (40) the basic form of the law of the wall has been assumed to be applicable to flows over a wide range of pressure gradients. However the 'severe adverse pressure gradient' data of Ludwig and Tillmann corresponds only to values of $\alpha \leq 0.0035$; typical values for the present tests ($\bar{L}/\Delta R_1 = 7.5$ diffuser) are given in Table 4.8 where it can be seen that the values of α are very

much greater than those recorded in Ludweig and Tillmann's experiments.

TABLE 4.8
APPROXIMATE VALUES OF α PARAMETER

$\bar{L}/\Delta R_1 = 7.5$		$B_1 = 0.028$					
X/N	0.167	0.294	0.420	0.546	0.675	0.800	0.980
α	0.055	0.060	0.080	0.089	0.093	0.112	0.109
α_i	0.032	0.041	0.050	0.061	0.055	0.049	0.032

Fig. 4.38, taken from the work of MacDonald, illustrates the effect of the α parameter on the law of the wall. If the simple form $\tau = \tau_w + \frac{dp}{dx} y$ is assumed then it is possible to generate a 'Clauser plot' profile by applying experimental test values of $\frac{dp}{dx}$ in equation 4.10. For a chosen station in the $\bar{L}/\Delta R_1 = 7.5$ diffuser with $B_1 = 0.028$ this has been done and the comparison of the generated and measured Clauser profiles is shown in Fig. 4.39. While the absolute levels are not in full agreement the trend of the Clauser plot is successfully reproduced.

Though a single comparison of this sort is encouraging, to use MacDonald's relationship in a Clauser plot form would be excessively complicated and the conclusion must be drawn that reliable direct measurement techniques would give wall shear data more reliably and more quickly.

4.1.10 Mixing Length and Eddy Viscosity

The mixing length and eddy viscosity concepts represent early attempts to relate the local turbulent shear stress to the local mean velocity gradient. As turbulence models they are necessarily limited but none the less are representative of many of the simpler turbulent flow situations, and have found wide application in theoretical prediction methods, e.g. Spalding and Patankar (63).

Prandtl postulated a 'mixing length', analogous to the 'mean free path' in the kinetic theory of gases, where:

$$\tau = \rho \ell^2 \left[\frac{\partial u}{\partial y} \right]^2$$

or in the present formulation

$$\tau = \rho \ell^2 \left[\frac{\partial u}{\partial R} \right]^2 \quad 4.14$$

This concept is known to have limitations in that, for instance, it cannot allow for the so-called 'history effect' in turbulent flow but as a simple turbulence model it has stood the test of many years. A form of mixing length distribution widely adopted is a ramp function in the near wall region, with a constant value in the outer region of the boundary layer, thus:

$$\ell = k_1 y \quad 0 \leq y \leq k_2 \delta / k_1 \quad 4.15$$

$$\ell = k_2 \delta \quad k_2 \delta / k_1 < y \leq \delta \quad 4.16$$

where k_1 and k_2 are numerical constants.

The experimental mixing length distributions, non-dimensionalised in the terms $\frac{\ell}{\delta^*}$, are given in Figs. 4.40 and 4.41 for the $\bar{L}/\Delta R_1 = 10.0, 7.5$ diffuser geometries. These plots show that the ramp/constant mixing length distribution is indeed evident except in the early stages of diffusion. The choice of a non-dimensionalising length for ℓ is somewhat arbitrary and in the present case δ_{2-D}^* has been adopted in order to be consistent with Clauser's work on eddy viscosity. However, if δ is chosen as the non-dimensionalising parameter then comparison may be made with the work of Bradshaw (4, 5) for equilibrium flow and mild adverse pressure gradient, and Goldberg (25) for more severe adverse pressure gradient. Thus, in Table 4.9, a comparison of the k_2 values shows that in all three adverse pressure gradient cases the lag in turbulent shear stress development tends to depress the level of mixing length below the equilibrium value of $k_2 = 0.08$.

TABLE 4.9

DEVELOPMENT OF MIXING LENGTH

$\bar{L}/\Delta R_1 = 10.0, B_1 = 0.028$						
OUTER WALL						
X/N	0.100	0.225	0.325	0.425	0.545	0.725
{ l/δ } expt	0.045	0.040	0.049	0.054	0.054	0.054
{ l/δ } Bradshaw	0.06	→				
{ l/δ } Goldberg	0.10 } max. 0.04 } min.	→				
INNER WALL						
X/N	0.100	0.225	0.325	0.425	0.545	0.725
{ l/δ } expt	0.051	0.051	0.049	0.052	0.053	0.062
{ l/δ } Bradshaw	0.06	→				
{ l/δ } Goldberg	0.10 } max. 0.04 } min.	→				
$\bar{L}/\Delta R_1 = 7.5, B_1 = 0.028$						
OUTER WALL						
X/N	0.167	0.293	0.420	0.547	0.673	0.800
{ l/δ } expt	0.045	0.061	0.070	0.066	0.071	0.071
{ l/δ } Bradshaw	0.06	→				
{ l/δ } Goldberg	0.10 } max. 0.04 } min.	→				
INNER WALL						
X/N	0.167	0.293	0.420	0.547	0.673	0.800
{ l/δ } expt	0.045	0.054	0.062	0.050	0.063	0.057
{ l/δ } Bradshaw	0.06	→				
{ l/δ } Goldberg	0.10 } max. 0.45 } min.	→				

In respect of eddy viscosity the Boussinesq relation assumes that the turbulent shear stress

$$\tau_t = \rho \epsilon \frac{\partial u}{\partial y} \quad 4.17$$

where the total shear stress

$$\tau = \rho (\nu + \epsilon) \frac{\partial u}{\partial y} \quad 4.18$$

ϵ being termed the 'eddy viscosity'; in turbulent flow the term ν is negligible except in the immediate vicinity of the wall.

Clauser (14) showed that in the outer region of an equilibrium boundary layer the value

$$\epsilon = 0.018 U \delta_{2-D}^*$$

4.19

gave a reasonable match to experimental velocity profile data; however, later experimental investigation by Bradshaw (4) has shown that $\left[\frac{\epsilon}{U \delta_{2-D}^*} \right]$ is not constant over the whole outer region of the boundary layer.

The eddy viscosity variation exhibited in the present work is shown in Figs. 4.42 and 4.43 and, indeed, a similar eddy viscosity distribution to that of Bradshaw's work is found, but there are variations in the constant of proportionality due, no doubt, to history effects. Unfortunately the degree of scatter in this particular data precludes exact values being quoted, but the following approximate levels, shown in Table 4.10, would appear to be indicated.

TABLE 4.10

EDDY VISCOSITY VARIATION

$\bar{L}/\Delta R_1 = 10.0, B_1 = 0.028$		
OUTER WALL		
$(\epsilon/U\delta_{2-D}^*)_{max.}$	0.010	Early stages of diffusion
$(\epsilon/U\delta_{2-D}^*)_{max.}$	0.012	Latter stages of diffusion
INNER WALL		
$(\epsilon/U\delta_{2-D}^*)_{max.}$	0.011	Early stages of diffusion
$(\epsilon/U\delta_{2-D}^*)_{max.}$	0.013	Latter stages of diffusion
$\bar{L}/\Delta R_1 = 7.5, B_1 = 0.028$		
OUTER WALL		
$(\epsilon/U\delta_{2-D}^*)_{max.}$	0.013	Early stages of diffusion
$(\epsilon/U\delta_{2-D}^*)_{max.}$	0.017	Latter stages of diffusion
INNER WALL		
$(\epsilon/U\delta_{2-D}^*)_{max.}$	0.012	Early stages of diffusion
$(\epsilon/U\delta_{2-D}^*)_{max.}$	0.016	Latter stages of diffusion

4.1.11 Balance of Momentum

The Momentum Integral Equation, derived in Appendix 4, is quoted here in full in its axi-symmetric form for the outer wall of the test diffuser geometry:

$$\begin{aligned} \frac{d\theta_o}{dx} = & \frac{c_{f_o}}{2} - \frac{\theta_o}{R_o} \frac{dR_o}{dx} - \frac{\theta_o}{U} \frac{dU}{dx} (H_o + 2) + \frac{R_o^2 - R_\delta^2}{2\rho U^2 R_o} \left[\frac{dP}{dx} \right]_\delta \\ & + \frac{1}{U^2} \frac{d}{dx} \int_{R_\delta}^{R_o} (\overline{u'^2} + \overline{v'_\delta^2} - \overline{v'^2}) dR \end{aligned} \quad 4.20$$

The weighting due to $\frac{R}{R_o}$ in the Reynolds normal stress term has been neglected as being of second order importance in this case.

Since this equation is derived assuming an axi-symmetric flow free of three-dimensional effects, it provides a very useful check on the accuracy of the experimental data. Any marked divergence of the two sides of the equation is generally attributed to three-dimensional effects, and curtails the usefulness of the data as a basis for the evaluation of theoretical methods.

The comparison of the measured value of $\frac{d\theta}{dx}$ with that given by the R.H.S. of equation 4.20 is given for all three test diffuser geometries under selected inlet conditions in Appendix 11, and a typical example for the $\bar{L}/\Delta R_1 = 10.0$ diffuser geometry ($B_1 = 0.028$) is given in Fig. 4.44.

The comparison for the $\bar{L}/\Delta R_1 = 10.0, 7.5$ diffusers is excellent, and while that for the $\bar{L}/\Delta R_1 = 5.0$ geometry is not quite as good, it represents a marked improvement over much of the experimental data previously available. This point is illustrated in Fig. 4.45 where the momentum balance given by MacDonald and Stoddart (42), which is based on the data of Schubauer and Klebanoff (60), is shown to deviate massively as the boundary layer tends

towards separation, indicating major three-dimensional effects.

For the $\bar{L}/AR_1 = 10.0$, 7.5 diffuser geometries ($B_1 = 0.028$) the contribution of the term due to gradient of the Reynolds normal stresses was found to be negligible. This term was not measured for the $\bar{L}/AR_1 = 5.0$ geometry but in this case probably becomes significant only as the flow approaches transitory stall.

Thus on the basis of these comparisons the indications are that the experimental flows are substantially free of three-dimensional effects and, with the further evidence of a good mass flow balance and the symmetry of the velocity profiles, may be used with confidence in the evaluation of theoretical methods.

4.2 Flow Mixing at Inlet Generated by a Flow Spoiler on the Outer Wall

As noted in Section 4.1.2 the diffuser of non-dimensional length $\bar{L}/AR_1 = 5.0$ exhibited transitory stall in the exit flow, when running with naturally developed 'potential core' inlet conditions. The object of the test series described in this section was to investigate the feasibility of eliminating this stall by increasing the level of radial flow mixing in the affected region. This mixing was artificially introduced by a flow spoiler upstream of diffuser inlet and it was hoped to sensibly retain, if possible, the naturally developed form of inlet velocity profile.

A preliminary series of tests in a two-dimensional duct indicated that the spoiler geometry shown in Fig. 4.46(a) should achieve the desired effect.

4.2.1 Optimisation of Wall Spoiler Upstream Position

Prior to a detailed investigation of the diffuser internal flow, the upstream position of the outer wall flow spoiler was optimised to give the maximum improvement in terms of static pressure recovery (\overline{Cp}_{1-2}), allied with stable exit flow conditions. The following sections present pertinent

data for the test range of spoiler positions, $L_s/D_{h_1} = 0.0 \rightarrow 8.0$.

4.2.1.1 Diffuser Inlet Conditions

As with naturally developed inflow the symmetry of the inlet flow, indicated by measurements taken at three circumferential positions, is excellent. Thus the inlet velocity profiles for the range of spoiler positions $(L_s/D_{h_1}) = 2.0 \rightarrow 8.0$ are presented as mean lines in Fig. 4.47.

It is gratifying to note that the modification of the velocity profile was confined to the outer region and the flows may best be described by adopting the 'type' descriptions given by Wolf and Johnston (83), as illustrated in Fig. 4.48, where the flow may be said to progress from a 'half-jet' profile, $(L_s/D_{h_1}) = 2.0$, to a mildly sheared profile with thick boundary layers, $(L_s/D_{h_1}) = 8.0$.

The variation of the velocity profile integral parameters, given in Table 4.11, would appear to suggest that for spoiler positions $\frac{L_s}{D_{h_1}} > 4.0$ the 'adjustment' of the velocity profile is very slow. However, inspection of Figs. 4.49 and 4.50, which show the development of axial turbulence intensity $\frac{\sqrt{u'^2}}{U}$ and turbulent shear stress $(\frac{2\overline{u'v'}}{U^2})$ respectively, indicates that the inlet turbulence structure is changing more rapidly.

Fig. 4.50 is the more interesting since the variation of turbulent shear is indicative of the level of radial flow mixing, and it was this feature of the artificially generated inlet flow which was expected to exert a stabilising influence on the diffuser flow. Thus, on this basis, it could be concluded that the profiles at $(L_e/D_{h_1}) = 4.0, 5.0$ should give the best results; however, as will be shown in the following sections, this is not the case since the influence of both the velocity profile and turbulence structure must be considered.

* exit flow stalled for $L_s/D_{h_1} = 0.0 \rightarrow 1.0$

TABLE 4.11

INLET VELOCITY PROFILE INTEGRAL PARAMETERS

$\frac{L_e}{D_{h1}}$	$\frac{L_s}{D_{h1}}$	B_1	$\left[\frac{\theta_o}{\Delta R}\right]_1$	$\left[\frac{\theta_i}{\Delta R}\right]_1$	H_{o1}	H_{i1}	α_1	β_1
9.5 ↓	2.0	0.172	0.0528	0.0256	2.46	1.31	1.229	1.090
	3.0	0.134	0.0610	0.0302	1.47	1.34	1.085	1.030
	4.0	0.129	0.0616	0.0306	1.35	1.37	1.064	1.022
	5.0	0.123	0.0597	0.0320	1.29	1.35	1.051	1.018
	6.0	0.119	0.0600	0.0298	1.27	1.34	1.045	1.016
	7.0	0.117	0.0550	0.0321	1.28	1.37	1.049	1.018
	8.0	0.115	0.0521	0.0332	1.30	1.36	1.052	1.019

$$Re_{D_{h1}} \approx 1.6 \times 10^5$$

4.2.1.2 Outlet Conditions and Flow Stability

Exit velocity profiles were measured and are presented in Fig. 4.51. The integral parameters generated from these profiles are given in Table 4.12, which also indicates the diffuser exit flow behaviour for the spoiler position range $(L_s/D_{h1}) = 0.0 \rightarrow 8.0$. In view of the reasonable symmetry of the exit velocity profiles mean values have been quoted in this Table.

The improvement in the exit velocity profile, when compared with the naturally developed data included in Table 4.12, is clearly demonstrated. Significantly, for spoiler positions $(\frac{L_s}{D_{h1}}) = 6.0, 7.0$ stable exit flow behaviour was observed together with marked reductions in blockage, distortion, and exit kinetic energy flux, as characterised by B_2 , H_{o2} , and α_2 respectively.

These improvements in the exit flow are reflected in appreciable increases in pressure recovery over the naturally developed inflow case, as the following sections show.

TABLE 4.12

OUTLET VELOCITY PROFILE INTEGRAL PARAMETERS AND FLOW CONDITION

$\frac{L_e}{D_{h_1}}$	$\frac{L_s}{D_{h_1}}$	B_2	θ_{o_2} (in.)	θ_{i_2} (in.)	H_{o_2}	H_{i_2}	α_2	β_2	*Flow Condition
9.5 ↓	0.0	-	-	-	-	-	-	-	F
	0.5	-	-	-	-	-	-	-	F
	1.0	-	-	-	-	-	-	-	T
	2.0	0.404	0.1894	0.0943	2.81	1.66	1.646	1.224	T
	3.0	0.379	0.1824	0.0997	2.64	1.72	1.564	1.196	} T (patches)
	4.0	0.349	0.1738	0.1023	2.46	1.76	1.482	1.170	
	5.0	0.370	0.1694	0.1098	2.63	1.84	1.551	1.195	
	6.0	0.358	0.1682	0.1091	2.55	1.81	1.515	1.182	IT
	7.0	0.356	0.1630	0.1080	2.63	1.80	1.530	1.189	U
	8.0	-	-	-	-	-	-	-	TI
50.0	* -	0.390	0.1366	0.0949	3.70	1.71	1.807	1.293	T
	* -	0.349	0.1405	0.1107	3.24	1.67	1.657	1.237	TI

$$R_{e_{D_{h_1}}} \approx 1.6 \times 10^5$$

* naturally developed flow.

4.2.1.3 Static Pressure Recovery

The plots of static pressure recovery for $L_s/D_{h_1} = 2.0 \rightarrow 8.0$ are given in Fig. 4.52 with the local pressure variation in the region of the diffuser inlet plane being detailed in Fig. 4.53. The measured pressures showed good circumferential symmetry.

At $L_s/D_{h_1} = 2.0$ Fig. 4.52 shows evidence of a slight radial pressure gradient in the diffuser which is attributable to pre-entry effects caused by the proximity of the wall flow spoiler to diffuser inlet (see Fig. 4.53).

Fig. 4.53 further illustrates that the high local adverse pressure gradient in the region of the outer wall inlet bend is again present (see Section 4.1.3), and there is no evidence that this condition is alleviated

* For definitions of flow behaviour see Fig. 4.5

to any perceptible degree by the increase in radial flow mixing.

4.2.1.4 Overall Performance

Data collated from the previous Sections 4.2.1.1-3 is presented in Table 4.13 in terms of overall performance and compared with relevant data from tests under naturally developed inflow conditions.

TABLE 4.13
OVERALL PERFORMANCE

$\frac{\bar{L}}{\Delta R_1}$	$\frac{L_e}{D_{h_1}}$	$\frac{L_s}{D_{h_1}}$	B_1	\overline{Cp}_{1-2}	$\overline{Cp}_{1-2}/\alpha_1$	λ_{1-2}	B_2	α_2	H_{o_2}	H_{i_2}	Flow Condition
5.0	9.5	2.0	0.172	0.65	0.53	0.17	0.404	1.646	2.81	1.66	T
		3.0	0.134	0.58	0.535	0.115	0.379	1.564	2.64	1.72	T } patches
		4.0	0.129	0.58	0.545	0.115	0.349	1.482	2.46	1.76	
		5.0	0.123	0.59	0.56	0.075	0.370	1.551	2.63	1.84	IT
		6.0	0.119	0.58	0.555	0.085	0.358	1.515	2.55	1.81	U
		7.0	0.117	0.61	0.58	0.06	0.356	1.530	2.63	1.80	U
		8.0	0.115	0.56	0.535	-	-	-	-	-	TI
	↓	-	0.090	0.475	0.453	0.125	0.390	1.810	3.70	1.71	IT
↓	39.5	-	0.102	0.540	0.520	0.085	0.369	1.660	3.24	1.67	TI

$Re_{D_{h_1}} \approx 1.6 \times 10^5$

Comparing the two sets of data it can be seen that the increased turbulent mixing results in a reduction in the distortion of the outlet velocity profile, as indicated by the lower values of outer wall boundary layer shape parameter H_{o_2} . This in turn lowers α_2 and B_2 and gives a consequent

increase in the static pressure coefficient. The value for \overline{Cp}_{1-2} of 0.65 achieved with the spoiler at position $\frac{L_s}{D_{h1}} = 2.0$ is due to the 'peaky' inlet profile for this spoiler position, where the profile has a higher energy, for a given value of \overline{u}_1 , than that of a naturally developed profile having the same \overline{u}_1 . Thus it does not mean that the pressure recovery capability of the diffuser is any greater but that a higher initial kinetic energy is available for recovery. This is confirmed by the values of $\overline{Cp}_{1-2}/\alpha_1$ quoted in Table 4.13.

Study of Table 4.13 shows that for the $\frac{L_s}{D_{h1}} = 7.0$ spoiler position the maximum value of pressure recovery coefficient of 0.61 was obtained together with a stable outlet flow. This configuration was therefore taken as the optimum for further investigation.

4.2.1.5 Comparison with Published Data

Since the test series described in this section was of an exploratory nature this precludes any detailed comparison with published data; it is felt that discussion may be aided by considering the following questions:

- (i) Does the diffuser performance under artificially generated inlet conditions show any improvement over the 'nearest equivalent' naturally developed inflow case?
- (ii) Is the artificially generated inflow typical of 'industrial' flow situations?
- (iii) Can any 'general principles' be deduced from the results?

As regards (i), Fig. 4.54 compares the inlet velocity profile to the diffuser of non-dimensional length $\overline{L}/AR_1 = 5.0$, for optimum spoiler position, with the naturally developed inlet profiles for inlet lengths $\frac{L_e}{D_{h1}} = 9.5$ (same external geometry), and 39.5 (fully developed flow) respectively. In all cases the non-dimensional axial velocities in the near wall regions ($y/(R_o - R_1) \leq 0.1$) are the same, and the values of blockage

fraction (B_1) are approximately equal. However, notable differences are evident in the levels of radial flow mixing as indicated by the turbulent shear stress ($\frac{2\overline{u'v'}}{U^2}$). This relative increase in radial mixing with the artificially developed inflow is reflected in an improvement in pressure recovery, as shown in Table 4.14, with substantially the same losses as for the naturally developed, fully developed inflow. The higher losses apparent for the $\frac{L_e}{D_{h1}} = 9.5$ naturally developed inlet flow are attributed to energy losses inherent in the stalling diffuser exit flow.

TABLE 4.14

IMPROVEMENT IN DIFFUSER PERFORMANCE WITH ARTIFICIALLY GENERATED INFLOW

$\bar{L}/\Delta R_1$	L_e/D_{h_1}	L_s/D_{h_1}	\overline{Cp}_{1-2}	λ_{1-2}
5.0	9.5	7.0	0.610	0.06
5.0	9.5	~	0.475	0.125
5.0	39.5	~	0.540	0.085

$$Re_{D_{h_1}} \approx 1.6 \times 10^5$$

Thus, taking the fully developed flow as the 'nearest equivalent' naturally developed inflow case, the improvement in pressure recovery, attributable to an approximate doubling of the level of flow mixing at diffuser inlet, is $12\% \left[\frac{\Delta Cp_{1-2}}{Cp_{N.D.}} \right]$ accompanied by a major improvement in the stability of the diffuser exit flow.

The similarity of the artificially generated flow, using the inlet wall spoiler, with 'industrial' flow conditions, mentioned in (ii), is difficult to quantify. It is probably true to say that 'classical' naturally developed flow very rarely occurs in industrial flows, and both the velocity profile and turbulence structure may be modified by, for example, struts, surface imperfections, forced fluctuation frequencies, etc. In short it is virtually impossible to specify a 'typical' industrial flow. Realising this, it was decided to focus comparison on turbo-machinery applications and to this end a short series of tests was undertaken by Williams and Terrell (81) on the National Gas Turbine Establishment research compressor. The instrumentation available allowed the measurement of axial turbulence intensity $\frac{\sqrt{u'^2}}{u}$ distribution at compressor exit, and this is compared with the radial variation of turbulence intensity for the present artificially developed inflow in Fig. 4.55. This shows good agreement for

the inner wall. The wide deviation at the outer wall is attributable to stalled flow conditions in the exit outer casing boundary layer in the N.G.T.E. compressor. The flow in the inner casing region was near uniform. Thus on the basis of these tests the artificially generated turbulence levels are apparently similar to those occurring in a typical turbomachine flow.

Under heading (iii) the most general principle to arise is that, given a well behaved inflow velocity profile, increased radial momentum transfer assists the flow to proceed against adverse pressure gradients in downstream flow components. With special reference to the present tests, quite modest increases in turbulent mixing have been shown to lead to a useful improvement in diffuser performance and a quite striking improvement in exit flow stability.

4.2.1.6 Effect of Downstream Settling Length

The beneficial effect of momentum transfer in the diffuser downstream settling length has been previously noted in Section 4.1.5. With the artificially developed diffuser inflow the same flow behaviour and levels of improvement in static pressure recovery are apparent as shown in Figs. 4.56, 4.57, where comparison is made between the naturally developed fully developed inflow data and the optimum spoiler position results.

4.2.2 Internal Flow Development for Optimum Spoiler Position

To allow detailed comparison of the naturally developed and artificially generated diffuser flows, and thus highlight the main differences, a full investigation of the diffuser internal flow was carried out for the optimum spoiler position, as detailed in the following sections.

4.2.2.1 Internal Boundary Layer Development

The velocity profile data for this 'optimum' geometry is presented in Appendix 9 together with tabulated boundary layer integral parameters. Over the majority of the diffuser length the indicated symmetry of flow is good, and the tabulated quantity flows are in good agreement, allowing

presentation of the flow development in terms of a mean velocity profile, as given in Figs. 4.58, 4.59 while the boundary layer integral parameters are summarised in Fig. 4.60.

Comparison with data for naturally developed fully developed inflow, given in Fig. 4.60, shows that major effects of flow mixing cannot be attributed for $X/N < 0.50$ as, for instance, comparison of the outer wall shape parameters (H_0) indicates. However for $X/N > 0.50$ considerable suppression of distortion is evident, which results in both an improvement in flow stability and a considerable increase in velocity near the outer wall at exit, with attendant lower exit blockage as shown in Fig. 4.61

4.2.2.2 Shear Stress and Turbulence Intensity

With the spoiler artificially generated inflow the mean bridge voltage (\bar{E}) given by the hot-wire anemometer was well behaved allowing complete measurement of turbulence parameters up to diffuser exit and into the settling length; as with naturally developed inflow, measurements were taken at one circumferential position with checks for the degree of asymmetry (see Appendix 3, A.3.4).

The development of turbulent shear stress and turbulence intensity along the diffuser, calculated on the assumption of King's law and the Cosine rule (see Appendix 3), is presented in Appendix 9 and summarised in terms of contour plots in Fig. 4.62. The shear stress maximum away from the wall associated with the retarded flow near the wall is again evident; however, the gradient of shear stress at the wall does not compare with the axial pressure gradient as shown in Table 4.15.

Consideration of the mean flow equation:

$$u \frac{\partial u}{\partial x} + v \frac{\partial u}{\partial R} = - \frac{1}{\rho} \frac{dp}{dx} - \frac{\partial}{\partial x} (\overline{u'^2}) + \frac{1}{\rho R} \frac{d}{dR} (\tau R) \quad 4.2$$

shows that the Reynolds normal stress term $\frac{d}{dx} (\rho \overline{u'^2})$ could account for this difference and this term is therefore included in Table 4.15. It is seen

that only in part does the Reynolds normal stress term assist in balancing the axial pressure gradient and it must be concluded that other terms in the mean flow equation contribute in this flow situation, as in the case of fully developed inflow (see Section 4.1.8).

TABLE 4.15

BALANCE OF SHEAR STRESS AND AXIAL PRESSURE GRADIENT

x/N	$\frac{1}{\rho U^2} \frac{dp}{dx}$	$\frac{1}{\rho U^2} \left[\frac{d\tau}{dR} \right]_o$	$\frac{1}{U^2} \frac{d}{dx} (\overline{u'^2})_o$	$\frac{1}{\rho U^2} \left[\frac{\partial \tau}{\partial R} \right]_o + \frac{1}{U^2} (\overline{u'^2})_o$	
0.63	-	-	-	-	$\bar{L}/\Delta R_1 = 5.0$
0.060	-	-	-	-	$L_e/D_{h_1} = 9.5$
0.150	-	-	-	-	$L_s/D_{h_1} = 7.0$
0.270	1.50	0.39	-	-	
0.390	1.00	0.33	-	-	
0.510	0.81	0.27	-	-	
0.630	0.72	0.20	0.05	0.25	OUTER WALL
0.750	0.59	0.10	0.07	0.17	
0.963	0.53	0.07	0.12	0.19	

$$Re_{D_{h_1}} = 1.6 \times 10^5$$

Table 4.16 compares the experimental value of dissipation coefficient (d) with that given by the relationship of Walz (80). An early departure from equilibrium is observed with subsequent equilibrium and overshoot in the reducing pressure gradient toward diffuser exit.

TABLE 4.16

COMPARISON WITH EQUILIBRIUM BOUNDARY LAYER SHEAR STRUCTURE

x/N	$\mathcal{D}_{EXPT.}$	$\mathcal{D}_{EQUILIBRIUM}$
0.06	0.00078	0.0028
0.15	0.00085	0.0029
0.27	0.00246	0.0030
0.39	0.0034	0.0033
0.51	0.0037	0.0035
0.63	0.0037	0.0037
0.75	0.0057	0.0041
0.96	0.0071	0.0042

$$\bar{L}/\Delta R_1 = 5.0$$

$$L_e/D_{h_1} = 9.5$$

$$L_s/D_{h_1} = 7.0$$

OUTER WALL

$$Re_{D_{h_1}} = 1.6 \times 10^5$$

If the turbulent shear stress distribution for the spoiler generated inflow is compared, at representative stations, with the distribution for fully developed inflow then, as Fig. 4.63 shows, the increase in flow mixing indicated by this shear stress comparison is seen to persist into the final stages of diffusion where, in the near wall region, the increase in the mixing level is evident. This apparently small increase in mixing exerts a beneficial influence on the diffuser flow as illustrated in Section 4.2.1.4.

The data for turbulence intensity given in Appendix 9 has been non-dimensionalised in terms of the station maximum velocity $\frac{\sqrt{u'^2}}{U}$. If the local mean velocity is used as a non-dimensionalising parameter then very high local turbulence intensities of the order $\frac{\sqrt{u'^2}}{u} \approx 0.60$ are indicated in the outer wall region, which is well in excess of the criterion noted by Spangenberg et al (64) for transitory stall, $\frac{\sqrt{u'^2}}{u} > 0.33$. In fact no transitory stall was observed. Thus in this flow situation, where the eddy motion is of the same order as the mean velocity, turbulence measurements taken using the standard hot-wire technique are clearly inaccurate. For this type of flow the most useful instrument is the pulsed double wire probe described by Bradbury (2) where the 'time of flight' of a heated packet of fluid is measured.

4.2.2.3 Law of the Wall - Estimation of Skin Friction

The mean velocity profile data is presented in terms of Clauser plots in Appendix 9. These exhibit the same behaviour as the plots for naturally developed flow e.g. deviation from the log-linear law of the wall for $y^+ < 100$, with the attendant difficulty in establishing an accurate c_f value.

4.2.2.4 Mixing Length and Eddy Viscosity

The mixing length distributions shown in Fig. 4.64 exhibit a ramp function in the early stages of diffusion with a constant level over the

outer region of the boundary layer in the latter stages of diffusion.

Comparison of the levels of mixing length along the diffuser with those of naturally developed, fully developed flow is made in Table 4.17. where the higher mixing levels in the artificially generated flow are reflected in the higher mixing length values as directly compared by the values of $\ell/(R_o - R_i)$.

Presentation of the non-dimensional eddy viscosity ($\frac{\epsilon}{U\delta_{2-D}^*}$) in Fig. 4.65 shows ($\frac{\epsilon}{U\delta_{2-D}^*}$) = 0.010 + 0.016 over the majority of the diffuser, which is typical of the values noted for naturally developed inflow in Section 4.1.10.

TABLE 4.17
COMPARISON OF MIXING LENGTH WITH FULLY DEVELOPED INFLOW LEVELS

Fully developed data - Stevens (67)

X/N	$\frac{\ell}{\delta^*}$	$\frac{\ell}{\delta_{FD}^*}$	$\left[\frac{\ell}{R_o - R_i}\right]$	$\left[\frac{\ell}{R_o - R_i}\right]_{FD}$
0.63	1.50	1.00	0.110	0.075
0.06	1.50	0.70	0.105	0.054
0.15	0.70	0.60	0.062	0.055
0.27	0.60	0.40	0.065	0.038
0.39	0.40	0.40	0.052	0.039
0.51	0.35	0.17	0.052	0.019
0.63	0.25	0.17	0.043	0.019
0.75	0.25	0.17	0.047	0.019
0.856	-	-	-	-
0.963	0.20	0.17	0.048	0.019

$\bar{L}/\Delta R_1 = 5.0$
 $L_e/D_{h_1} = 9.5$
 $L_s/D_{h_1} = 7.0$
 OUTER WALL

$$Re_{D_{h_1}} \approx 1.6 \times 10^5$$

4.2.2.5 Balance of Momentum

The Momentum Integral Equation is quoted in Section 4.1.11 for the diffuser outer wall:

$$\frac{d\theta_o}{dx} = \frac{c_{f_o}}{2} - \frac{\theta_o}{R_o} \frac{dR_o}{dx} - \frac{\theta_o}{U} \frac{dU}{dx} (H_o + 2) + \frac{R_o^2 - R_\delta^2}{2\rho U^2 R_o} \left[\frac{dP}{dx}\right]_\delta + \frac{1}{U^2} \frac{d}{dx} \int_{R_\delta}^{R_o} (\overline{u'^2} + \overline{v'^2} - \overline{w'^2}) dR \tag{4.20}$$

For the case of spoiler artificially generated inflow the Reynolds normal stress and total pressure gradient terms assume significant values as demonstrated in Fig. 4.66, which values, in this case, are approximately self cancelling. The comparison of $\left[\frac{d\theta}{dx}\right]_{\text{expt.}}$ with the value calculated from the R.H.S. is well within the limits attributable to experimental error, and indicates that the flow does not suffer from three-dimensional effects. As for the case of naturally developed inflow the pressure gradient parameter $\left(\frac{\theta}{U} \frac{dU}{dx} (H_o + 2)\right)$ is seen to be the dominant term in the momentum integral equation for this adverse pressure gradient situation.

4.3 Inlet Flow Mixing Generated by Coarse Gauze

The preceding section describes the effect of inlet flow mixing applied to an essentially fully developed diffuser inflow. The tests described in this section were intended to provide data on the effect of mixing applied to a near uniform inlet flow. Further, to provide more general information, all three test diffusers were investigated.

The necessity of maintaining a near uniform inlet flow precluded the use of 'flow spoiler' methods since these, as the previous section has shown, tend to thicken the boundary layer. Thus for this test series a 'coarse gauze' method was employed to generate turbulent mixing, as illustrated in Fig. 4.46(b). The coarse gauze was mounted across the face of the inlet flare and the acceleration in the inlet flare employed to ensure a near uniform inflow. Some reduction in the generated turbulence was inevitable, but a high residual level was maintained at diffuser inlet.

4.3.1 Diffuser Inlet Conditions

The inlet velocity profile data is compared with the equivalent $(L_e/D_{h_1} = 2.0)$ naturally developed flow in Fig. 4.67 where it is seen that the profiles are virtually the same. There is a slight blockage (B_1) variation but this is insufficient in itself to cause any major variation

in diffuser performance.

Comparison of the level of inlet turbulent shear stress in Fig. 4.67 shows marked increases in the near wall region over both the naturally developed and spoiler generated inlet flows. Hence the generated inlet conditions may be summarised as a near uniform inlet velocity profile coupled with a high rate of mixing in the near wall regions. Comparison of the inlet velocity profile integral parameters with those for natural development is given in Table 4.18.

TABLE 4.18

INLET VELOCITY PROFILE INTEGRAL PARAMETERS

L_e/D_{h1}	B_1	$(\theta_o/\Delta R)_1$	$(\theta_i/\Delta R)_1$	H_{o1}	H_{i1}	α_1	β_1
⁺ 2.0	0.028	0.0100	0.0100	1.38	1.37	1.02	1.007
2.0	0.044	0.0180	0.0135	1.40	1.35	1.03	1.011

⁺ natural development

$$Re_{D_{h1}} = 1.6 \rightarrow 1.7 \times 10^5$$

4.3.2 Outlet Conditions and Flow Stability

The measured exit velocity profiles are shown in Fig. 4.68 and the tabulated integral parameters given in Appendix 10. The comparison with data for naturally developed inflow given in Fig. 4.68 shows that the increased level of radial momentum transfer reduces the degree of distortion. The values of profile shape factor and energy flux coefficient are given in Table 4.19 together with comments on the exit flow state.

TABLE 4.19

COMPARISON OF EXIT VELOCITY PROFILE PARAMETERS

$\bar{L}/\Delta R_1$	L_e/D_{h1}	H_{o2}	H_{i2}	α_2	EXIT FLOW CONDITION
10.0	⁺ 2.0	2.00	1.86	1.29	S
10.0	2.0	1.48	1.49	1.11	U
7.5	⁺ 2.0	2.35	1.92	1.36	U
7.5	2.0	1.72	1.47	1.16	U
5.0	⁺ 2.0	3.40	1.80	1.56	IT
5.0	2.0	1.90	1.50	1.17	U
5.0	*9.5	2.63	1.80	1.53	U

$$Re_{D_{h1}} \approx 1.6 \rightarrow 1.7 \times 10^5$$

⁺ natural development

* spoiler optimum ($\frac{L_s}{D_{h1}} = 7.0$)

As a consequence of the increased mixing the shape parameter at exit on both inner and outer walls is reduced considerably, resulting in a lower kinetic energy flux (α_2). Furthermore the state of the exit flow shows marked improvement. Comparison with the results for the $\bar{L}/\Delta R_1 = 5.0$ diffuser indicate that the influence of increased mixing is confined to the relevant wall boundary layer since, for the case of the flow spoiler on the outer wall, only the outer wall shape parameters are affected, and the shape parameter at exit on the inner wall remains virtually the same as that measured with naturally developed inflow, at approximately the same inlet blockage fraction.

4.3.3 Static Pressure Recovery

The static pressure recovery in the test diffusers is presented in Fig. 4.69. The measured static pressures showed good circumferential symmetry and there was no indication of radial pressure gradient within the diffuser.

Comparison with the data for naturally developed inflow ($B_1 = 0.028$)

in Fig. 4.69 shows the level of improvement in static pressure recovery attributable to increased flow mixing.

4.3.4 Overall Performance

The diffuser performance data from the tests with grid generated inflow is summarised below in Table 4.20; comparison is made in each case with the data for naturally developed inflow.

TABLE 4.20

DIFFUSER OVERALL PERFORMANCE WITH 'GRID GENERATED' INLET CONDITIONS

\bar{L}/AR_1	L_e/D_{h1}	B_1	\overline{Cp}_{1-2}	$\overline{Cp}_{1-2}/\alpha_1$	λ_{1-2}	Flow Condition
10.0	⁺ 2.0	0.028	0.615	0.605	0.085	S
10.0	2.0	0.044	0.660	0.640	0.100	U
7.5	⁺ 2.0	0.028	0.600	0.590	0.085	U
7.5	2.0	0.044	0.655	0.635	0.090	U
5.0	⁺ 2.0	0.028	0.515	0.505	0.120	IT
5.0	2.0	0.044	0.610	0.595	0.125	U

⁺ natural development

$$Re_{D_{h1}} \approx 1.6 \rightarrow 1.7 \times 10^5$$

It will be noted that there is a marked increase in overall pressure recovery (\overline{Cp}_{1-2}) from 7% $\left[\frac{\Delta \overline{Cp}_{1-2}}{\overline{Cp}_{1-2, N.D.}} \right]$ for the $\bar{L}/AR_1 = 10.0$ diffuser geometry to some 18% for the $\bar{L}/AR_1 = 5.0$ diffuser. With the generated inflow slight increases in the diffuser loss coefficient (λ_{1-2}) are registered but these are of a low level, presumably due to suppression of boundary layer distortion at diffuser exit.

4.3.5 Effect of Downstream Settling Length

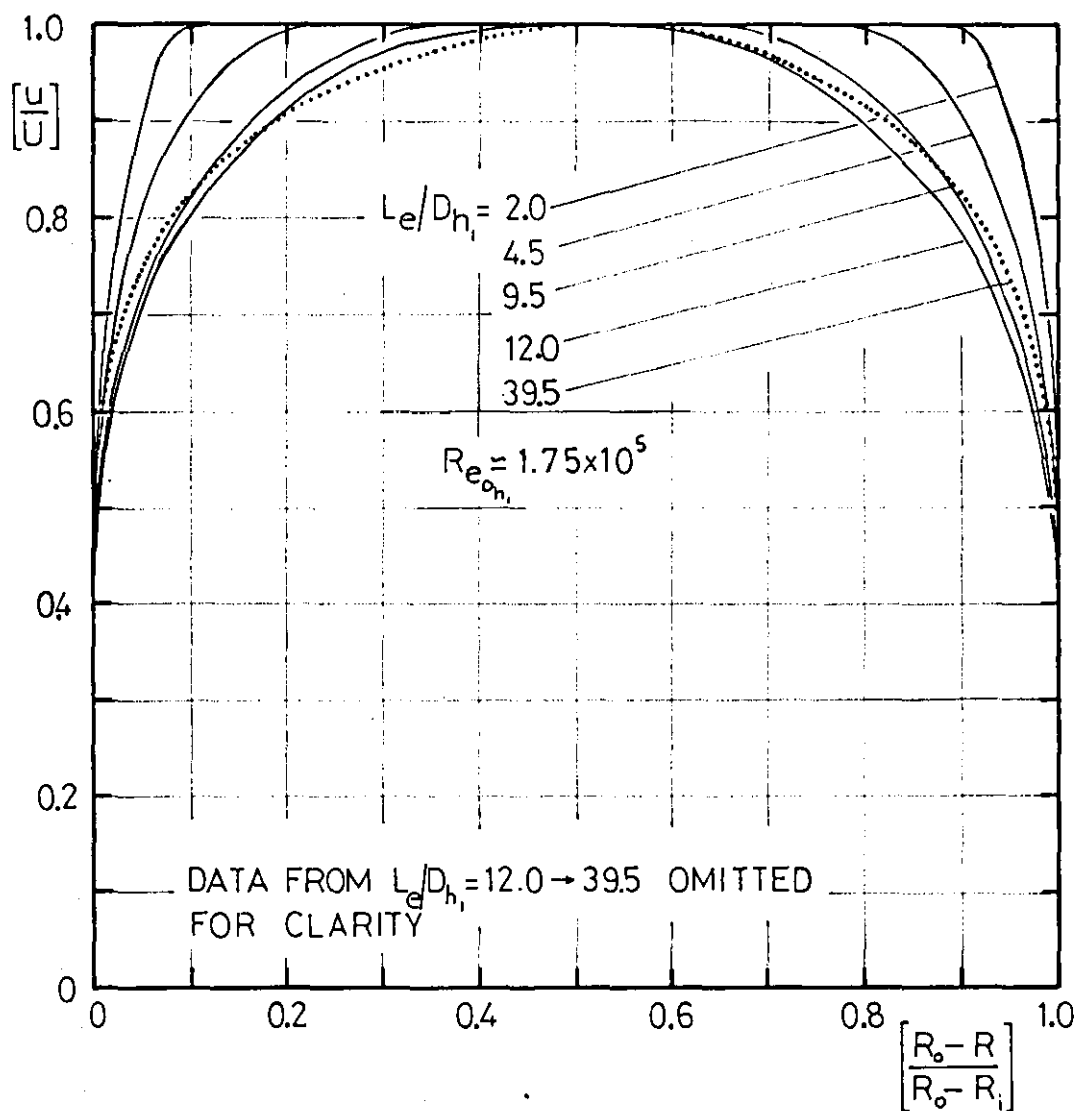
Due to the high rate of mixing in the diffusers with the grid generated inflow the settling length exerts less influence, as Fig. 4.70 illustrates. For the $\bar{L}/AR_1 = 10.0$ diffuser the exit profile is relatively undistorted

and only a minimal pressure recovery is evident in the settling length.

The $\bar{L}/\Delta R_1 = 7.5$, 5.0 diffusers suffer a slight distortion of the exit velocity profile ($H_0 \approx 1.9$) and in the subsequent momentum transfer in the settling length some pressure recovery is evident, but this is below the level found for naturally developed diffuser inflow.

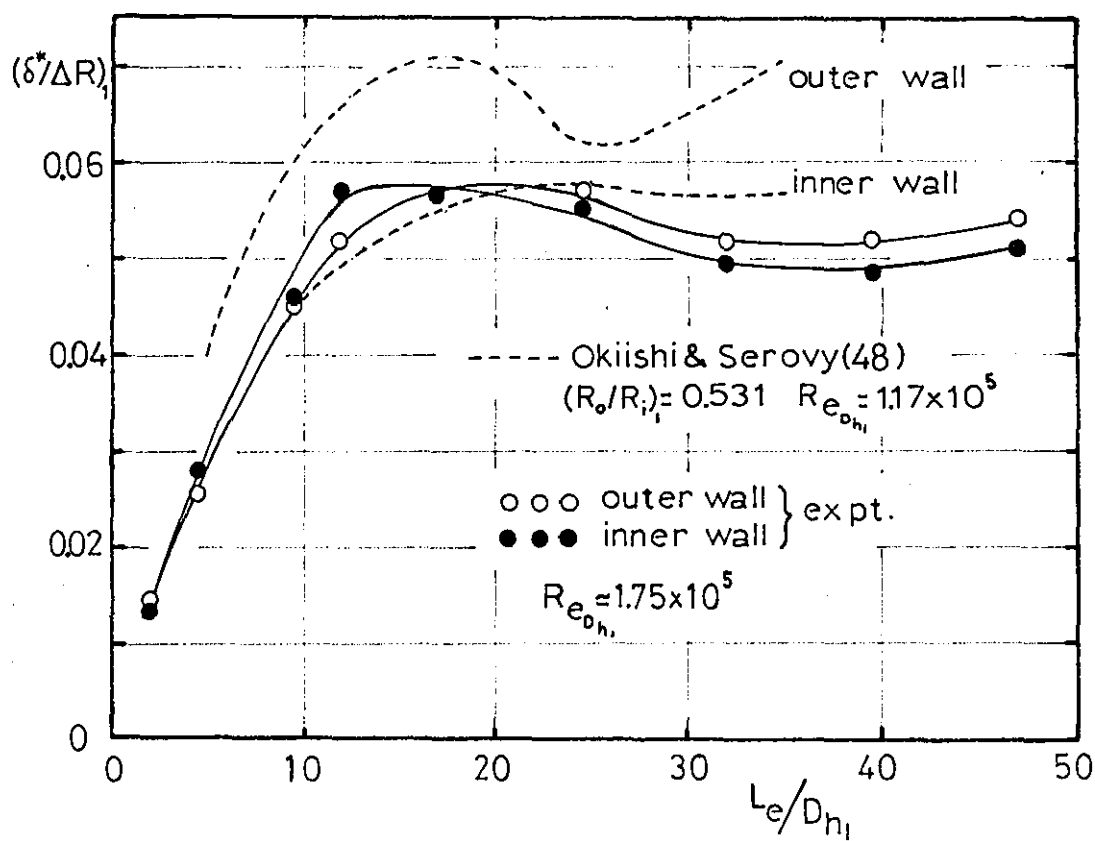
RANGE OF NATURALLY DEVELOPED
INFLOW VELOCITY PROFILES.

FIGURE 4.1



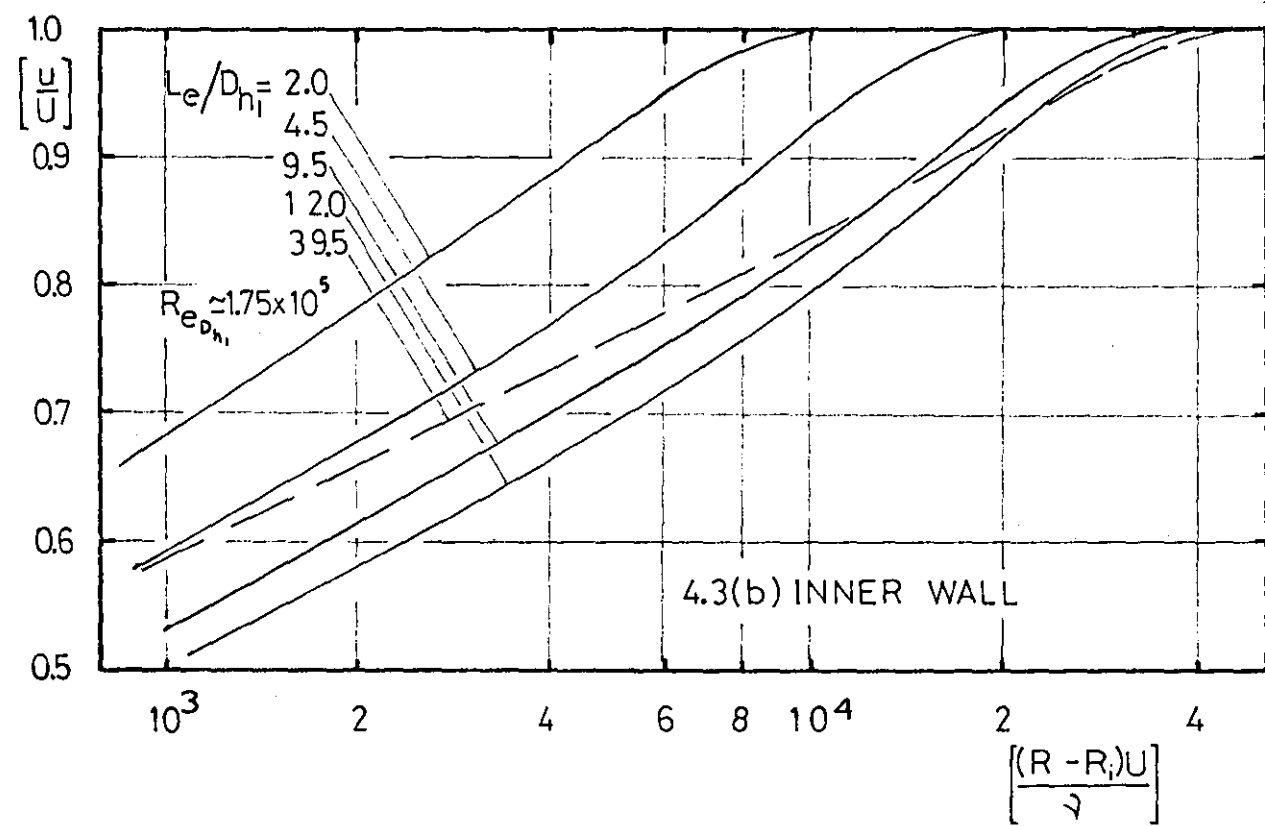
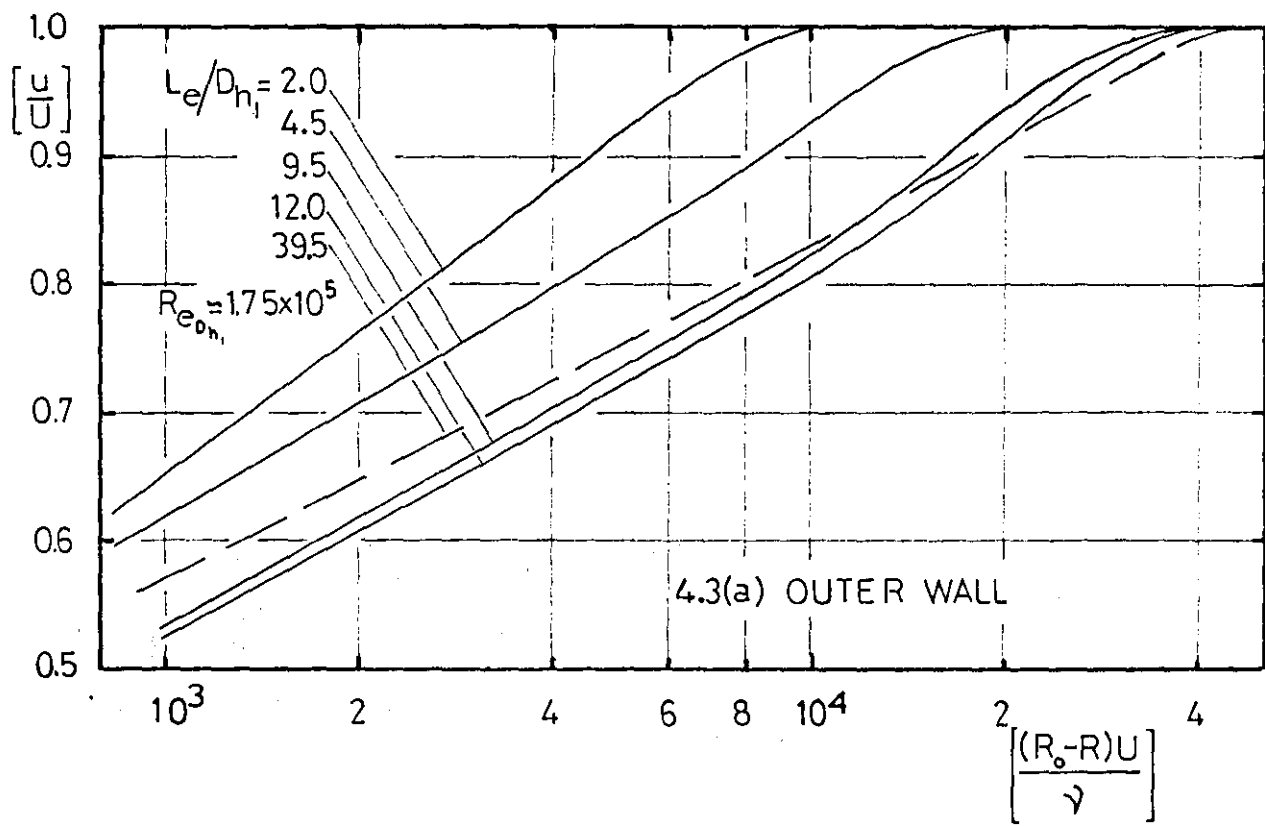
GROWTH OF BOUNDARY LAYER
ALONG APPROACH LENGTHS.

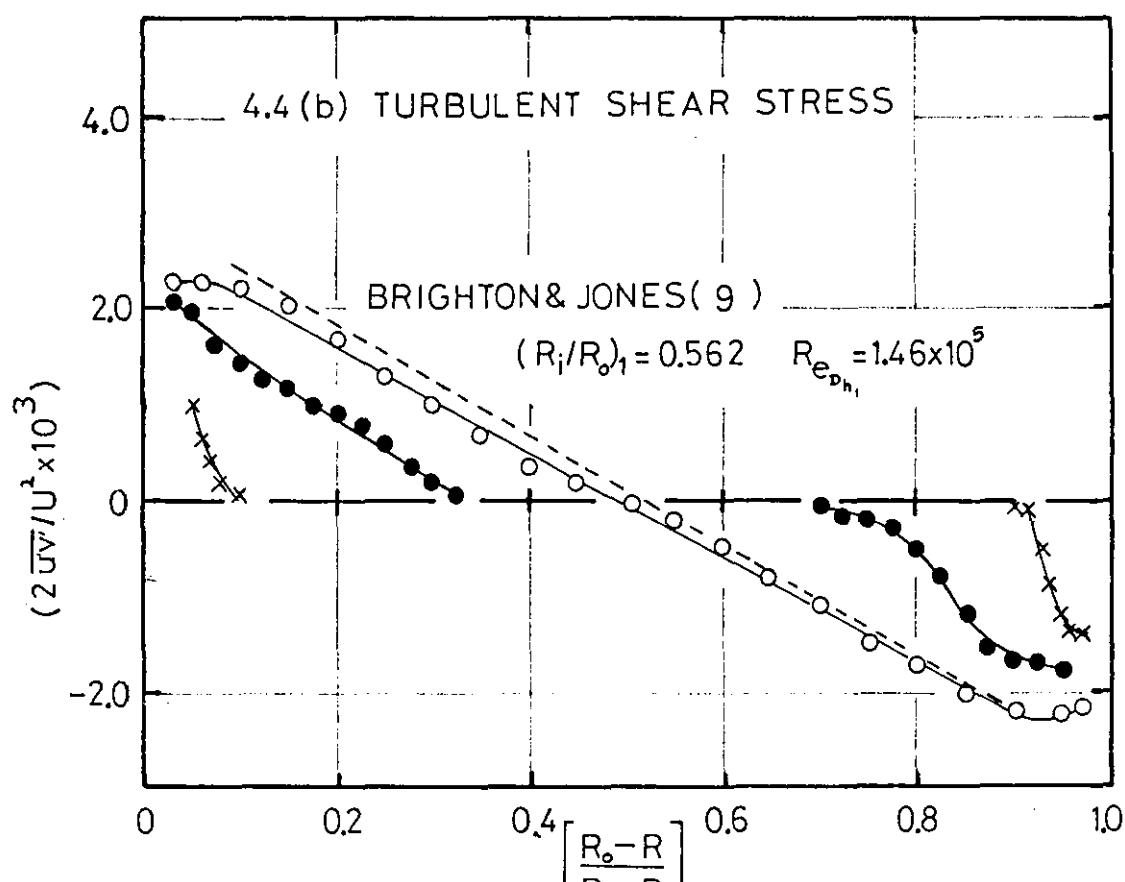
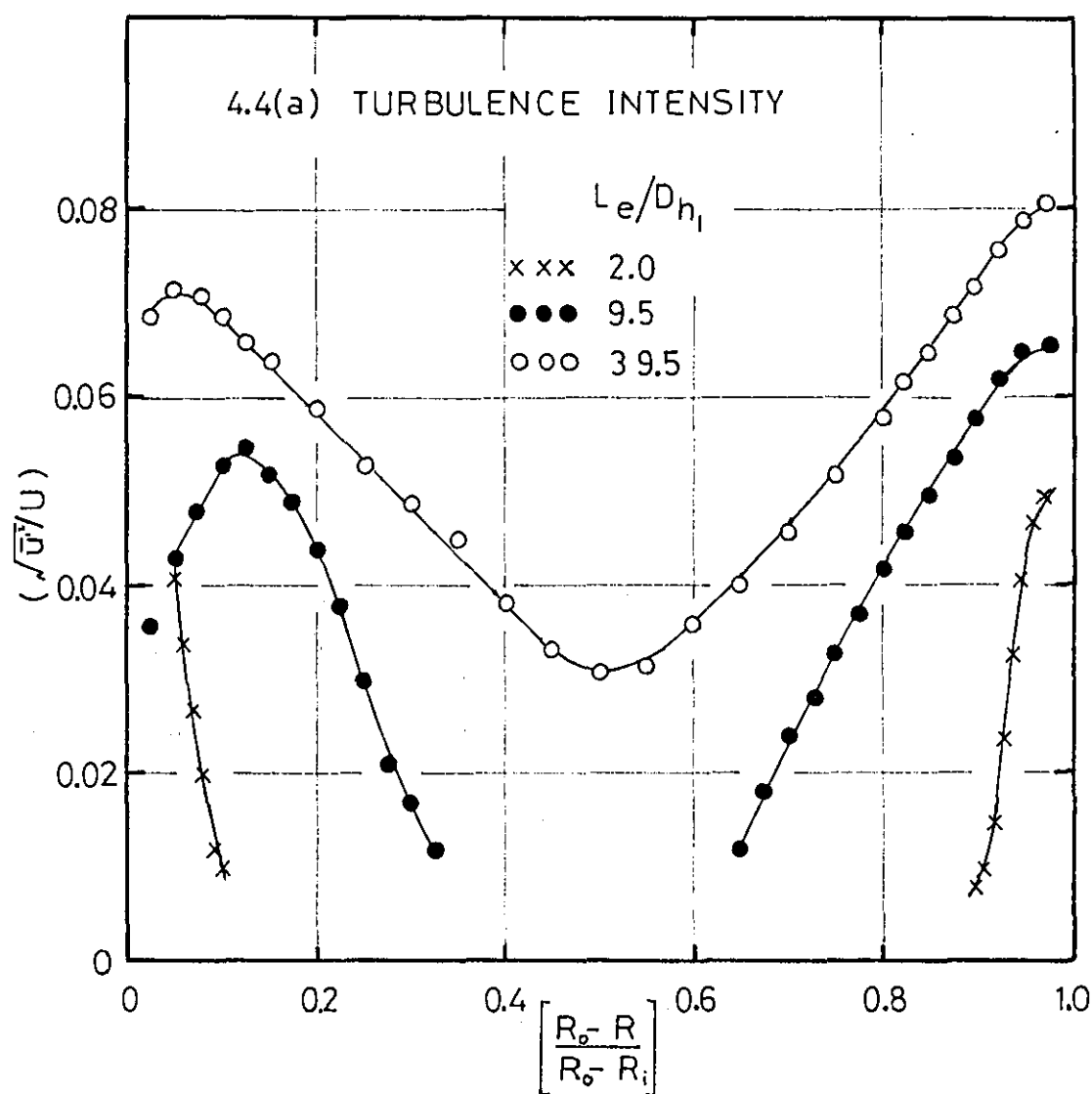
FIGURE 4.2



INFLOW VELOCITY PROFILES IN
CLAUSER PLOT FORM

FIGURE 4.3





FLOW REGIONS


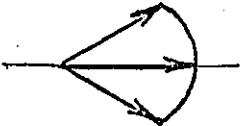
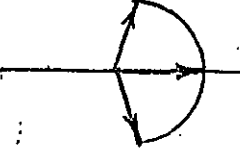
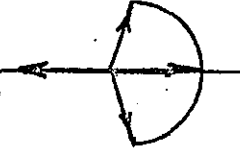


<u>Tuft Pattern</u>	<u>Symbol</u>	<u>Description</u>
	S	Steady flow - small or no oscillations of tufts.
	U	Unsteady flow - medium amplitude oscillations of tufts with no back flow observed.
	TI	Incipient transitory stall - large amplitude oscillations of tufts on the verge of the tuft pointing upstream.
	IT	Intermittent transitory stall - large amplitude oscillations of tufts with the tuft pointing upstream for short periods of time.
	T	Transitory stall - tuft points upstream for approximately the same period of time as it points downstream.
	F	Fixed stall - tuft points upstream for long periods of time.

FIGURE 4.6

STATIC PRESSURE RECOVERY OVER RANGE OF
INFLOW BLOCKAGE (B_1)

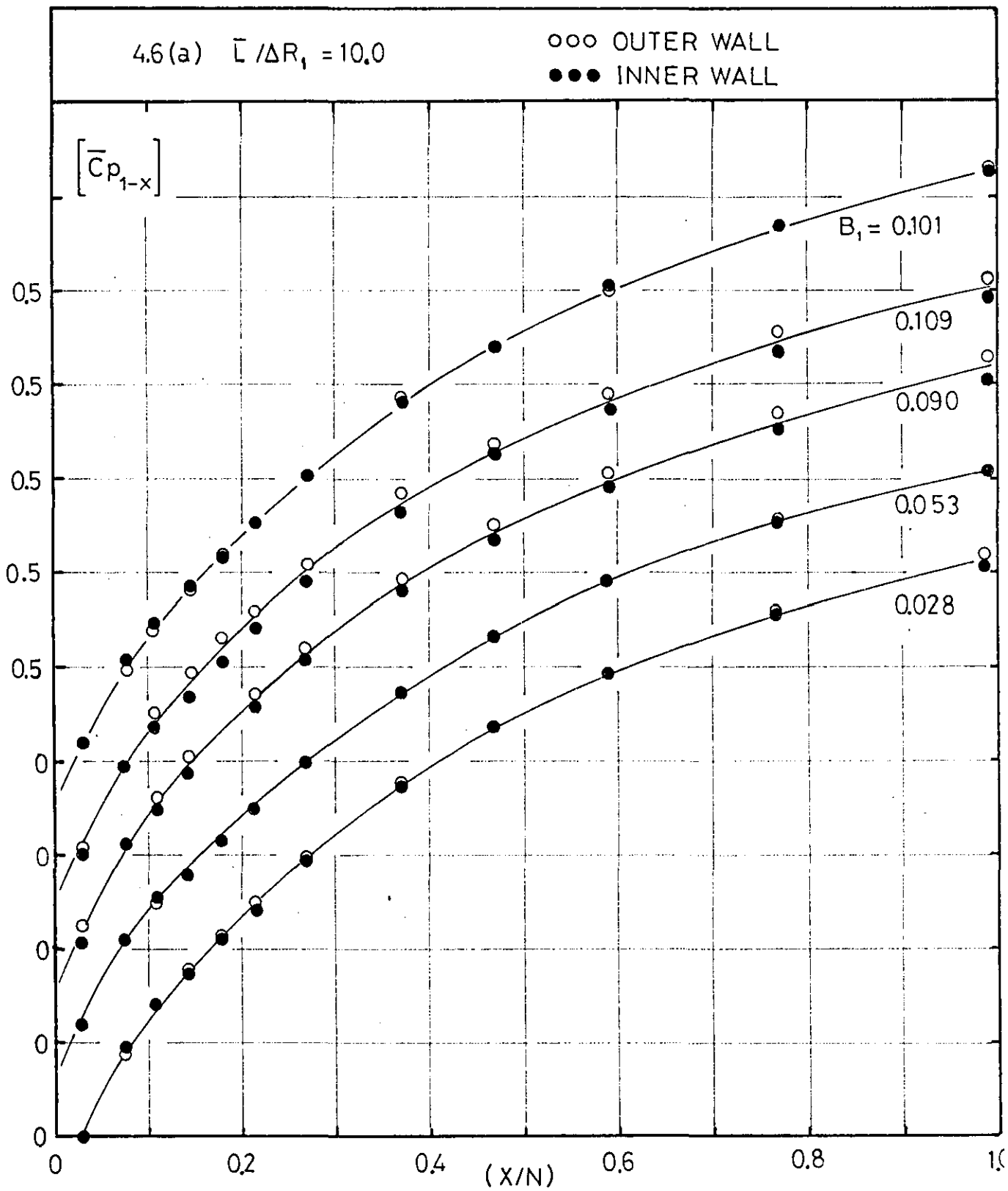


FIGURE 4.6(cont.)

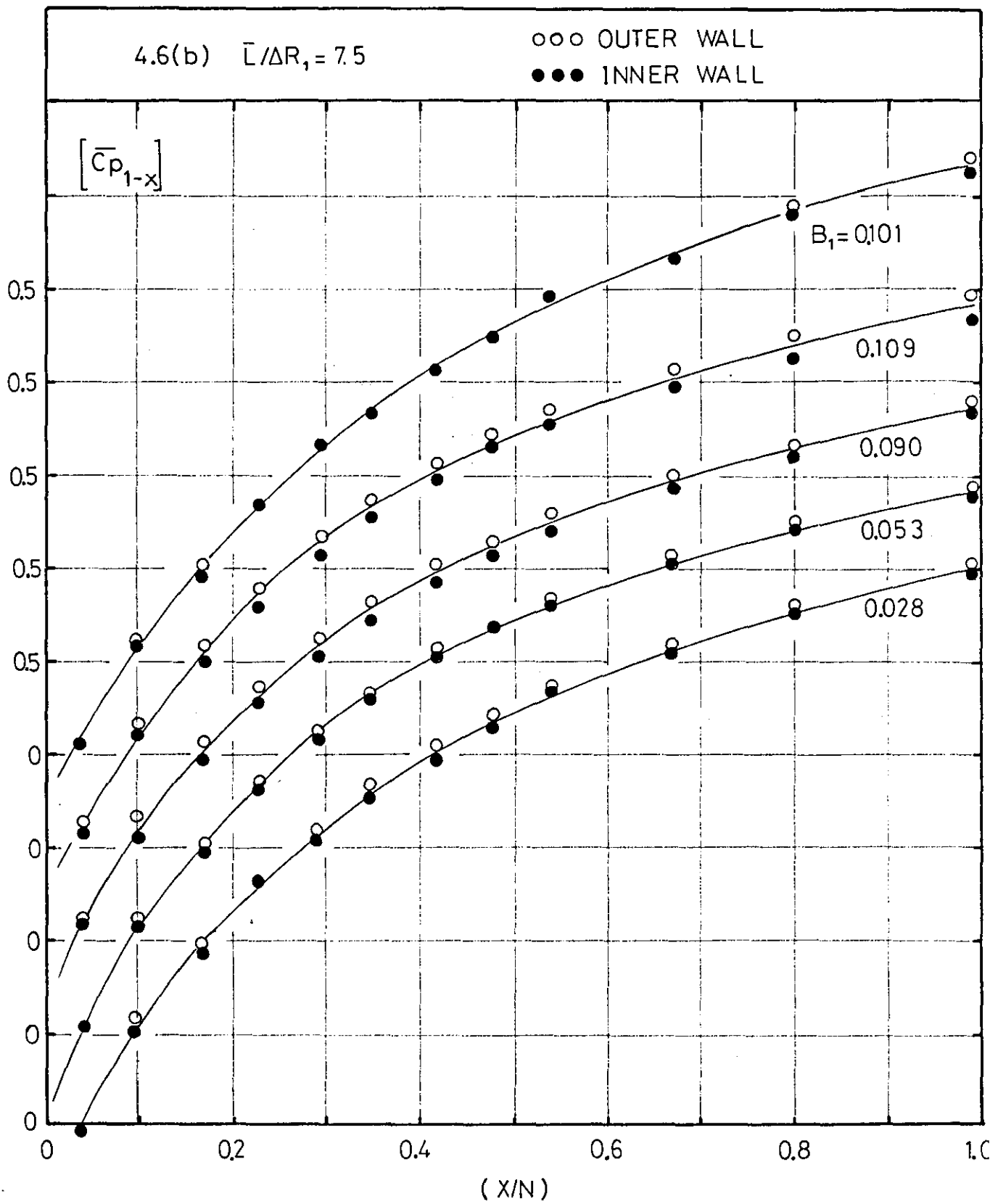


FIGURE 4.6(cont.)

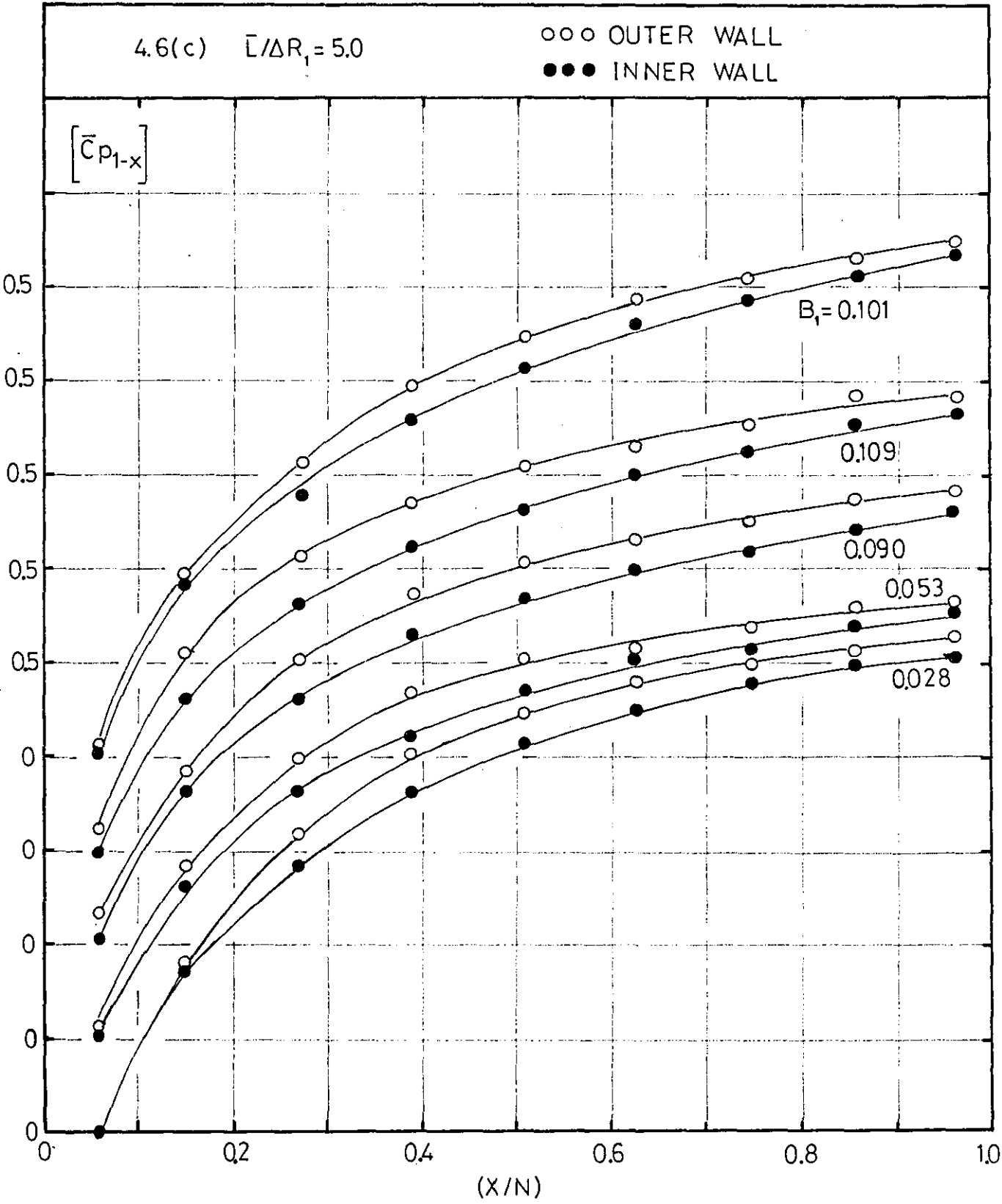


FIGURE 4.7

VARIATION OF STATIC PRESSURE IN
DIFFUSER INLET REGION

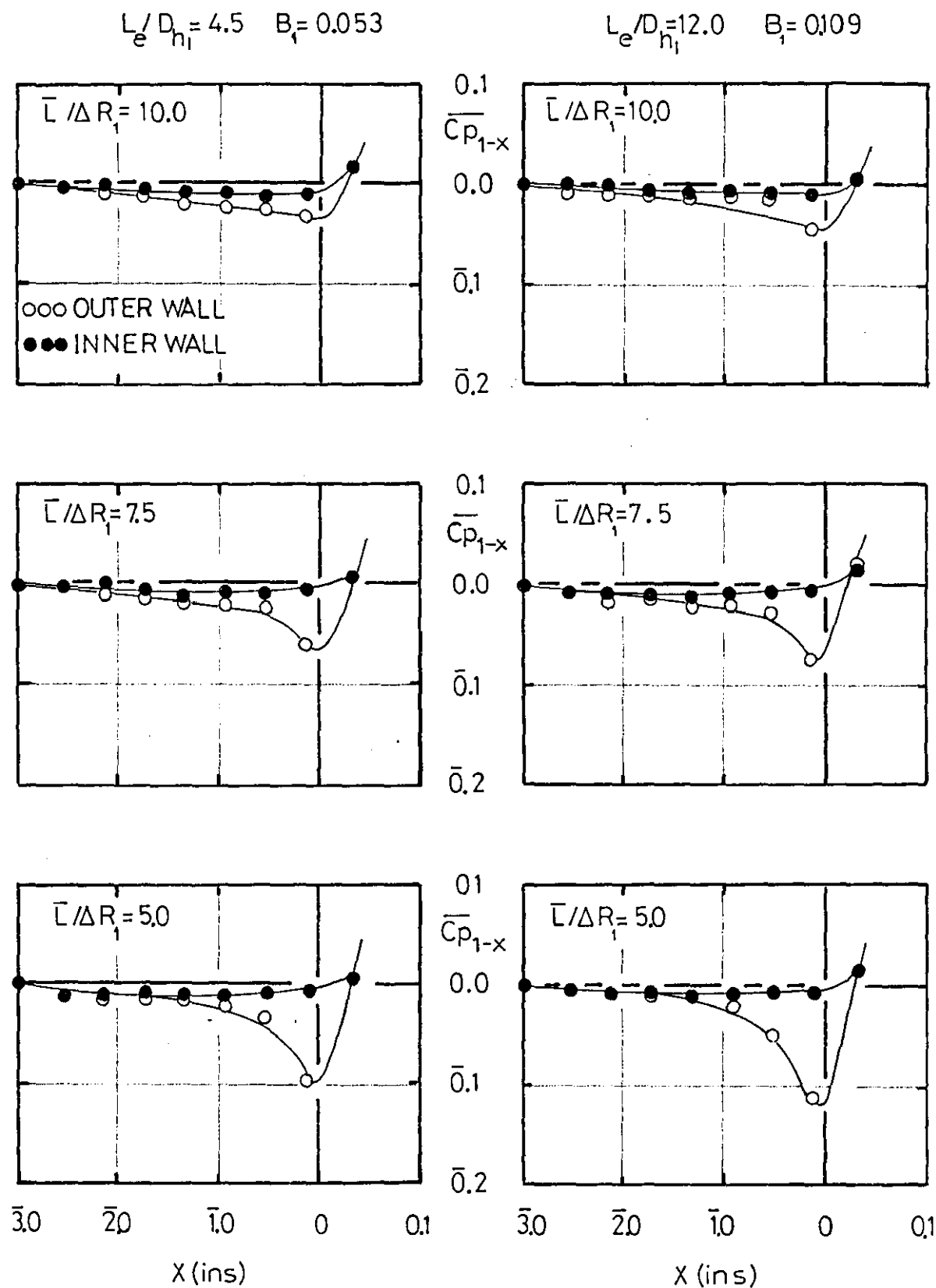


FIGURE 4.8

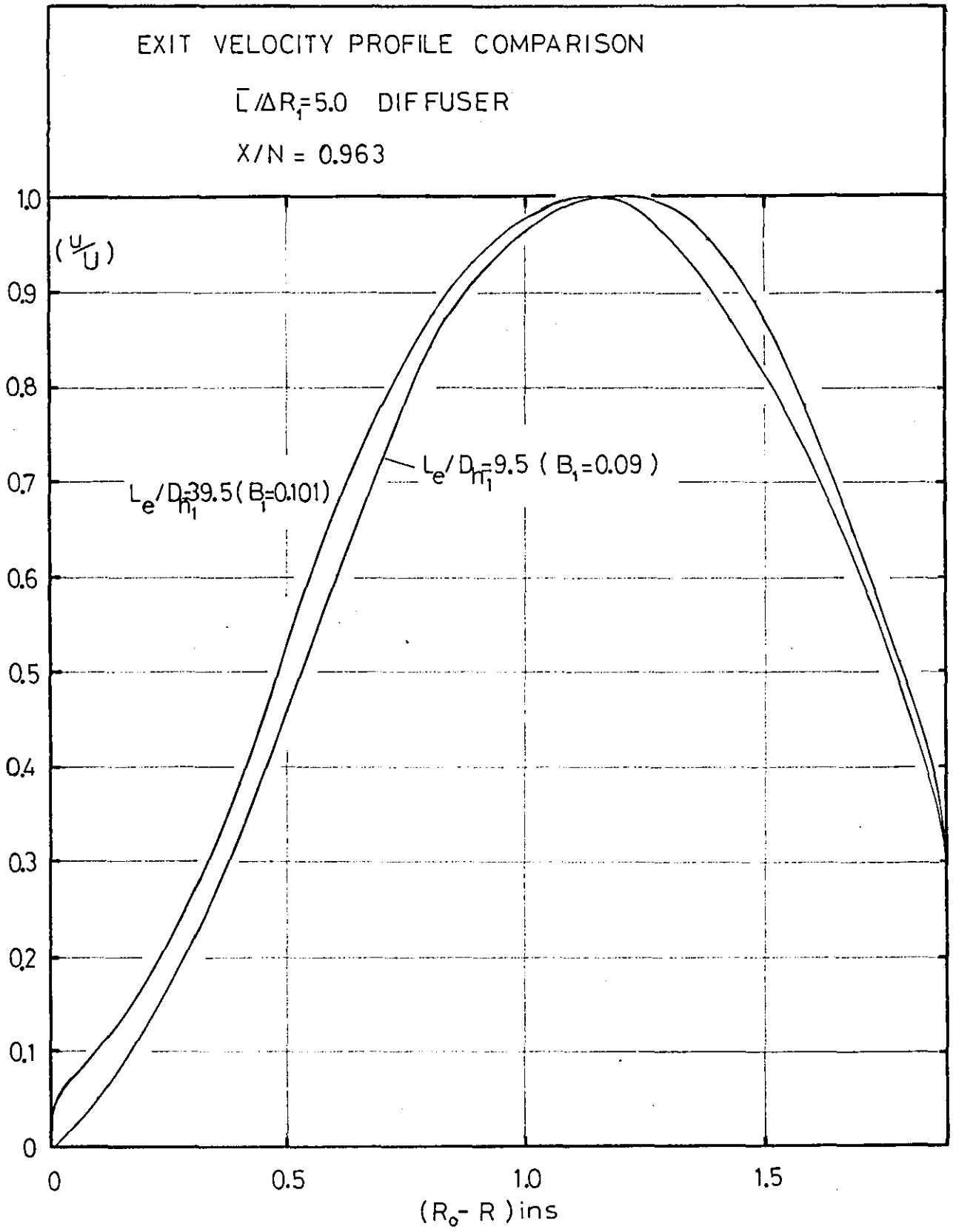


FIGURE 4.9

EFFECTIVENESS LOSS IN ANNULAR DIFFUSERS
FROM REFERENCE

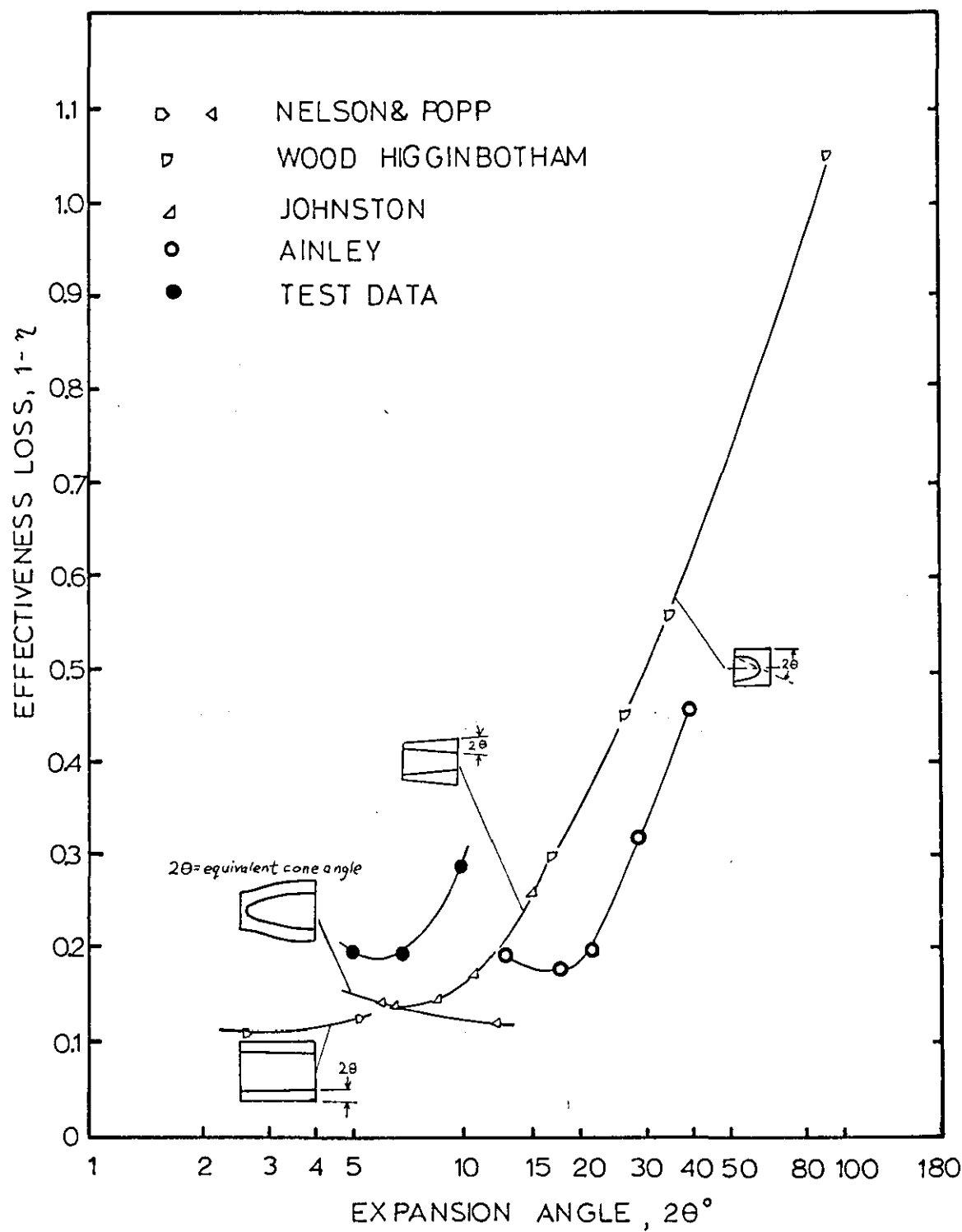
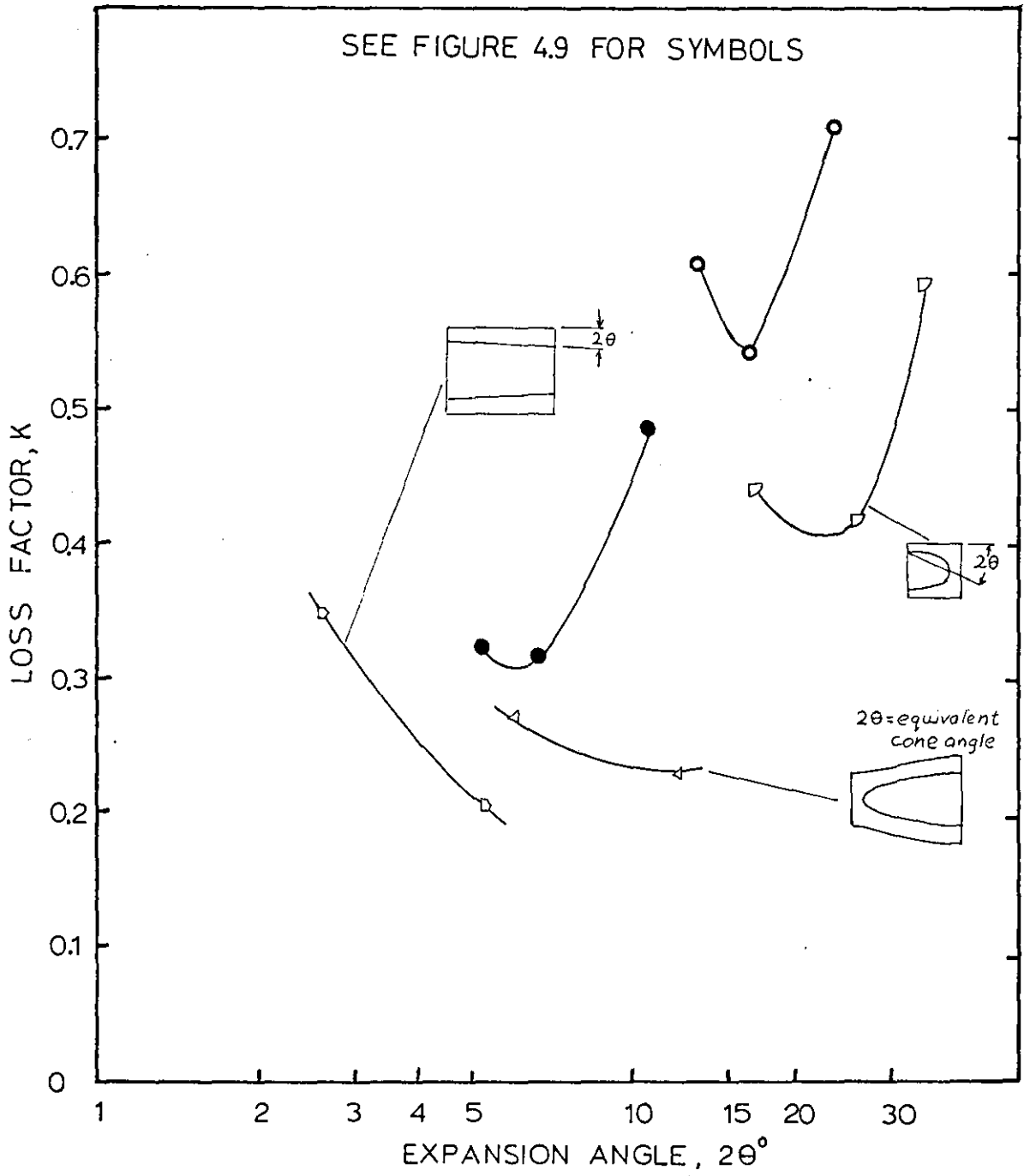
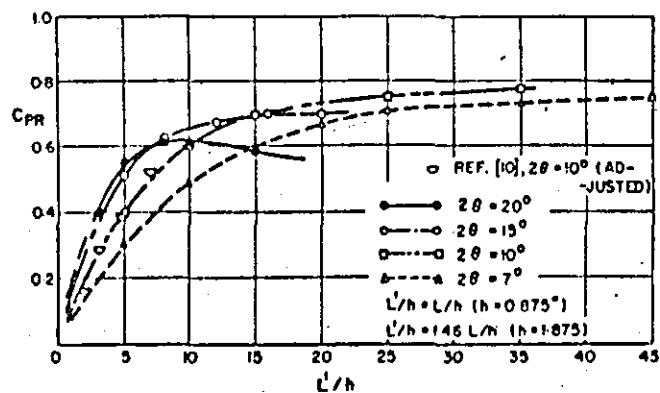
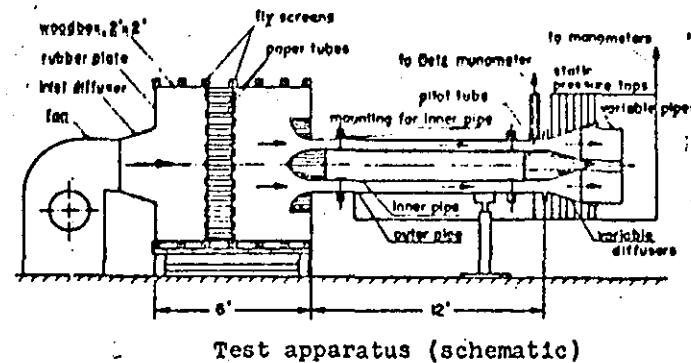
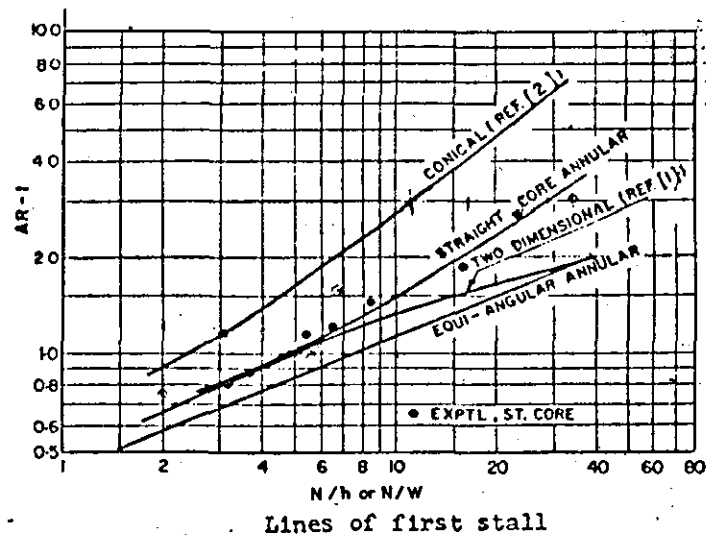


FIGURE 4.10

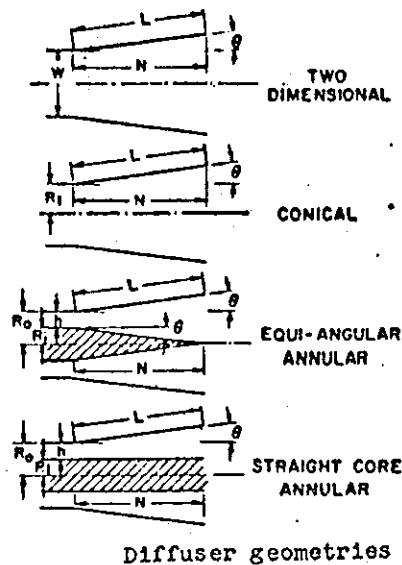
LOSS FACTOR IN ANNULAR DIFFUSERS
FROM REFERENCE



HOWARD ET AL(30)
ANNULAR DIFFUSER PERFORMANCE & STABILITY LIMITS



Pressure recovery for straight-core annular diffusers -- including comparison with Sovran and Klomp for $2\theta = 10$ deg, straight core, $R_1/R_0 = 0.55$ for which $L'/h = 1.40 L/h$ by linear interpolation. Recovery adjusted for fully developed entry flow



SOVRAN & KLOMP(62)
ANNULAR DIFFUSER PERFORMANCE & STABILITY LIMITS

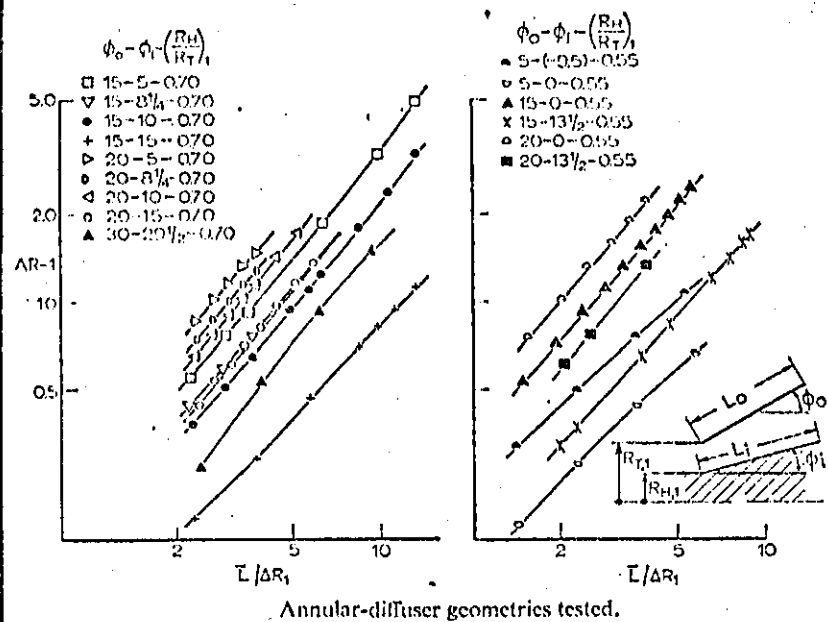
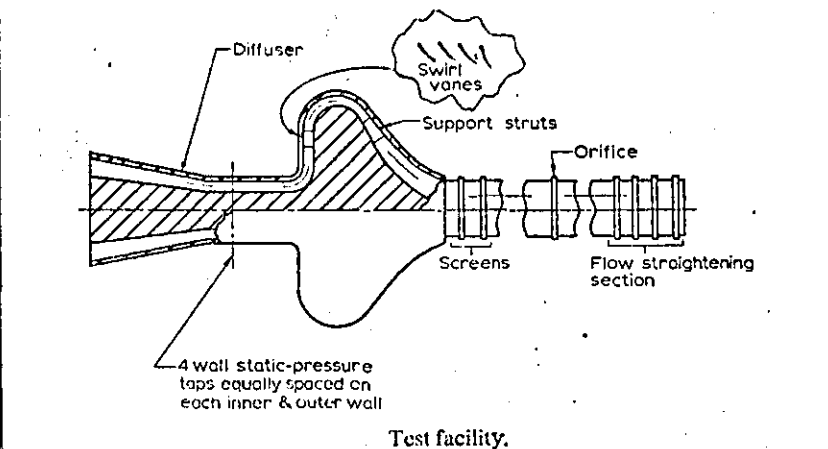
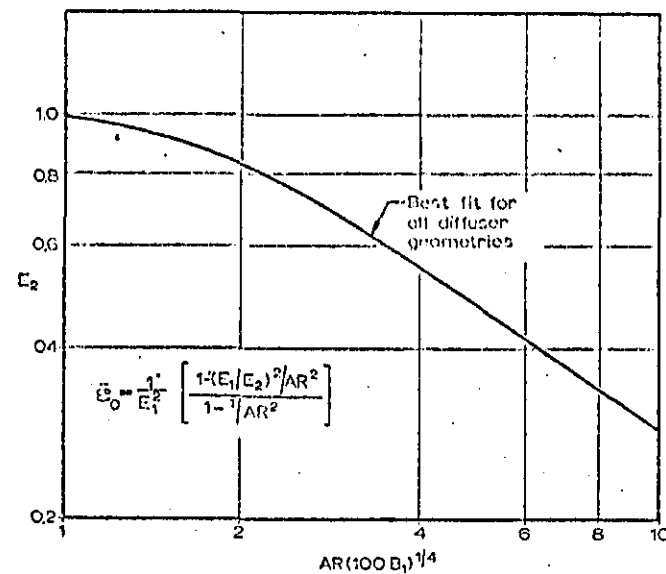
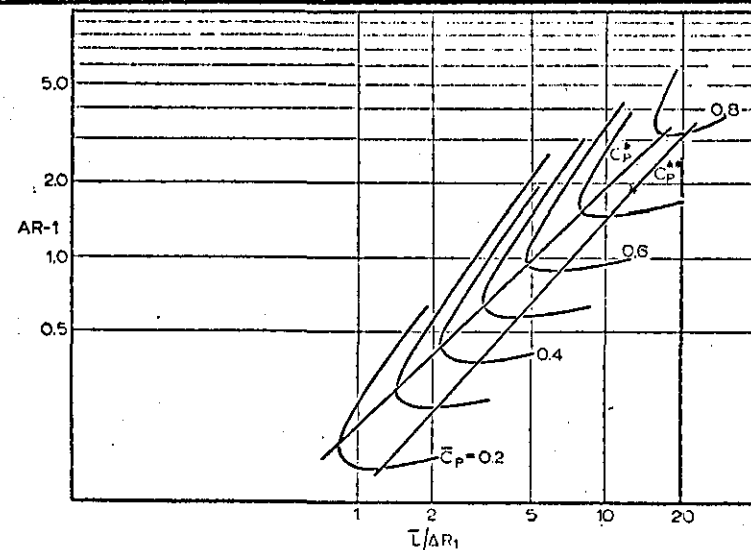


FIGURE 4.13

PRESSURE RECOVERY IN SETTLING LENGTH

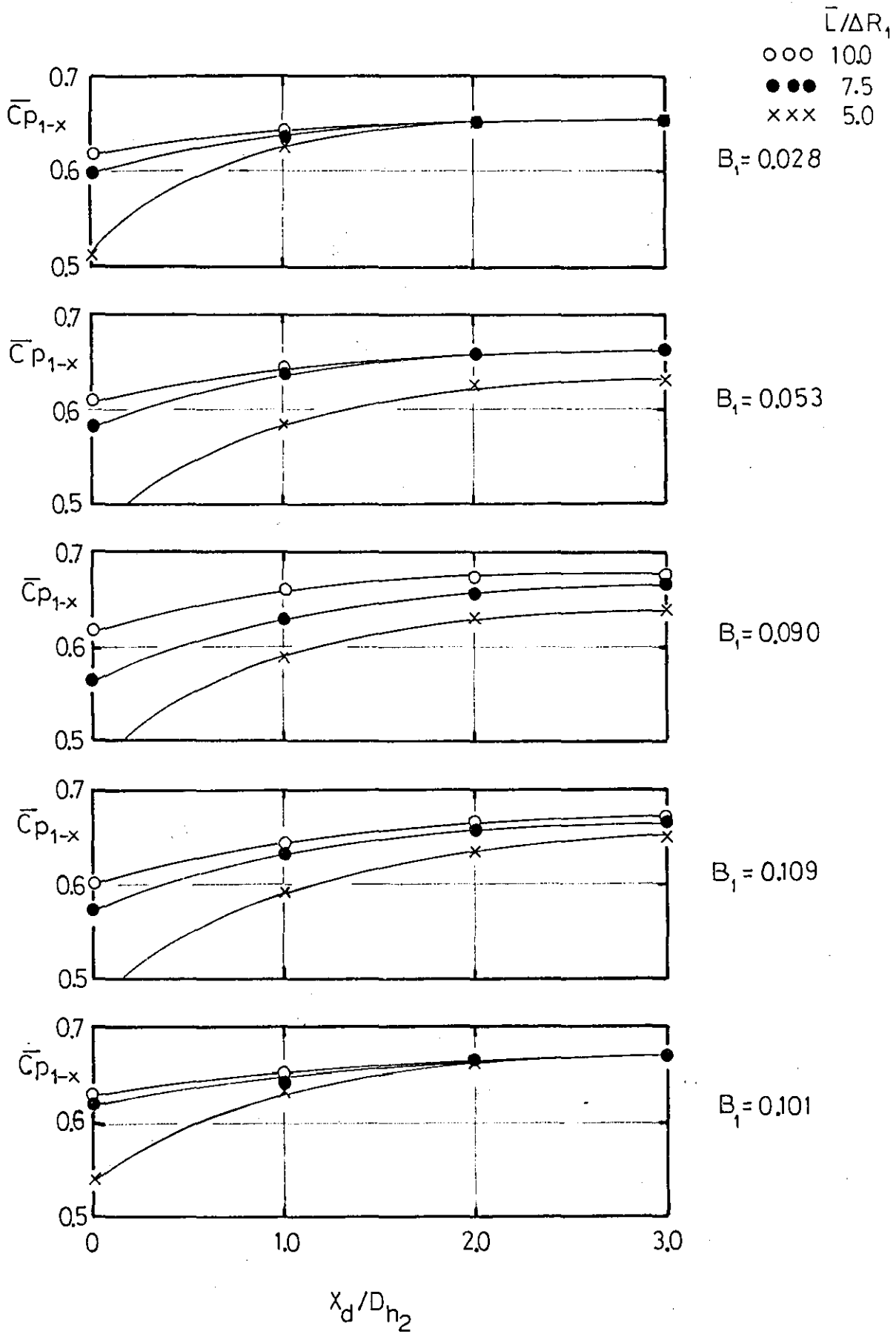
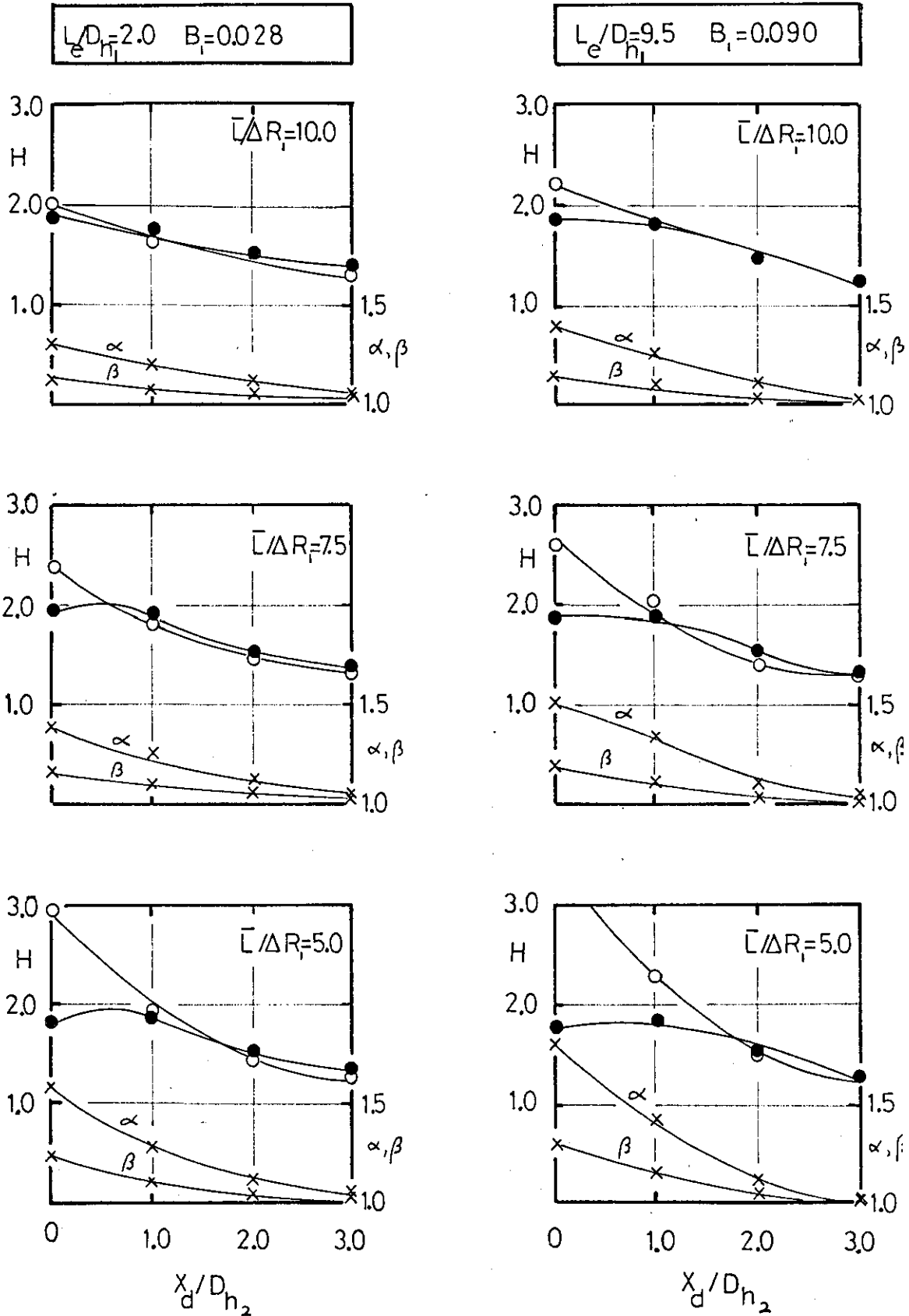


FIGURE 4.14

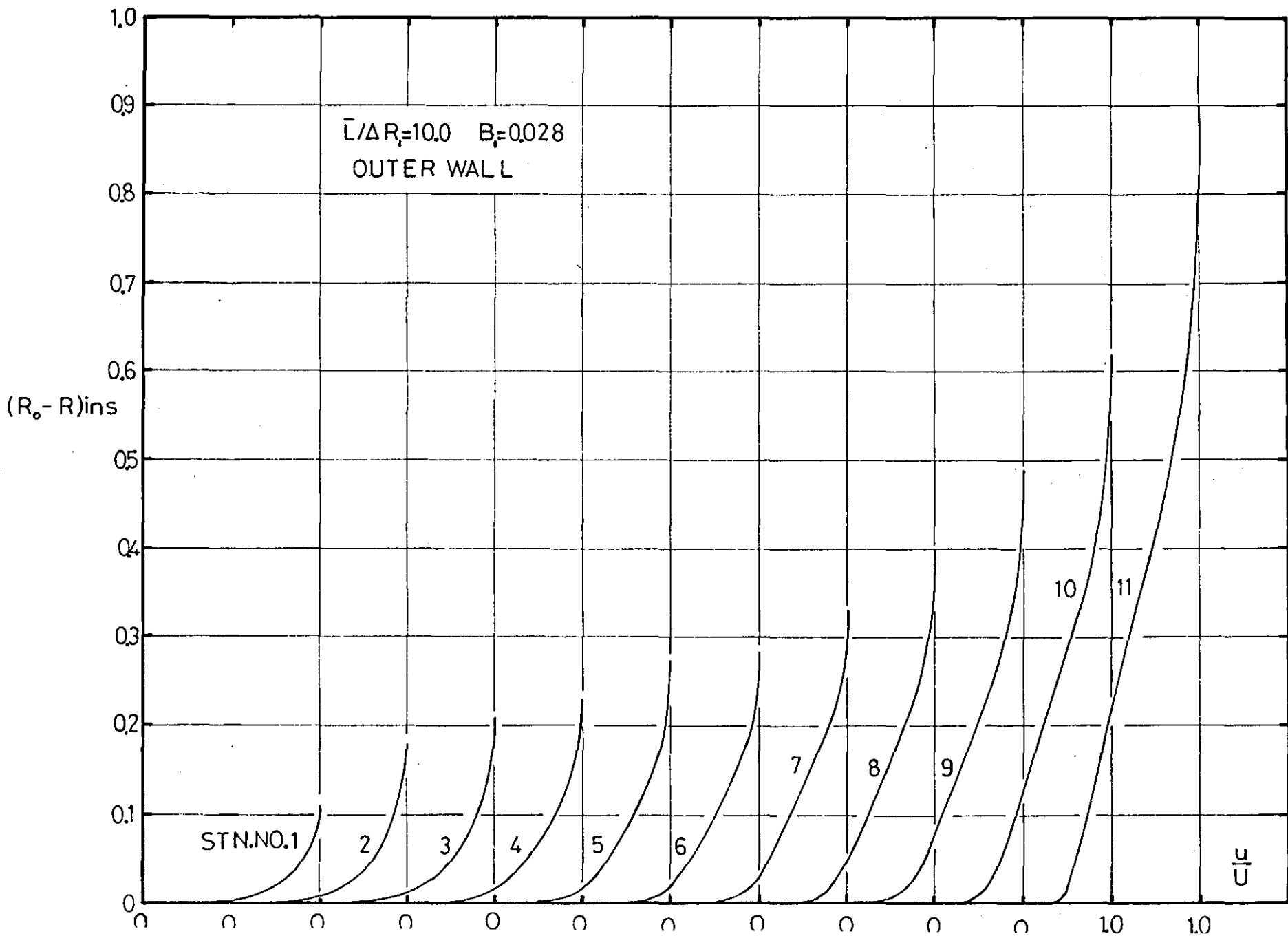
BEHAVIOUR OF VELOCITY PROFILE
PARAMETERS IN SETTLING LENGTH

○ ○ ○ OUTER WALL
● ● ● INNER WALL



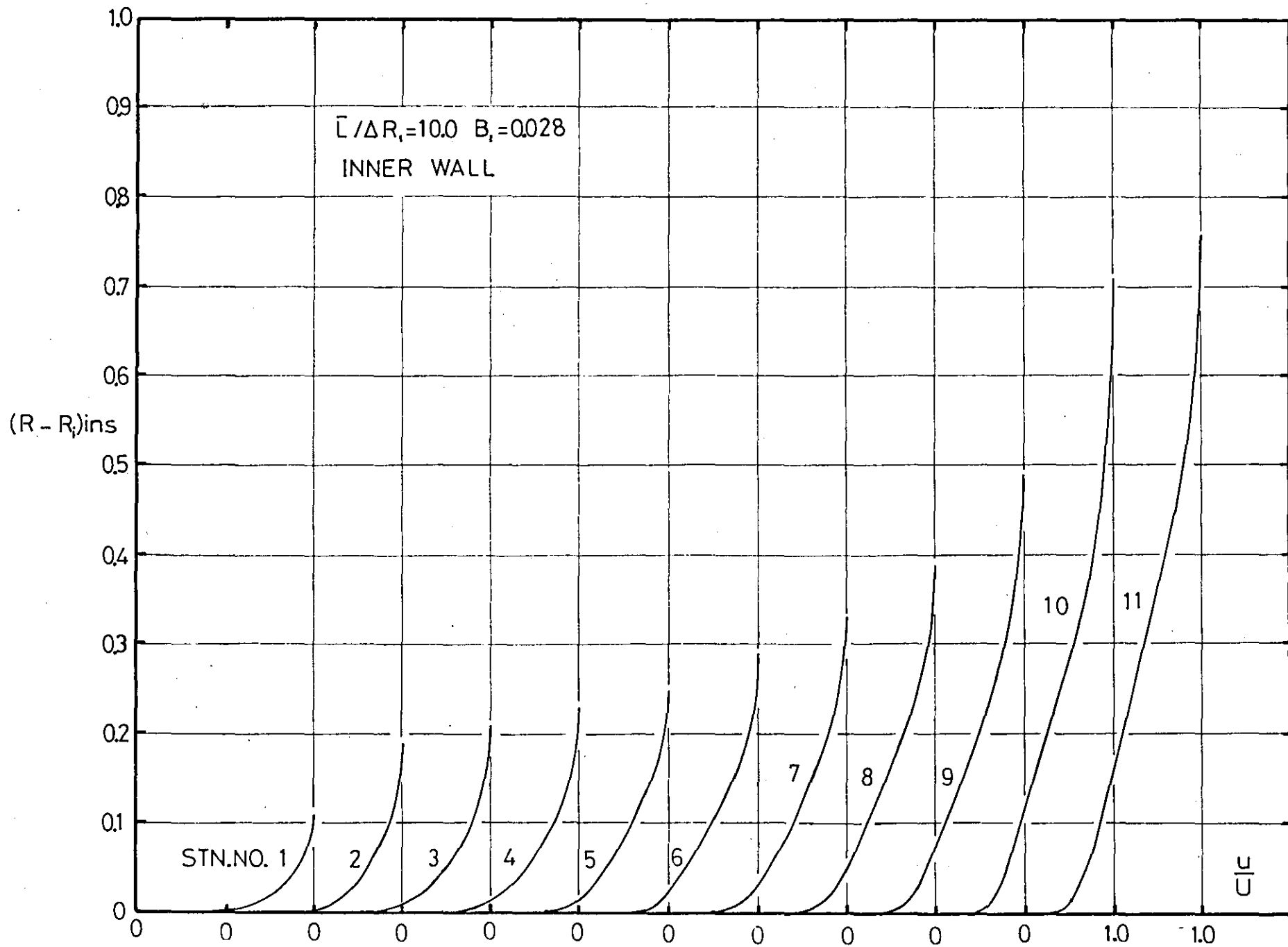
MEAN VELOCITY PROFILE DEVELOPMENT

FIGURE 4.15



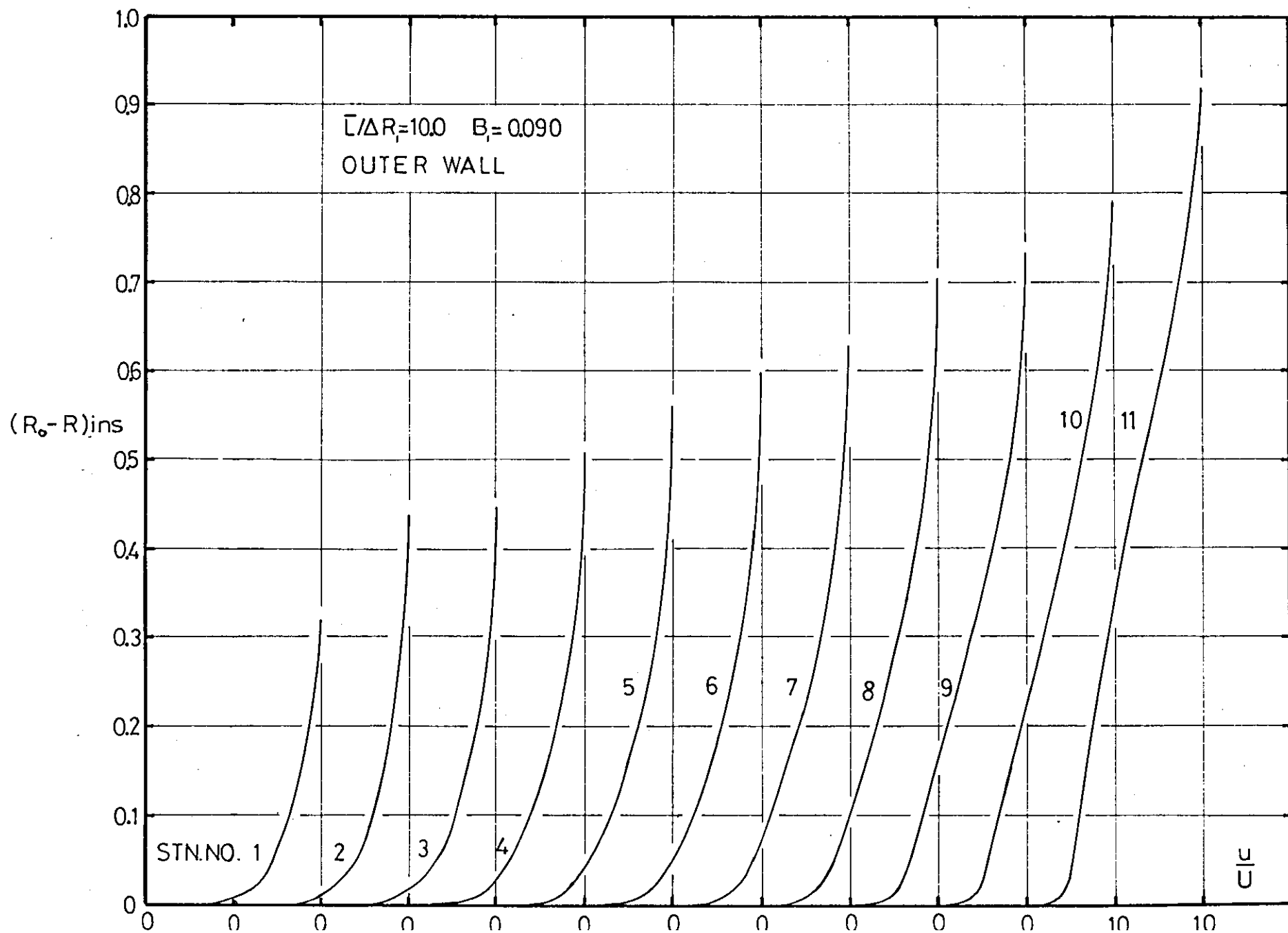
MEAN VELOCITY PROFILE DEVELOPMENT

FIGURE 4.16



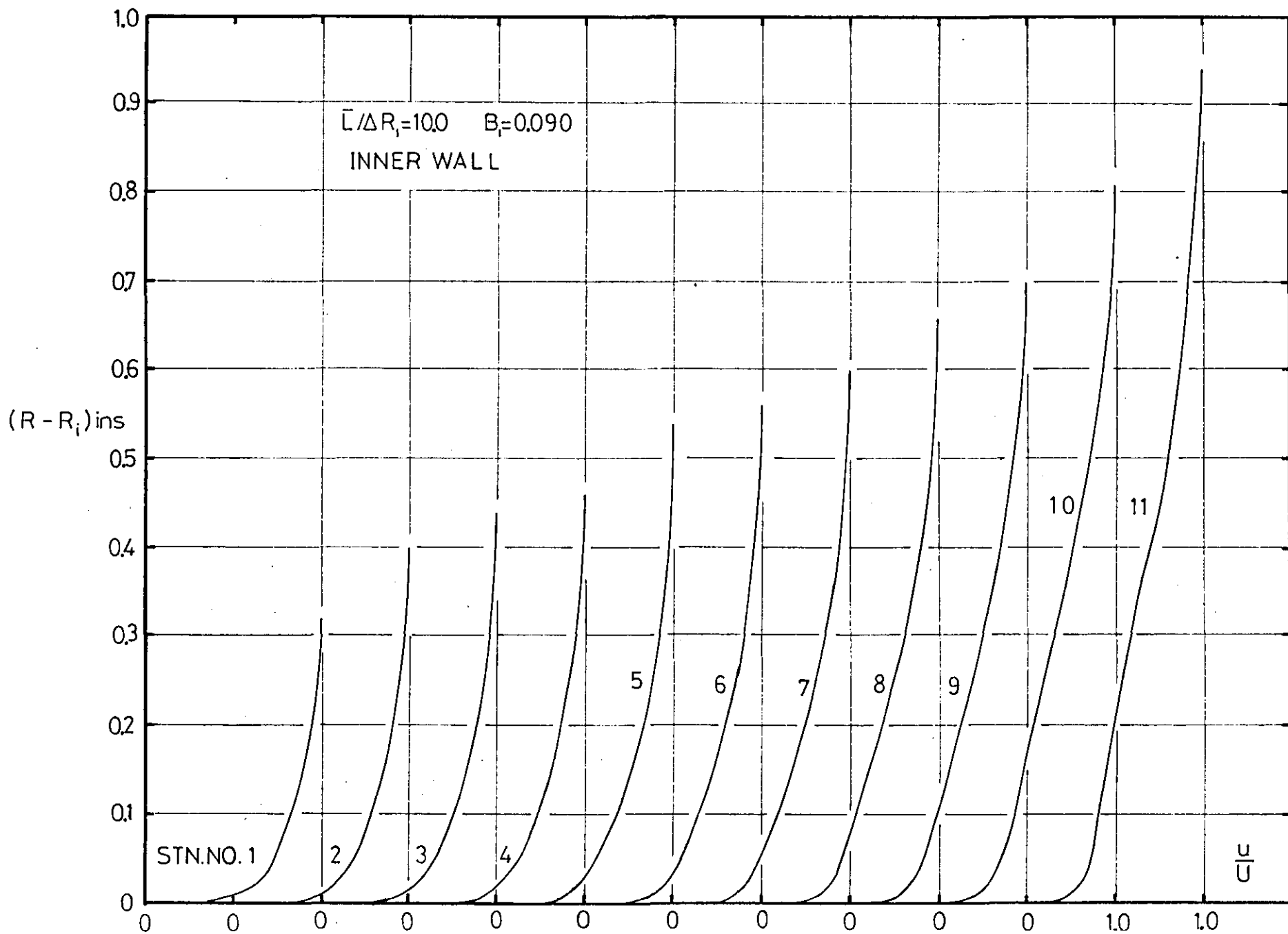
MEAN VELOCITY PROFILE DEVELOPMENT

FIGURE 4.17



MEAN VELOCITY PROFILE DEVELOPMENT

FIGURE 4.18



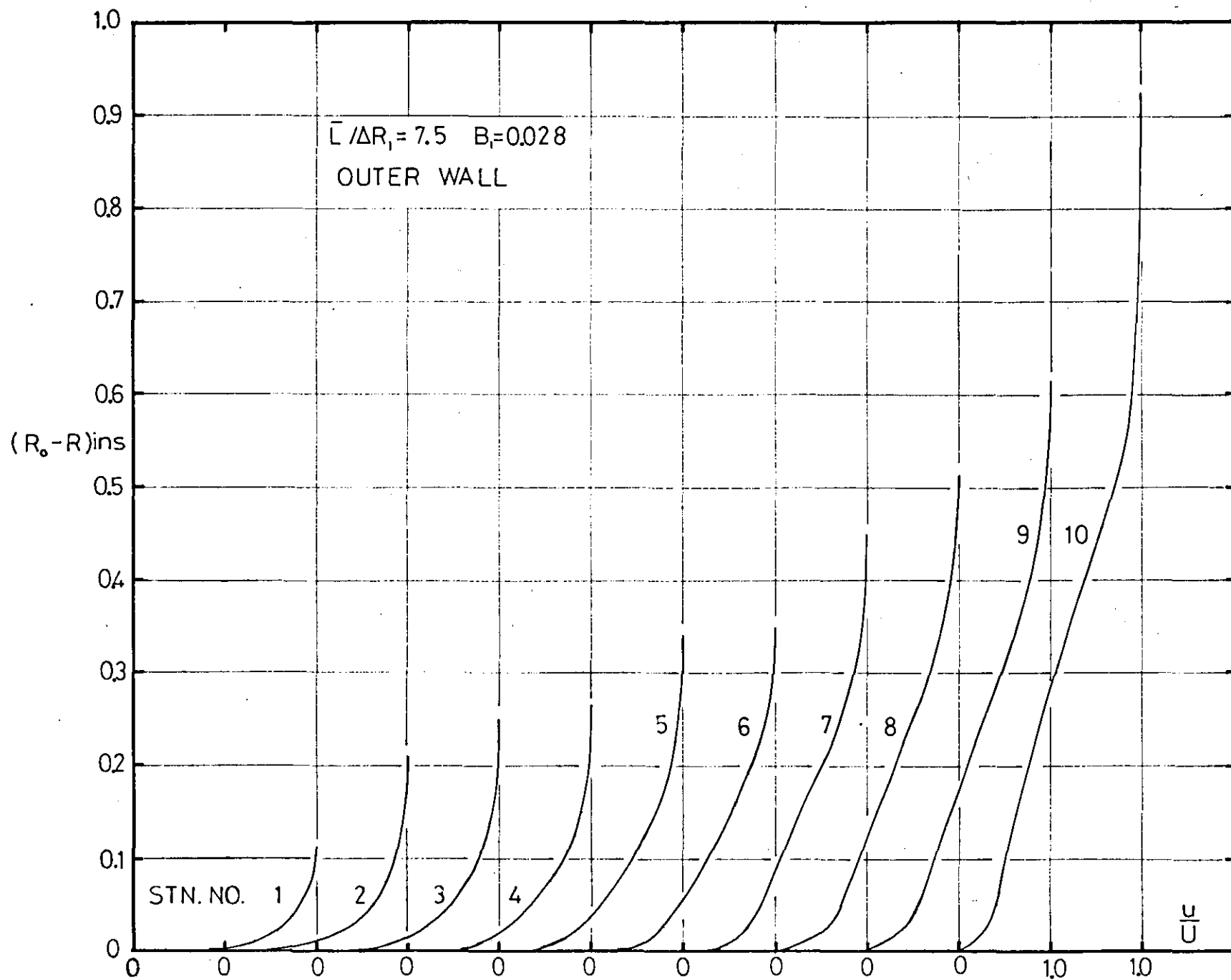
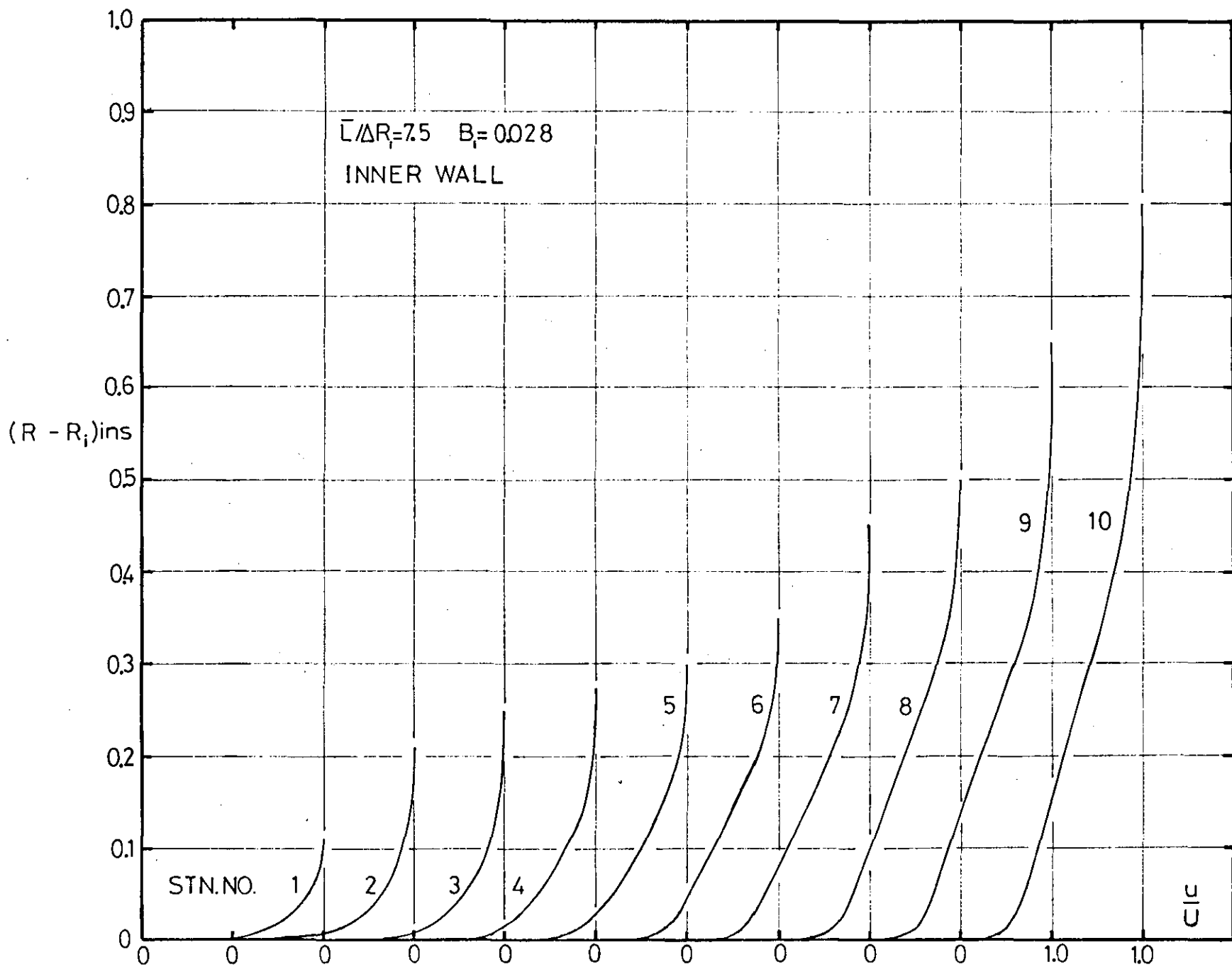
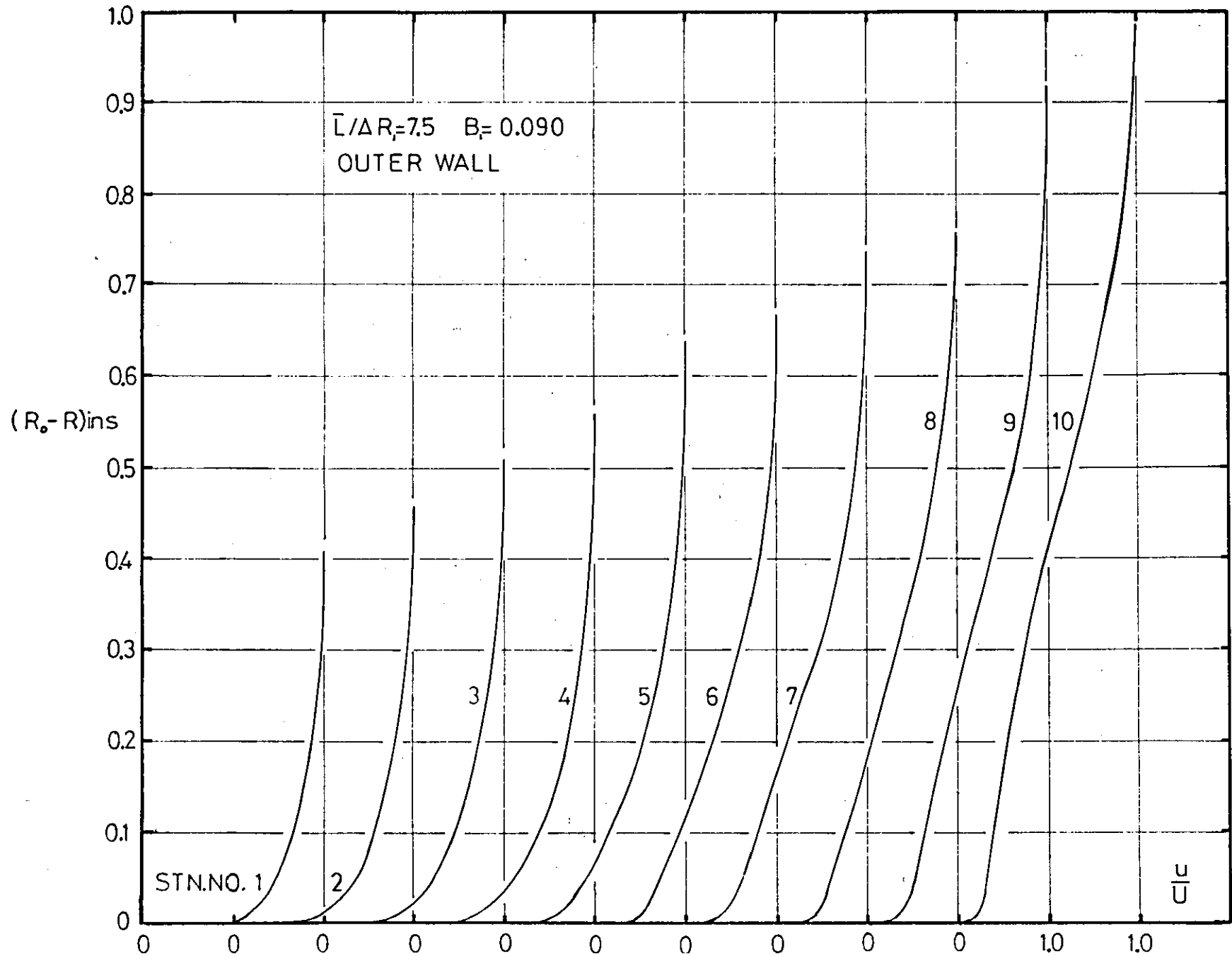


FIGURE 4.19

MEAN VELOCITY PROFILE DEVELOPMENT

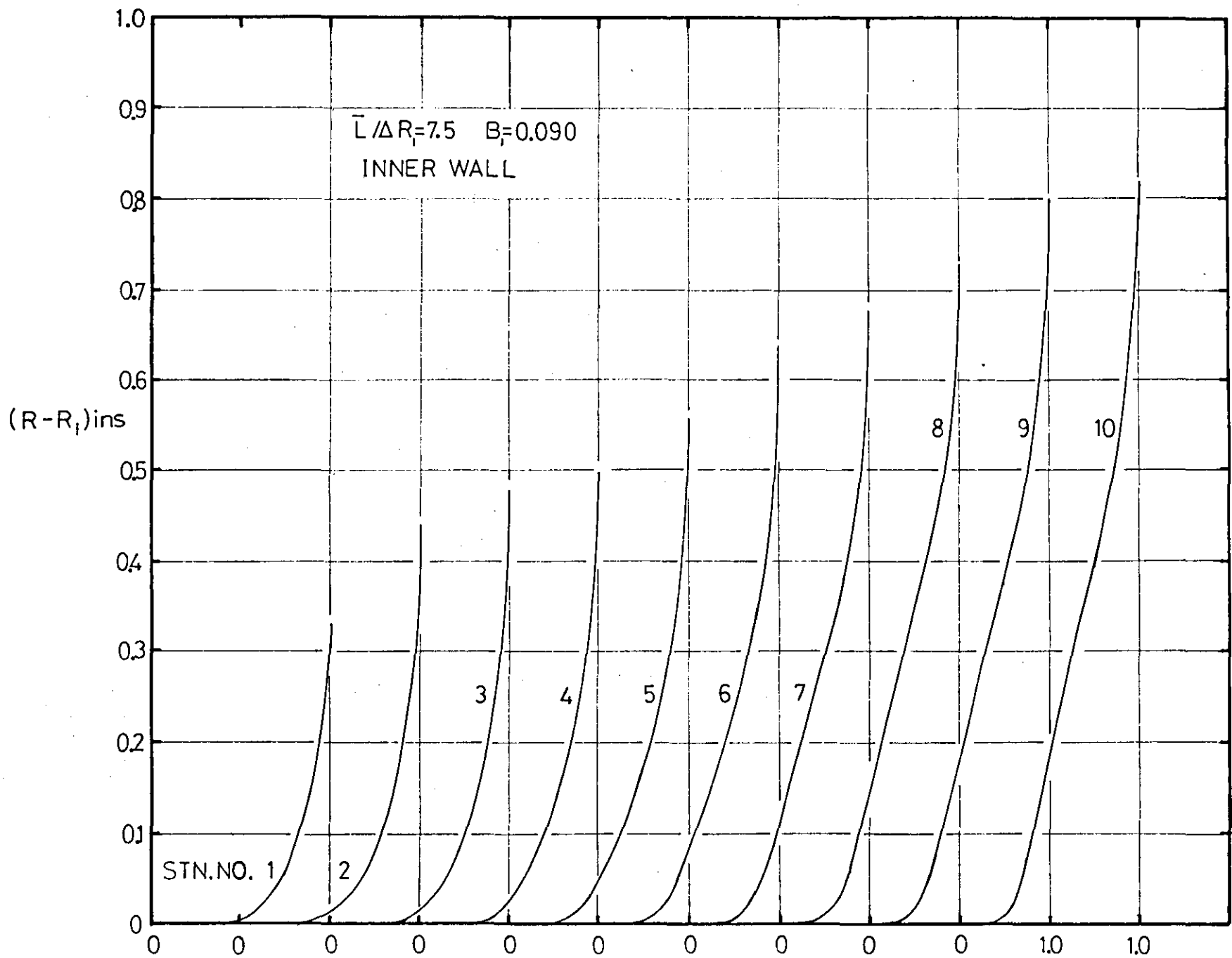
FIGURE 4.20





MEAN VELOCITY PROFILE DEVELOPMENT

FIGURE 4.21



MEAN VELOCITY PROFILE DEVELOPMENT

FIGURE 4.22

MEAN VELOCITY PROFILE DEVELOPMENT

FIGURE 4.23

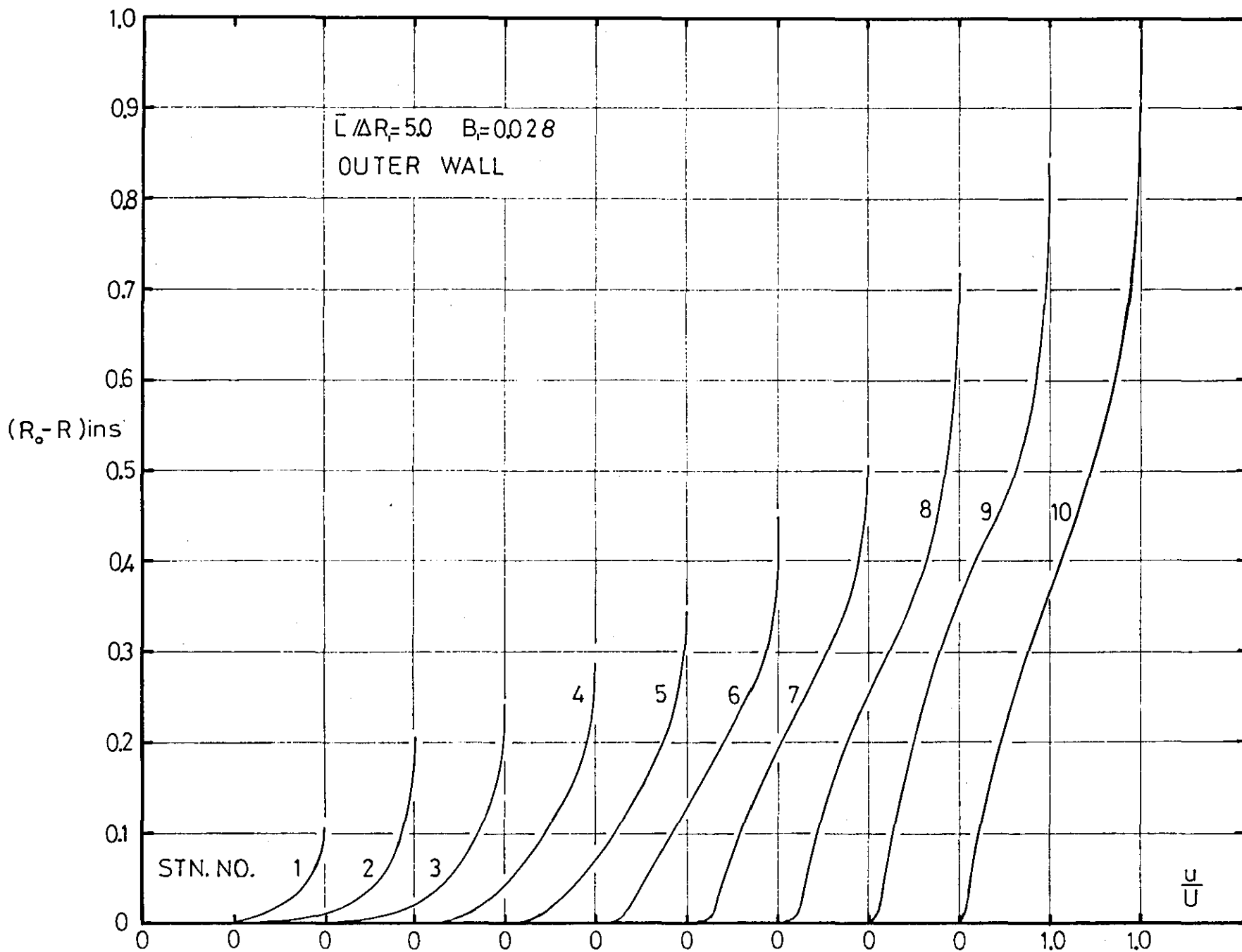
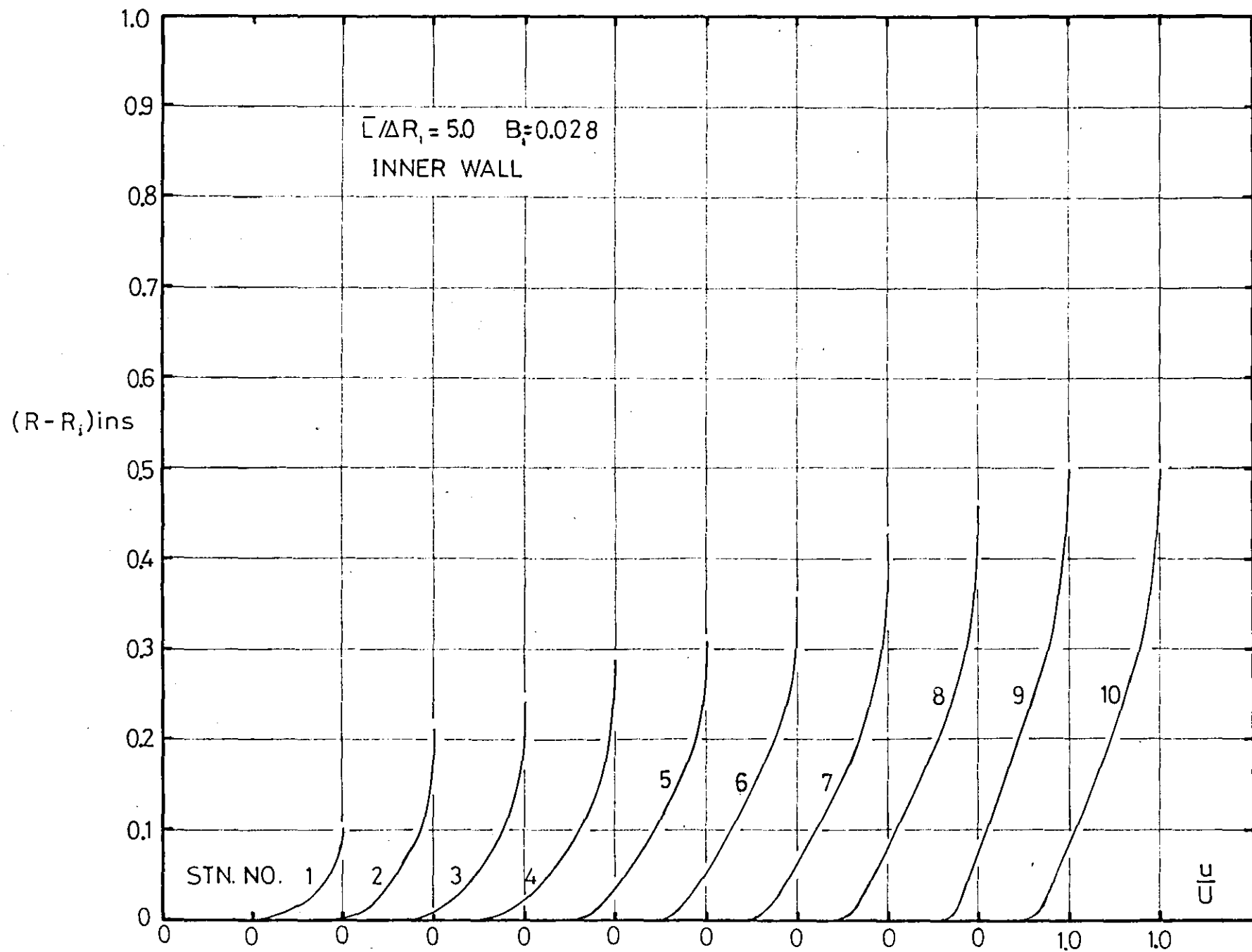
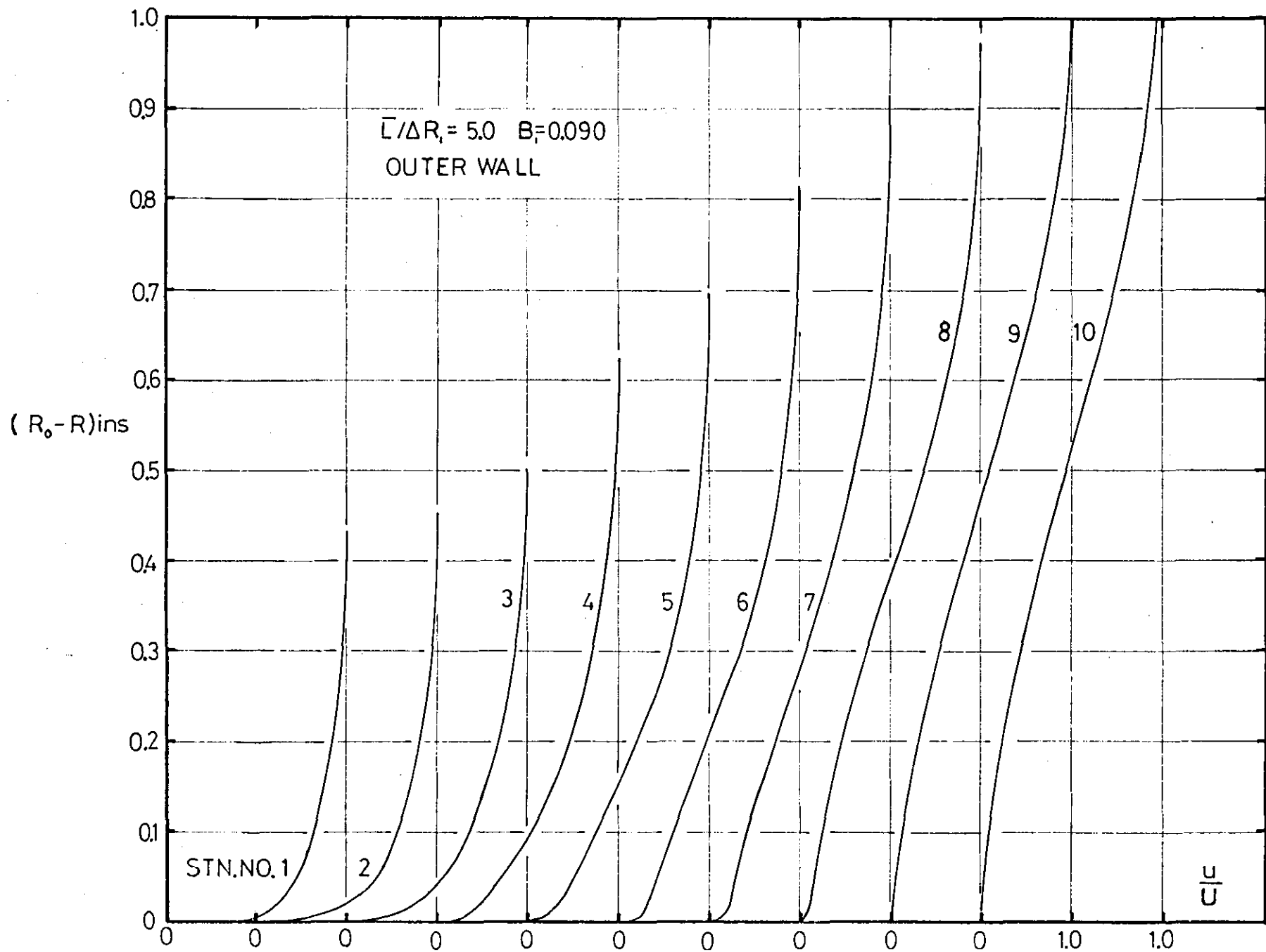


FIGURE 4.24





MEAN VELOCITY PROFILE DEVELOPMENT

FIGURE 4.25

MEAN VELOCITY PROFILE DEVELOPMENT

FIGURE 4.26

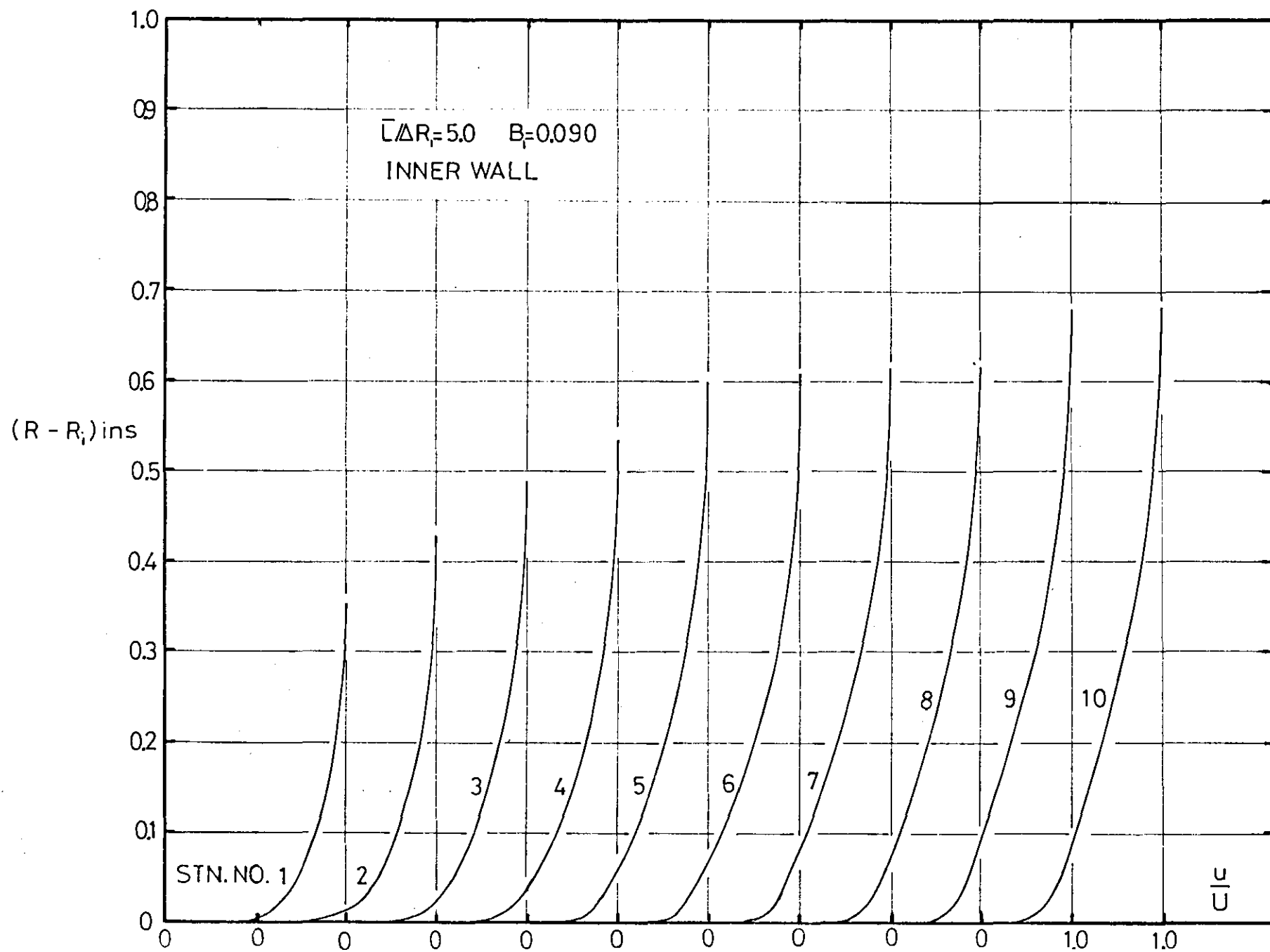


FIGURE 4.27

FLOW ASYMMETRY ANALYSIS

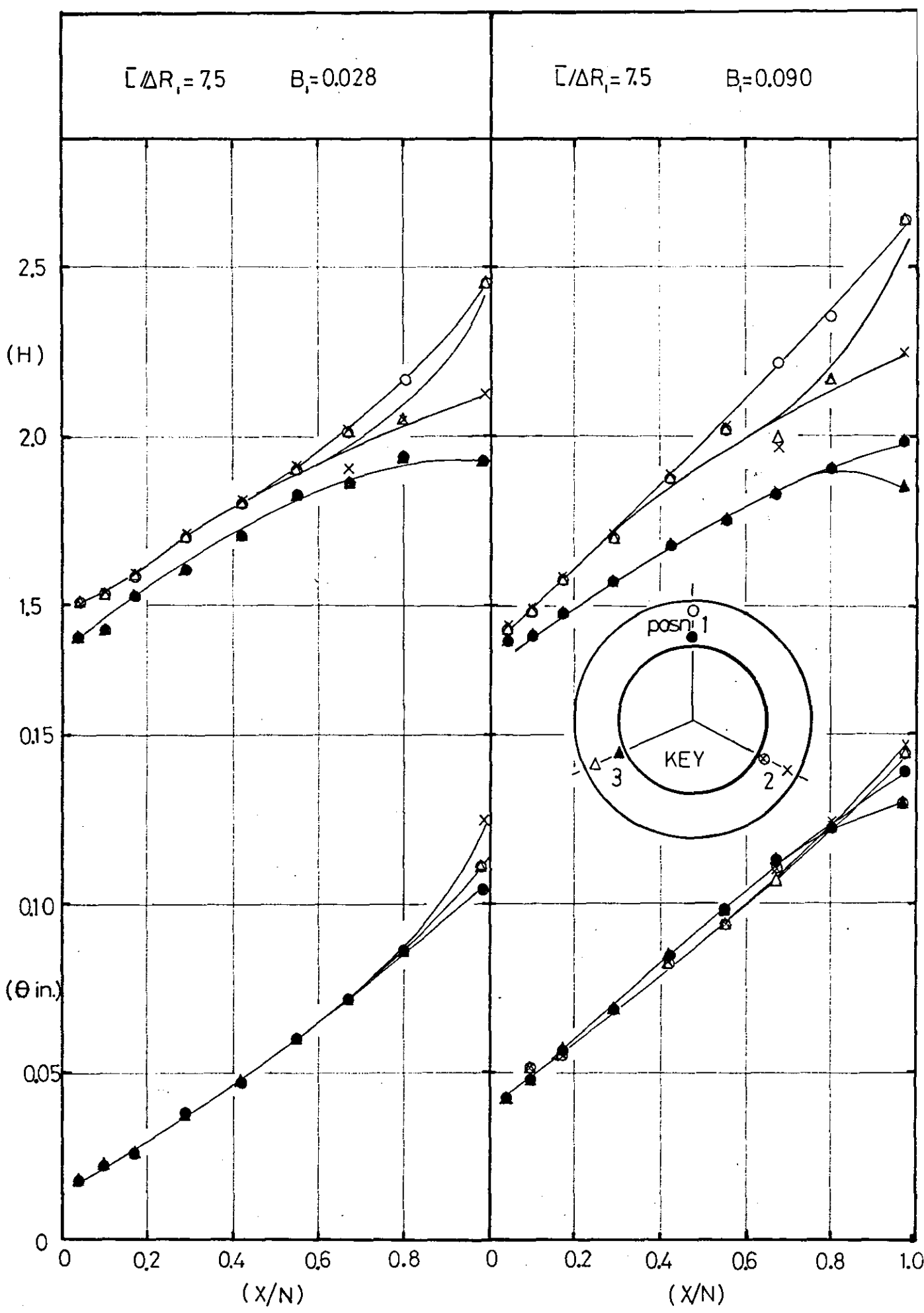


FIGURE 4.28

BOUNDARY LAYER DEVELOPMENT IN TEST DIFFUSERS

$B_i = 0.028$ ($L_e/D_{h_i} = 2.0$) $Re_{\phi_{h_i}} \approx 1.75 \times 10^5$

○ ○ ○ OUTER WALL
● ● ● INNER WALL

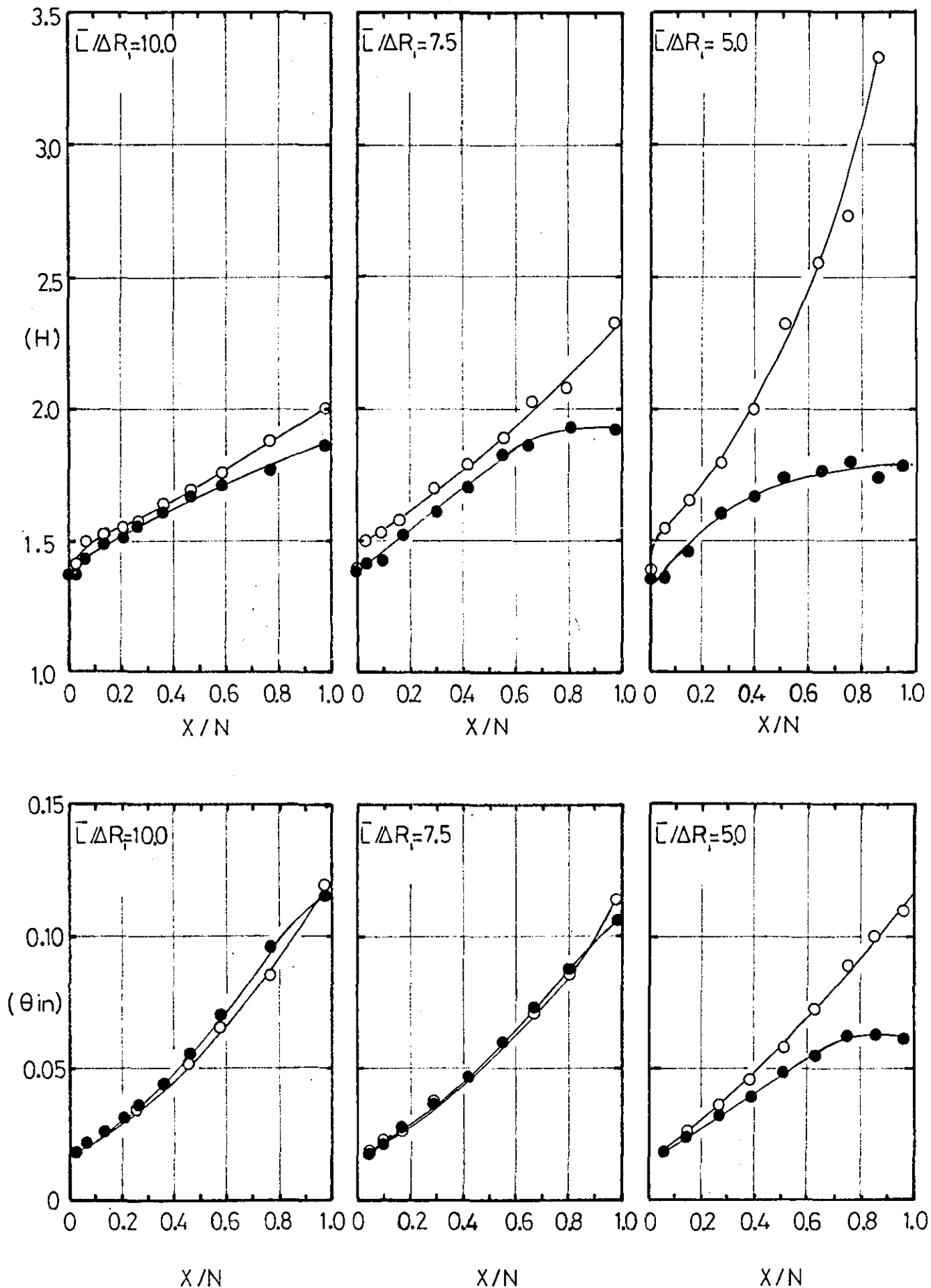


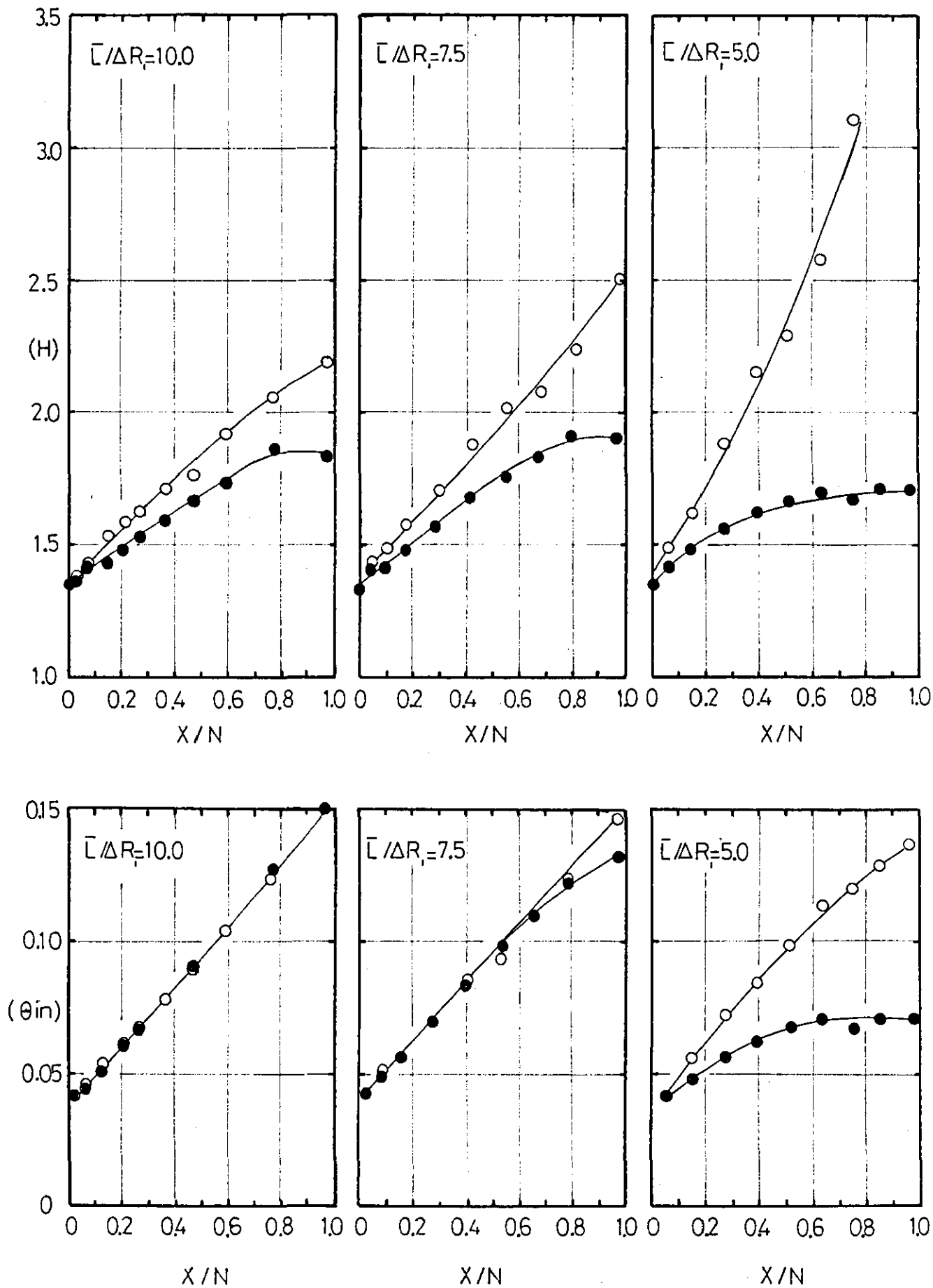
FIGURE 4.29

BOUNDARY LAYER DEVELOPMENT IN TEST DIFFUSERS

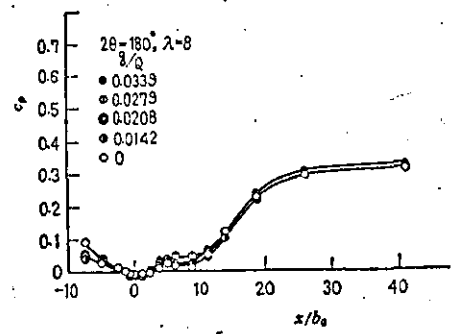
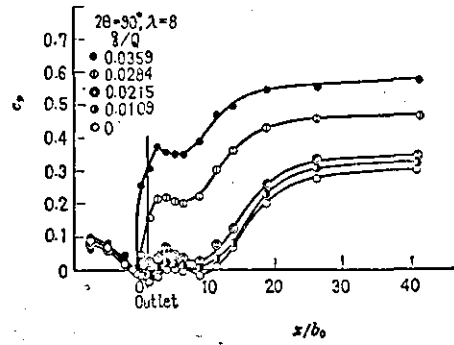
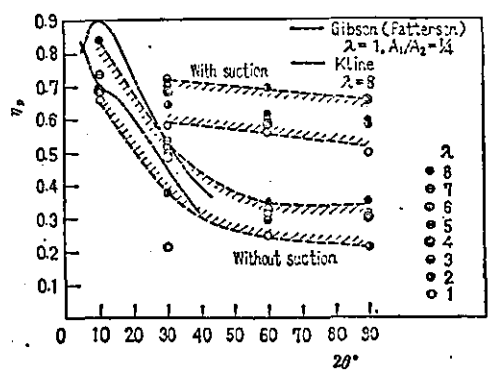
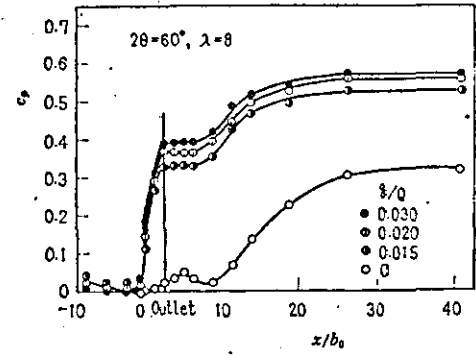
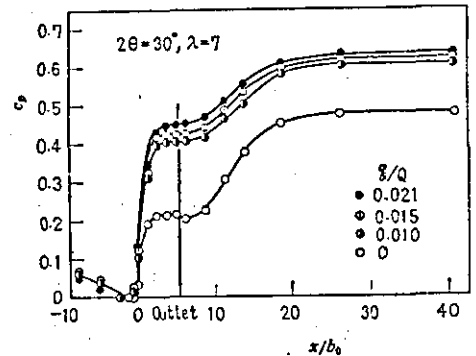
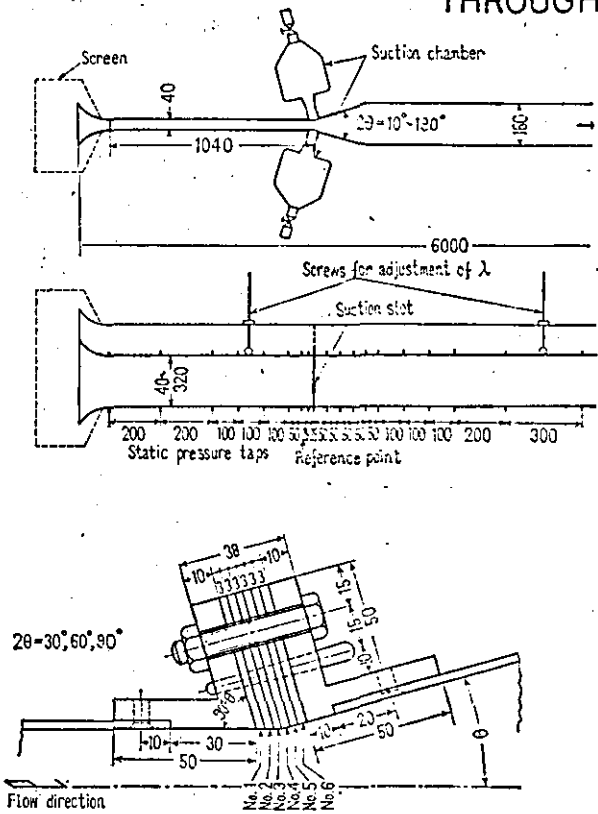
$$B_1 = 0.090 \left(L_e / D_{h_1} = 9.5 \right)$$

$$Re_{D_{h_1}} \approx 1.75 \times 10^5$$

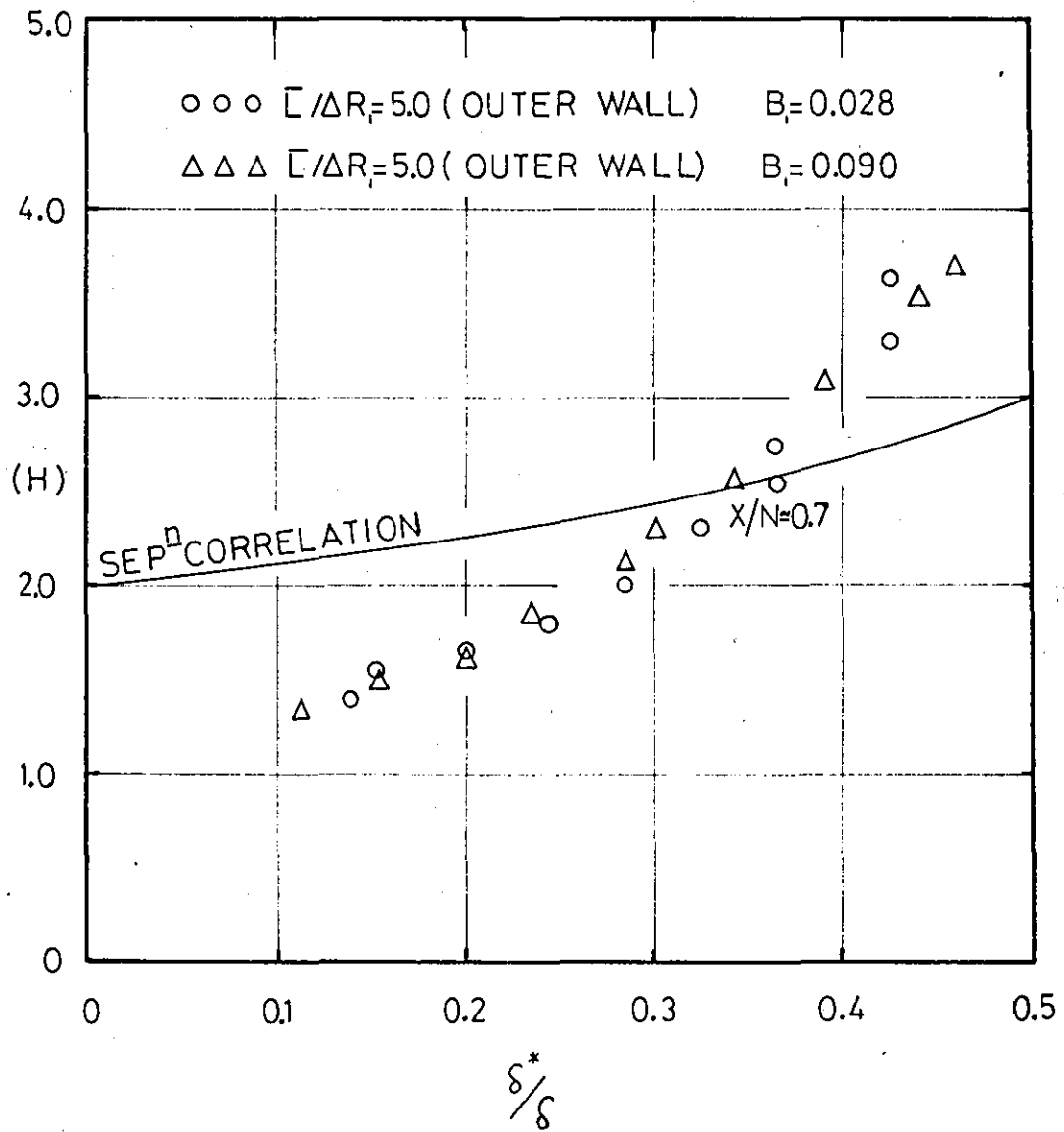
○○ OUTER WALL
●● INNER WALL



FURUYA ET AL(24) DIFFUSER PERFORMANCE IMPROVEMENT
THROUGH INLET SUCTION



COMPARISON OF TEST DATA WITH THE TURBULENT
FLOW CORRELATION OF SANDBORN & KLINE(56).



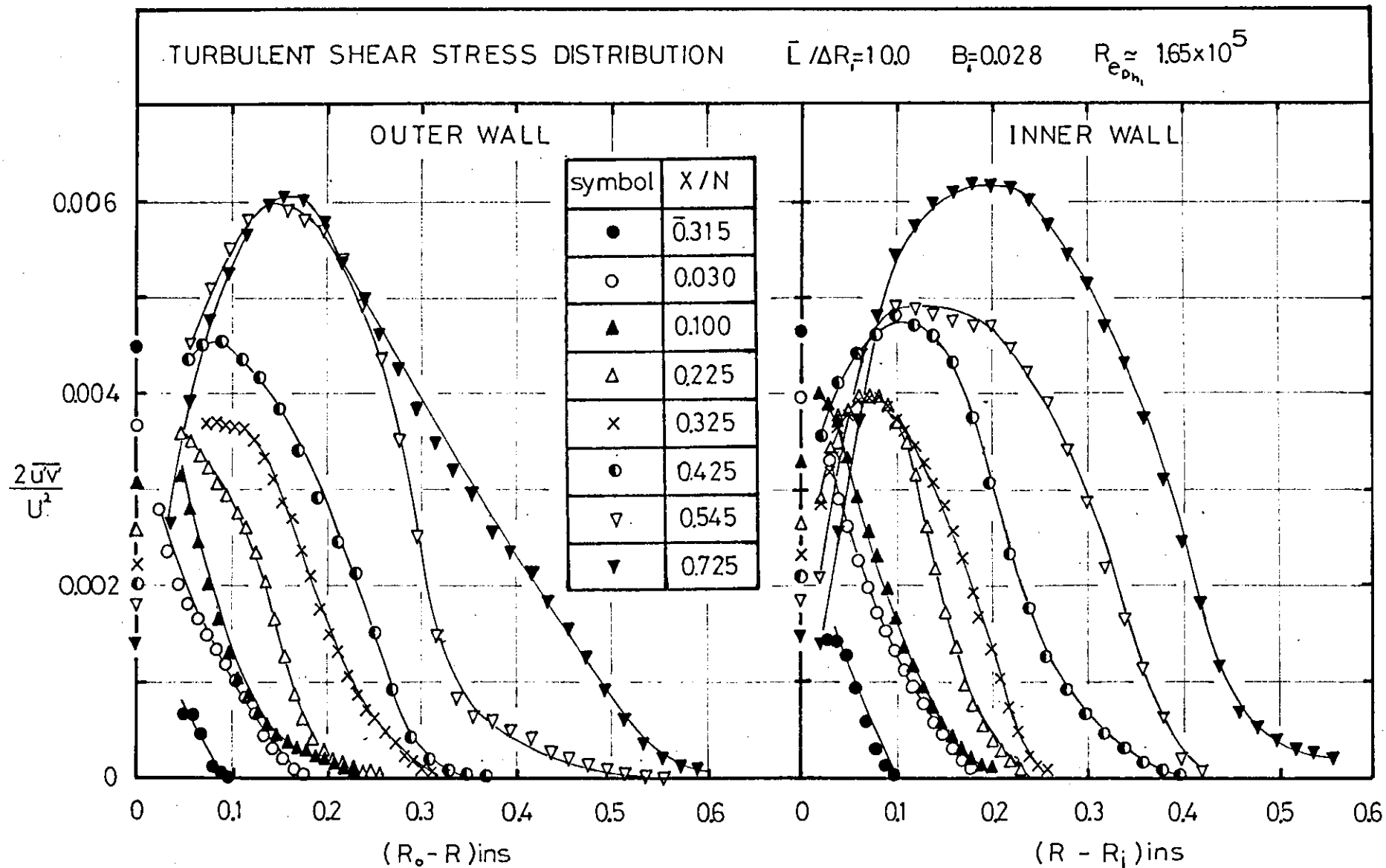


FIGURE 4.32

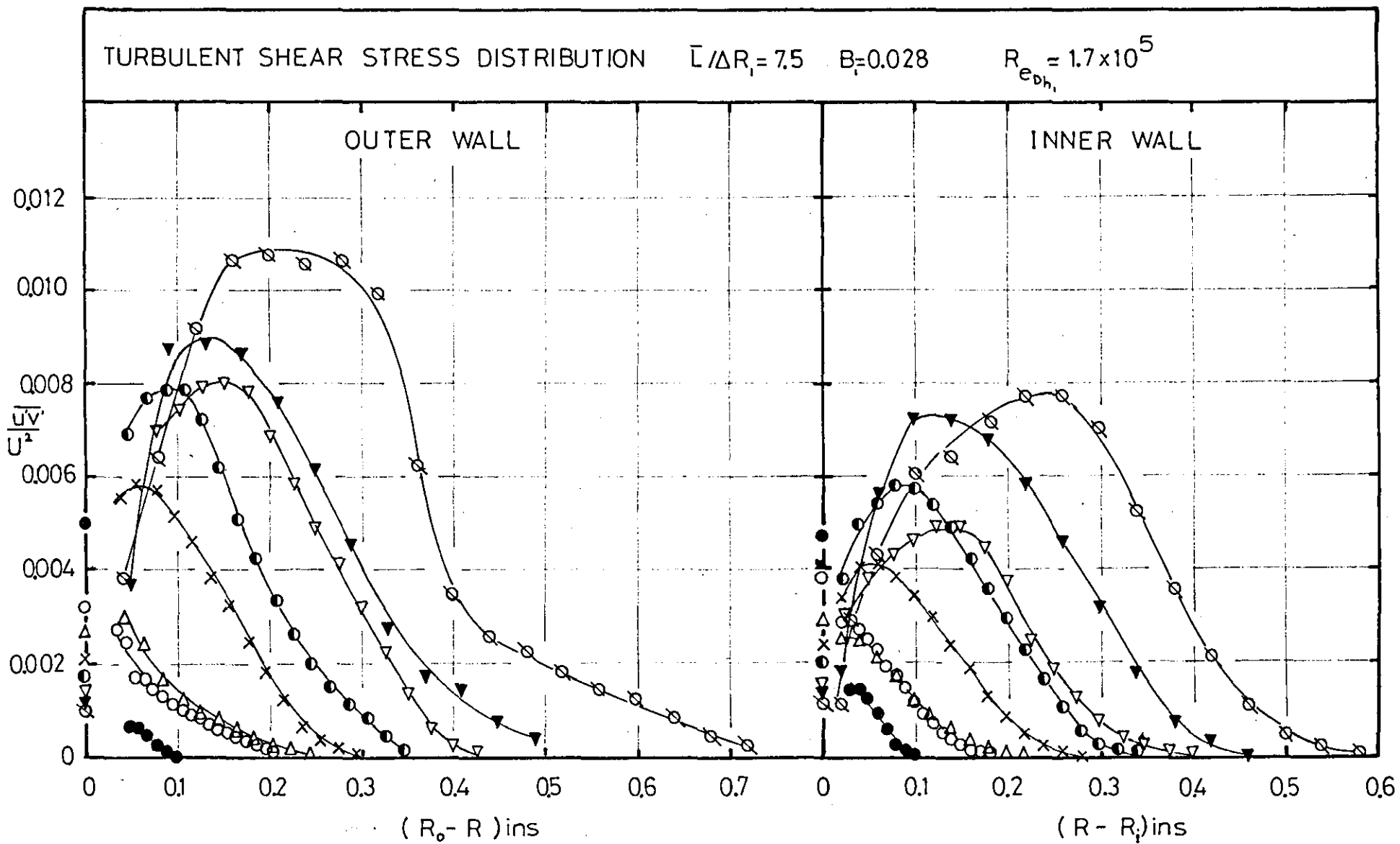
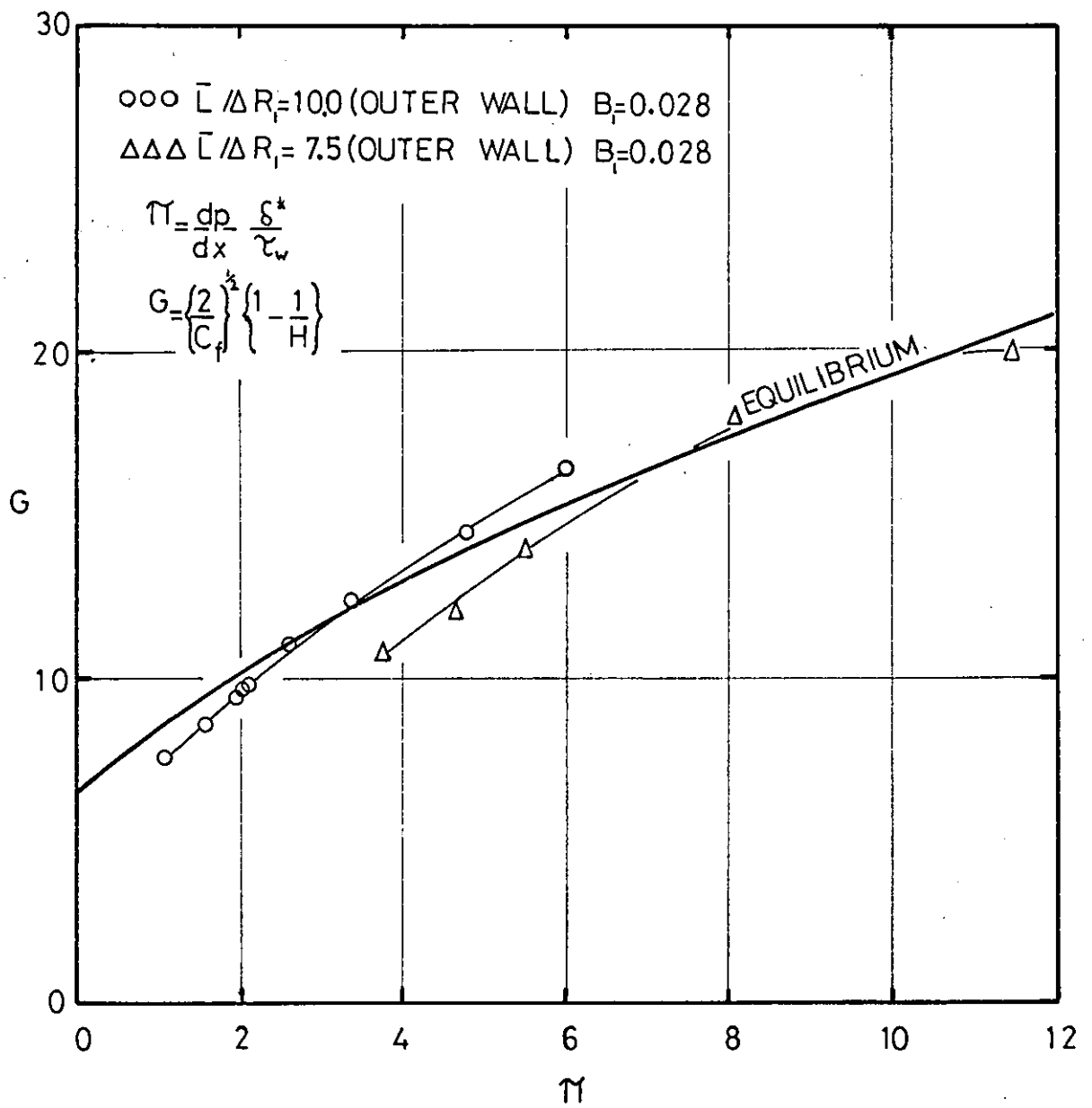


FIGURE 4.33

FIGURE 4.34

COMPARISON WITH EQUILIBRIUM BOUNDARY

LAYER PROFILE OF NASH(45)



COMPARISON WITH THE TRANSITORY STALL
CRITERION OF SPANGENBERG ET AL(64)

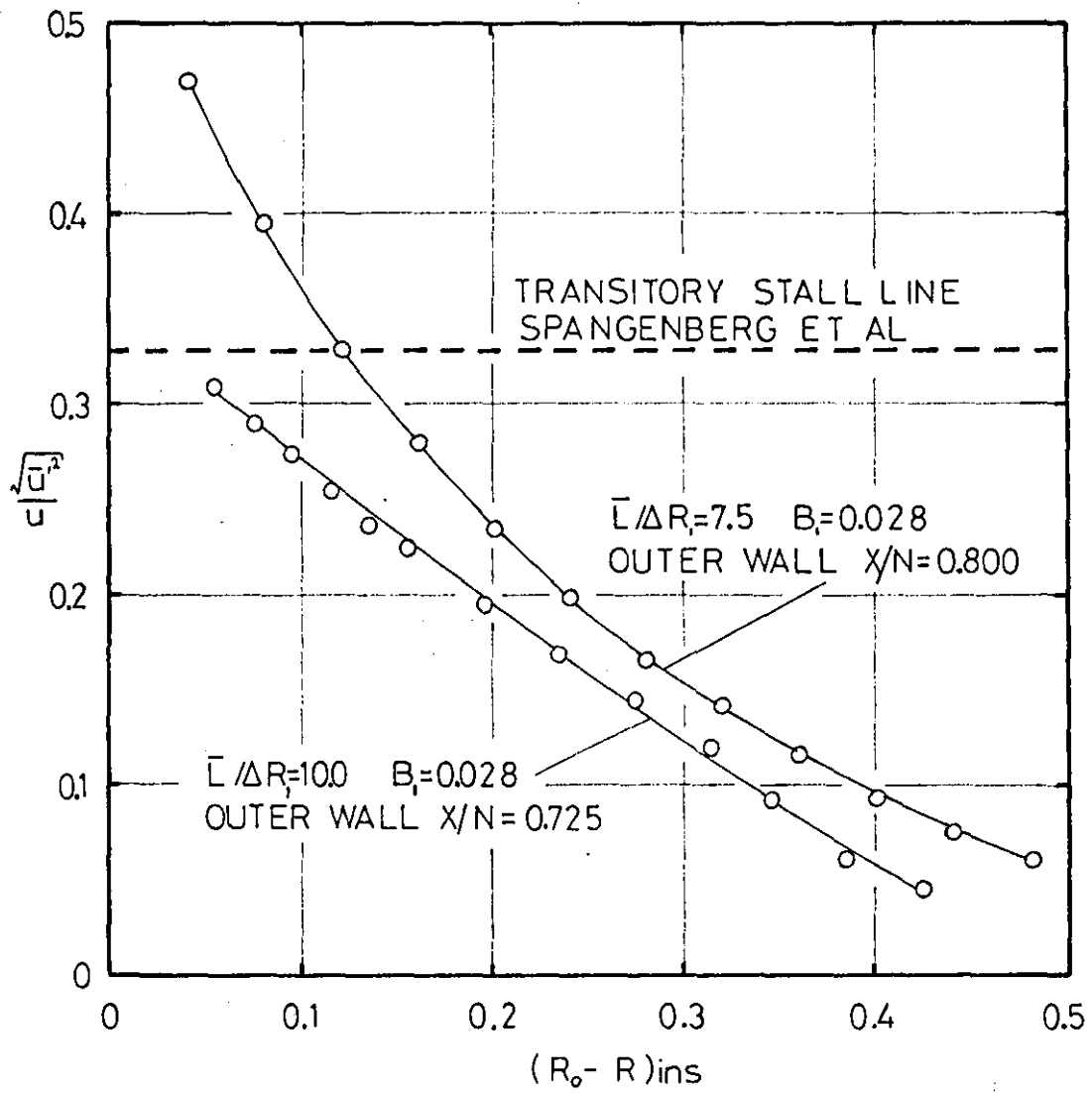


FIGURE 4.36

DETERMINATION OF SKIN FRICTION COEFFICIENT AFTER
CLAUSER(15) $\bar{C}/\Delta R_1 = 7.5$; $L_e/D_{h1} = 2.0$; $B_1 = 0.028$
NATURALLY DEVELOPED INLET CONDITIONS

OUTER WALL

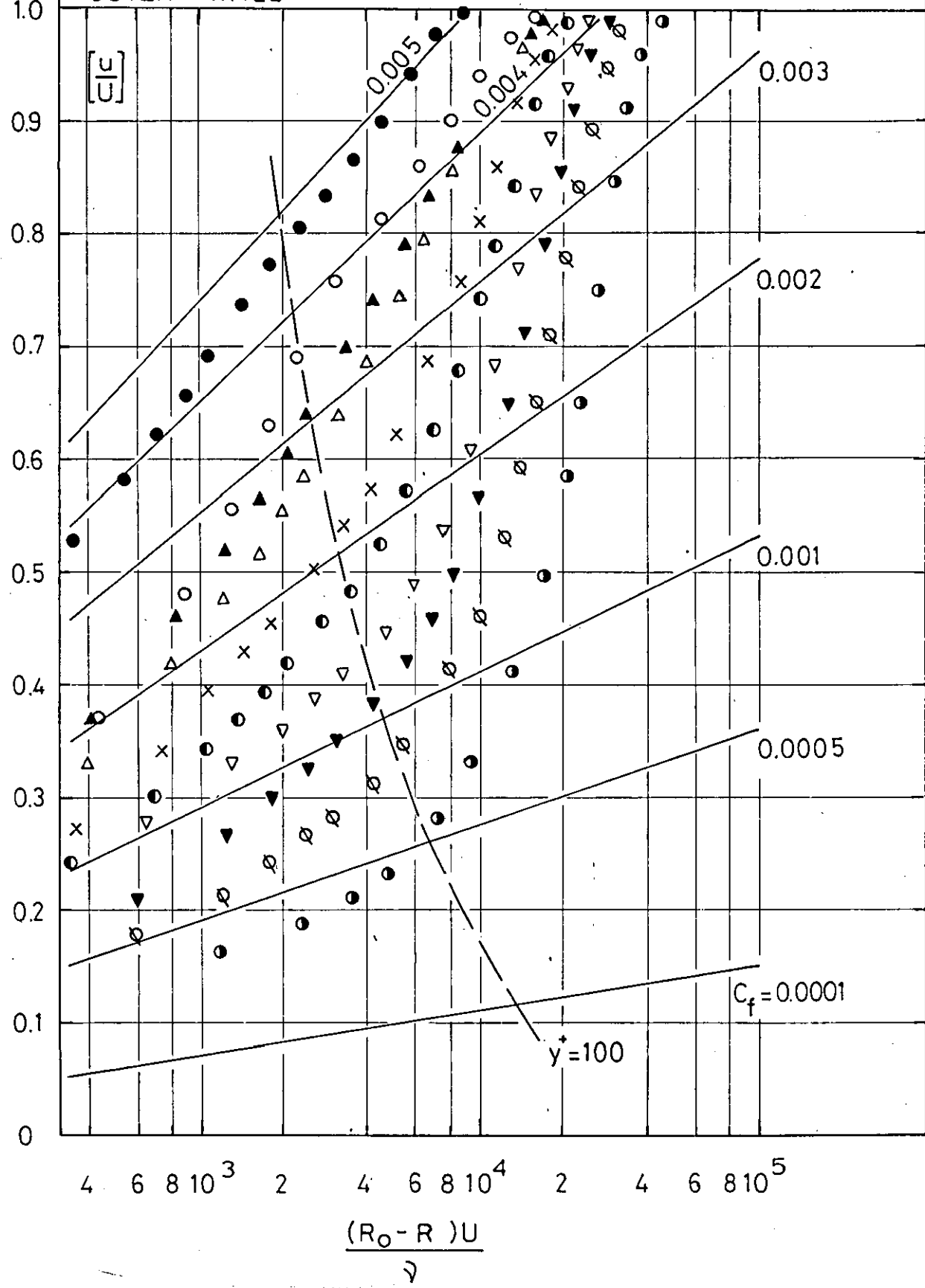
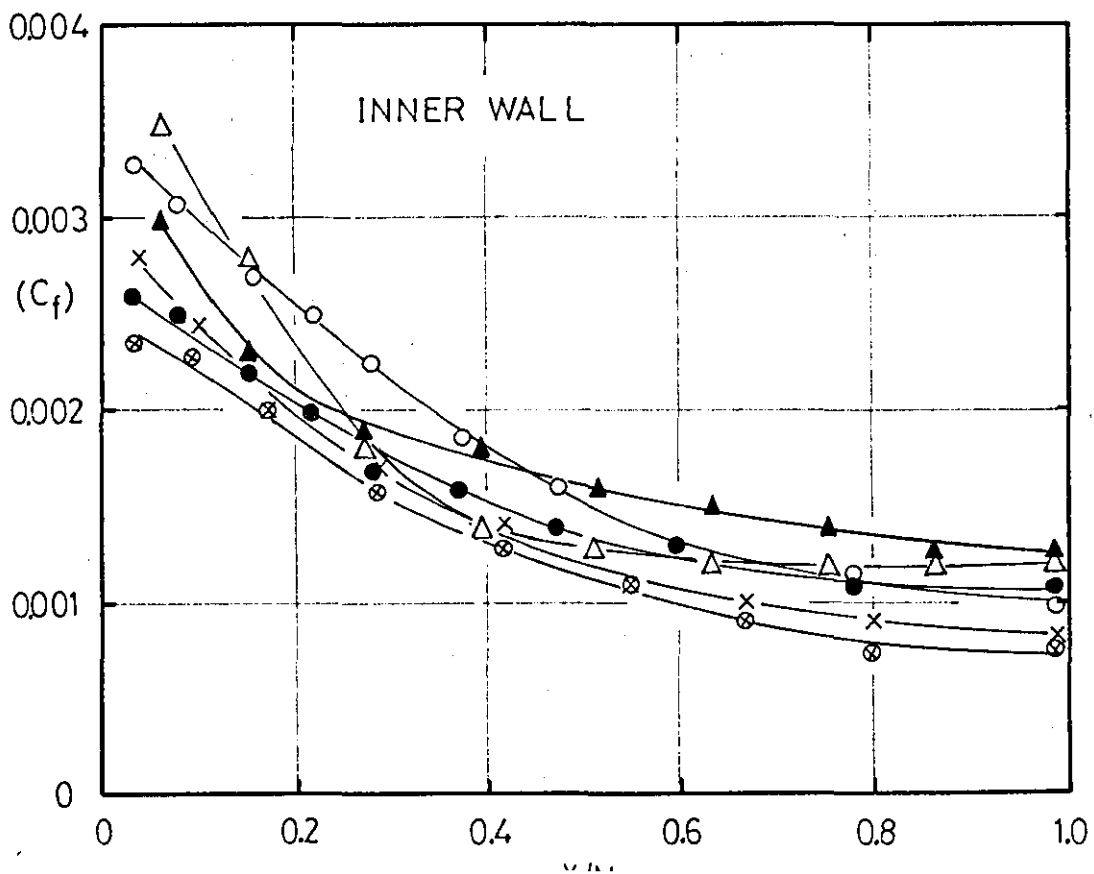
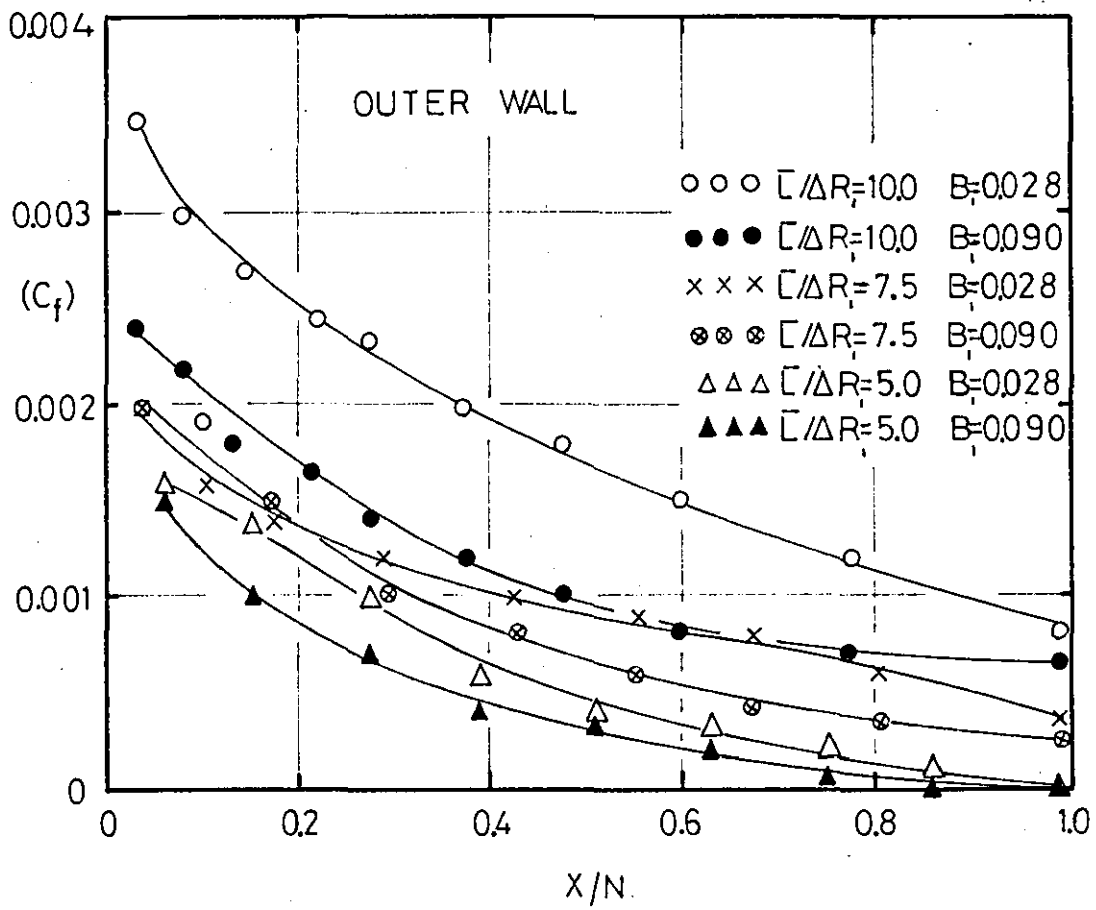
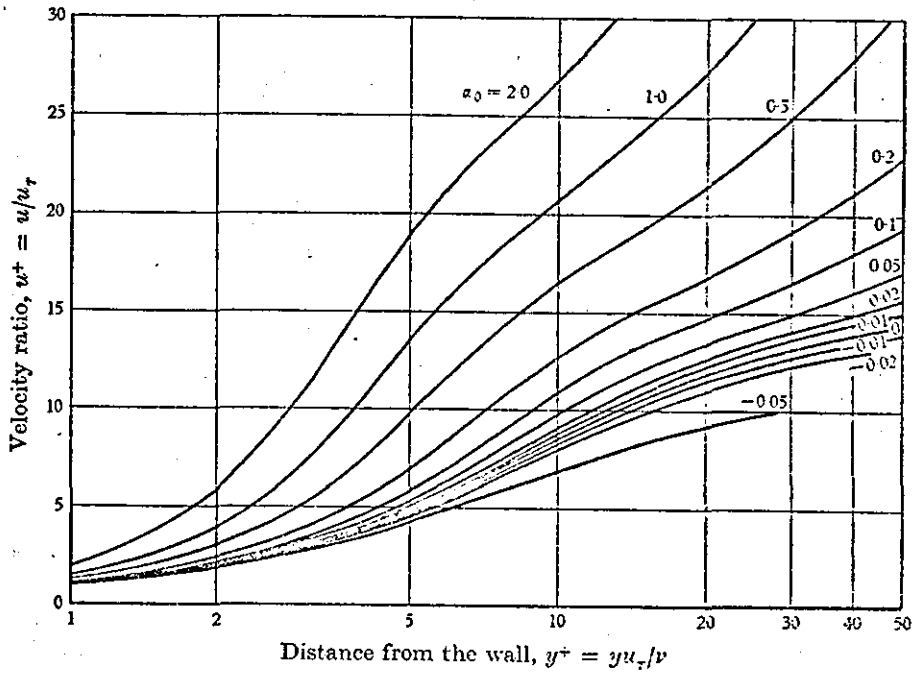


FIGURE 4.37

VARIATION OF SKIN FRICTION COEFFICIENT IN
TEST DIFFUSERS—ESTIMATED FROM CLAUSER PLOTS



EFFECT OF PRESSURE GRADIENT ON THE 'LAW OF THE WALL' AFTER McDONALD(41).



Effect of pressure gradient on the velocity profile near the wall. A semi-logarithmic plot. Stress gradient $\alpha =$ pressure gradient $\alpha_0 = (\nu/\rho u_\tau^2)/(dp/dx)$.

FIGURE 4.39

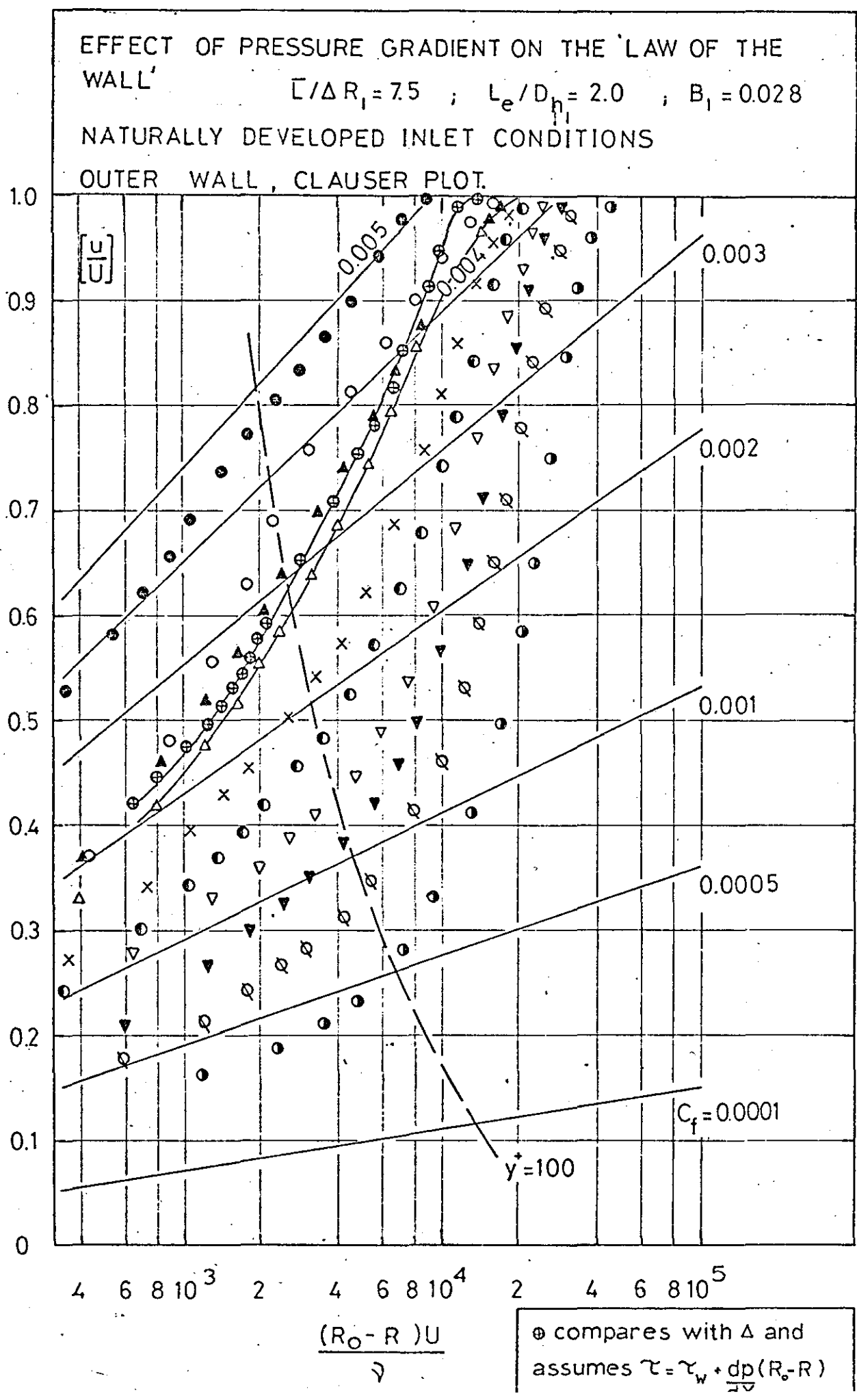


FIGURE 4.40

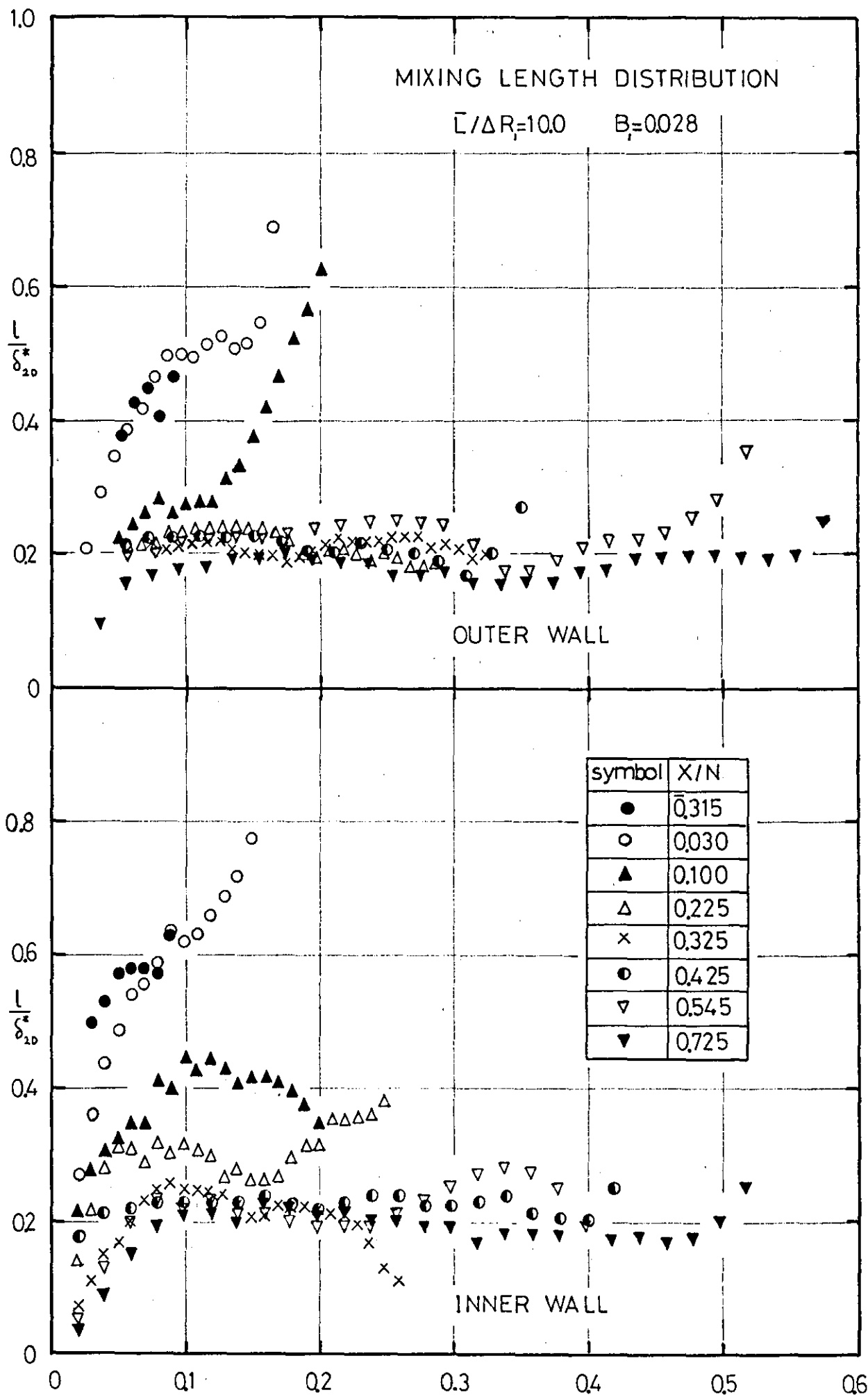
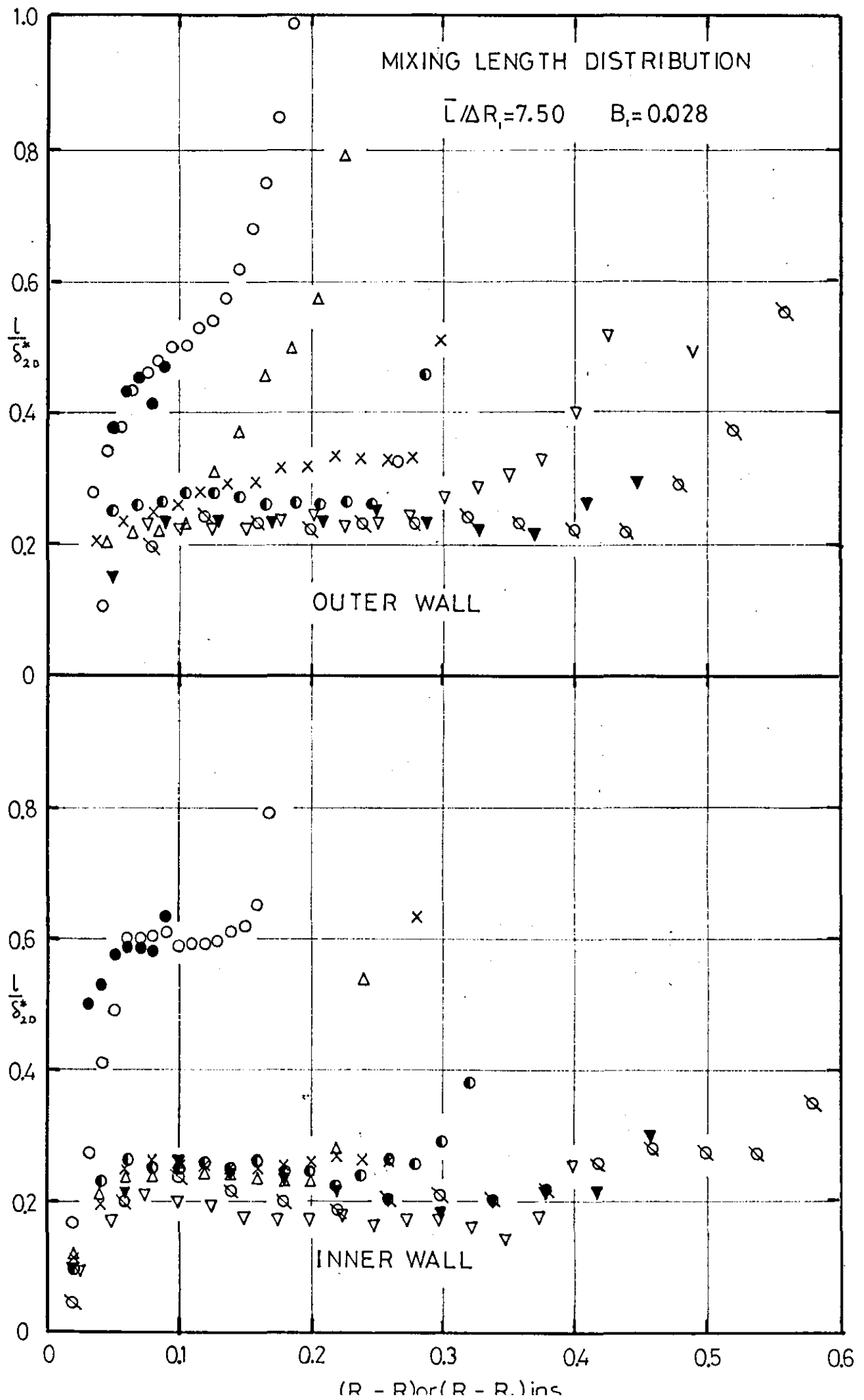
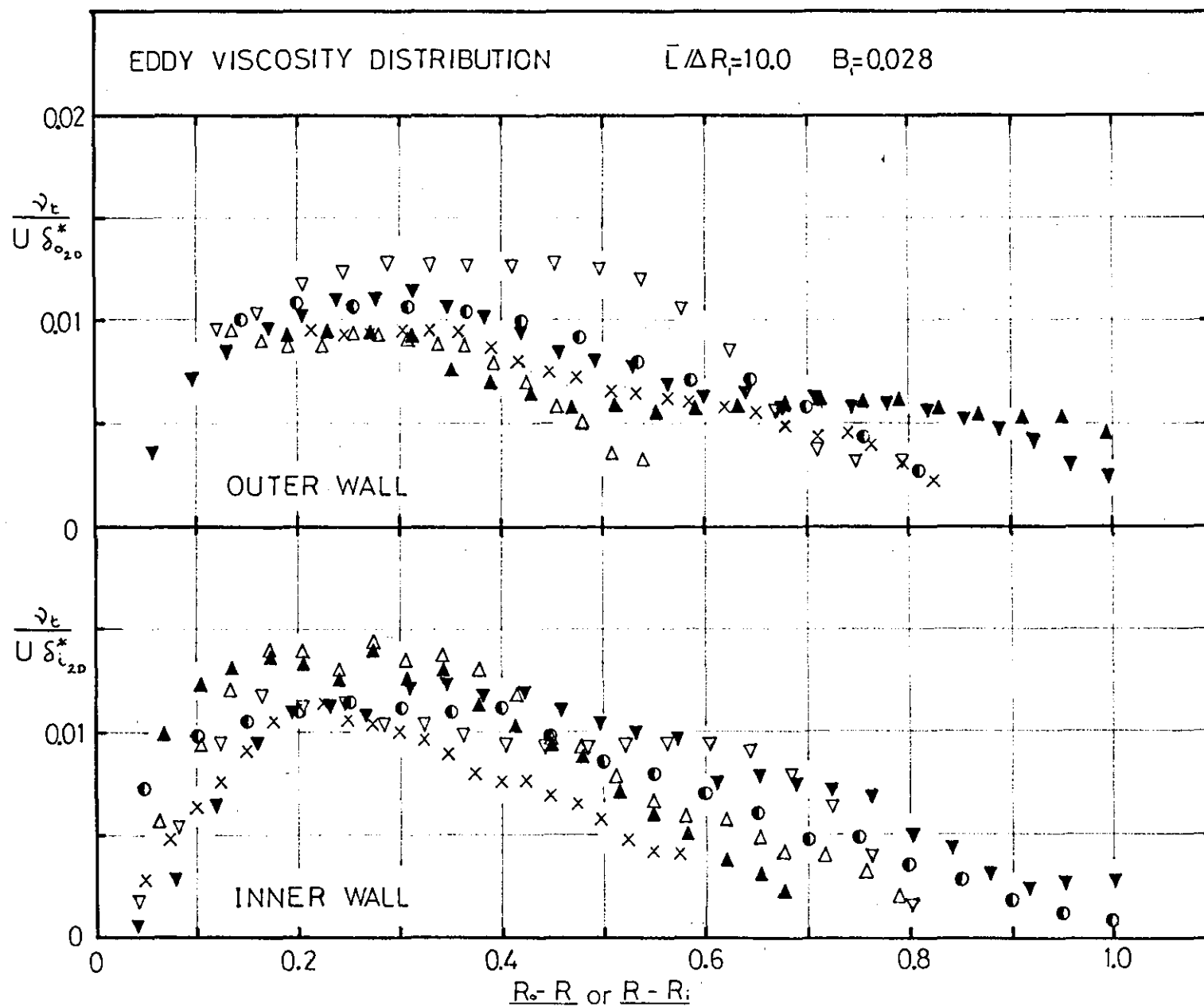


FIGURE 4.41





symbol	X/N
▲	0.100
△	0.225
×	0.325
●	0.425
▽	0.545
▼	0.725

FIGURE 4.42

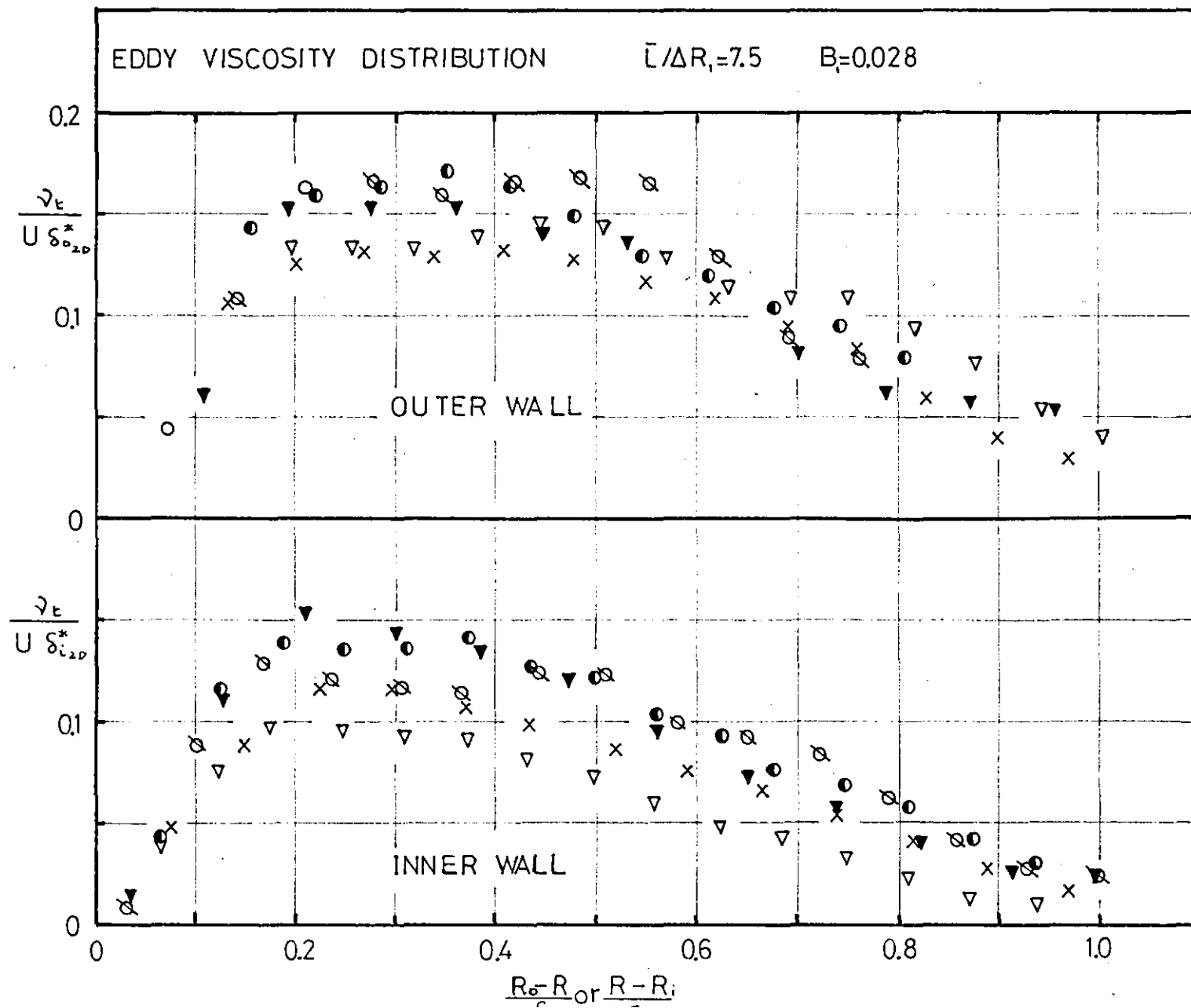
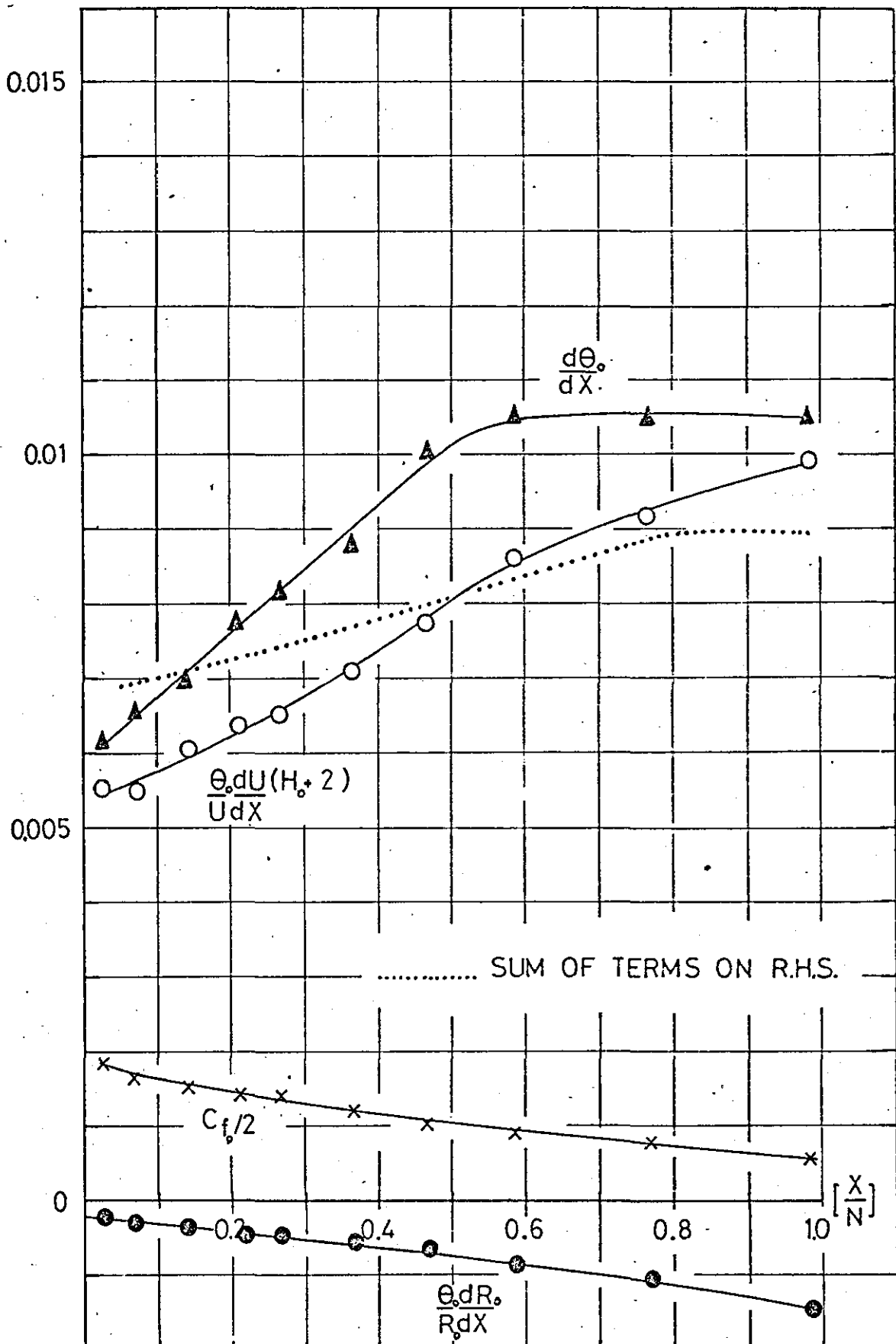


FIGURE 4.43



MOMENTUM INTEGRAL EQUATION BALANCE

$\bar{\Gamma}/\Delta R_1 = 10.0$

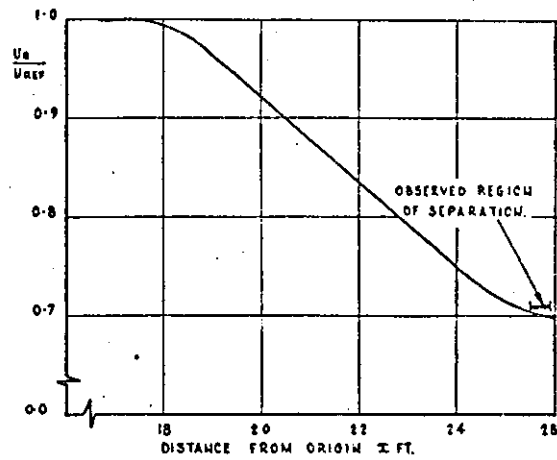
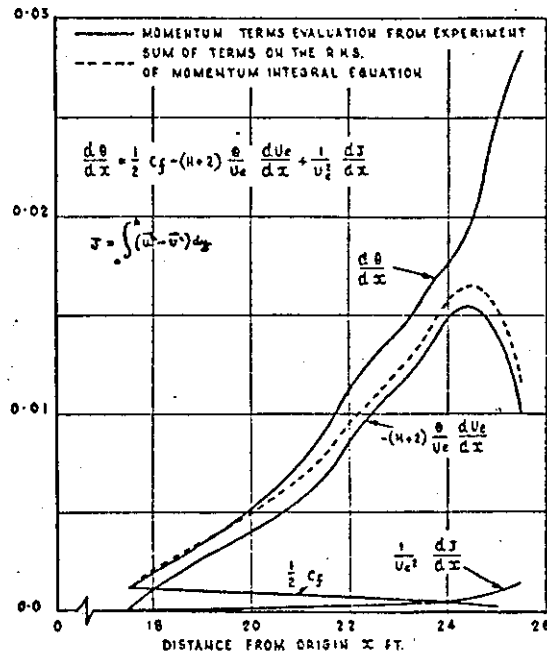
$L_e/D_{h_1} = 2.0$

$B_1 = 0.028$

OUTER WALL

$$\frac{d\theta_0}{dX} = \frac{C_{f_0}}{2} - \frac{\theta_0}{U} \frac{dU}{dX} (H_0 + 2) - \frac{\theta_0}{R_0} \frac{dR_0}{dX}$$

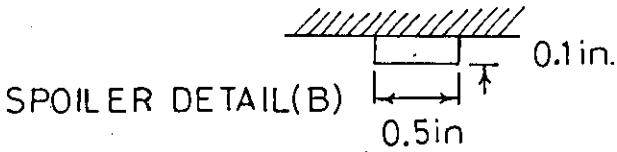
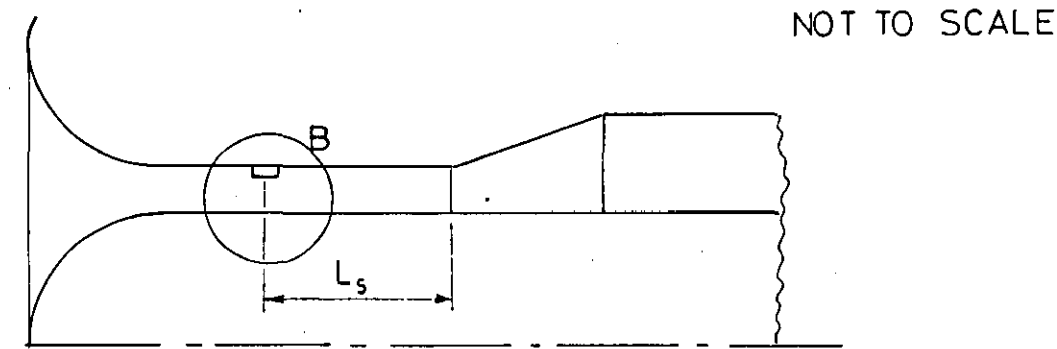
MOMENTUM BALANCE—McDONALD & STODDART(42)



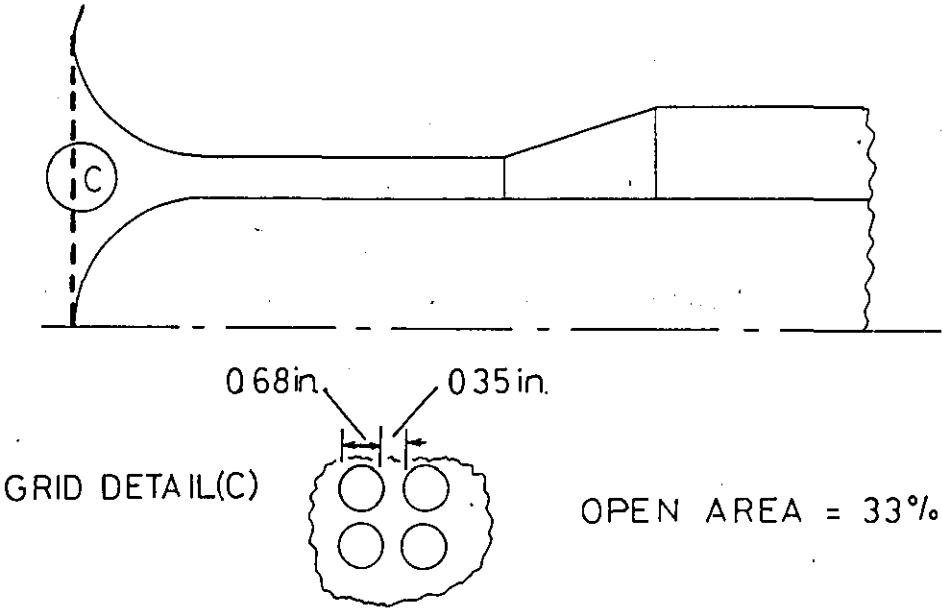
Two-dimensional momentum balance for
the N.B.S. boundary layer.

Schubauer and Klebanoff²⁸.

METHODS EMPLOYED FOR THE GENERATION OF HIGHLY
TURBULENT INLET PROFILES



4.46(a) FLOW SPOILER



4.46(b) COARSE GRID.

FIGURE 4.47

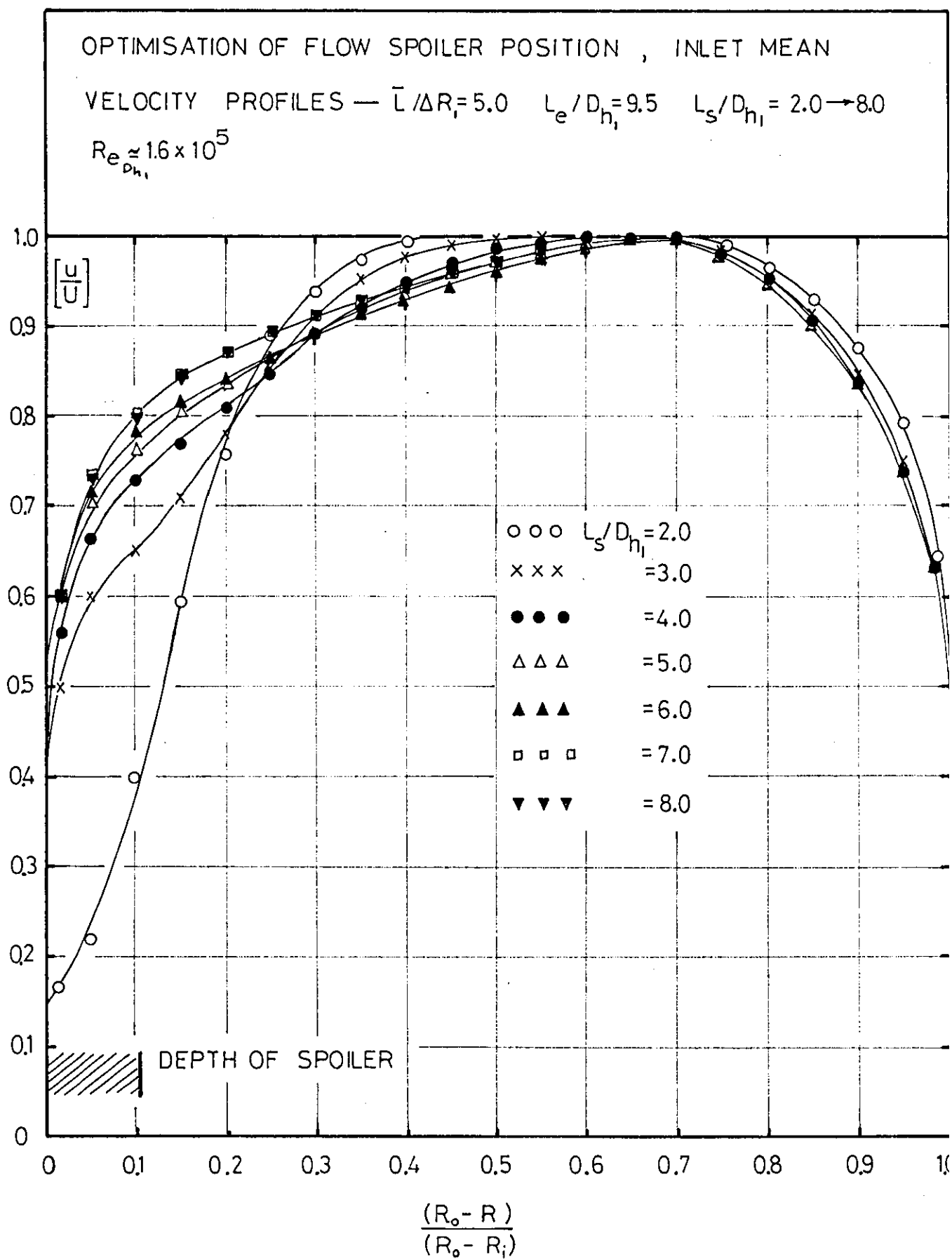


FIGURE 4.48

TYPICAL INLET VELOCITY PROFILES WOLF & JOHNSTON(83)

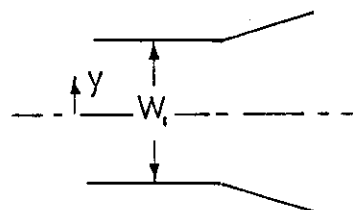
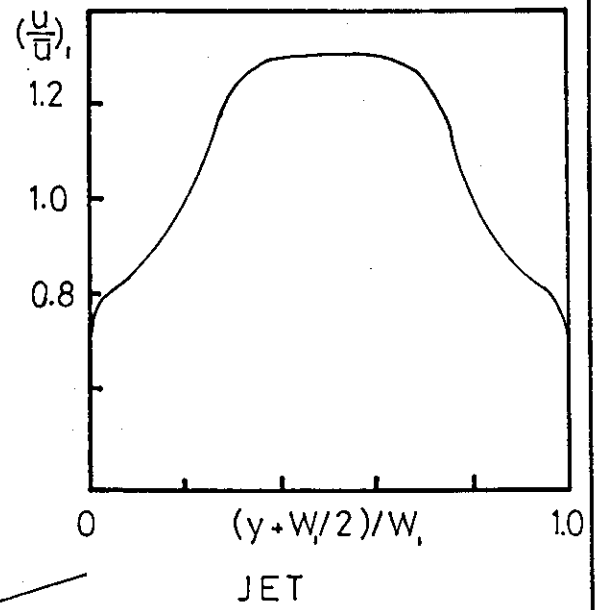
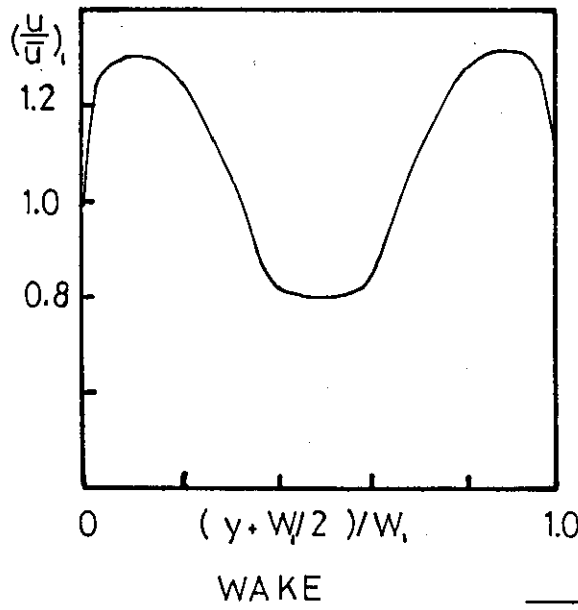
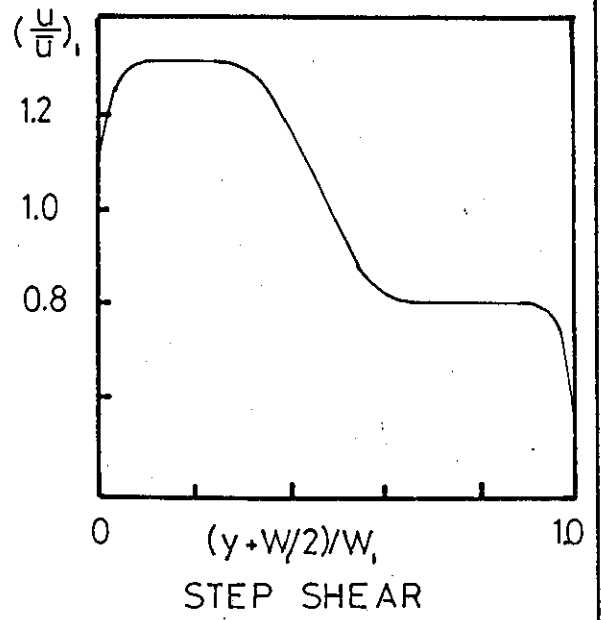
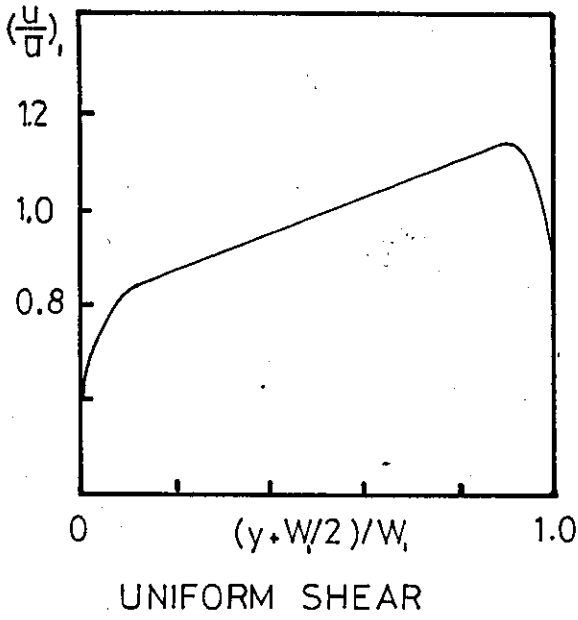


FIGURE 4.49

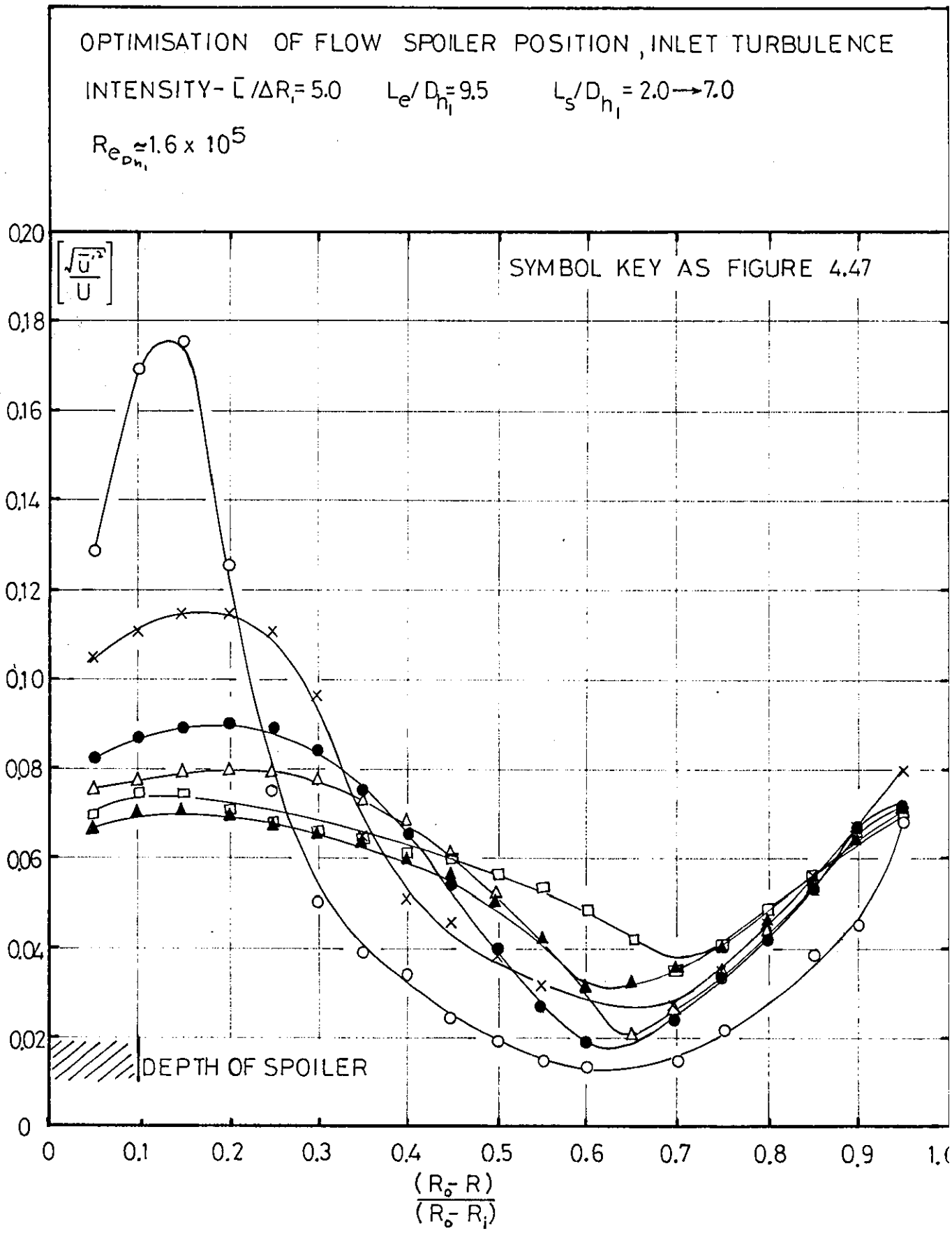


FIGURE 4.50

OPTIMISATION OF FLOW SPOILER POSITION , INLET TURBULENT

SHEAR STRESS— $\bar{\tau}$ $\Delta R_i = 5.0$

$L_e/D_{h_i} = 9.5$

$L_s/D_{h_i} = 4.0 \rightarrow 7.0$

$Re_{D_{h_i}} \approx 1.6 \times 10^5$

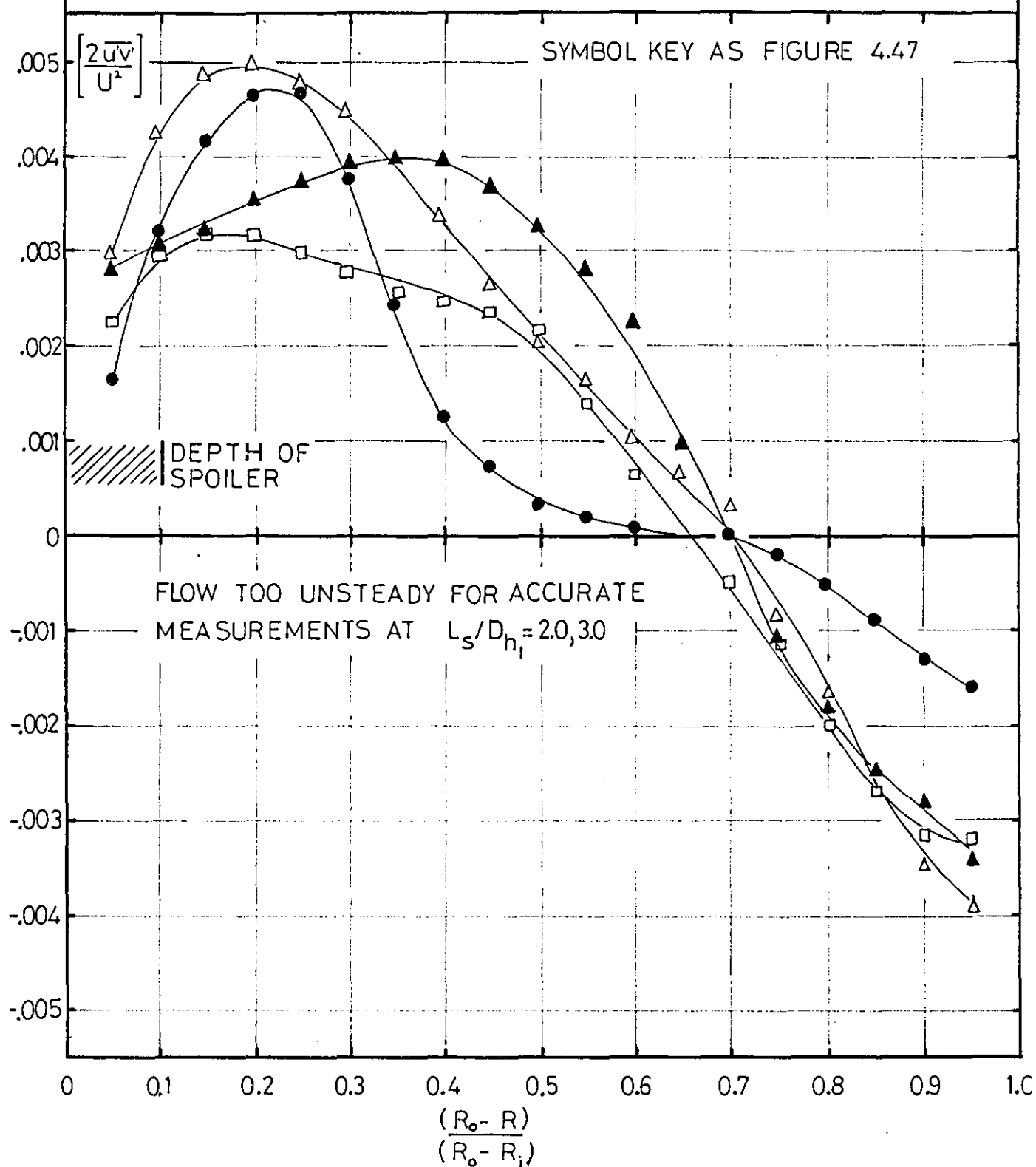


FIGURE 4.51

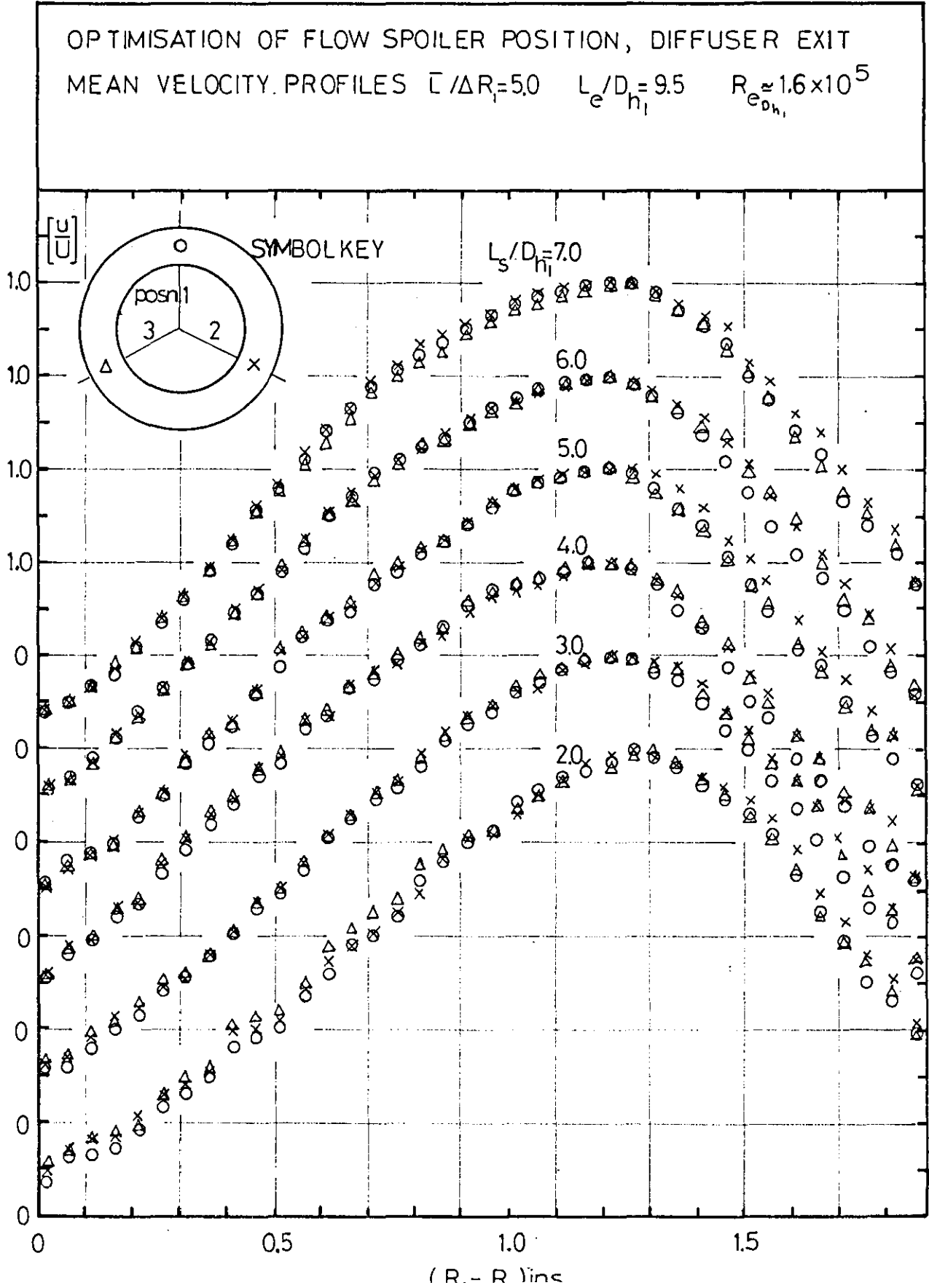


FIGURE 4.52

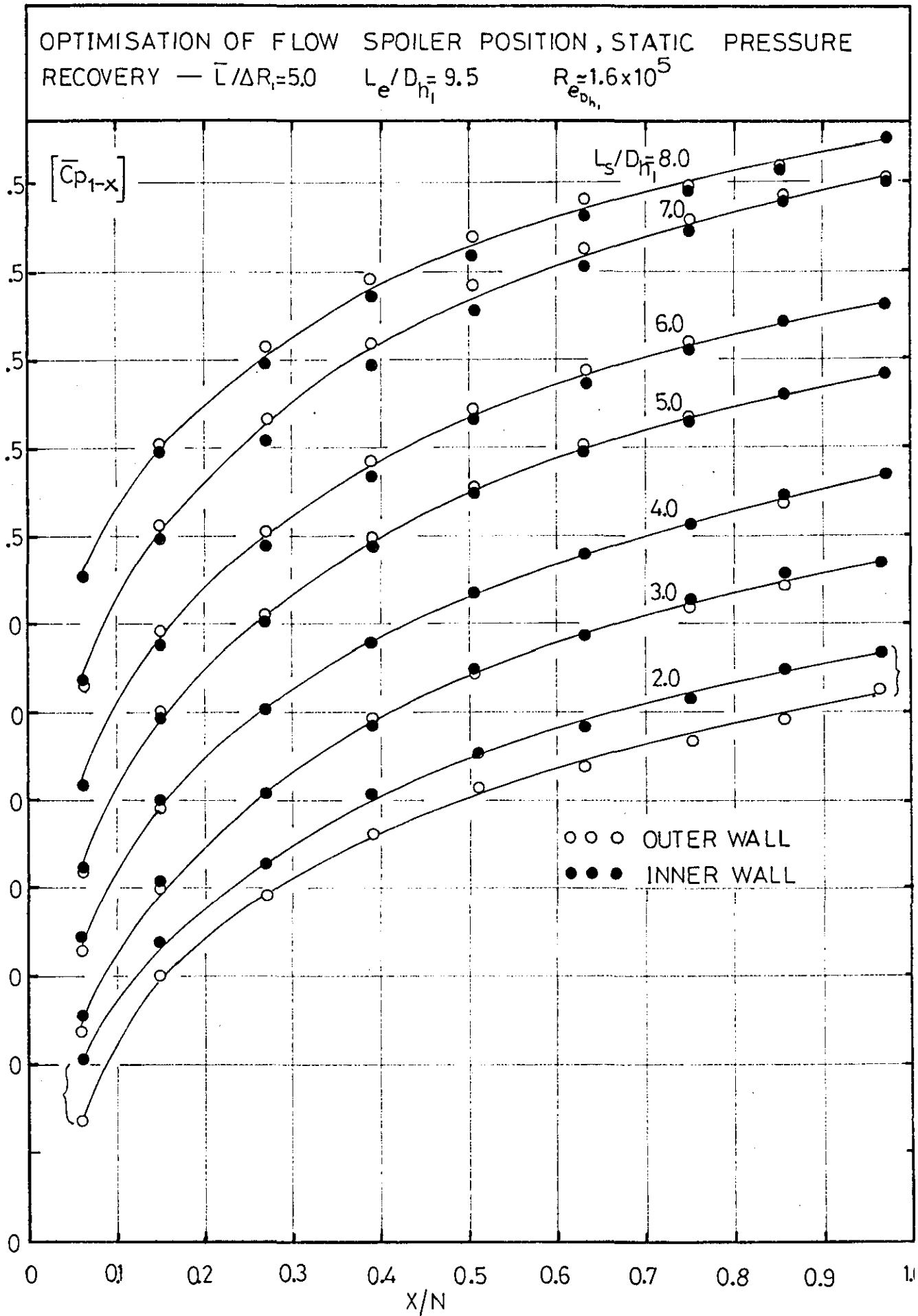


FIGURE 4.53

OPTIMISATION OF FLOW SPOILER POSITION, VARIATION OF
STATIC PRESSURE IN DIFFUSER INLET REGION.

$$\bar{L}/\Delta R_1 = 5.0$$

$$L_e/D_{h1} = 9.5$$

$$Re_{D_{h1}} \approx 1.6 \times 10^5$$

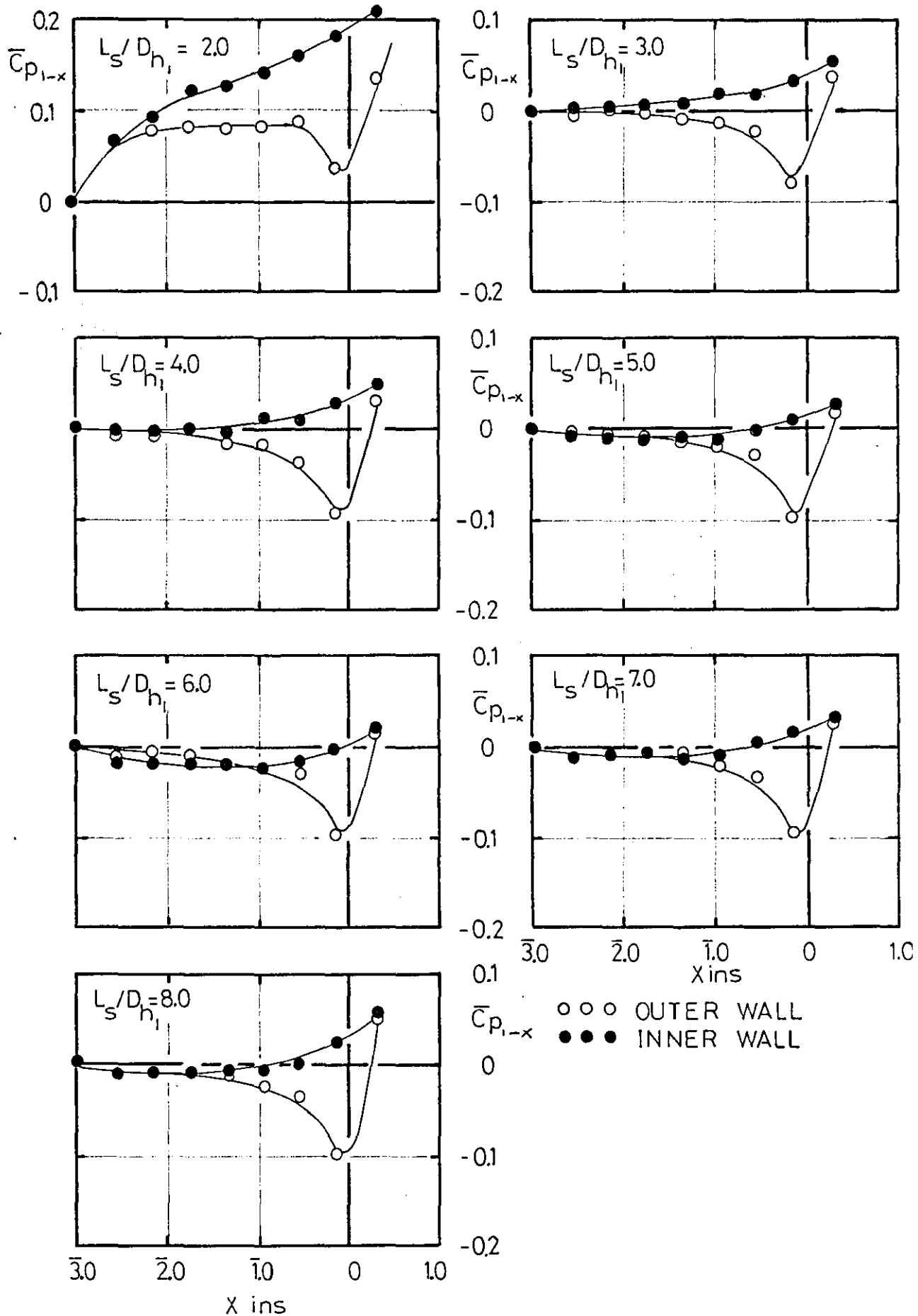
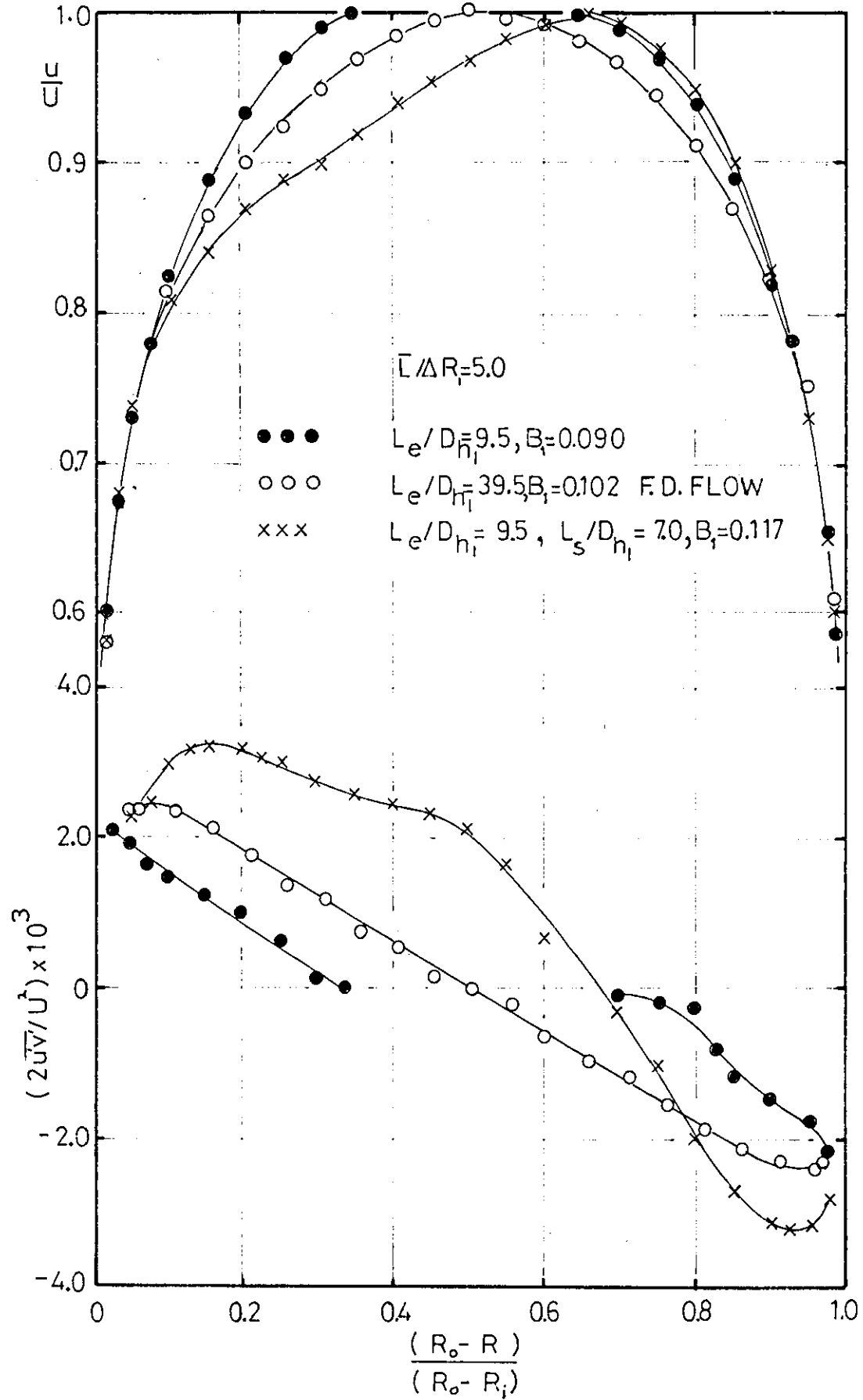


FIGURE 4.54

COMPARISON WITH INLET CONDITIONS GENERATED BY A FLOW SPOILER ON OUTER WALL.



COMPARISON WITH COMPRESSOR EXIT TURBULENCE
INTENSITY – WILLIAMS & TERRELL (81) – AT DIFFUSER
INLET STATION.

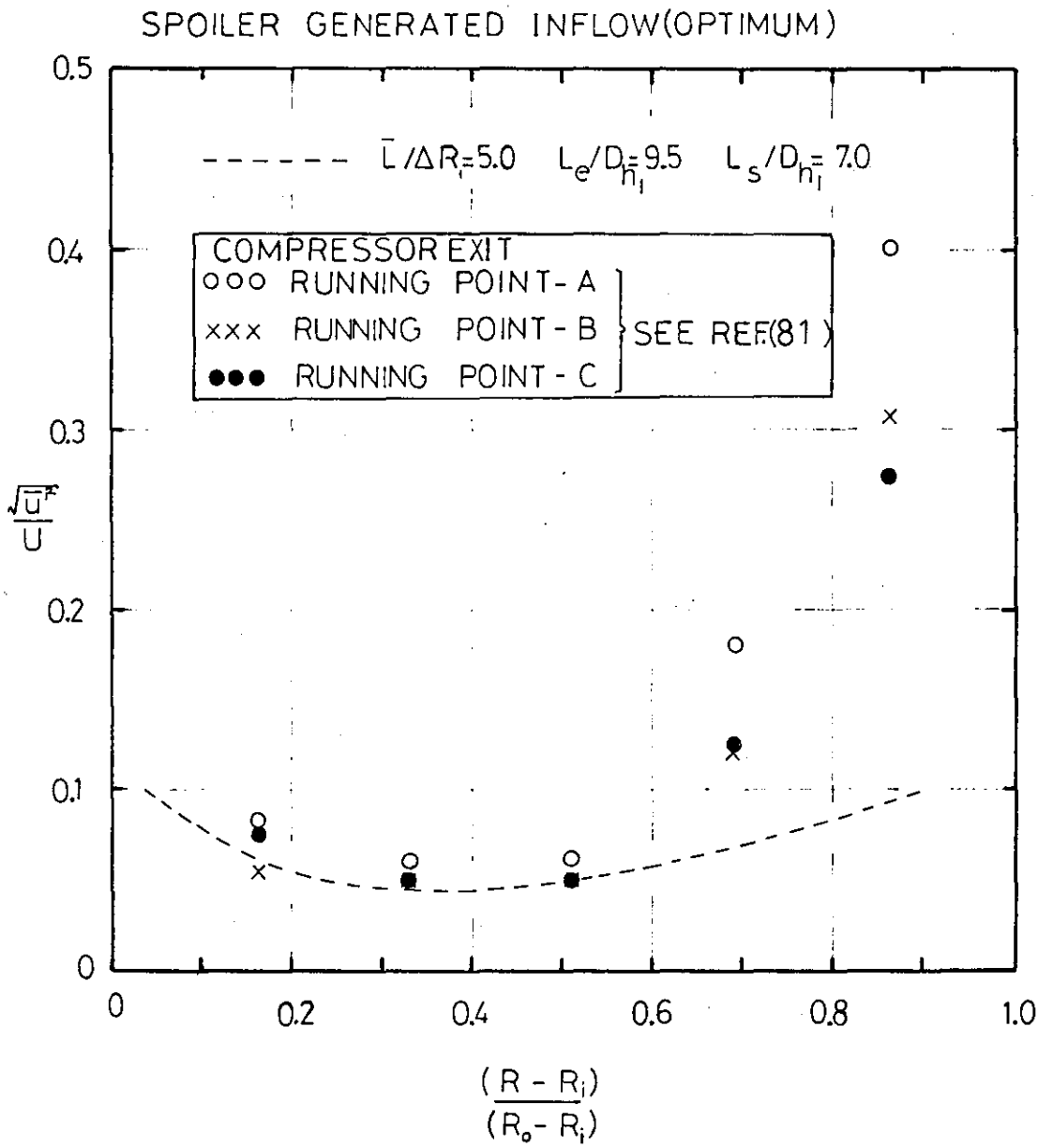


FIGURE 4.56

FLOW SPOILER AT INLET — PRESSURE RECOVERY IN
SETTLING LENGTH, $\bar{L}/\Delta R_i = 5.0$ $L_e/D_{h1} = 9.5$

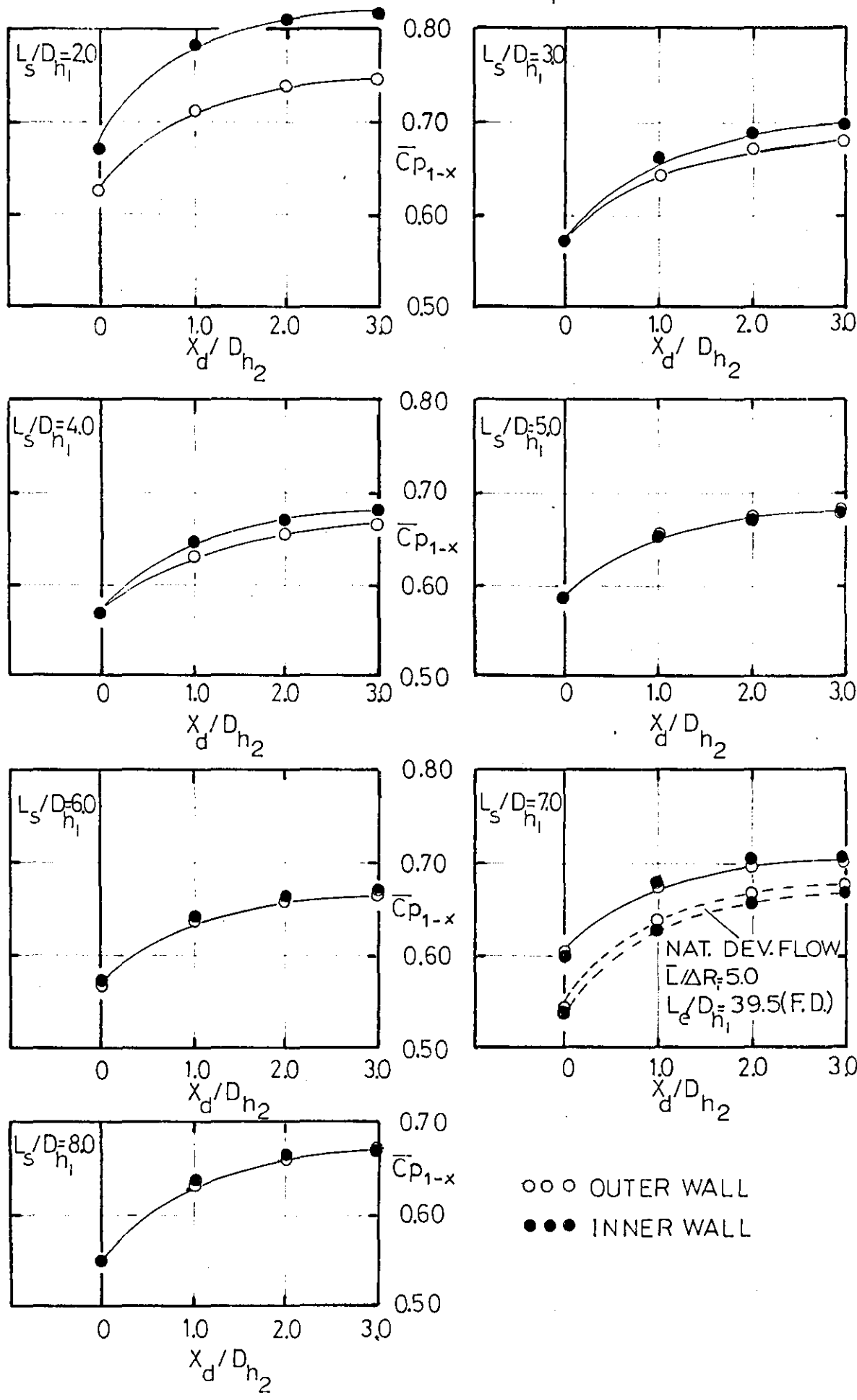
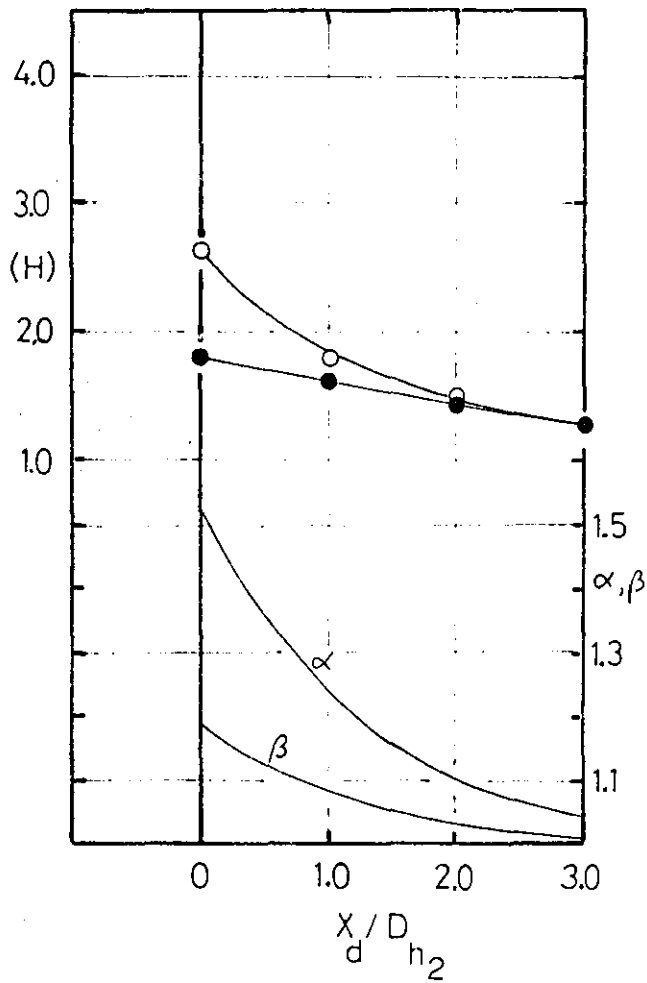


FIGURE 4.57

OPTIMUM FLOW SPOILER POSITION — BEHAVIOUR OF
VELOCITY PROFILE INTEGRAL PARAMETERS IN
SETTLING LENGTH. $\bar{L}/\Delta R_i = 5.0$ $L_e/D_{h_1} = 9.5$ $L_s/D_{h_1} = 7.0$



○ ○ ○ OUTER WALL
● ● ● INNER WALL

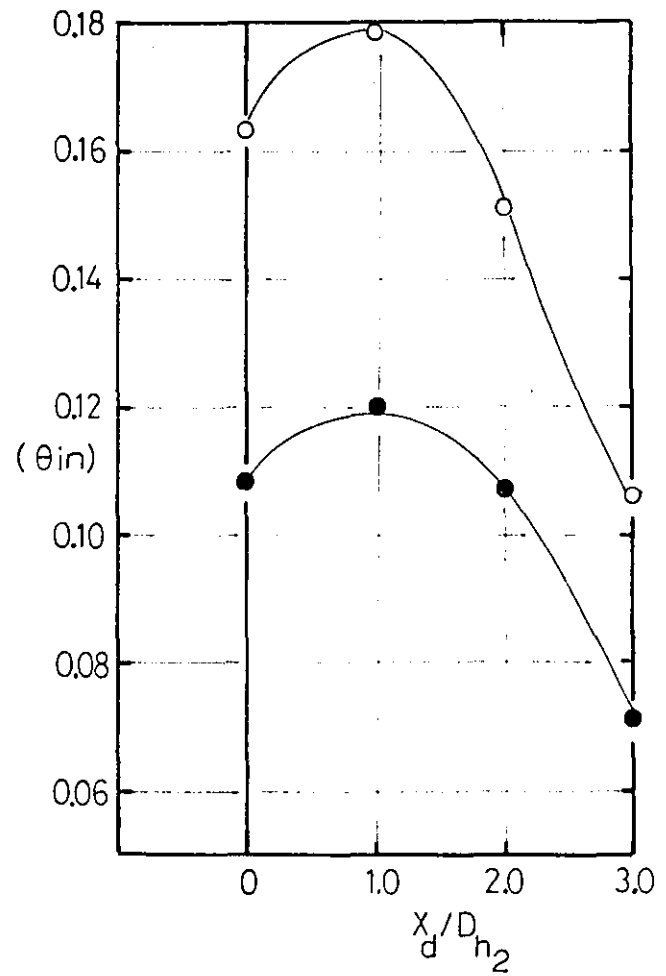


FIGURE 4.58

MEAN VELOCITY PROFILE DEVELOPMENT — OPTIMUM FLOW
SPOILER POSITION

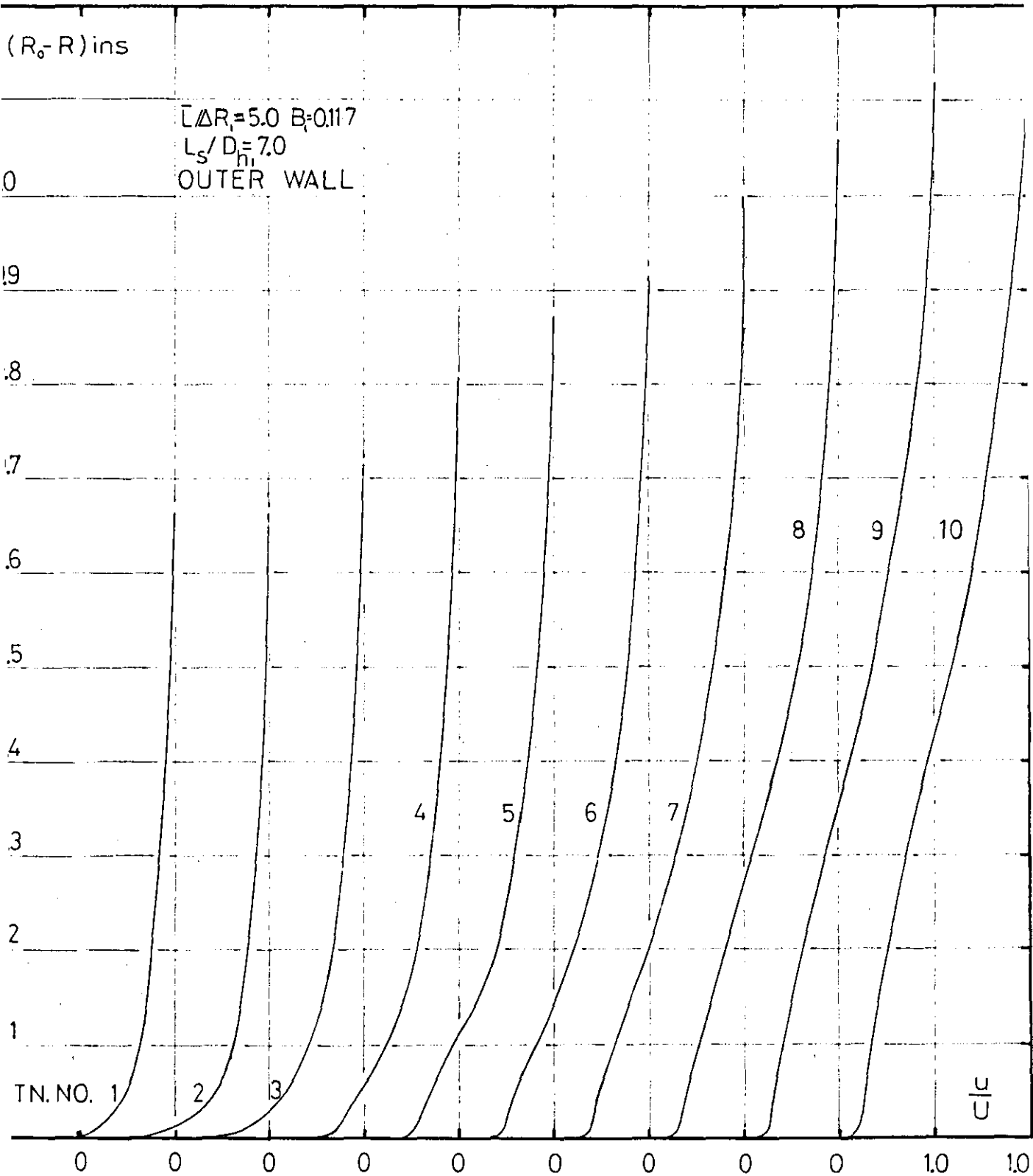


FIGURE 4.59

MEAN VELOCITY PROFILE DEVELOPMENT — OPTIMUM FLOW
SPOILER POSITION

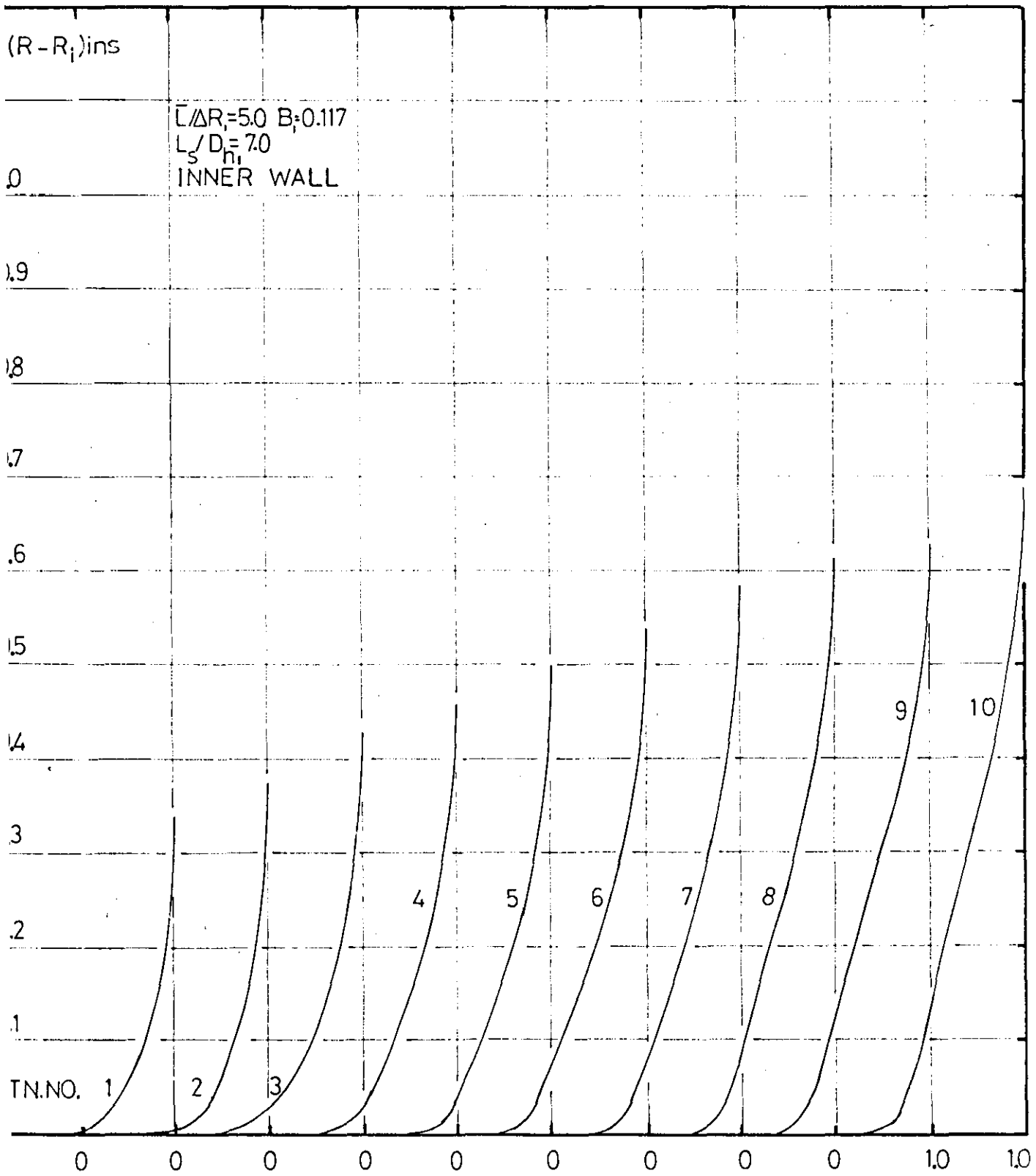


FIGURE 4.60

OPTIMUM FLOW SPOILER POSITION — BOUNDARY LAYER
DEVELOPMENT $\bar{L}/\Delta R_i = 5.0$ $Re_{\phi h_i} \approx 1.6 \times 10^5$

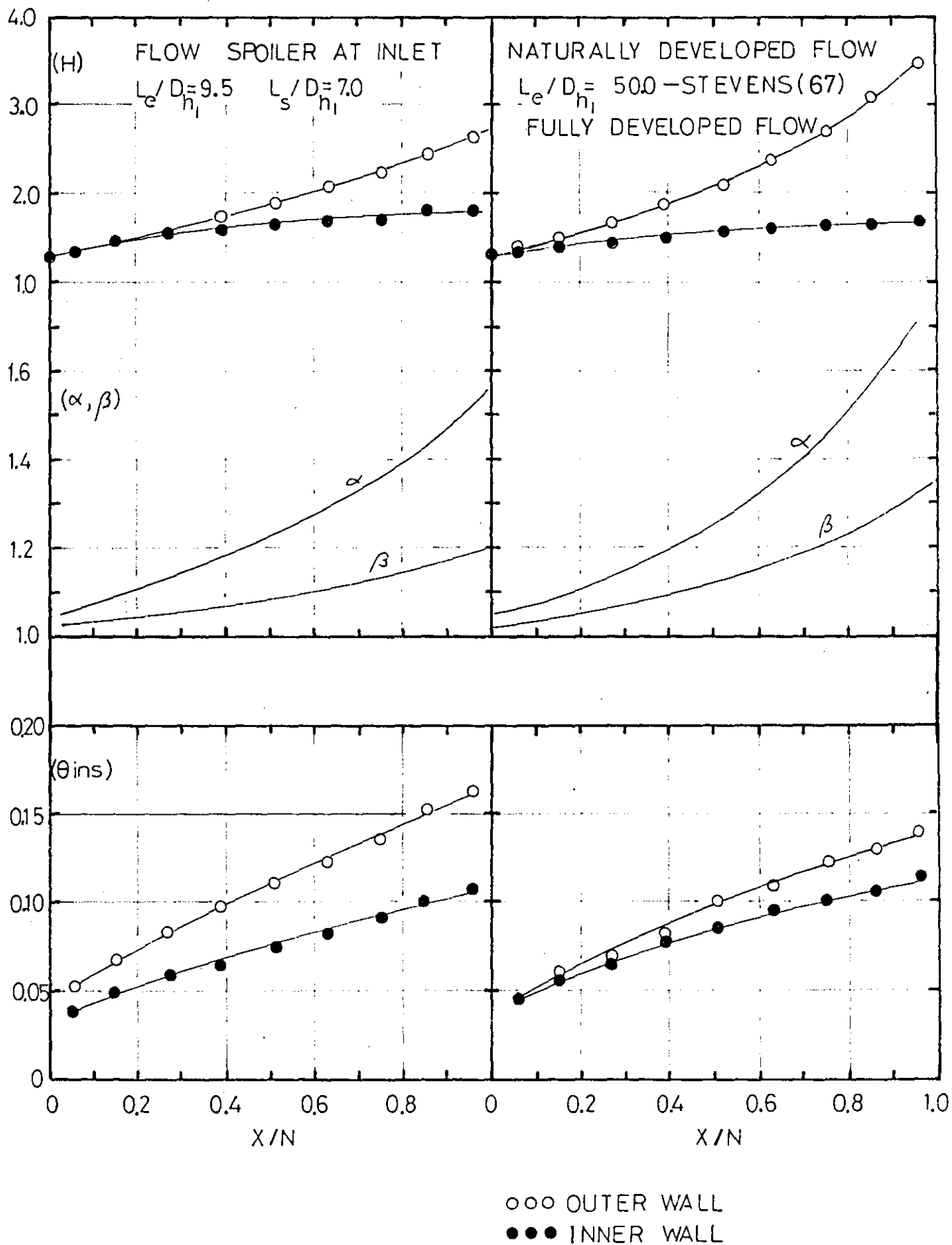
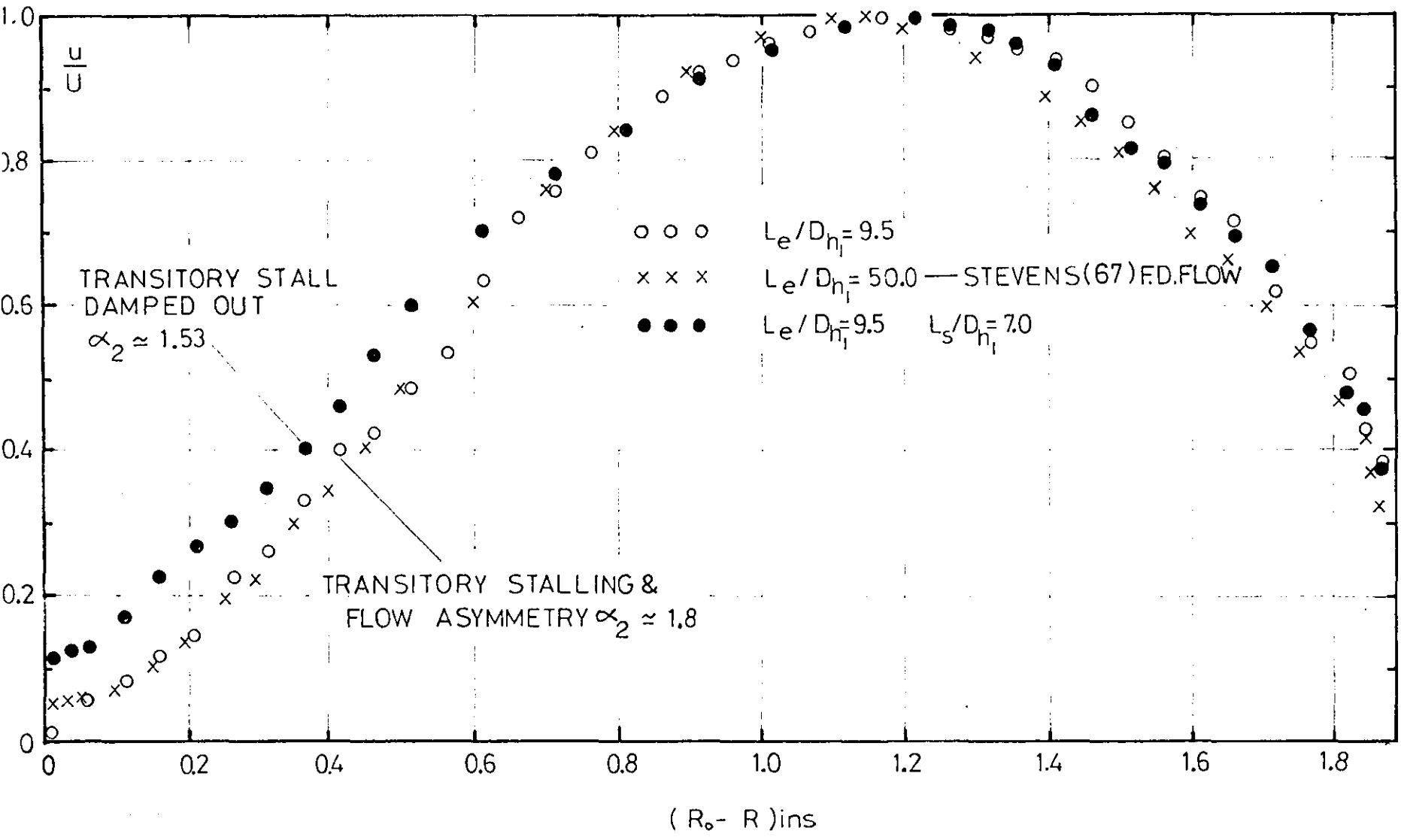


FIGURE 4.61

DIFFUSER EXIT VELOCITY PROFILE COMPARISON
 $L/\Delta R_1=5.0$ DIFFUSER



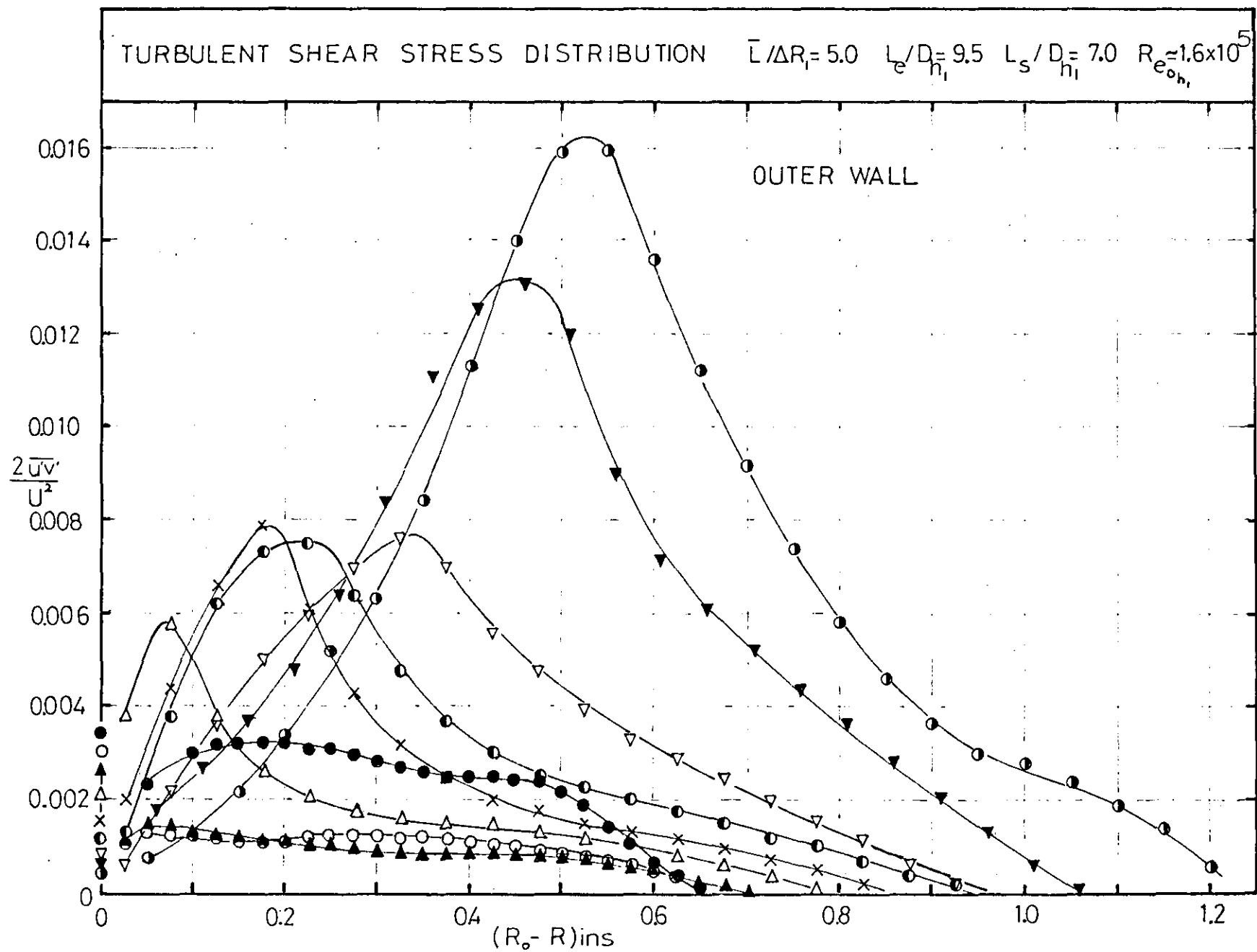


FIGURE 4.62

DIFFUSER EXIT SHEAR STRESS COMPARISON
 $L/R_0=50$ DIFFUSER

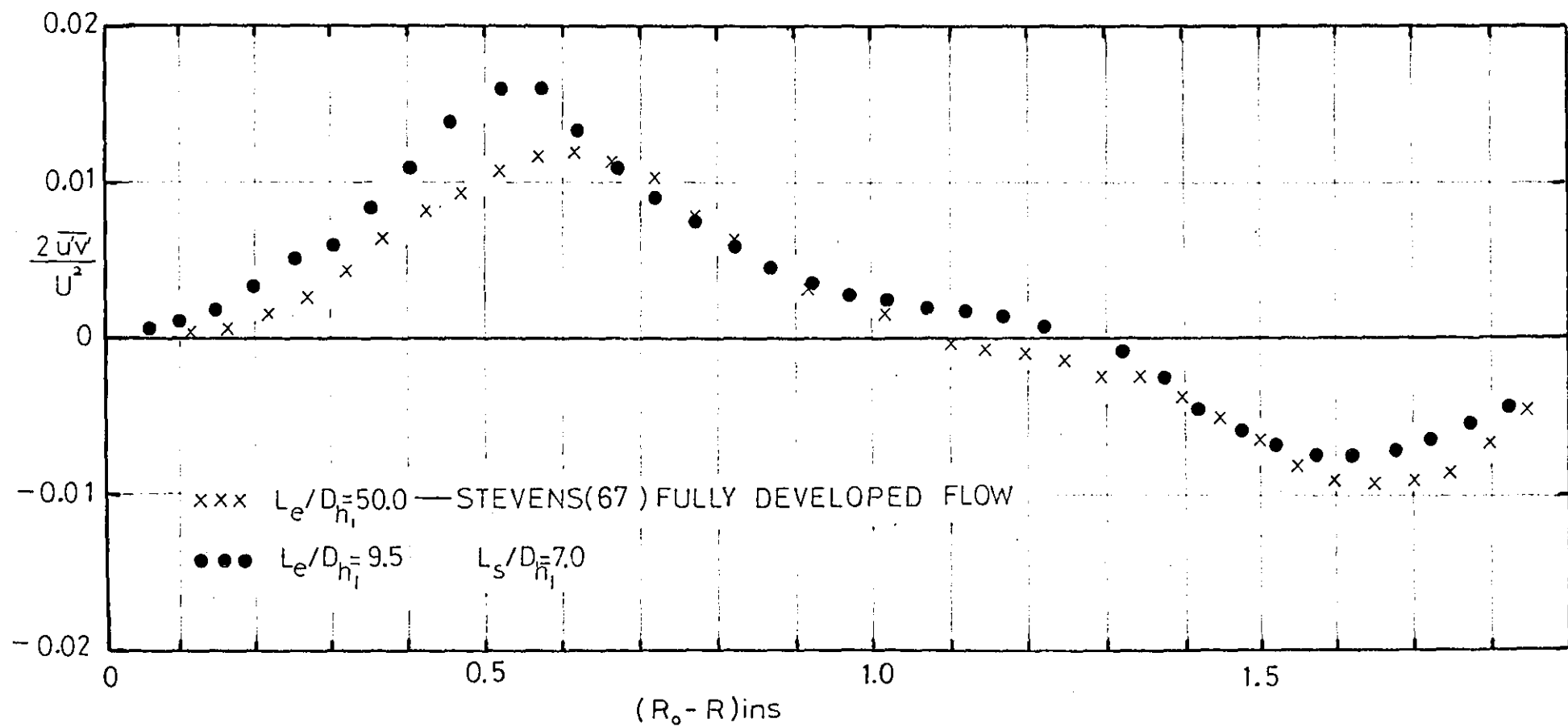
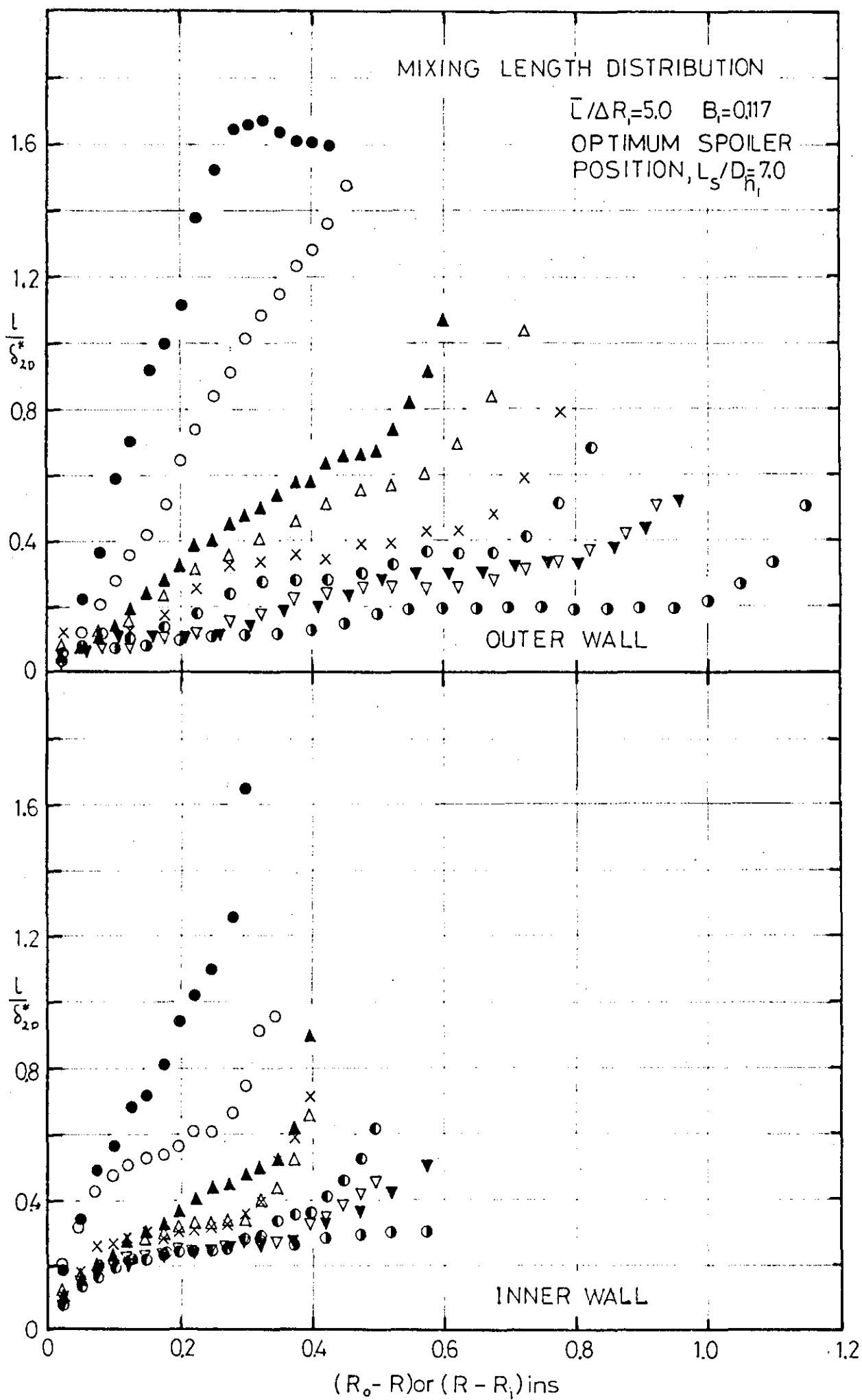


FIGURE 4.63

FIGURE 4.64



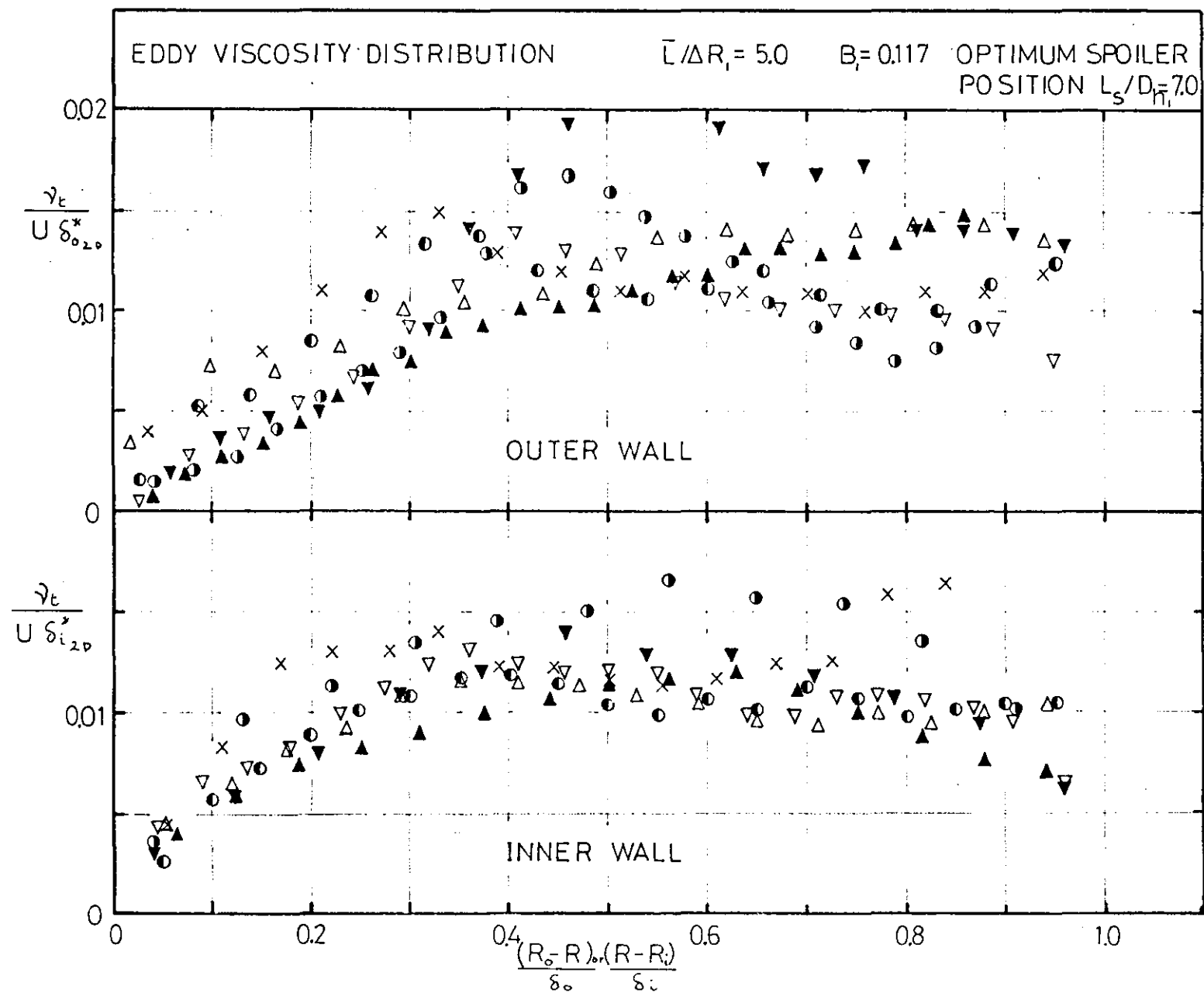


FIGURE 4.65

FIGURE 4.66

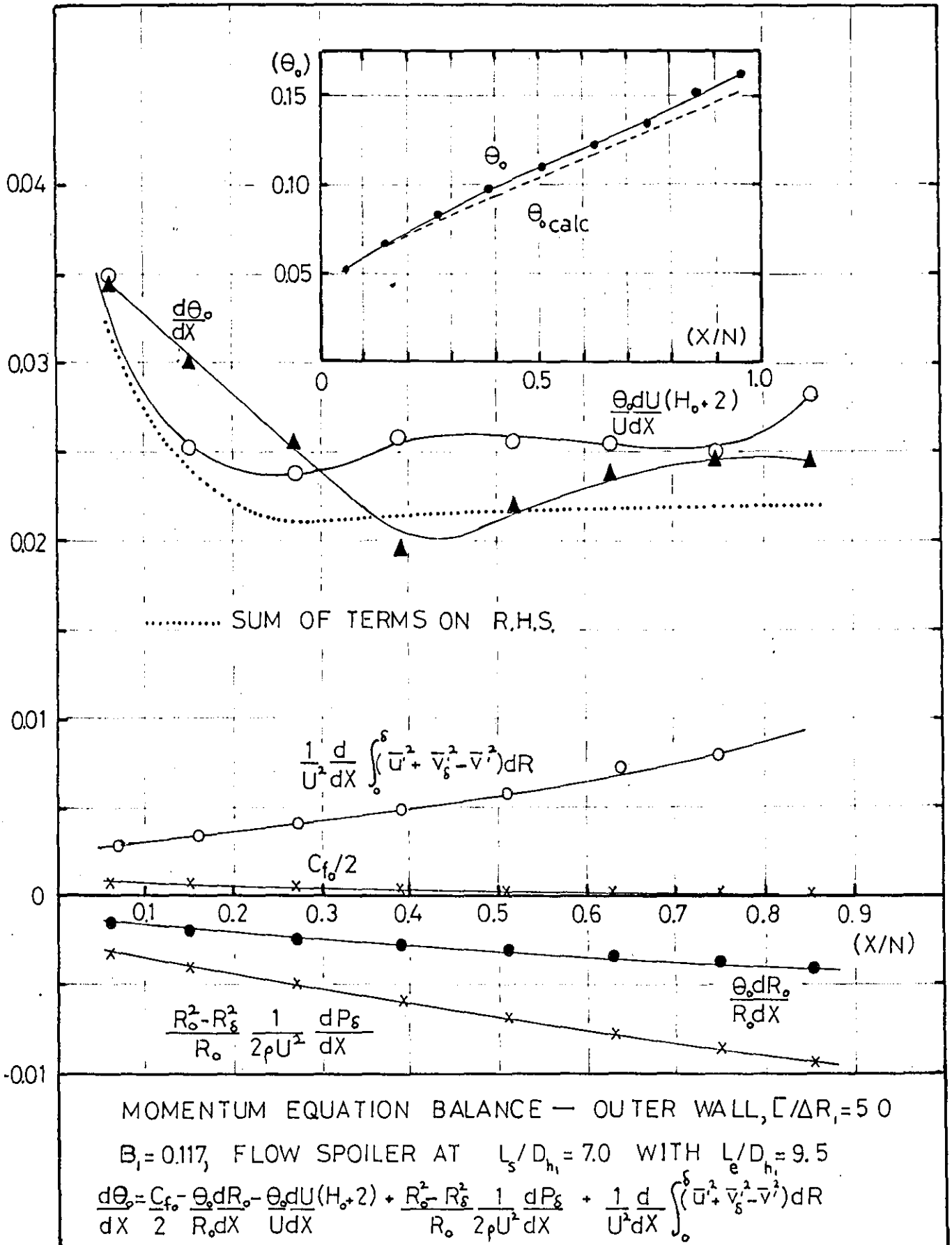


FIGURE 4.67

COMPARISON OF INFLOW CONDITIONS GENERATED
WITH A COARSE GRID

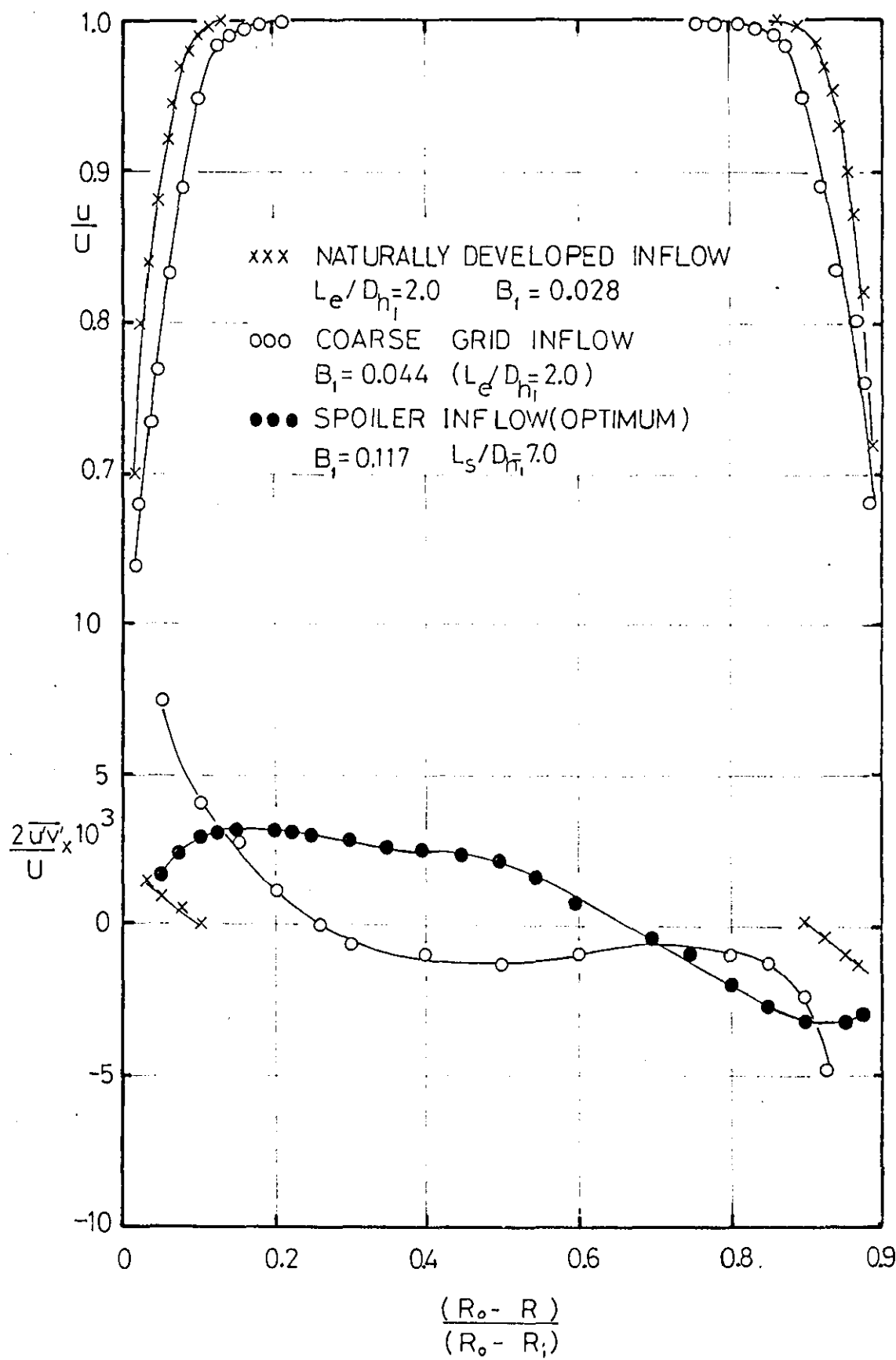


FIGURE 4.68

DIFFUSER EXIT VELOCITY PROFILE COMPARISON

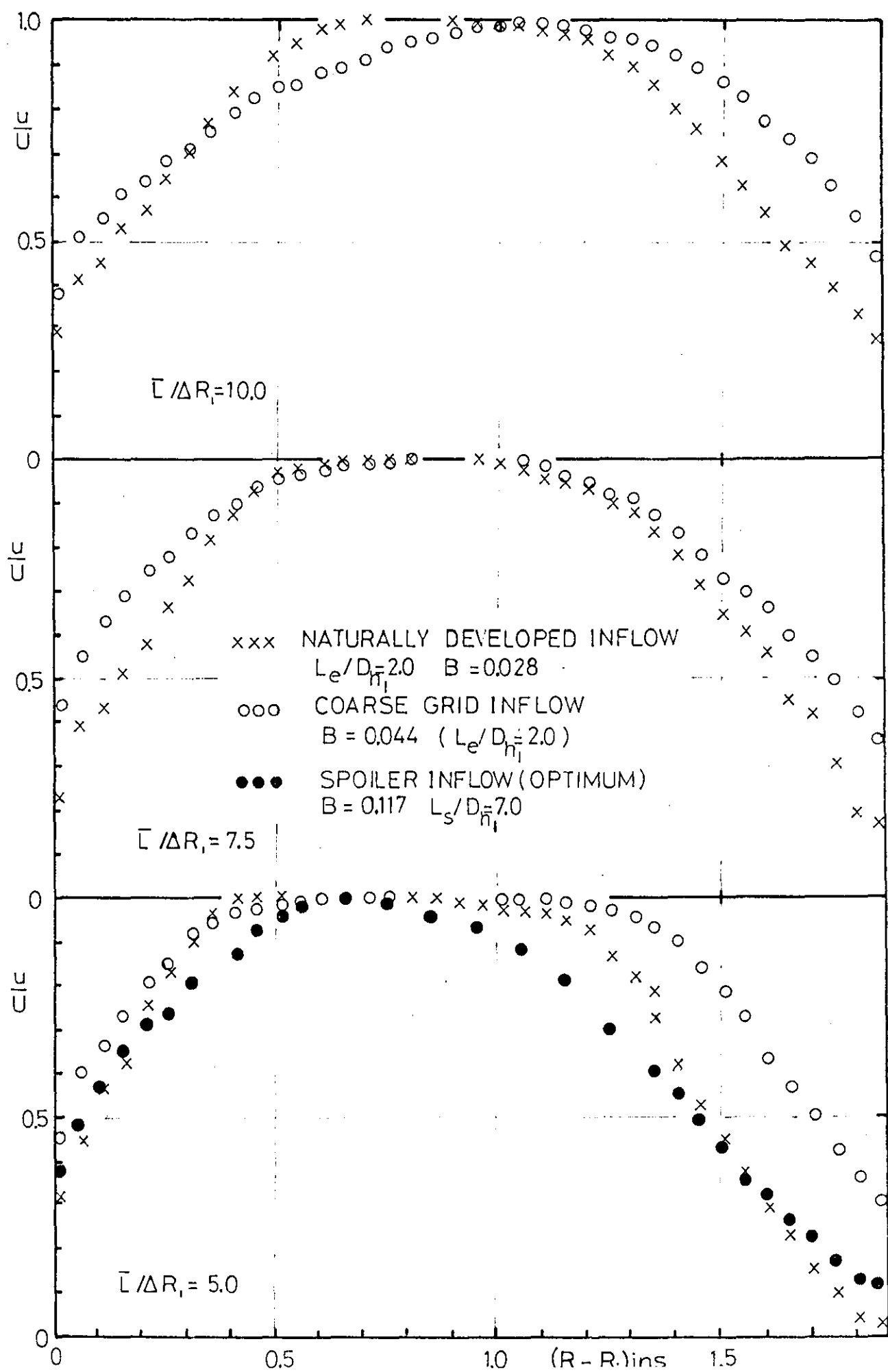


FIGURE 4.69

COARSE GRID INFLOW — STATIC PRESSURE RECOVERY

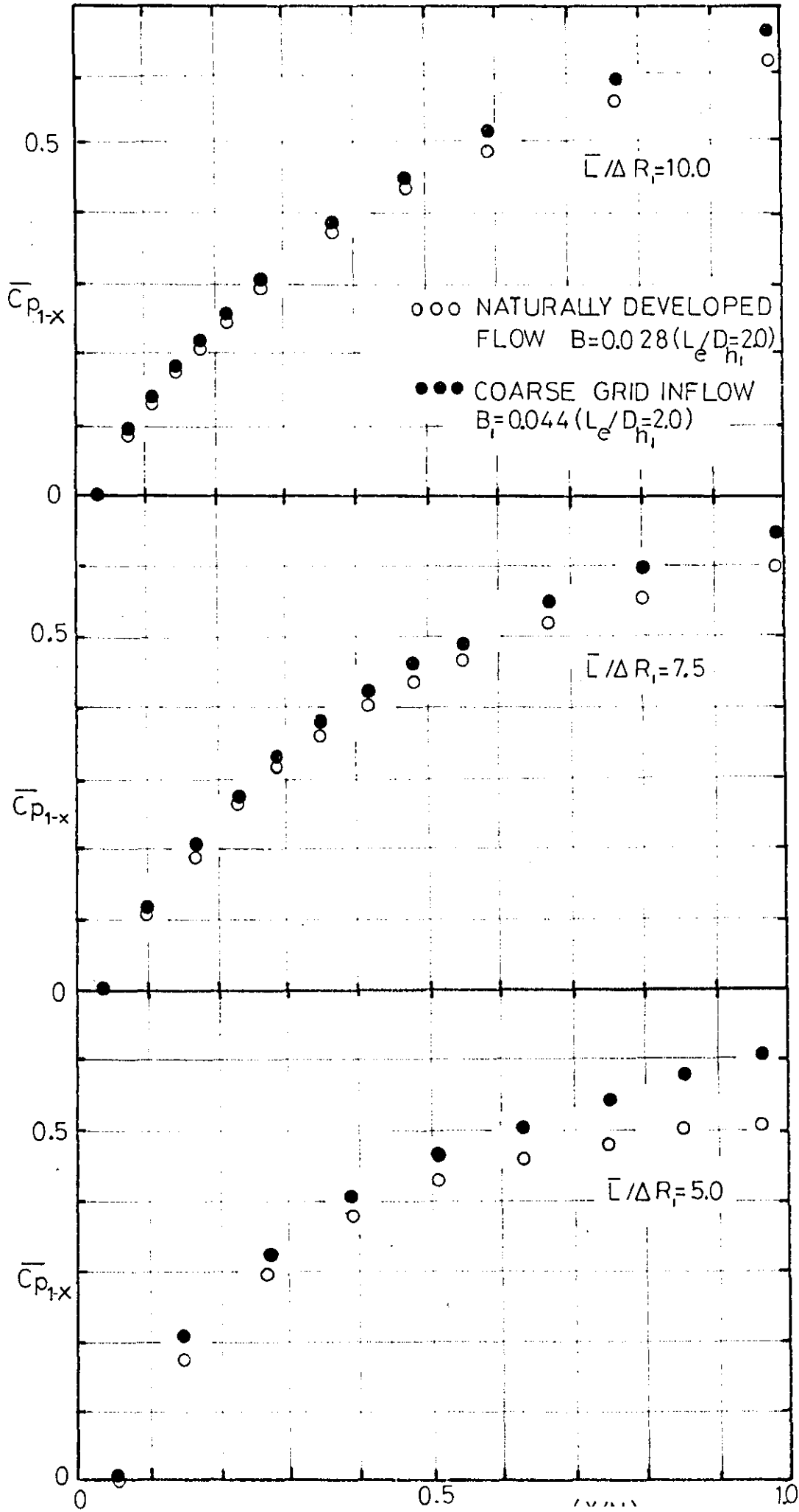
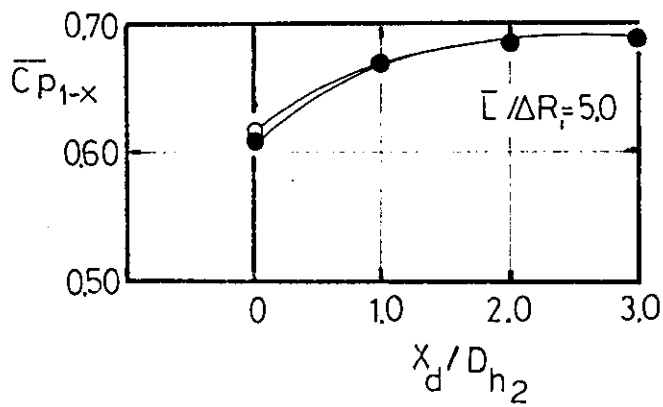
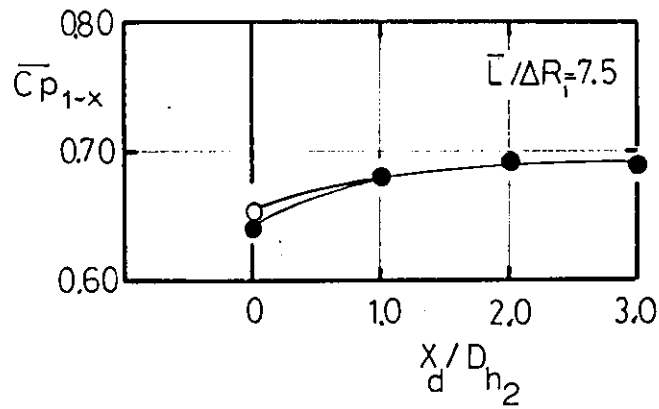
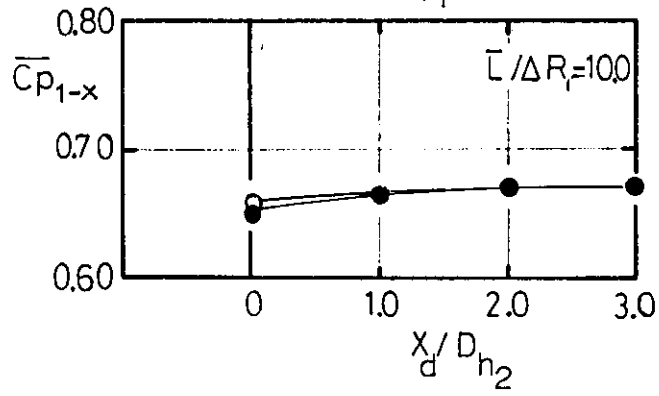


FIGURE 4.70

COARSE GRID INFLOW—STATIC PRESSURE
RECOVERY IN SETTLING LENGTH

$$B_1 = 0.044(L_e/D_{h1})$$



○ ○ ○ OUTER WALL
● ● ● INNER WALL

CHAPTER 5

5.0 THE APPLICATION OF INTEGRAL METHODS TO THE PREDICTION OF DIFFUSER PERFORMANCE AND STABILITY

5.1 Introduction

Theoretical analysis of the flow in diffusers is a problem in predicting the rate of growth, and possible eventual separation of a turbulent boundary layer. However, in contrast to the case of a body surrounded by a free-stream, the pressure is not determined by the frictionless external flow, but by the development of the boundary layer itself. Therefore one of the main difficulties in calculating diffuser flow is that the pressure distribution is unknown to begin with, and is only established in the course of the calculations.

All theoretical prediction methods incorporate equations derived from the Navier-Stokes equations by separating the velocity field into mean and fluctuating components. For axi-symmetric flows these may be written as follows:

X-direction

$$\rho u \frac{\partial u}{\partial x} + \rho v \frac{\partial u}{\partial R} = - \frac{\partial p}{\partial x} - \rho \left[\frac{\partial}{\partial x} (\overline{u'^2}) + \frac{1}{\rho R} \frac{\partial}{\partial R} (\tau R) \right] \quad 5.1$$

R-direction

$$\rho u \frac{\partial v}{\partial x} + \rho v \frac{\partial v}{\partial R} = - \frac{\partial p}{\partial R} - \rho \left[\frac{1}{\rho} \frac{\partial}{\partial x} (\tau) + \frac{\partial}{\partial R} (\overline{v'^2}) \right] \quad 5.2$$

The continuity equation for axially symmetric flow is

$$\frac{\partial}{\partial x} (Ru) + \frac{\partial}{\partial R} (Rv) = 0 \quad 5.3$$

If equations 5.1 and 5.2 are combined together with the continuity relationship, and the Reynolds normal stress terms neglected, this yields two equations for three unknowns u , v , τ . These partial differential equations may be reduced to ordinary differential equations by integrating

across the boundary layer, thereby avoiding explicit local turbulence assumptions. This treatment gives rise to the class of 'integral' methods.

If the basic partial differential equations are solved by numerical techniques as, for example, in the methods of Spalding and Patankar (63), and Bradshaw (6), then the turbulent shear stress structure may either be related to the mean velocity profile or directly to other turbulence parameters e.g. via the turbulent kinetic energy equation. This technique gives the general class of 'differential' methods.

Differential methods are at present under vigorous development and, with the application of increasingly sophisticated turbulence models, are able to solve quite complex flows. They suffer from the small amount of reliable experimental data available both for prediction comparison, and for the supply of improved turbulence models. Considering these facts it was decided to initially predict diffuser performance and stability using an integral approach and, at a later stage, apply the measured data to the evaluation of the Spalding and Patankar (63) differential method.

The application of selected integral methods to the prediction of performance and flow stability in the straight core annular diffuser with near uniform inflow is described in detail in the following sections. Where the flow is fully developed the method due to Stevens (67) may be applied.

5.2 Integral Methods

The basic elements of integral methods may be isolated by considering the momentum integral equation for incompressible turbulent flow, which is generated by integrating the equations of motion across the boundary layer. This is derived in Appendix 4 and is quoted here in its fullest form for axi-symmetric flow with transverse wall curvature R' , and the integral parameters take their axi-symmetric definitions:

$$\frac{d\theta}{dx} = \frac{c_f}{2} - \frac{\theta}{U} \frac{dU}{dx} (H + 2) - \frac{\theta}{R'} \frac{dR'}{dx} + \frac{1}{U^2} \int_{R_\delta}^{R'} \frac{\partial}{\partial x} (\overline{u'^2} + \overline{v'^2} - \overline{v'^2}) dR$$

$$+ \frac{1}{2\rho U^2} \frac{dP_\delta}{dx} \frac{(R'^2 - R_\delta^2)}{R'} \quad 5.4$$

In the case of flow having a potential core the last term, involving the gradient of total pressure at the point of maximum velocity in fully developed flow, vanishes. The Reynolds normal stress term, $\frac{1}{U^2} \int_{R_\delta}^{R'} \frac{\partial}{\partial x} (\overline{u'^2} - \overline{v'^2}) dR$ in potential core flow, is normally neglected as being of second order importance, which the data given in Chapter 4.0 on the overall momentum balance in the test diffusers has substantiated. Further consideration of equation 5.4 shows that the following information is required:

- (i) The maximum velocity (U) variation which, for internal flow, satisfies continuity. In its turn continuity requires a model of the velocity profile which must be suitably described in terms of known integral parameters.
- (ii) Information on wall shear stress (c_f), again in terms of known integral parameters.
- (iii) A reliable criterion for the imminence of separation.
- (iv) A relationship describing the rate of change of shape parameter (H), normally termed the 'auxiliary equation'.

The information specified in paragraphs (i) - (iii) is available in various forms which are given in Sections 5.2.1-3, while the choice of a suitable auxiliary equation is discussed in Section 5.2.4.

5.2.1 Continuity - Mean Velocity Profile

Continuity of internal flow, provided there is no flow addition or removal, may be expressed as follows:

$$\dot{m} = \int_A \rho u dA \quad 5.5$$

Thus the need arises for an accurate representation of the mean velocity profile related to local integral parameters.

Power-Law Velocity Profile

The power law, in two-dimensional flow, may be stated as:

$$\frac{u}{U} = \left(\frac{y}{\delta}\right)^n \quad 0 \leq y \leq \delta \quad 5.6$$

It was formulated by Prandtl who used $n = \frac{1}{7}$ to describe the mean velocity profile for the flat plate boundary layer. Pretsch (51) generalised these profiles allowing 'n' to vary and adopted the characterising shape parameter $H = \delta^*/\theta$ to give:

$$\left(\frac{u}{U}\right) = \left(\frac{y}{\delta}\right)^{\frac{1}{2}(H-1)} \quad 5.7$$

Later Von Doenhoff and Tetervin (78) conducted a series of experiments which verified this method of profile representation as Fig. 5.1, quoted from their work, shows.

The application of this profile representation to diffuser flows with walls having transverse curvature is supported by the recent work of Joseph et al (32) who showed that transverse curvature must be extreme before there is deviation from the $1/7$ power law in zero pressure gradient. Assuming that this finding is true in all pressure gradients leads to the following expressions for flow in diffusers of small divergence angle:

Conical Diffuser

$$Q = \int_0^{R_0} 2\pi RU \left[\frac{R_0 - R}{R_0} \right]^{\frac{1}{2}(H-1)} dR \quad 5.8$$

for fully developed flow, and

$$Q = \int_0^{R_0 - \delta_0} 2\pi RU dR + \int_{R_0 - \delta_0}^{R_0} 2\pi RU \left[\frac{R_0 - R}{\delta_0} \right]^{\frac{1}{2}(H-1)} dR \quad 5.9$$

where there is a potential core.

Annular Diffuser

$$Q = \int_{R_i}^{R_i + \delta_i} 2\pi R U \left(\frac{R - R_i}{\delta_i} \right)^{\frac{1}{2}(H_i - 1)} dR + \int_{R_i + \delta_i}^{R_o} 2\pi R U \left(\frac{R_o - R}{\delta_o} \right)^{\frac{1}{2}(H_o - 1)} dR \quad 5.10$$

for fully developed flow, and

$$Q = \int_{R_i}^{R_i + \delta_i} 2\pi R U \left(\frac{R - R_i}{\delta_i} \right)^{\frac{1}{2}(H_i - 1)} dR + \int_{R_i + \delta_i}^{R_o - \delta_o} 2\pi R U dR + \int_{R_o - \delta_o}^{R_o} 2\pi R U \left(\frac{R_o - R}{\delta_o} \right)^{\frac{1}{2}(H_o - 1)} dR \quad 5.11$$

where there is a potential core. Expressions 5.8 - 5.11 all reduce to simple functions of R_o , R_i , δ_o , δ_i , H_o , H_i , U and are thus ideal for inclusion in integral methods.

An evaluation of the accuracy of the method of profile representation may be gained from comparison with velocity profile data from Chapter 4 for the test diffusers with near uniform inflow ($B_1 = 0.028$). Experimental velocity profile data is compared with the power law mean velocity profile representation in Fig. 5.2(a) where the same values of shape parameter (H) and boundary layer thickness (δ) have been assumed.

Whether the axi-symmetric or two-dimensional shape parameter is adopted is seen to be of secondary importance. The main conclusion is that agreement with experiment is not good. However, it is found that if the momentum thickness (θ) is adopted as the boundary layer thickness parameter, then overall agreement with experiment is much improved, as Fig. 5.2(b) illustrates. This improvement is at the expense of a poor match to the actual boundary layer thickness.

To summarise, the power-law velocity profile representation is simple to apply to the evaluation of diffuser flow, preferably using momentum thickness (θ) as the boundary layer thickness parameter, and yields reasonable accuracy.

Two-Part Velocity Profile

It is now generally accepted on physical grounds that the turbulent boundary layer velocity profile can best be described in terms of a minimum of two regions (inner and outer) each having different characteristics, see Rotta (55), and this necessitates the use of at least two independent parameters to define the profile.

In general form the mean velocity profile in turbulent shear flow may be expressed as

$$\frac{u}{U_\tau} = f\left(\frac{u_\tau y}{\nu}\right) + h(x,y) \quad 5.12$$

where the term $h(x,y)$ gives the departure from the logarithmic law of the wall i.e. $\frac{u}{U_\tau} = \frac{1}{k} \log\left(\frac{u_\tau y}{\nu}\right) + c$.

The law of the wake postulated by Coles (19), where $h(x,y) = \frac{\pi(x)}{k} w\left(\frac{y}{\delta}\right)$, has been used in many theoretical prediction methods applied over a wide variety of conditions; however a more recent formulation by Thompson (73), based on the work of Sarnecki (58), would appear to be more deeply rooted in the physics of turbulent flow and may be briefly described as follows:

The edge of a boundary layer is deeply convoluted with incursions of the turbulence front into the potential flow region. The fraction of time for which the flow is turbulent at any given distance y from the surface is termed the intermittency factor (γ) where,

$$u = \gamma u_t + (1 - \gamma) u_p \quad 5.13$$

and

u_t = mean velocity over 'time turbulent'

u_p = mean velocity over 'time potential' .

The assumption is then made that the mean velocity over 'time turbulent' may be represented by the universal semi-logarithmic wall law profile and, using the mean constants adopted by Sarnecki,

$$u_t = u_\tau (5.4 + 5.5 \log_{10} (\frac{u_\tau y}{\nu})) \quad 5.14$$

Further assuming $u_p = U$ 5.15

Thompson shows

$$u = \gamma_s u_t + (1 - \gamma_s) U \quad 5.16$$

where γ_s indicates 5.15 applies

thus

$$\gamma_s = \frac{u - U}{u_t - U} \quad 5.17$$

Using equation 5.17 Sarnecki analysed a comprehensive range of experimental data to give the correlation shown in Fig. 5.3 which leads to the conclusion that γ_s is a universal function of $(\frac{y}{\delta_s})$, where $\delta_s = 2(y_{\gamma_s=0.5})$.

From equation 5.16 a number of profiles were generated for a range of c_f and $R_{\delta_s} = \frac{U \delta_s}{\nu}$ so that $\frac{u}{U} = f(\frac{y}{\delta_s}, c_f, R_{\delta_s})$.

Numerical integration, and cross plotting, then yielded the relationship:

$$\frac{u}{U} = f(\frac{y}{\theta}, H, R_\theta)$$

presented in the form of charts for a range of fixed values of $\frac{u}{U}$ as, for example, in Fig. 5.4.

Using this velocity profile method comparisons are again made with experimental velocity profile data from Chapter 4 as shown in Fig. 5.5(a), (b). Agreement with the experimental velocity profiles is greatly improved in the latter stages of diffusion where the law of the wall contribution is minor. In the early stages of diffusion however the profile match is somewhat poorer due, no doubt, to modification of the law of the wall in severe adverse pressure gradient, where in this case the law of the wall component makes a major contribution to the velocity profile.

However, this two-part profile does represent a marked improvement over

the power law representation. Both are later evaluated in the context of the theoretical prediction methods employed.

5.2.2 Wall Shear Stress

Where the mean velocity profile can be described in two-parameter form, and the universal law of the wall holds, experimental evidence has shown that it is possible to relate the shear stress, to a good approximation, to some characteristic boundary layer thickness and to the shape of the boundary layer velocity profile.

The requirements for a knowledge of wall shear stress may be stated as:

- (i) a separation criterion when $c_f \rightarrow 0$
- (ii) its contribution to the momentum integral equation.

Unfortunately, near to separation the assumptions on which the two-parameter representation for c_f is based fail, severely curtailing the use of the two-parameter form for accurate prediction of separation point.

The present application of the momentum integral equation is to diffuser flow where there is a strong adverse pressure gradient and, as the integrated momentum balance plots given in Chapter 4 have shown, the value of c_f is of relatively minor importance. The various forms for c_f have been adequately reviewed by, among others, Rotta (55) and Nash (44) and from these the simple relationship given by Ludweig and Tillmann (40) has been assumed for use in conjunction with the power law mean velocity profile:

$$c_f = 0.246 \cdot 10^{-0.678H} (R_0)^{-0.268} \quad 5.18$$

This relationship is based on the assumption of two-dimensional flow; however its use in the prediction of annular diffuser flow where the inlet radius ratio is high ($\frac{R_i}{R_0} \approx 0.8$) can be justified by the quasi two-dimensional nature of the flow and the relative unimportance of the c_f assumption.

Where a two-part velocity profile has been assumed the value of c_f is implied, through the law of the wall.

5.2.3 Separation Criterion

In general terms the separation of the boundary layer in a fluid mechanical device can cause a rapid decline in performance with the possible addition of large scale instabilities and allied vibration loads.

Unfortunately the 'best performance' of many flow components occurs just prior to separation and thus the successful prediction of the imminence of separation is of major importance in any theoretical method.

The separation point has, in the past, been predicted via the wall skin friction (c_f) which was assumed to be zero at the point of separation. As noted in the previous section this approach is invalidated by the inherent inaccuracy in the determination of c_f near separation, and will probably yield optimistic estimations of the separation point.

Historically another widely used separation criterion has been the boundary layer shape factor (H) with turbulent flow separation being predicted at shape factor values in the range $H = 1.8 \rightarrow 4.0$. Such a wide spread gives rise to unacceptable variation in the predicted point of separation and thus the engineer is usually forced into conservative designs with attendant size penalties.

The problems associated with the prediction of flow separation have recently been reviewed in detail by Sovran (66) who highlights the pressing need for more research in this area. For the purposes of separation prediction in the theoretical methods subsequently described it was decided to employ the transitory stall correlation, based on experimental data, given by Sandborn and Kline (56), as shown in Fig. 5.6. This has been shown in Chapter 4 to agree with present experimental test observations of the point of transitory stall, and could this be applied with a fair degree of confidence.

5.2.4 The Auxiliary Equation

The auxiliary equation is a broad term applied to the means employed

for predicting the rate of change of the shape parameter (H), or any other suitable boundary layer integral parameter. Many of the equations employed are empirically based making their extension to a wider class of flows questionable, as has been noted by both Rotta (55) and Thompson (72) in critical examination. The most reliable auxiliary equations have been found to be those firmly based in the physics of turbulent flow rather than on specific experimental data. This physical basis is found in very few cases and by far the most widely acknowledged is the entrainment based auxiliary equation of Head (26), later modified by Thompson (71). The Stanford Conference Proceedings of 1968 (66) showed that integral methods based on this entrainment model gave consistently good results for a wide range of experimental flows, as Fig. 5.7 illustrates, and thus it was decided to adapt these methods to the prediction of incompressible turbulent flow behaviour in straight-core annular diffusers.

5.3 Entrainment Model due to Head (26)

The following sections describe the physical basis of Head's entrainment model and its application to the generation of an auxiliary equation for incorporation into an integral method. This method is then applied to the specific problem of predicting the performance and flow stability limits of the straight core annular diffuser having near uniform inflow.

5.3.1 Physical Basis

Considering the case of incompressible two-dimensional turbulent flow, as defined in Fig. 5.8, the basis of Head's entrainment model is that the amount of fluid entrained from the freestream by the boundary layer over unit length, denoted $\frac{dQ}{dx}$, is dictated by the shape of the velocity profile, by the freestream velocity, and by some measure of boundary layer thickness. Thus it was stated:

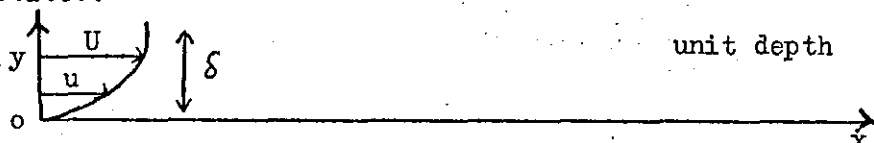


Figure 5.8

$$\frac{dQ}{dx} = f(\text{profile shape, freestream velocity, a boundary layer thickness})$$

5.19

Now
$$Q = \int_0^{\delta} u dy = U(\delta - \delta^*)$$

thus
$$\frac{dQ}{dx} = \frac{d}{dx} [U(\delta - \delta^*)]$$
 5.20

and choosing convenient parameters, viz.

$$\begin{aligned} \text{profile shape} & \text{---} H_{\delta-\delta^*} = \frac{\delta - \delta^*}{\theta} \\ \text{boundary layer thickness} & \text{---} \delta - \delta^* \end{aligned}$$

gave

$$\frac{dQ}{dx} = \frac{d}{dx} [U(\delta - \delta^*)] = f(H_{\delta-\delta^*}, U, \delta - \delta^*)$$
 5.21

which inherently assumes that the scale of the largest turbulent eddies is characterised by U and $\delta - \delta^*$.

Equation 5.21 gives, in non-dimensional terms:

$$\frac{1}{U} \left[\frac{d}{dx} [U(\delta - \delta^*)] \right] = F(H_{\delta-\delta^*})$$
 5.22

which on expansion gives:

$$\frac{d}{dx} (\delta - \delta^*) = F(H_{\delta-\delta^*}) - \frac{\delta - \delta^*}{U} \cdot \frac{dU}{dx}$$
 5.23

With the assumption of a one-parameter family of velocity profiles such that $H_{\delta-\delta^*} = G(H)$ it is possible, with experimental evaluation of F and G , to calculate the development of H and thus, in conjunction with the momentum integral equation and continuity, to predict the growth of internal turbulent flows, as detailed in the following section.

5.3.2 Application to Two-dimensional Internal Flow

Brief details of the application of Head's entrainment method to two-dimensional internal flow facilitates the description of its subsequent

application to axi-symmetric flows.

Consider an incompressible, two-dimensional, turbulent internal flow in a duct of small divergence of arbitrary cross-section (width $2W$) and unit depth. We have the following equations, where all integral parameters take their two-dimensional form:

Momentum integral equation (neglecting Reynolds normal stresses)

$$\frac{d\theta}{dx} = \frac{c_f}{2} - \frac{\theta}{U} \frac{dU}{dx} (H + 2) \quad 5.24$$

$$(\text{where } c_f = 0.246 \cdot 10^{-0.678H} (R_\theta)^{-0.268})$$

Auxiliary equation due to Head

$$\frac{d}{dx} (\delta - \delta^*) = F(H_{\delta-\delta^*}) - \frac{\delta - \delta^*}{U} \cdot \frac{dU}{dx} \quad 5.25$$

Continuity

$$Q = 2 \int_0^H u dy = 2U(W - \delta^*) \quad 5.26$$

A power-law form of the velocity profile is assumed since this is inherent in Head's auxiliary equation ($H_{\delta-\delta^*} = G(H)$) and the functions F and G , illustrated in Fig. 5.9, are quoted from the work of Head (26).

Given this basic information, prediction of the internal boundary layer growth is possible up to the point where the boundary layers meet. The method of solution is indicated, in terms of a 'block diagram', in Fig. 5.10, and may be briefly described as follows:

Over a step length dx a velocity increment dU is assumed. Applied to the momentum integral equation in mean terms, this gives θ_{x+dx} , and applied similarly to the Head auxiliary equation, using $F(H_{\delta-\delta^*})$ from Fig. 5.10, $(\delta - \delta^*)_{x+dx}$. This gives, through $H_{\delta-\delta^*} = G(H)$, the value of H_{x+dx} , and allows calculation of Q_{x+dx} . If $Q_{x+dx} \neq Q_x$ a simple predictor-corrector technique is applied, the mean values adjusted e.g. $\theta = \frac{\theta_x + \theta_{x+dx}}{2}$, and the calculation pursued until, within an acceptable tolerance, continuity is satisfied.

5.3.3 Application to Axi-Symmetric Internal Flow

The basic difference in the mechanism of entrainment in external and internal flow is, as Section 5.3.2 has indicated, that free entrainment ceases when the two boundary layers meet. The case of axi-symmetric internal flow adds a further dimension in that the actual 'front' over which entrainment takes place reduces or increases as the boundary layer develops. This is illustrated in Fig. 5.11, where the conical diffuser has been taken as an example.

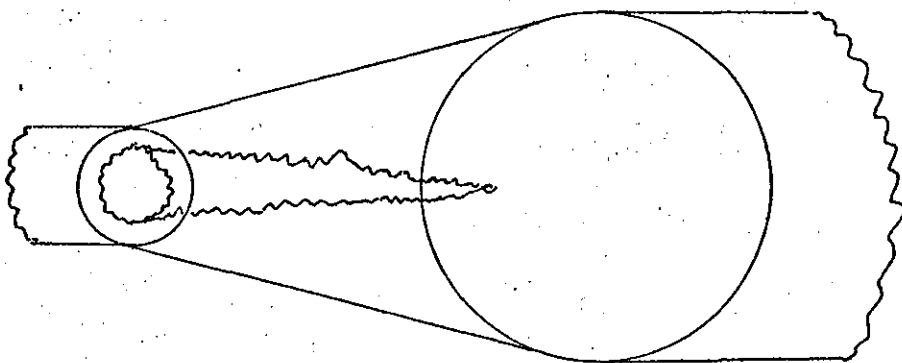


Figure 5.11

Similar behaviour is encountered in the annular diffuser where entrainment takes place on two fronts which may reduce or increase as diffusion takes place dependent on the diffuser geometry, with free entrainment ceasing when the fronts coincide.

Thus in axi-symmetric flow some re-definition is required when considering entrainment. Here it is assumed that the rate of entrainment of the free-stream by the boundary layer ($\frac{dQ}{dx}$) takes the following form:

$$\frac{dQ}{dx} = 2\pi R_{\text{eff}} \cdot U F(H') \quad 5.27$$

where R_{eff} is the effective radius of entrainment and H' some representative shape parameter equivalent to $H_{\delta-\delta^*}$ in two-dimensional flow. The relationship given in 5.27 fulfills all physical requirements in that $\frac{dQ}{dx}$ is directly proportional to the length of the entrainment front, and reduces to zero

when $R_{\text{eff}} = 0$.

The effective radius of entrainment can be found by reference to the experimental work on intermittency by Feidler and Head (22). The effective centre of entrainment $(\frac{\bar{Y}}{\delta})$ in adverse pressure gradient is given in terms of the shape parameter H as illustrated in Fig. 5.12. Thus assuming a conical diffuser, for purposes of illustration, where the radius is R and the boundary layer thickness δ , we have

$$R_{\text{eff}} = R - (\bar{Y}/\delta)\delta \quad 5.28$$

Turning to the specific case of the straight-core annular diffuser of small divergence, with the geometry and nomenclature as given in Fig. 5.13, we have boundary layers on both outer and inner walls experiencing an (assumed) equal axial pressure gradient. Neglecting Reynolds normal stresses the momentum integral equations on the outer and inner walls respectively, derived in Appendix 4, are as follows, assuming a potential core:

$$\frac{d\theta_o}{dx} = \frac{c_{f_o}}{2} - \frac{\theta_o}{U} \frac{dU}{dx} (H_o + 2) - \frac{\theta_o}{R_o} \frac{dR_o}{dx} \quad 5.29$$

$$\text{where } c_{f_o} = 0.246 \cdot 10^{-0.678 H_o} R_{\theta_o}^{-0.268}$$

$$\frac{d\theta_i}{dx} = \frac{c_{f_i}}{2} - \frac{\theta_i}{U} \frac{dU}{dx} (H_i + 2) - \frac{\theta_i}{R_o} \frac{dR_i}{dx} \quad 5.30$$

$$\text{where } c_{f_i} = 0.246 \cdot 10^{-0.678 H_i} R_{\theta_i}^{-0.268}$$

Note that the boundary layer integral parameters here take their axisymmetric form.

The boundary layer flows denoted Q_o and Q_i for the outer and inner walls respectively are derived in Appendix 5 and reduce to:

$$Q_o = 2\pi U R_o (\delta_o - \delta_o^2 / 2R_o - \delta_o^*) \quad 5.31$$

$$Q_i = 2\pi U R_i (\delta_i + \delta_i^2 / 2R_i - \delta_i^*) \quad 5.32$$

and letting $(\delta_o - \delta_o^2 / 2R_o - \delta_o^*) = DO$

$$(\delta_i + \delta_i^2 / 2R_i - \delta_i^*) = DI$$

The following convenient shape parameters are defined:

$$H'_o = DO / \theta_o$$

$$H'_i = DI / \theta_i$$

it being assumed that

$$H'_o = F_1(H_o) \quad 5.33$$

$$H'_i = F_2(H_i) \quad 5.34$$

Two entrainment functions are then assumed, viz.

$$F_3(H'_o) = \frac{dQ_o/dx}{2\pi R_{o\text{eff}} U} \quad 5.35$$

$$F_4(H'_i) = \frac{dQ_i/dx}{2\pi R_{i\text{eff}} U} \quad 5.36$$

Now differentiation of 5.31 gives

$$\frac{dQ_o}{dx} = 2\pi R_{o\text{eff}} \cdot F_3(H'_o) = 2\pi \left[R_o \cdot U \cdot \frac{d}{dx}(DO) + R_o \cdot DO \cdot \frac{dU}{dx} + U \cdot DO \cdot \frac{dR_o}{dx} \right]$$

from which, as detailed in Appendix 5:

$$\frac{d}{dx}(DO) = \frac{1}{R_o} \left[R_{o\text{eff}} \cdot F_3(H'_o) - \frac{R_o \cdot DO}{U} \frac{dU}{dx} - DO \cdot \frac{dR_o}{dx} \right] \quad 5.37$$

and similarly for the inner wall

$$\frac{d}{dx}(DI) = \frac{1}{R_i} \left[R_{i\text{eff}} \cdot F_4(H'_i) - \frac{R_i \cdot DI}{U} \frac{dU}{dx} - DI \cdot \frac{dR_i}{dx} \right] \quad 5.38$$

Equations 5.37 and 5.38 form the auxiliary equations and the remaining requirement for solution of the flow is to evaluate the functions F_{1-4} appearing in equations 5.33 - 5.36.

This requires detailed experimental data and the only independent information available was that due to Stevens and Markland (68), so initially this data was used. Unfortunately the degree of flow asymmetry was such as to invalidate the use of the data for this purpose, and recourse had to be made to data from the experimental tests described in Chapter 4. Using these results the functions F_{1-4} were generated, and are illustrated in Fig. 5.14. It will be noted that within acceptable limits $F_1 = F_2$ while $F_1 \neq F_4$ the latter result being discussed in detail in Chapter 6.

Thus for the purposes of computation a single function for the form of shape parameter was assumed ($H' = F(H)$) while separate functions were used for the inner and outer walls.

Assuming a power law mean velocity profile representation the total quantity flow (Q), as derived in Appendix 5, takes the form:

$$Q = 4\pi U \left[\frac{R_i \delta_i}{H_i + 1} + \frac{\delta_i^2}{H_i + 3} + \frac{((R_o - \delta_o)^2 - (R_i + \delta_i)^2)}{4} + \frac{R_o \delta_o}{H_o + 1} - \frac{\delta_o^2}{H_o + 3} \right] \quad 5.39$$

Sufficient information was then available to allow solution of the diffuser flow by basically the same process as indicated in Section 5.3.2.

Fig. 5.15 shows a flow diagram of the computer program employed in the case of annular diffuser flow.

Basic checks were carried out on the prediction method for sensitivity to:

- (i) tolerance (DIFF) on continuity
- (ii) variation of the step DX from 0.01(N) to 0.1(N)
- (iii) small changes in diffuser inlet parameters.

The significant results of these checks are illustrated in Fig. 5.16 where it is seen that a value of $\text{DIFF}/Q > 0.01$ causes inaccuracies; however, in practice a very close tolerance of the order $\frac{\text{DIFF}}{Q} = 0.00001$ was maintained.

Sensitivity to DX was negligible as was the effect of small variations in the inlet parameters.

Comparison of this prediction method with experimental results from the test diffusers is made in Chapter 6.

5.4 Entrainment Model due to Thompson (71)

The physical basis of Thompson's entrainment model is described and the resulting auxiliary equation is applied to the prediction of performance and stability limits of the straight core annular diffuser with near uniform flow.

5.4.1 Physical Basis

For the two-dimensional, incompressible turbulent boundary layer, Thompson considerably revised the entrainment concept of Head. Considering an entrainment front continuously propagating into the external flow he bases his arguments on relating the rate of increase of flux of the turbulent flow ($\frac{dQ_t}{dx}$) to the mean entrainment rate, denoted $\overline{v_{et}}$.

Considering equation 5.13 where

$$u = \gamma u_t + (1 - \gamma) u_p$$

then
$$Q_t = \int_0^{\delta} \gamma u_t dy = U t \quad 5.40$$

where t is defined as the 'turbulence flux thickness', and the basic entrainment equation could be written:

$$\frac{d}{dx}(U t) = \overline{v_{et}} \left(R_\theta \cdot \frac{t}{\theta} \right) = \overline{v_{et}} \quad 5.41$$

In the absence of experimental information, Thompson assumed that the intermittency distribution was in all cases that measured by Klebanoff (33) in the zero pressure gradient layer, and further, that the mean velocities in the turbulent fluid were given by the universal inner law projected out into the intermittent region, and that the velocity in the irrotational

regions was that of the freestream.

With these assumptions Thompson was able to construct a family of turbulence flux profiles corresponding to his velocity profile family, and to plot t/θ as a function of R_θ and H .

The entrainment velocity v_{et} was assumed to be proportional to the velocity defect Δu of the turbulence flux profile near the bottom of the intermittent region, as illustrated in Fig. 5.17, thus:

$$v \frac{d}{dx} (R_\theta \cdot t/\theta) = \alpha_e \Delta u$$

or

$$\frac{d}{dx} (R_\theta \cdot t/\theta) = \alpha_e \frac{\Delta u}{U} \frac{U}{v} \quad 5.42$$

where α_e was assumed to be a 'universal entrainment coefficient'.

From the family of turbulence flux profiles $\frac{\Delta u}{U}$ was plotted as a function of H and R_θ and, with t/θ and c_f similarly displayed, the entrainment equation, 5.42, and momentum integral equation could be applied to the solution of two-dimensional flows, using the computational techniques described in Section 5.3.2.

With $\alpha_e = 0.09$ good agreement was obtained for the equilibrium boundary layers of Clauser (15) and the flat plate boundary layer, but only poor agreement for separating flows. At this stage it was assumed that $\theta \frac{d}{dx} (t/\theta)$ could be used as a measure of the departure from similarity and this was introduced by assuming:

$$\alpha_e = \alpha + \beta \theta \frac{d}{dx} (t/\theta) \quad 5.43$$

Thus equation 5.42 then took the form

$$\frac{d}{dx} (t/\theta) = \frac{\alpha \frac{U}{v} \frac{\Delta u}{U} - (t/\theta) \frac{dR_\theta}{dx}}{R_\theta (1 - \beta \frac{\Delta u}{U})} \quad 5.44$$

With $\alpha = 0.09$ and $\beta = 1.0$ equation 5.44 was found to give satisfactory results, and where $\theta \frac{d}{dx} \left(\frac{t}{\theta} \right) > 0.003$ the assumption of $\beta = 2.0$ gave improved agreement with experimental data.

5.4.2 Application of Thompson's Method Using the Concept of 'Equivalent Two-Dimensional Flow'

In Thompson's method two-dimensional flow and definitions are assumed throughout, and the use of empirical constants generated from two-dimensional experimental data makes the rigorous application of the method to axi-symmetric turbulent flow impossible without complete re-definition of the method in axi-symmetric terms. This was beyond the scope of the present evaluation of entrainment based integral methods applied to the straight core annular diffuser and indeed presents a primary obstacle to the general application of this method.

For the specific case of straight core annular diffusers of high radius ratio, for the geometry shown in Fig. 5.13, the concept of a 'two-dimensional equivalent' annular diffuser was evolved.

The basic computational method outlined in Section 5.3.3 was retained and a diffuser inlet radius ratio of 0.98 assumed to give a quasi two-dimensional flow allowing the use of Thompson's entrainment equation. The diffuser non-dimensional length (N/AR_1) was maintained and the outer wall angle (ϕ_0) adjusted to give an area ratio $AR_{1-2} = 2.0$. The actual and modified diffuser geometry parameters are given in Table 5.1 below:

TABLE 5.1

EQUIVALENT DIFFUSER GEOMETRY

ACTUAL					EQUIVALENT				
$\left[\frac{R_i}{R_o}\right]_1$	$\frac{N}{\Delta R_1}$	AR_{1-2}	ϕ_o	ϕ_i	$\left[\frac{R_i}{R_o}\right]_1$	$\frac{N}{\Delta R_1}$	AR_{1-2}	ϕ_o	ϕ_i
0.83	10.0	2.0	5.0°	0°	0.98	10.0	2.0	5.733°	0°
0.83	7.5	2.0	6.65°	0°	0.98	7.5	2.0	7.617°	0°
0.83	5.0	2.0	10.0°	0°	0.98	5.0	2.0	11.433°	0°

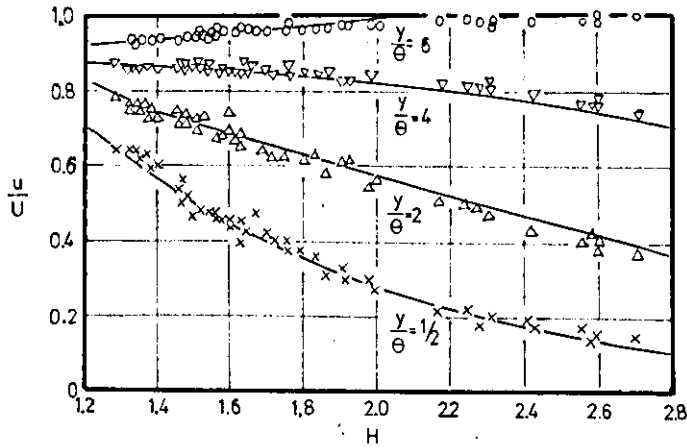
The validity of this concept was checked using the established Head's method with encouraging results, as Fig. 5.18 shows. This is probably mainly due to the high actual diffuser radius ratio, and the 'equivalent diffuser' concept is not advocated as being generally applicable.

Thus the Thompson entrainment equation 5.44 was assumed and also continuity based on the Thompson two-part velocity profile, both as detailed in Appendix 6. With the addition of the outer and inner wall momentum integral equations this allowed solution of the flow, using the techniques established in Section 5.3.3, as shown in the computer program flow diagram in Fig. 5.19.

The sensitivity of the method to the quantity flow tolerance, variation in the DX step, and variation in the initial parameters was checked with satisfactory results similar to those quoted in Fig. 5.16

Comparison of this prediction method with experimental results from the test diffusers is given in Chapter 6.

FIGURE 5.1



COMPARISON OF EXPERIMENTAL BOUNDARY LAYER VELOCITY PROFILES FROM V.DOENHOFF & TETERVIN(78) WITH POWER-LAW PROFILES, AS GIVEN BY ROTTA(55).

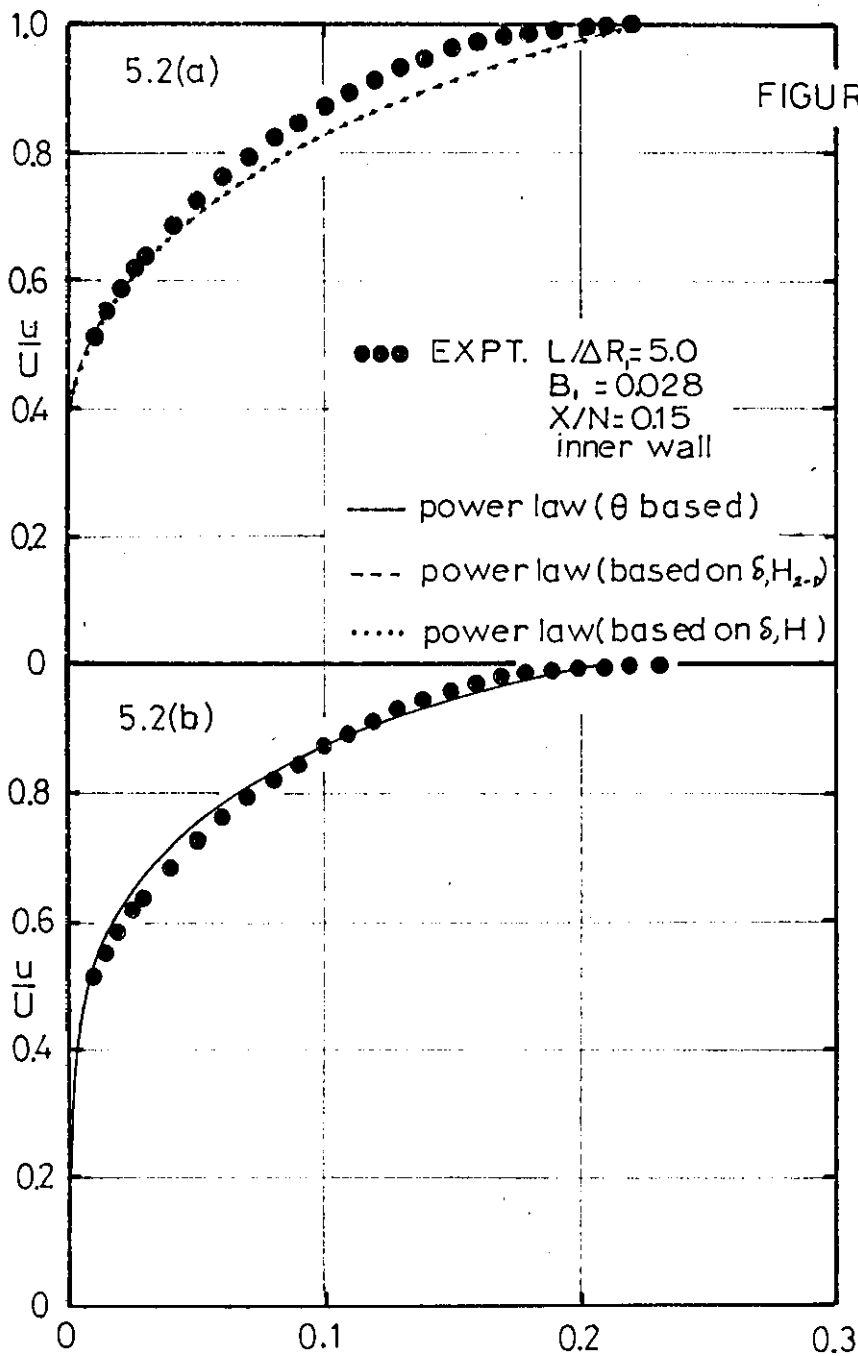
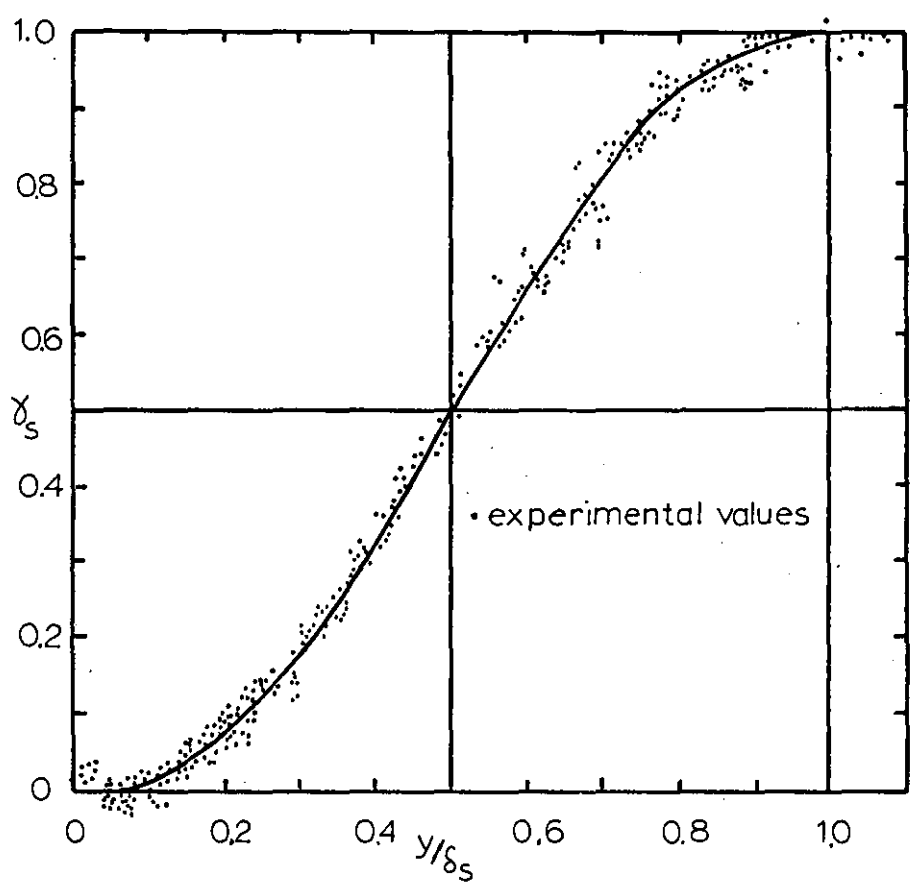


FIGURE 5.2

FIGURE 5.3

SARNECKI'S INTERMITTENCY CORRELATION
AS GIVEN BY THOMPSON(73).



CONTOURS OF (y/θ) FOR $u/U=0.30$ FIGURE 5.4
THOMPSON(73).

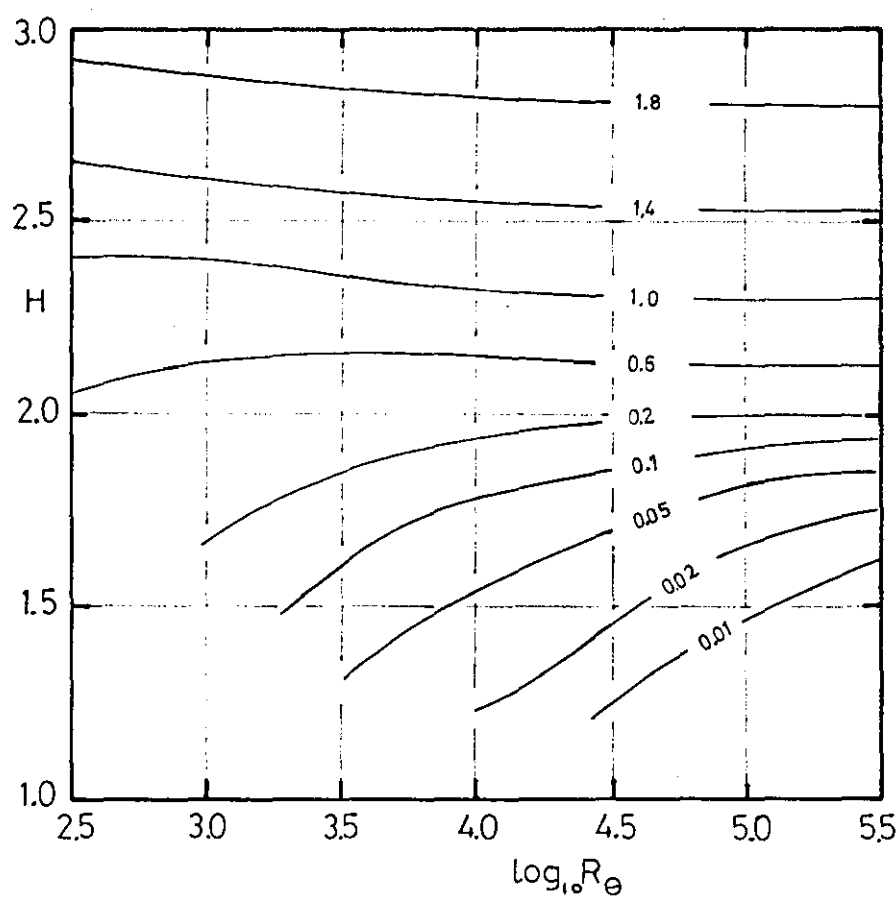
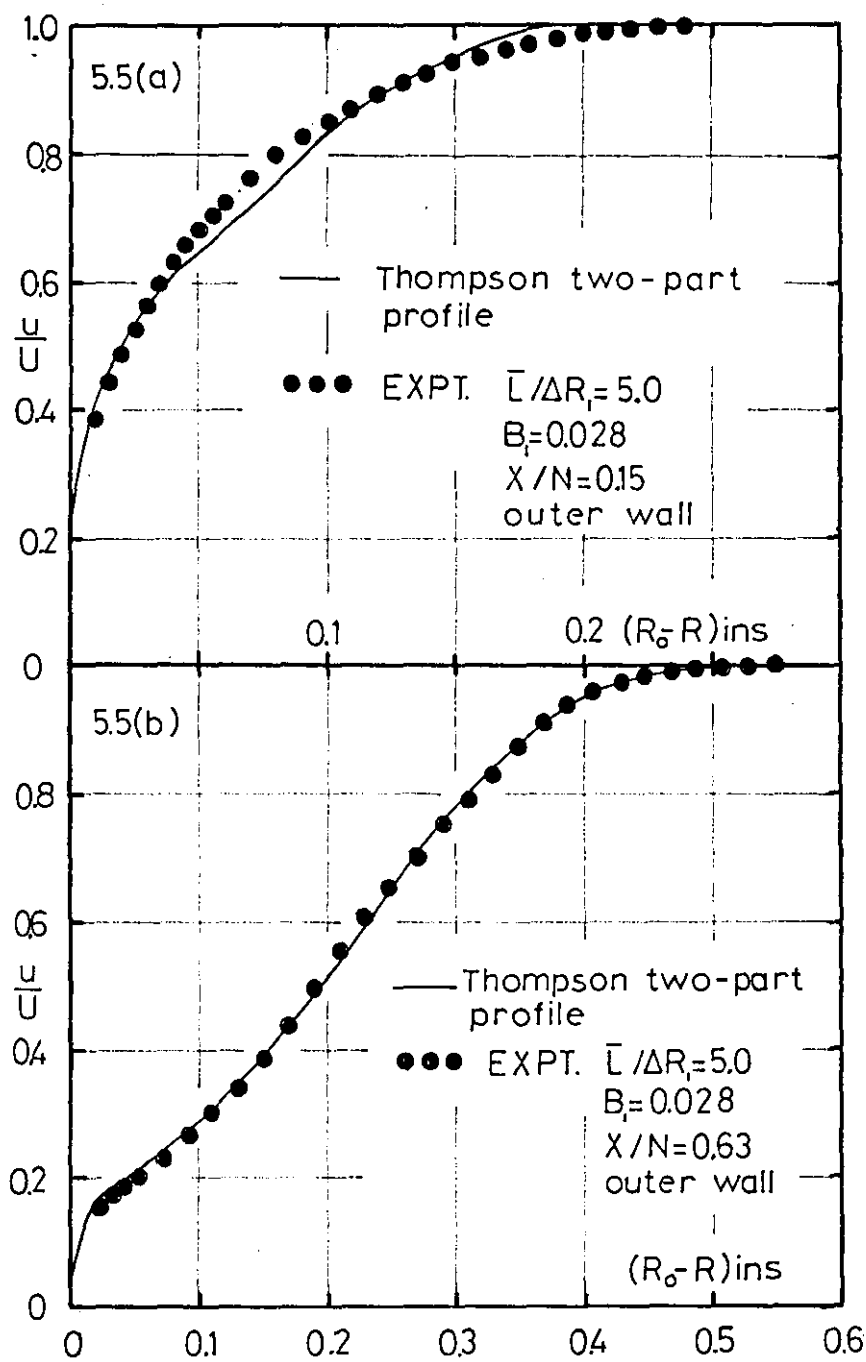
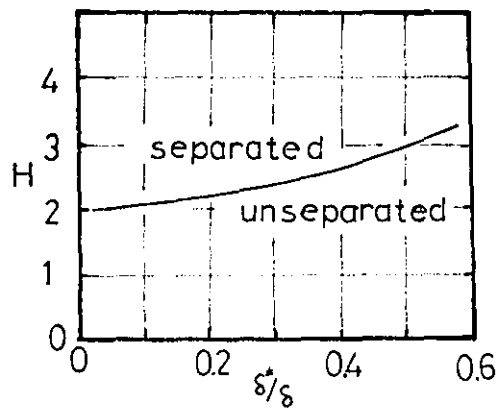


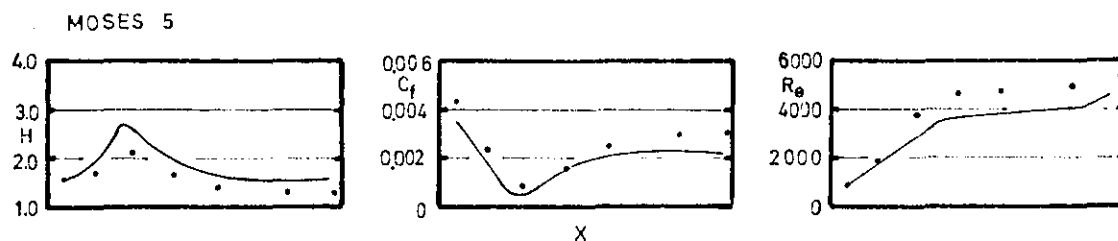
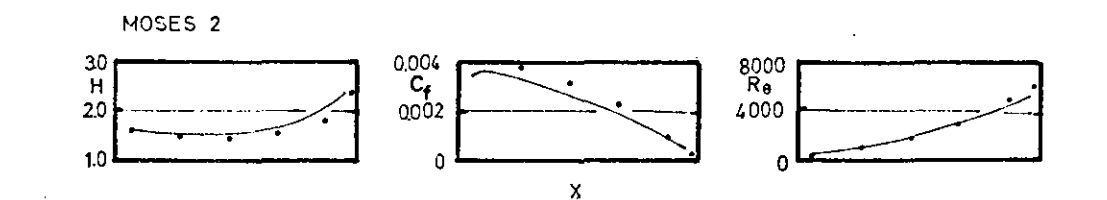
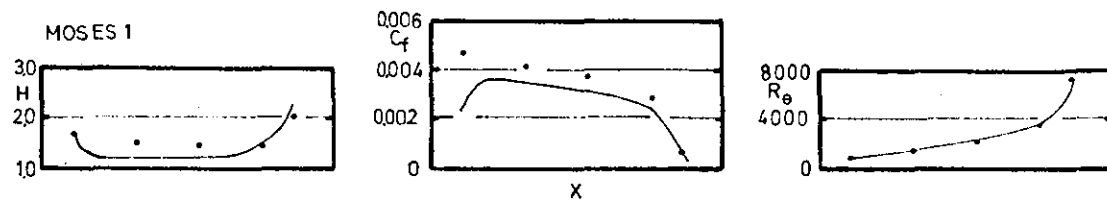
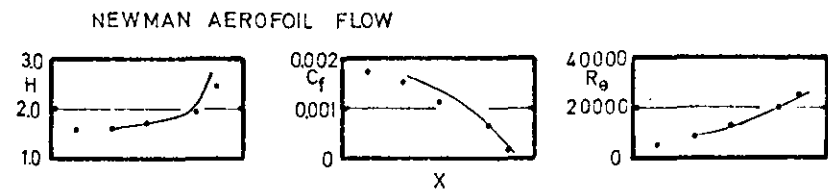
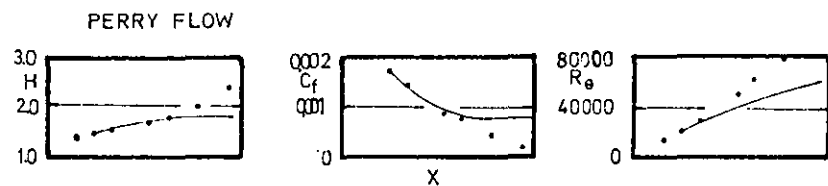
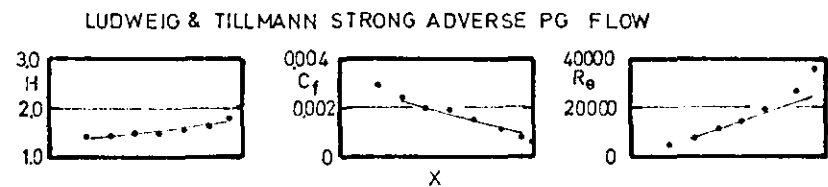
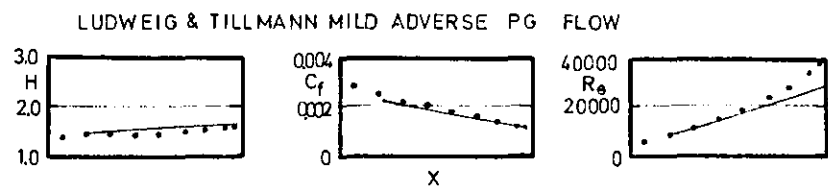
FIGURE 5.5

THOMPSON(73) TWO -PART VELOCITY
PROFILE ,COMPARISON WITH EXPERIMENT.



SANDBORN&KLINE(56) FIGURE 5.6
TURBULENT SEPARATION CORRELATION

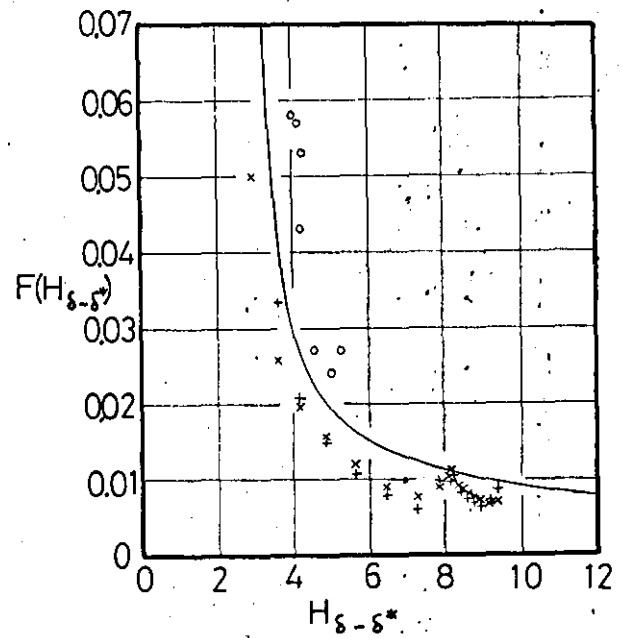
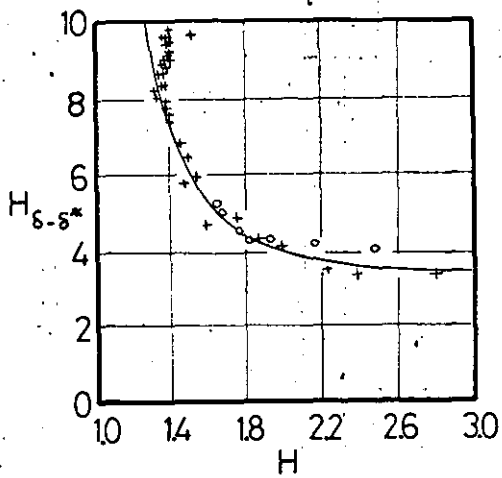




TYPICAL COMPARISONS WITH EXPERIMENTAL DATA—HEAD'S
PREDICTION METHOD —REFERENCE(66)

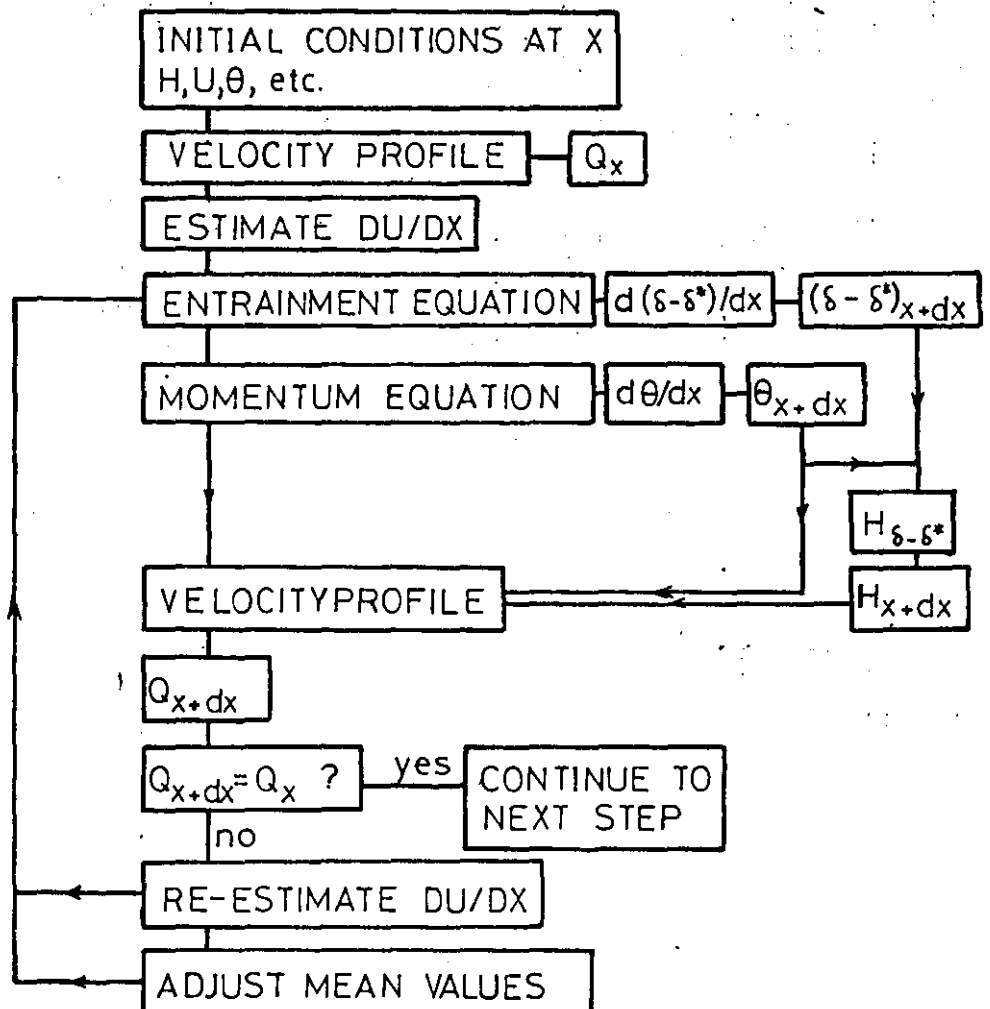
FIGURE 5.9

HEADS METHOD - SHAPE FACTOR & ENTRAINMENT FUNCTIONS.



HEADS METHOD - SOLUTION PROCEDURE

FIGURE 5.10



FEIDLER& HEAD(22) — EFFECTIVE
CENTRE OF INTERMITTENCY.

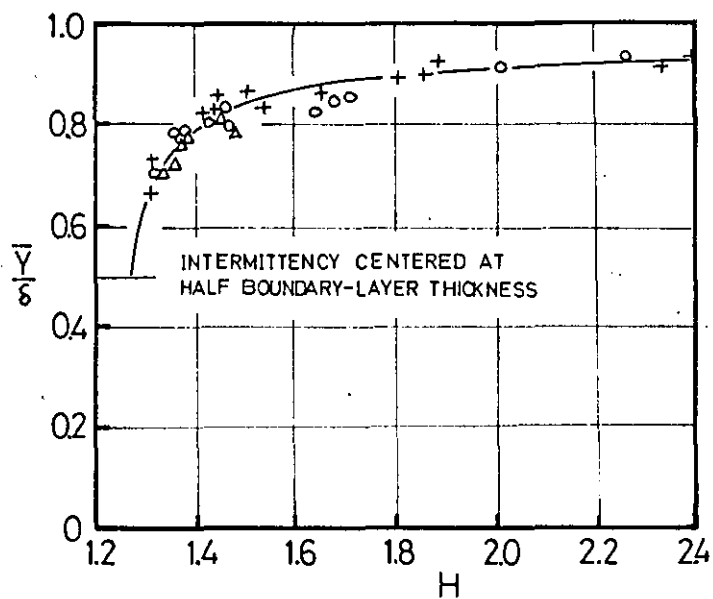
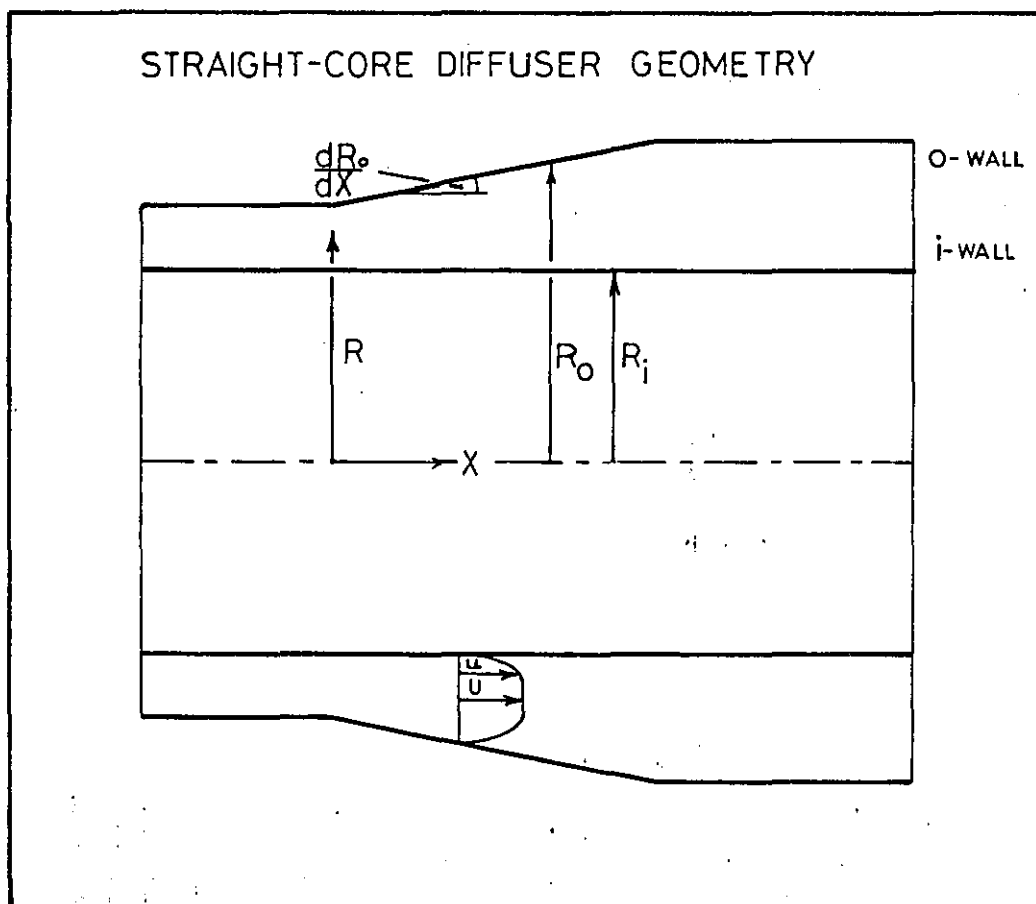
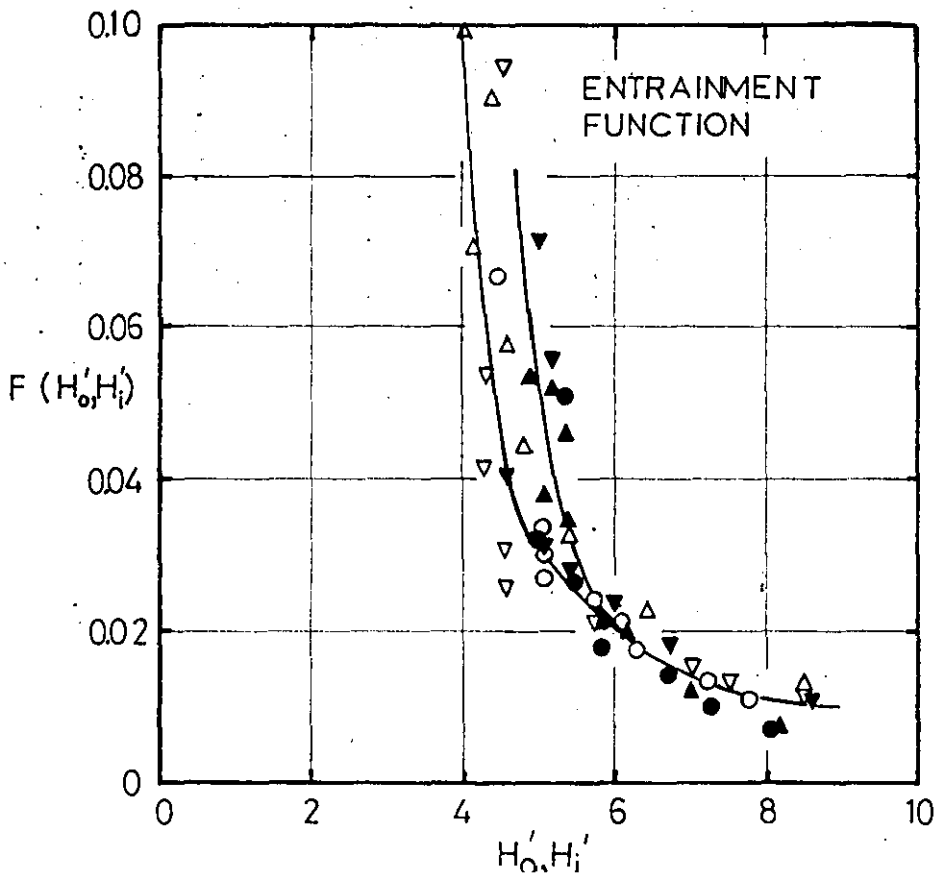
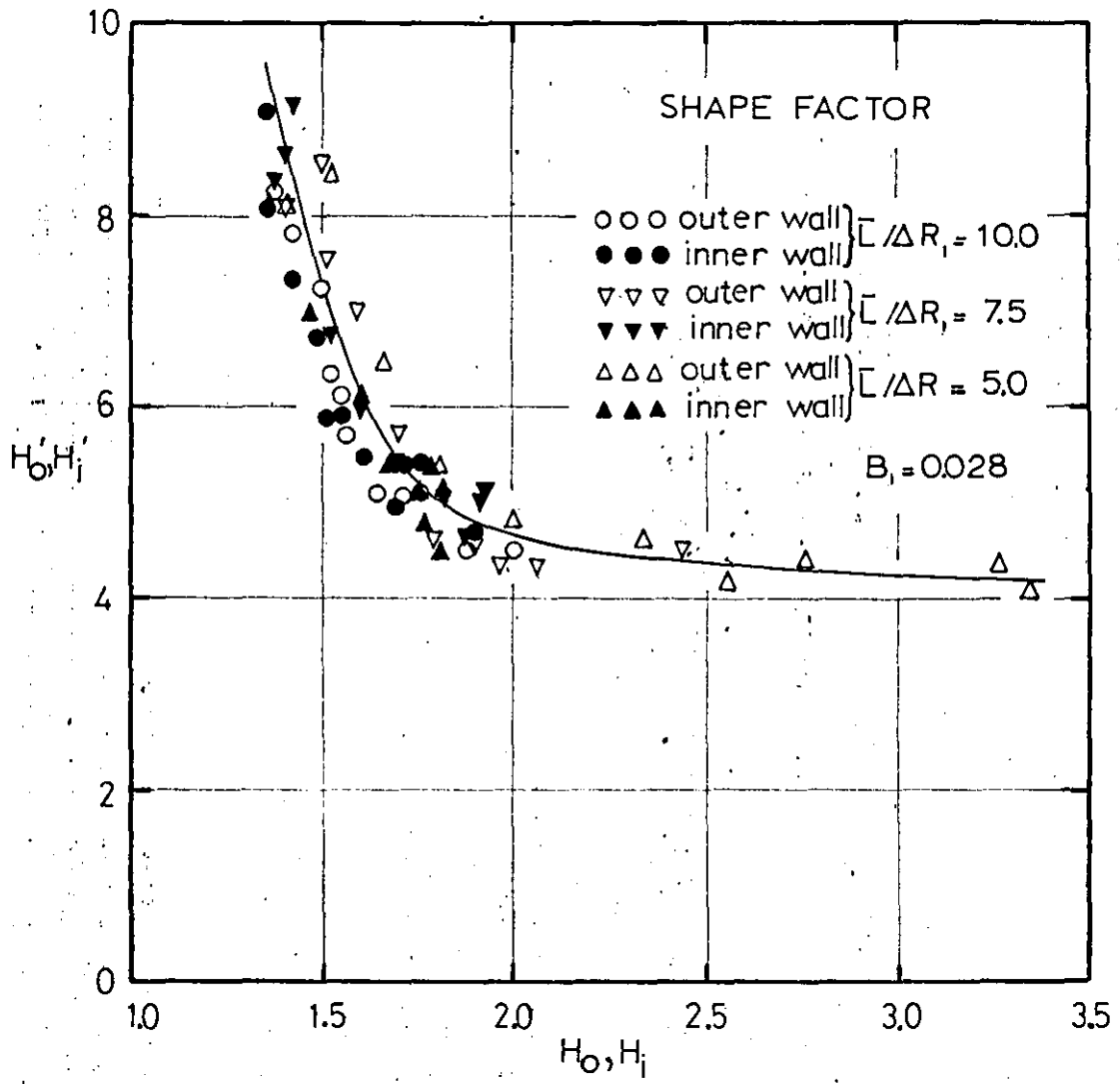


FIGURE 5.13

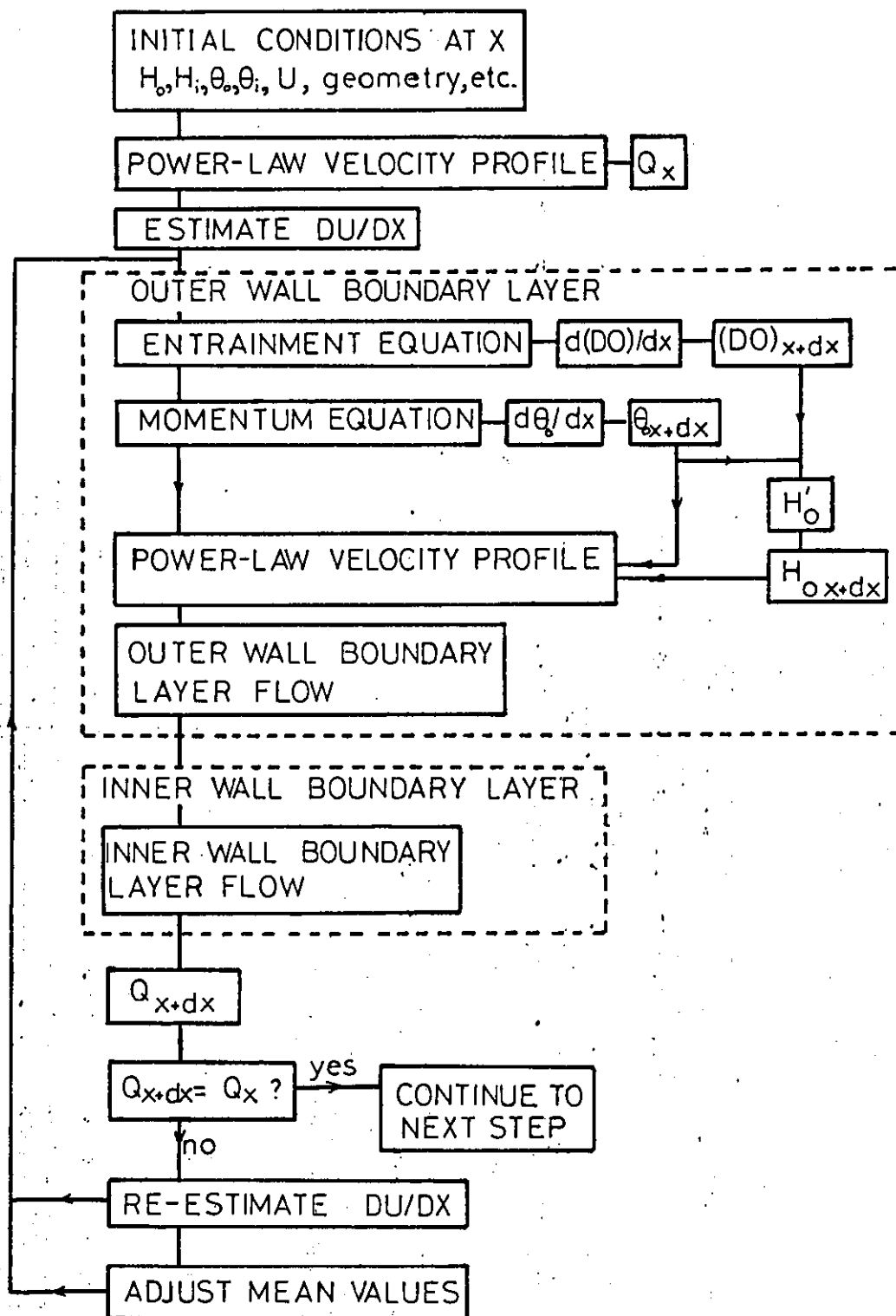


HEADS METHOD FUNCTIONS—AXI-SYMMETRIC FORM.



HEAD'S METHOD SOLUTION PROCEDURE IN AXI-SYMMETRIC FLOW

FIGURE 5.15



COMPUTER PROGRAM—EFFECT OF TOLERANCE

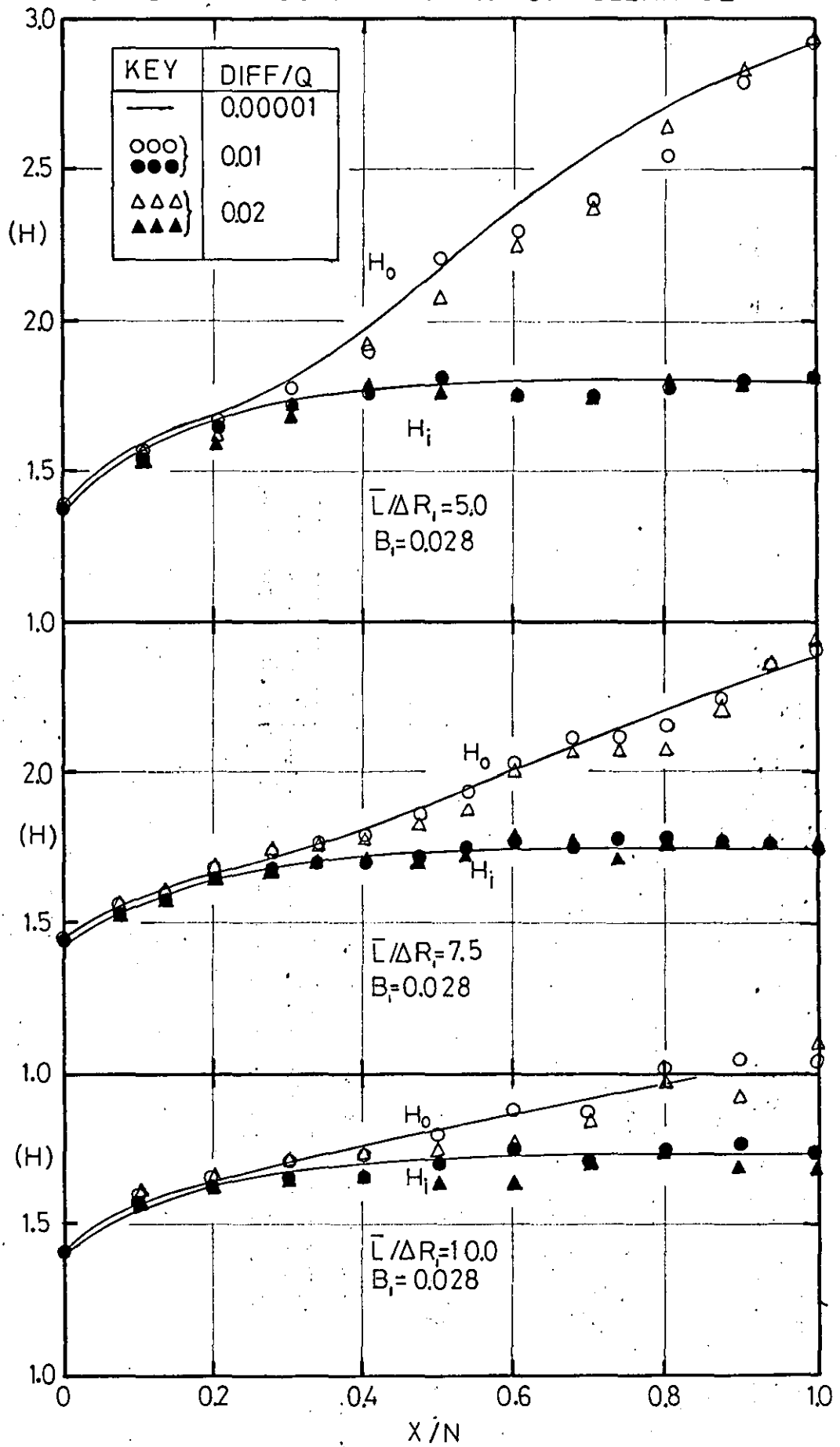


FIGURE 5.17

EXPLANATION OF TERMS—THOMPSON'S METHOD(71)

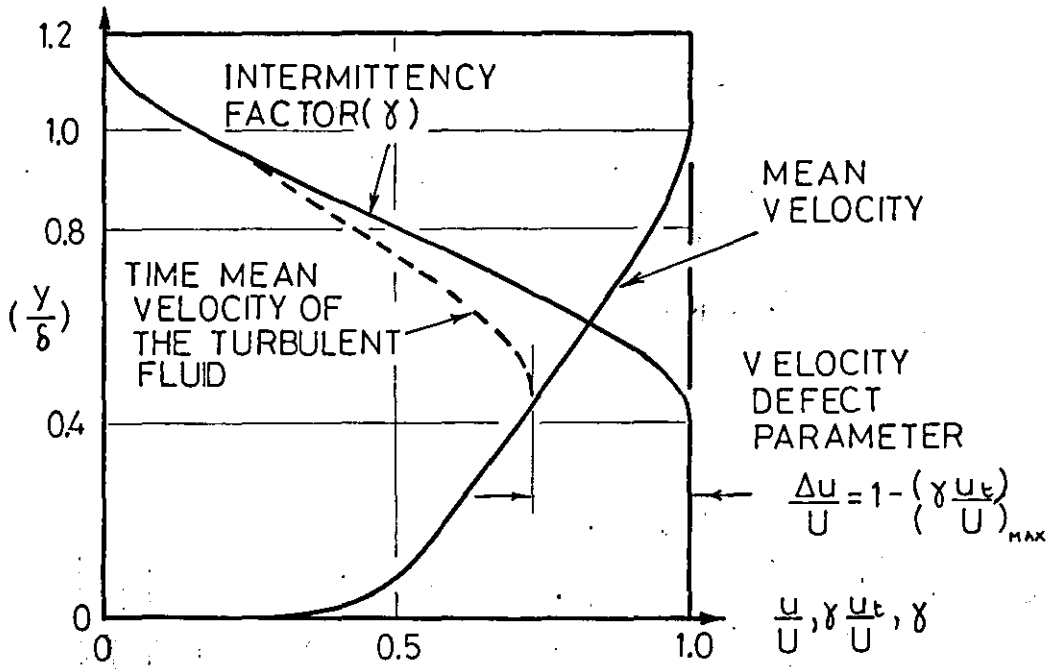


FIGURE 5.18

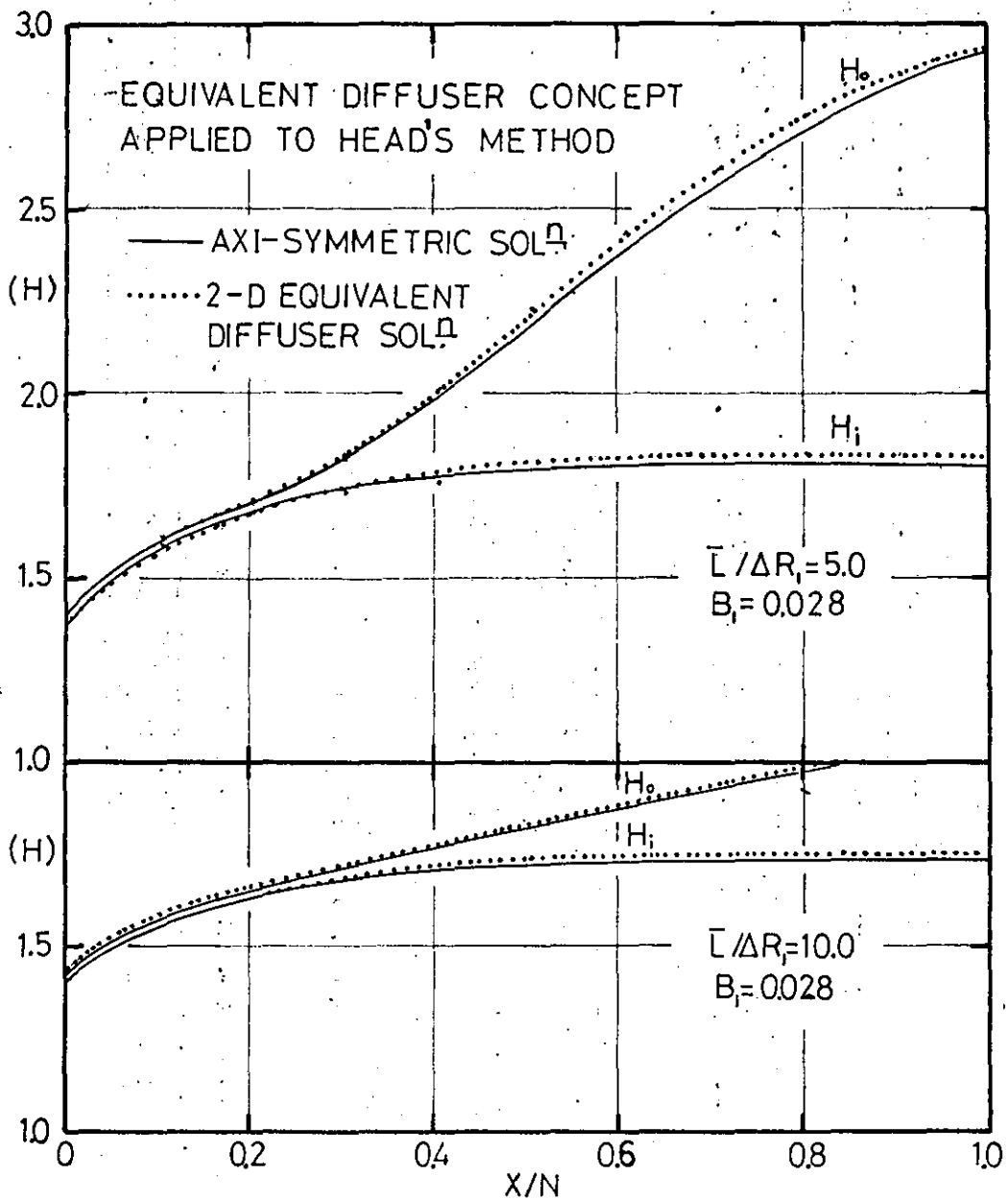
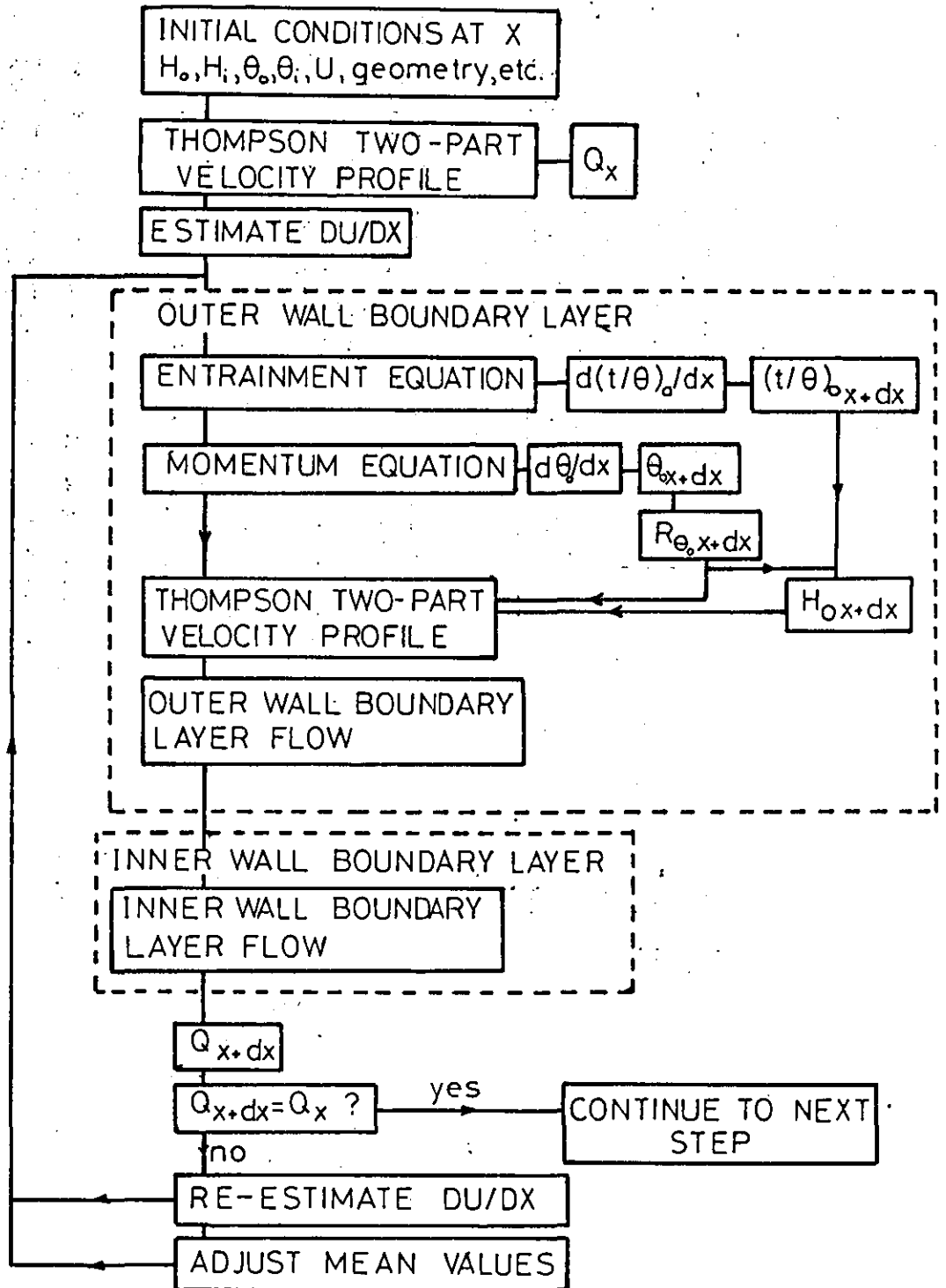


FIGURE 5.19

THOMPSON'S METHOD — SOLUTION PROCEDURE



CHAPTER 6

6.0 COMPARISON OF THEORY WITH EXPERIMENT

In this chapter the application of the turbulent boundary layer prediction methods to the straight-core annular diffuser, described in the previous chapter, is evaluated, in detailed and overall terms, through comparison with the experimental data given in Chapter 4, and other pertinent data.

The crucial test of any theoretical prediction method, as applied to the flow in diffusers, is its ability to successfully predict the growth of the boundary layers. Remarkably crude assumptions (e.g. Kunz (34), $H = 2.0$) will yield an acceptable prediction of the diffuser performance in terms of $\overline{C_p}$ while not giving the detailed growth of the boundary layers. For this reason it was not felt useful to overemphasise the comparison of the prediction methods with other diffuser performance data, and attention has been focussed on the ability of the methods to predict the diffuser boundary layer growth, from which an accurate prediction of diffuser performance inevitably arises.

6.1 The Effect of the Mean Velocity Profile Form on the Evaluation of Diffuser Quantity Flow

Since the continuity of flow forms the basis of the iterative procedure employed in the prediction methods, the correct evaluation of diffuser flow, using boundary layer integral parameters, is of great importance.

The two velocity profile representations employed viz. the power-law profile and the Thompson two-part profile, have been compared with typical experimental velocity profiles in Chapter 5. They are now evaluated in 'overall' terms in the following manner:

For the test diffusers ($\overline{L}/AR_1 = 5.0, 7.5, 10.0$) with near uniform inlet flow ($B_1 = 0.028$) the diffuser flow has been calculated from the 'raw data'

values of R_0 and H (inner and outer walls) using the two velocity profile models. These calculated values are then non-dimensionalised using the integrated mass flow at each respective station, as shown in Table 6.1.

TABLE 6.1

EVALUATION OF VELOCITY PROFILE MODELS

$\bar{L}/AR_1 = 10.0 \quad B_1 = 0.028$					
X/N	$Q_{EXPT} (FT^3/SEC)$	Power Law Profile $Q_P (FT^3/SEC)$	Two-Part Profile $Q_{TP} (FT^3/SEC)$	Q_P/Q_{EXPT}	Q_{TP}/Q_{EXPT}
0.030	40.95	40.00	39.98	0.980	0.975
0.075	40.40	40.00	40.07	0.990	0.990
0.145	40.40	40.05	40.10	0.990	0.990
0.215	40.45	40.12	40.12	0.990	0.990
0.270	40.65	40.20	40.30	0.990	0.990
0.370	40.75	40.20	40.20	0.990	0.990
0.470	40.65	40.10	40.15	0.985	0.990
0.590	40.77	40.04	40.20	0.980	0.985
0.770	40.75	39.72	40.15	0.975	0.985
0.985	40.83	39.60	40.45	0.970	0.990
$\bar{L}/AR_1 = 7.5 \quad B_1 = 0.028$					
X/N	$Q_{EXPT} (FT^3/SEC)$	Power Law Profile $Q_P (FT^3/SEC)$	Two-Part Profile $Q_{TP} (FT^3/SEC)$	Q_P/Q_{EXPT}	Q_{TP}/Q_{EXPT}
0.04	38.80	37.52	37.72	0.970	0.970
0.100	38.05	37.60	37.70	0.990	0.990
0.167	38.25	37.68	37.68	0.985	0.985
0.293	38.15	37.87	37.80	0.990	0.990
0.420	38.42	38.20	38.33	0.995	0.995
0.547	38.68	38.12	38.30	0.985	0.990
0.673	38.48	37.95	38.48	0.985	1.000
0.800	38.88	37.85	38.70	0.975	0.995
0.987	39.10	37.72	39.00	0.965	0.995
$\bar{L}/AR_1 = 5.0 \quad B_1 = 0.028$					
X/N	$Q_{EXPT} (FT^3/SEC)$	Power Law Profile $Q_P (FT^3/SEC)$	Two-Part Profile $Q_{TP} (FT^3/SEC)$	Q_P/Q_{EXPT}	Q_{TP}/Q_{EXPT}
0.06	39.60	37.40	37.40	0.945	0.945
0.15	37.82	37.50	37.50	0.990	0.990
0.27	38.18	37.82	37.90	0.990	0.990
0.39	38.60	38.22	38.55	0.990	1.000
0.51	38.98	38.12	38.80	0.980	0.995
0.63	39.10	37.87	39.30	0.970	1.005
0.75	39.55	37.30	39.10	0.945	0.990
0.856	38.37	37.30	39.30	0.970	1.020
0.963	40.07	37.68	*	0.940	-

* shape factor outside range of Thompson two-part profile

In the early stages of diffusion the two-part velocity profile yields no greater accuracy than the power-law, with both methods giving within 1% of the measured flow. However, in the latter stages, the two-part profile maintains this accuracy while the power-law profile exhibits errors of up to -6%. Thus the two-part profile based flow calculation is shown to have a constant 'calibration factor', for all practical purposes, of unity over the measured range of H and R_0 , while the power-law profile calculation gives rise to quite serious underestimation for $H > 1.8$. The effect on the prediction methods is to depress the calculated value of $\frac{dU}{dx}$ for $H > 1.8$ and thus inhibit the more rapid growth of shape parameter in excess of this value.

The departure from the one-parameter velocity profile is illustrated in Fig. 6.1 which shows the experimental variation of $\frac{\theta}{\delta_{0.995}} = f_n(H)$ on the outer wall of the test diffusers compared with the power law form, $\frac{\theta}{\delta} = \frac{H-1}{H(H+1)}$, showing a clear lack of agreement on the outer wall where $H > 1.8$. Fig. 6.2, which shows a similar comparison for the inner wall, confirms that for $H < 1.8$ the one-parameter form of the velocity profile is valid.

6.2 Internal Flow Development

6.2.1 Head's Prediction Method

The computer program based on Head's method was applied to the prediction of flow development in the test straight-core annular diffusers for which experimental data is given in Chapter 4. Comparison was confined to the data for the near uniform inlet velocity profile ($B_1 = 0.028$) where a 'potential core' was maintained up to diffuser exit. For the other naturally developed inflow case where detailed data was available ($B_1 = 0.09$) the flow became fully developed in the early stages of diffusion giving insufficient basis for comparison.

Initially prediction was started from the experimental values at the

upstream datum station ($x = -3.15\text{in}$) and allowed to proceed to diffuser exit unless terminated by any program check stops e.g. $H > 3.0$ or fully developed flow. For the three test diffuser geometries ($\bar{L}/\Delta R_1 = 10.0, 7.5, 5.0$) the comparison of the predicted development of the shape factor (H_0, H_1), momentum thickness (θ_0, θ_1) and pressure recovery ($\overline{C_p}$) with experimental data is shown in Figs. 6.3 \rightarrow 6.5, the detailed program outputs being given in Appendix 5. For the $\bar{L}/\Delta R_1 = 10.0, 7.5$ diffuser geometries the overall agreement of the predictions with the experimental data is excellent, and up to the estimated separation region this is also true for the $\bar{L}/\Delta R_1 = 5.0$ geometry. The estimated separation region was established from the values of shape parameter (H) and skin friction (c_f), applying the separation criteria of Sandborn and Kline (56). Separation, when predicted, always occurred on the outer wall. Fig. 6.6 shows the predicted values of H_0 and c_{f_0} for the test diffusers, and these indicate that the $\bar{L}/\Delta R_1 = 10.0, 7.5$ diffusers were free of separation while the flow in the $\bar{L}/\Delta R_1 = 5.0$ diffuser separated at the approximate position $X/N = 0.80$. This agrees well with the experimental observations noted in Chapter 4. In line with these findings $\overline{C_p}$ was correctly predicted for the $\bar{L}/\Delta R_1 = 10.0, 7.5$ diffusers, while for the $\bar{L}/\Delta R_1 = 5.0$ diffuser there is a marked deviation between the predicted and measured values of $\overline{C_p}$ after the estimated separation point.

Slight inaccuracy in the prediction of shape parameter in the early stages of diffusion was noted and this was attributed to the inability of the method to predict the radial pressure gradient in the diffuser inlet plane, due to the inherent assumption of equal pressure gradients on both diffuser walls. In an attempt to avoid this a series of predictions was carried out on the same diffuser geometries with the solution starting at a position just downstream of the diffuser inlet plane matched to the

experimental data at this point. The detailed tabulation of these predictions is given in Appendix 5, while Figs. 6.7 + 6.9 present the main parameters. Some slight improvement in the accuracy of prediction is evident but it is not sufficient to recommend the general use of this technique in view of its restrictive nature. Quite detailed experimental data is required before a prediction can be made, and this data is not normally available.

The two-dimensional form of Head's prediction method uses a single entrainment function and an attempt was made to predict the flow in the test diffusers on this basis where, adopting the nomenclature of Chapter 5, $F_3(H'_0) = F_4(H'_1)$. Thus the outer wall entrainment function ($F_3(H'_0)$) was assumed to apply to both diffuser walls and the predictions repeated for the set of test diffusers. Figs. 6.10 + 6.12 illustrate these results. The absence of the asymmetric growth of shape parameter will be readily noted, and it becomes clear that a single entrainment function will not satisfy the behaviour of the inner and outer wall flows in annular diffusers; the difference in the entrainment functions must be attributed to physical differences in the respective boundary layers. Two possible sources are considered here:

- (i) due to the transverse curvature on the diffuser walls, the entrainment front is either stretched or compressed according to whether the curvature is concave or convex. Thus the flow on the outer wall of the diffuser may exhibit deeper convolutions along the entrainment front, with the reverse behaviour occurring on the inner wall.
- (ii) modification of the mechanism of entrainment due to longitudinal stretching of the entrainment front caused by the curvature of the inlet bend at the outer wall.

Of these two possible effects, modification due to transverse curvature is probably only slight in the test diffusers since the radius dimensions are relatively large. Thus the difference between the inner and outer wall entrainment functions can be mainly attributed to the effect of the outer wall inlet bend.

The validity of the above argument has been independently checked by making minor modifications to the method to adapt it for the conical diffuser geometry and predicting the boundary layer development in the conical diffuser geometry tested by Uram (77), the 'inlet bend sensitive' outer wall entrainment function being used in this prediction. Fig. 6.13 shows a favourable comparison of the predicted values of H and θ with those measured by Uram and indicates that the entrainment functions generated from the test data are generally applicable.

6.2.2 Thompson's Prediction Method

Due to the graphical basis of this method it proved very cumbersome in use, taking up a large amount of computer space and running time.

In predicting the flow development in the test annular diffuser geometries, attempts to run the prediction method starting from the upstream datum station proved impossible since the method proved very sensitive to the high pressure gradient in the early stage of diffusion. Thus all predictions had to be started from a position downstream of the inlet which, as has been noted in Section 6.2.1, is unnecessarily restrictive.

In view of these problems it was not possible to carry out extensive predictions using Thompson's method, and attention was confined to evaluating the method in terms of the annular diffuser test data and of Head's prediction method.

The comparison of the predicted values of shape factor and momentum thickness with the annular diffuser test data for the $\bar{L}/AR_1 = 10.0, 7.5, 5.0$

geometries ($B_1 = 0.028$) is shown in Figs. 6.14 → 6.16. On the basis of this comparison the performance of the Thompson prediction method in this application is seen to be inferior to that of Head's method. Because of this the following section, which deals with the application of theoretical prediction to the establishment of diffuser stability limits, is based exclusively on Head's method.

In an attempt to explain the relatively poor performance of Thompson's method the value of the 'constant' β in equation 5.44 was investigated. Several sets of data were selected from the Stanford Conference Proceedings (66), care being taken to choose data which showed a reasonable momentum balance. The value β was then calculated from this data. While values of β of 1.0 or 2.0 were certainly given in approximately half of the cases, values as widely divergent as 6.0 and -2.0 were also recorded. Thus the conclusion must be drawn that the values of β quoted in Thompson's work are not universally applicable.

6.3 Prediction of Overall Performance and Stability Limits

As stated at the beginning of this chapter the basic test of any prediction method applied to diffuser flow must be to successfully predict the boundary layer growth in the diffuser for any particular geometry. Detailed performance maps giving the stability limits for the conical and annular diffuser geometries under near uniform inflow conditions are available from the report of Sovran and Klop (62), and an attempt was made to reproduce these maps using Head's prediction method.

In the case of conical diffusers the inlet data from Uram's work was assumed ($B_1 = 0.032$), and for the annular geometries the inlet data from the present tests has been used ($B_1 = 0.028$). For these fixed inlet conditions the internal flow development in a wide range of diffuser geometries was predicted and the Sandborn and Kline (56) separation

criterion applied to locate the stability limits. The performance data was then plotted in terms of $\overline{C_p}$ and lines of constant $\overline{C_p}$ generated, which are shown, for the conical and annular geometries respectively, in Figs. 6.17 and 6.18.

In both cases the agreement with the experimentally measured diffuser stability limits, while not in exact coincidence, is very good, especially in the 'useful' range of pressure recovery where $\overline{C_p} = 0.50 \rightarrow 0.70$. The deviation of the stability limit at the lower values of pressure recovery ($\overline{C_p} \approx 0.20$) can be attributed to the failure of the method to accommodate the large divergence angles which are implied by such low values of pressure recovery.

Performance prediction in terms of $\overline{C_p}$ is excellent except where there is marked deviation between the actual and predicted C_{p^*} lines at the lower values of $\overline{C_p}$.

6.4 Finite Difference Methods

The differential method of Spalding and Patankar (63) was applied by Nayak (46) to the prediction of boundary layer growth in the test diffuser geometries, the measured values of mixing length etc. being incorporated into the program.

Application of the method was adversely affected by the diffuser outer wall inlet bend and it proved necessary to adopt the practice of starting the prediction downstream of the inlet plane. With this restriction reasonable predictions of boundary layer growth were made.

POWER-LAW VELOCITY PROFILE

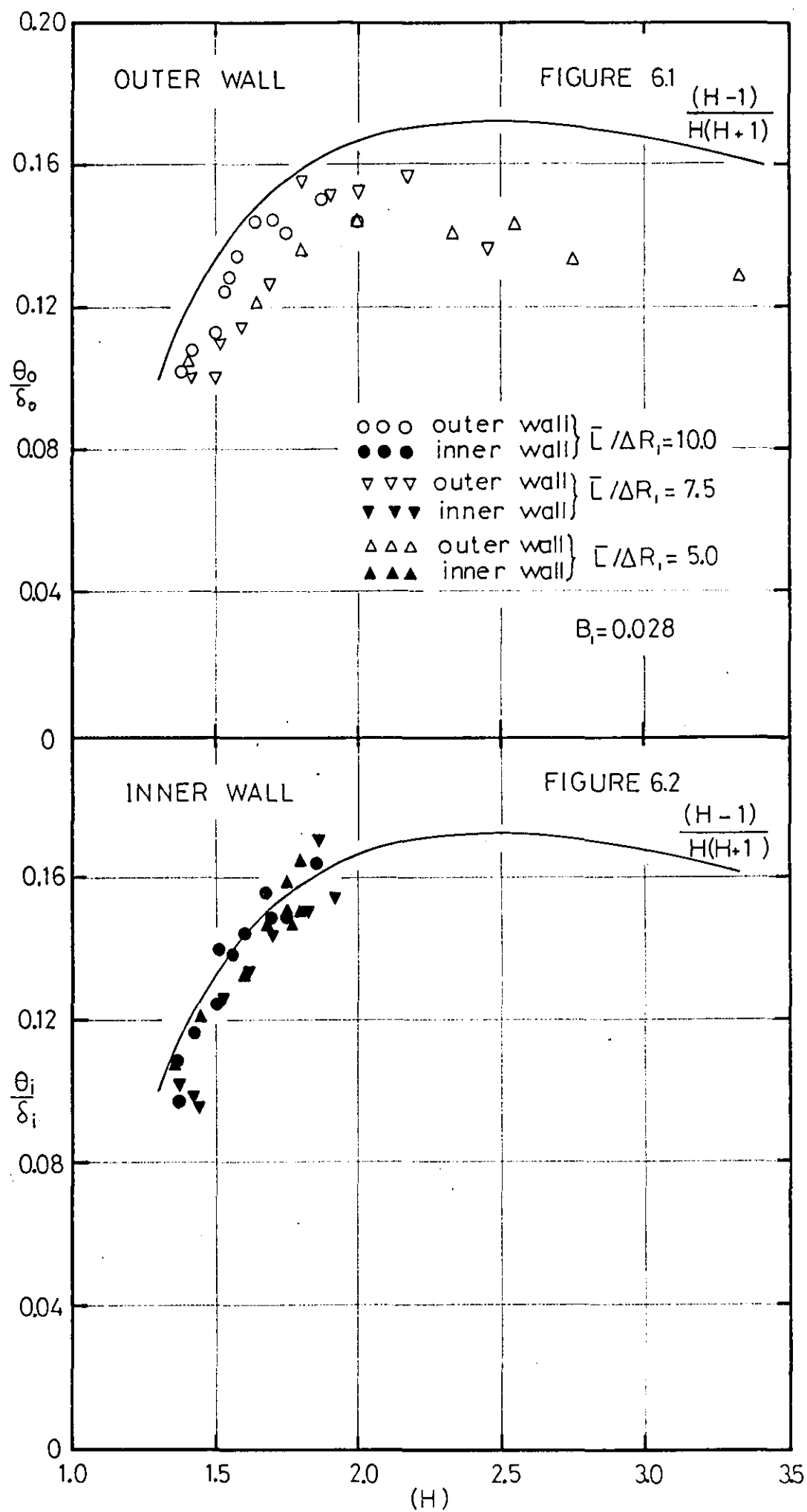
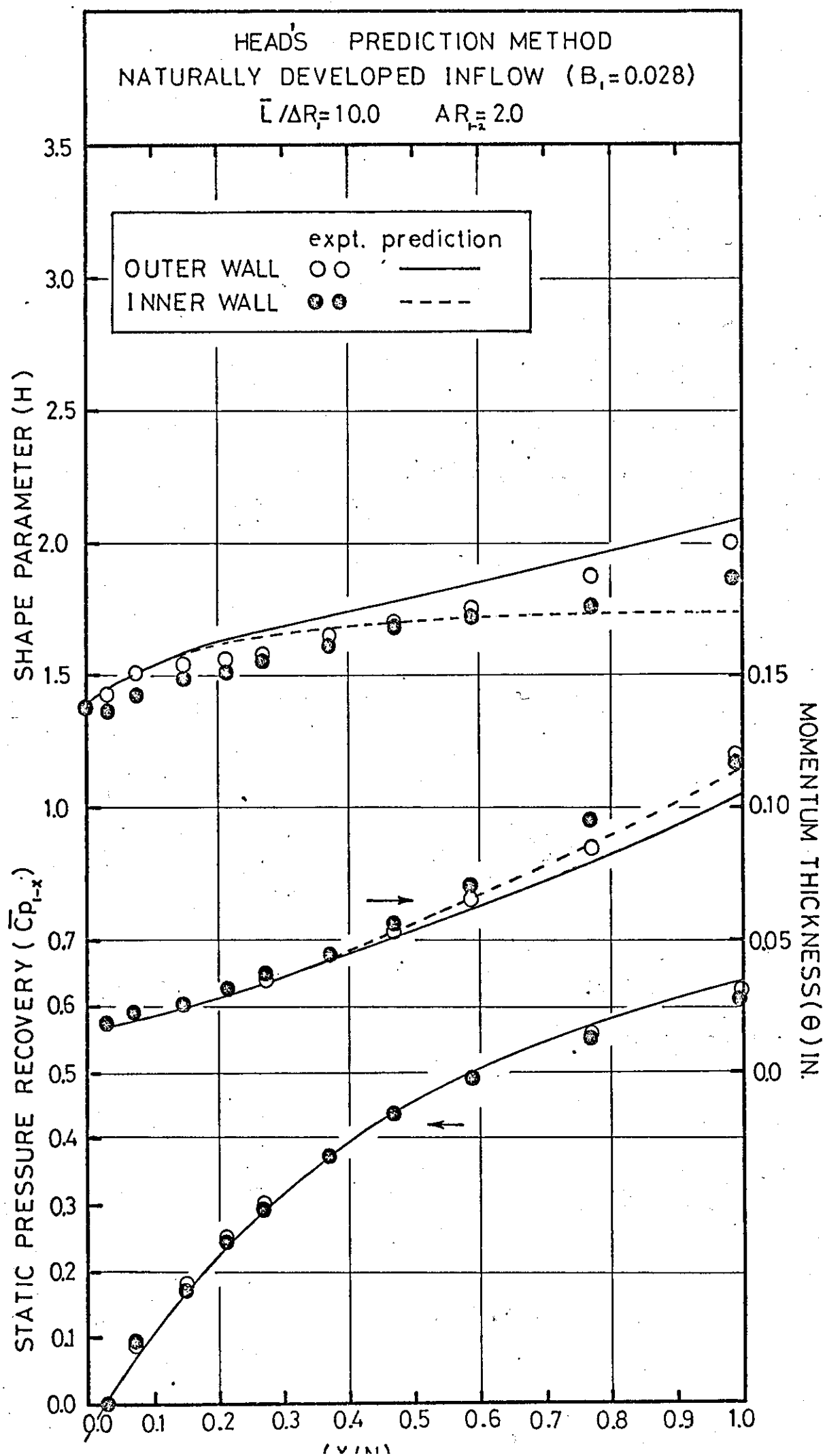
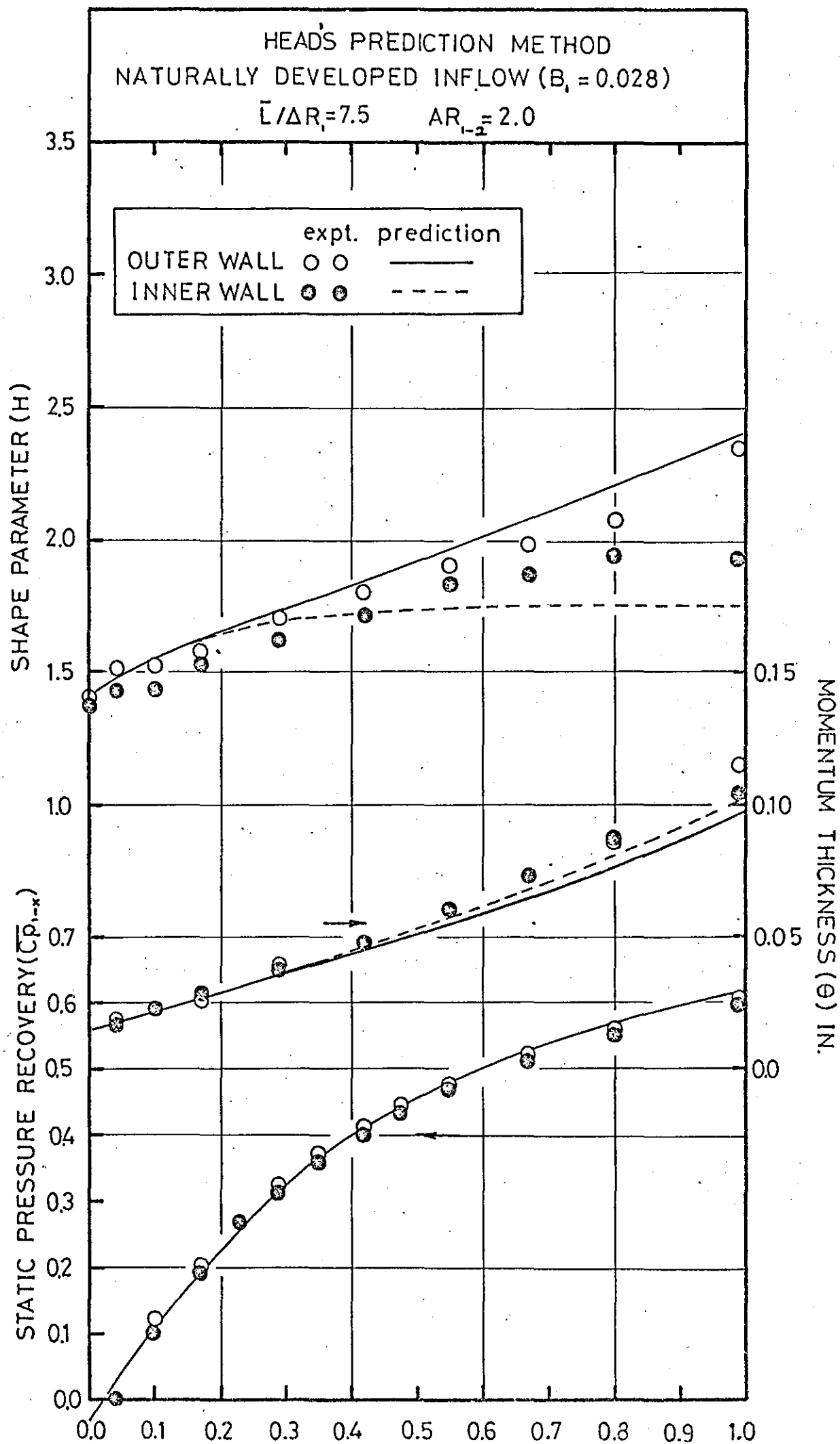


FIGURE 6.3





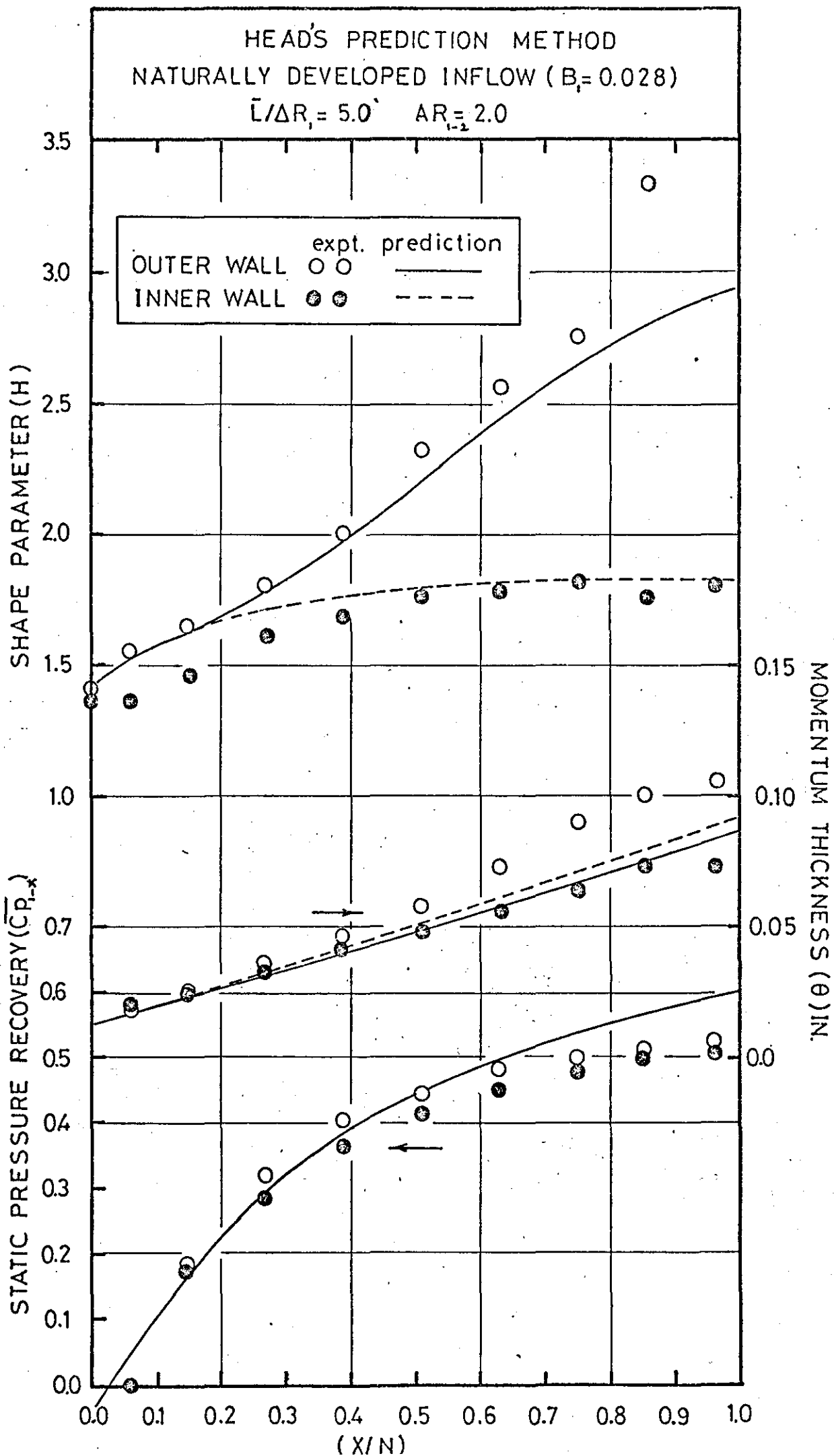
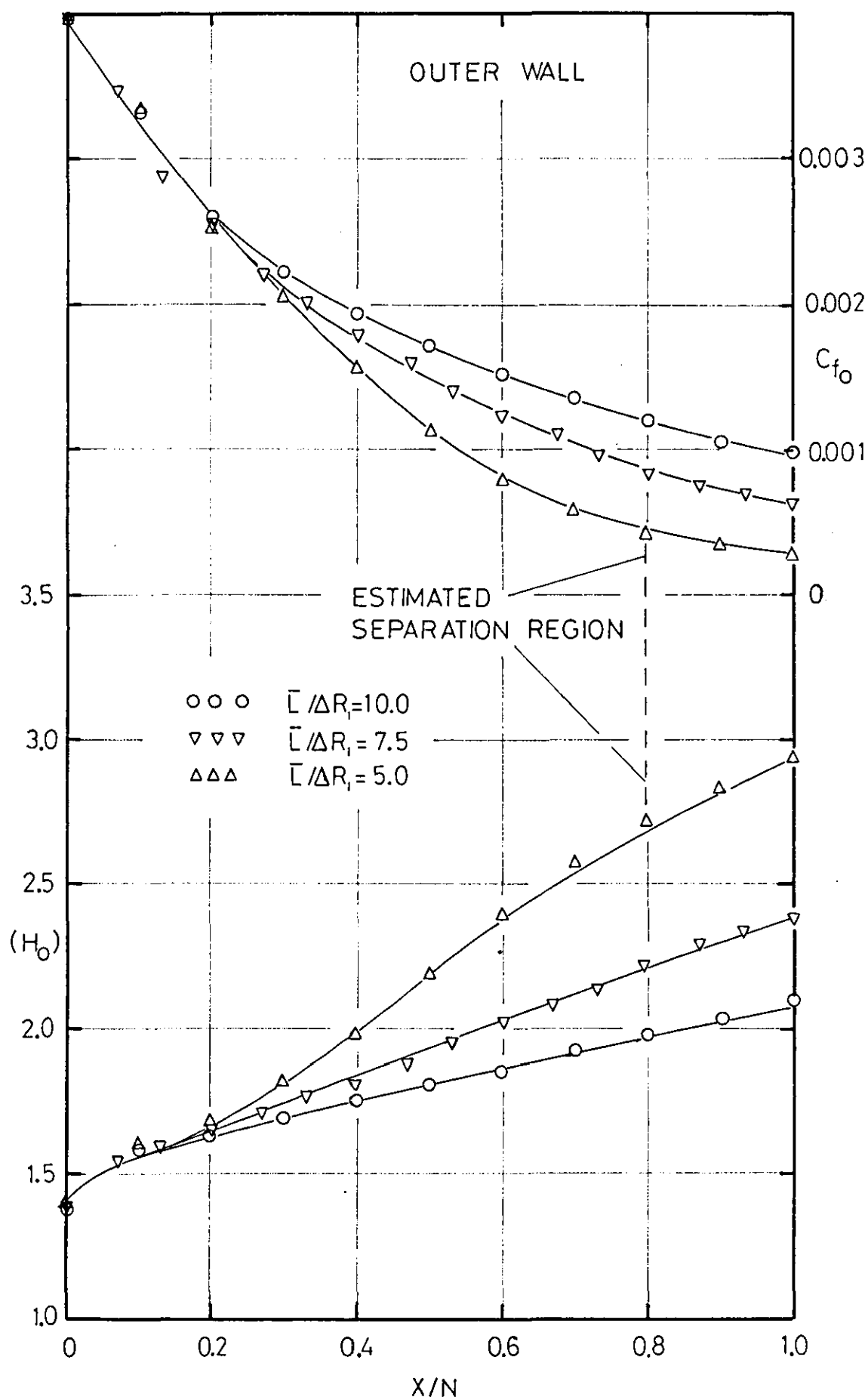
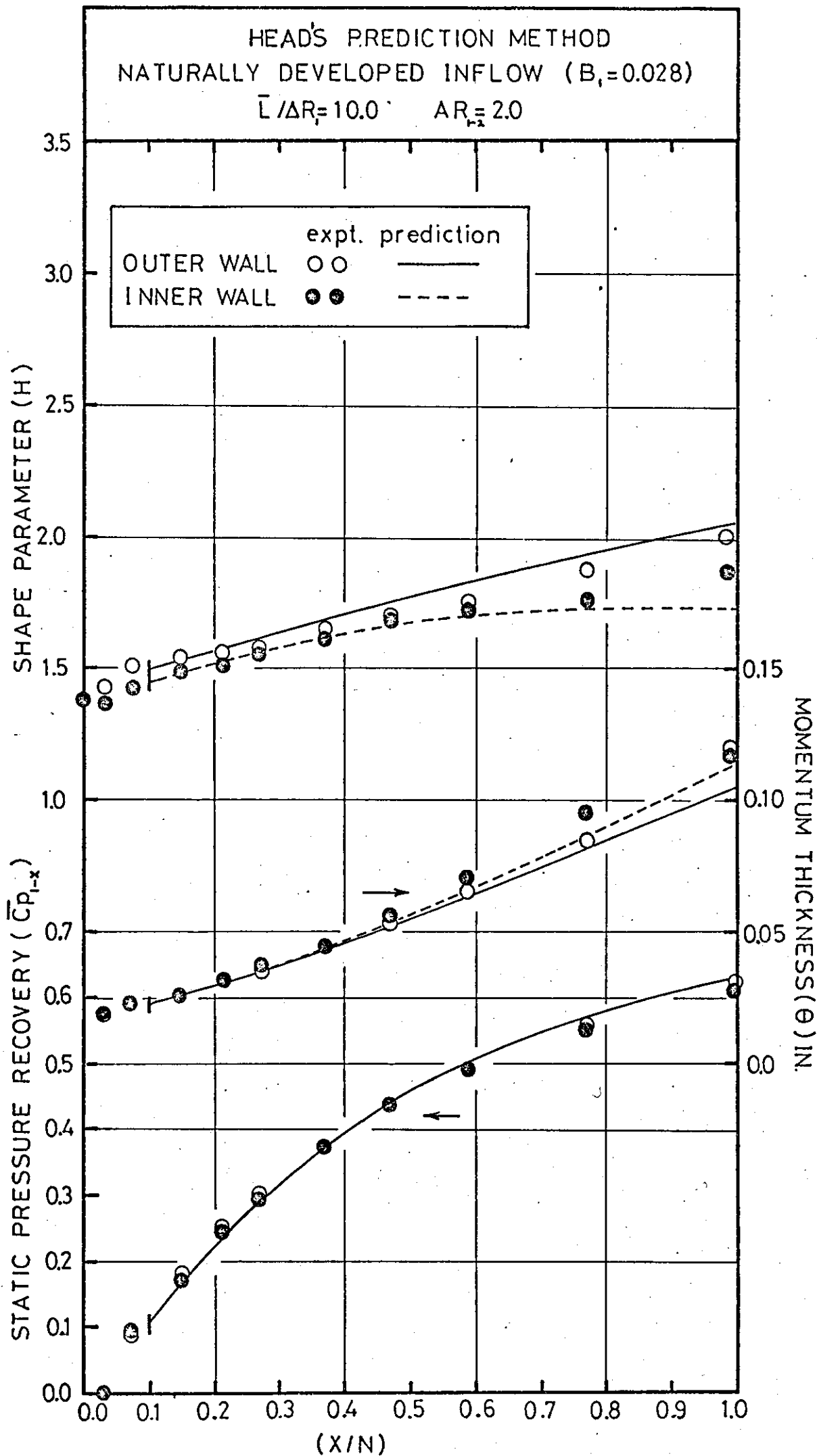


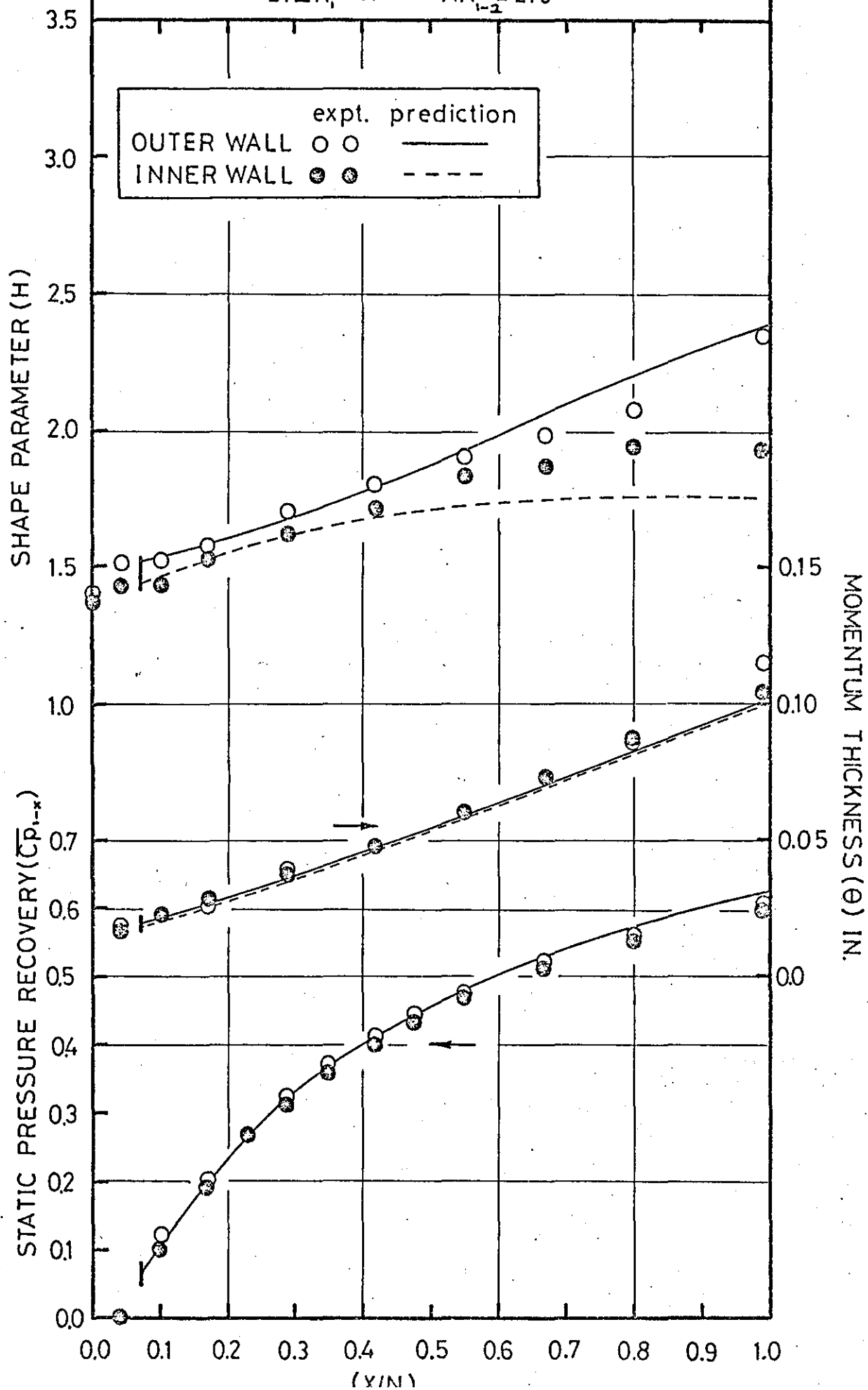
FIGURE 6.6

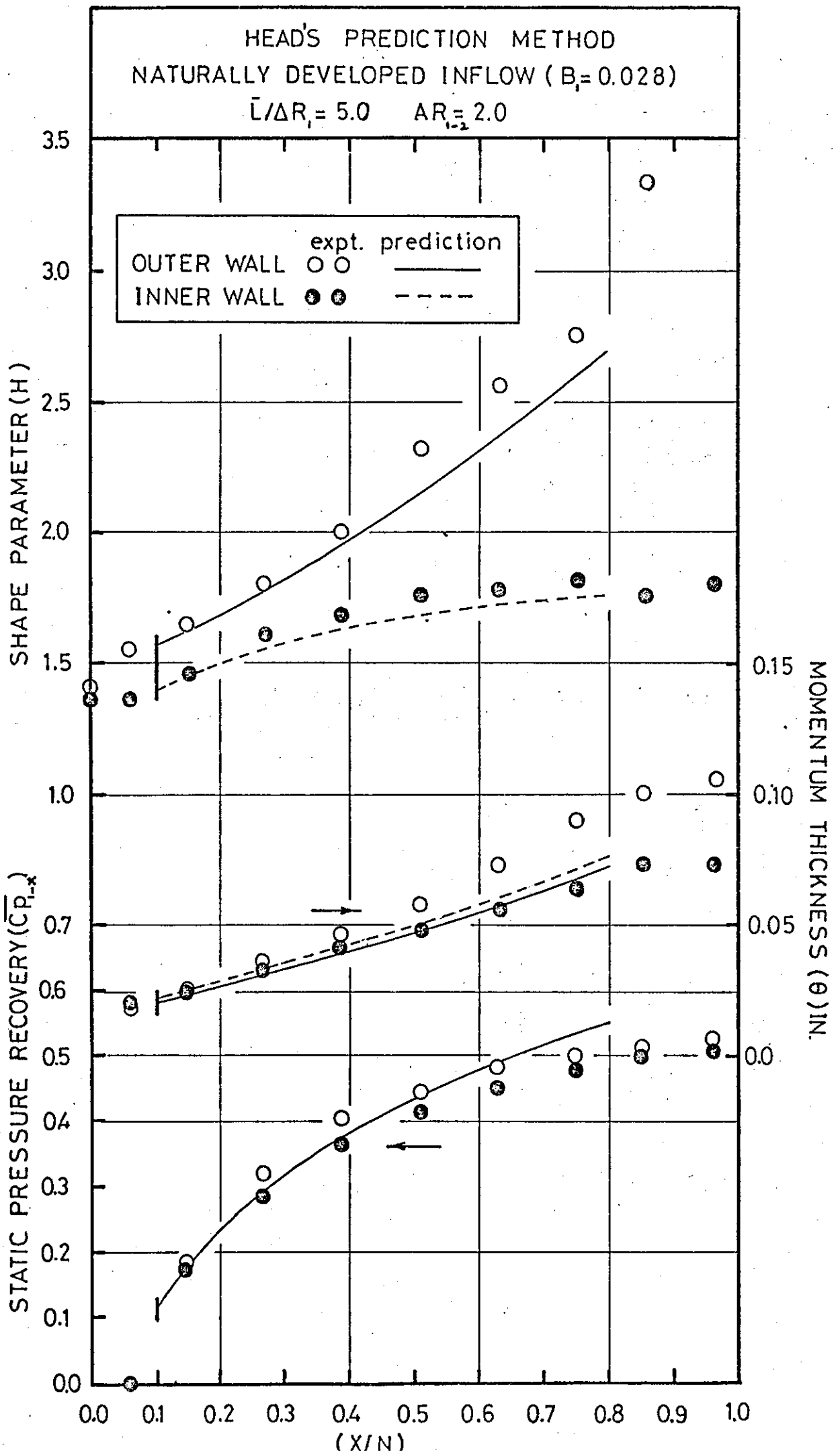
LOCATION OF PREDICTED SEPARATION POINT.

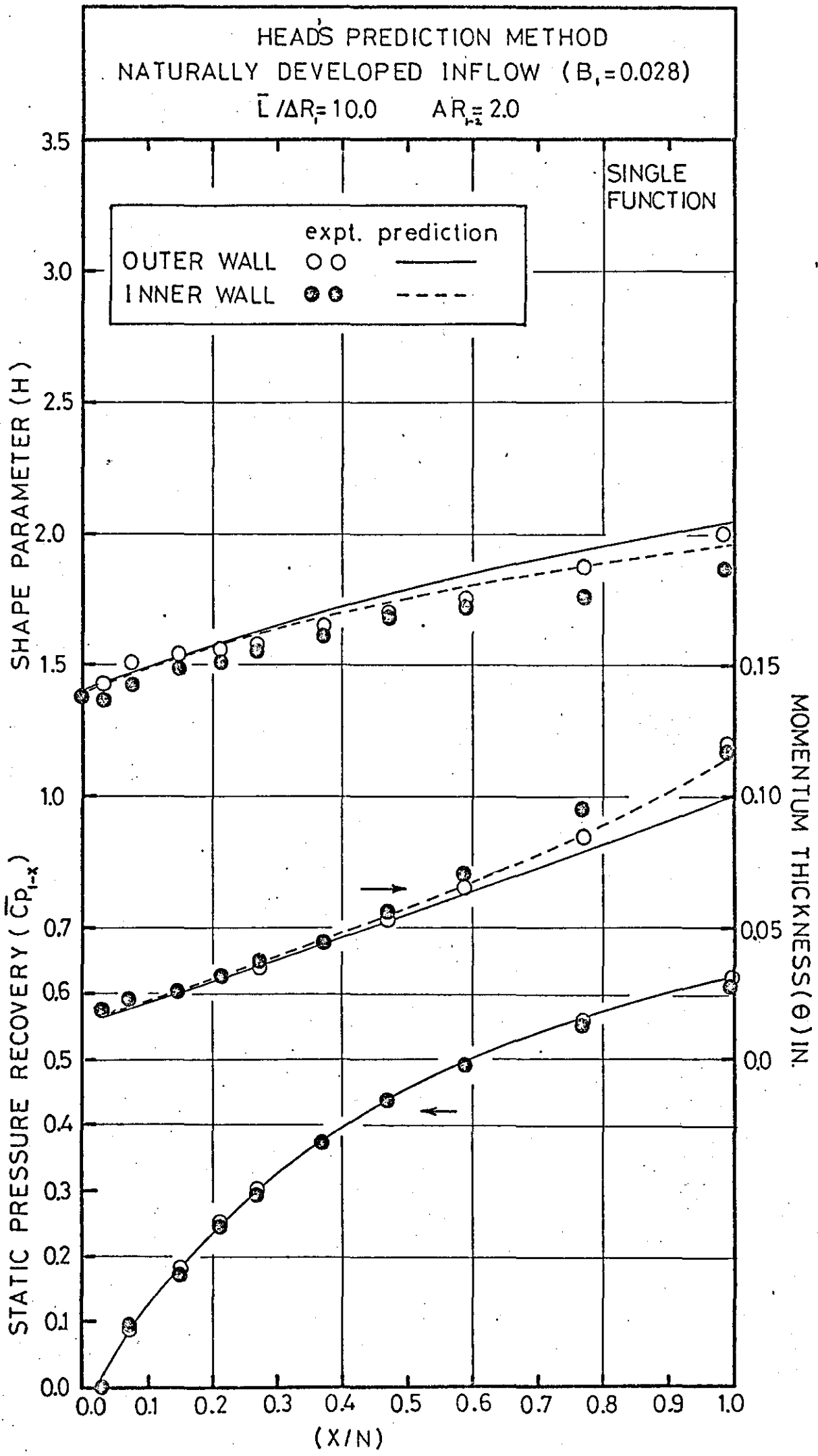


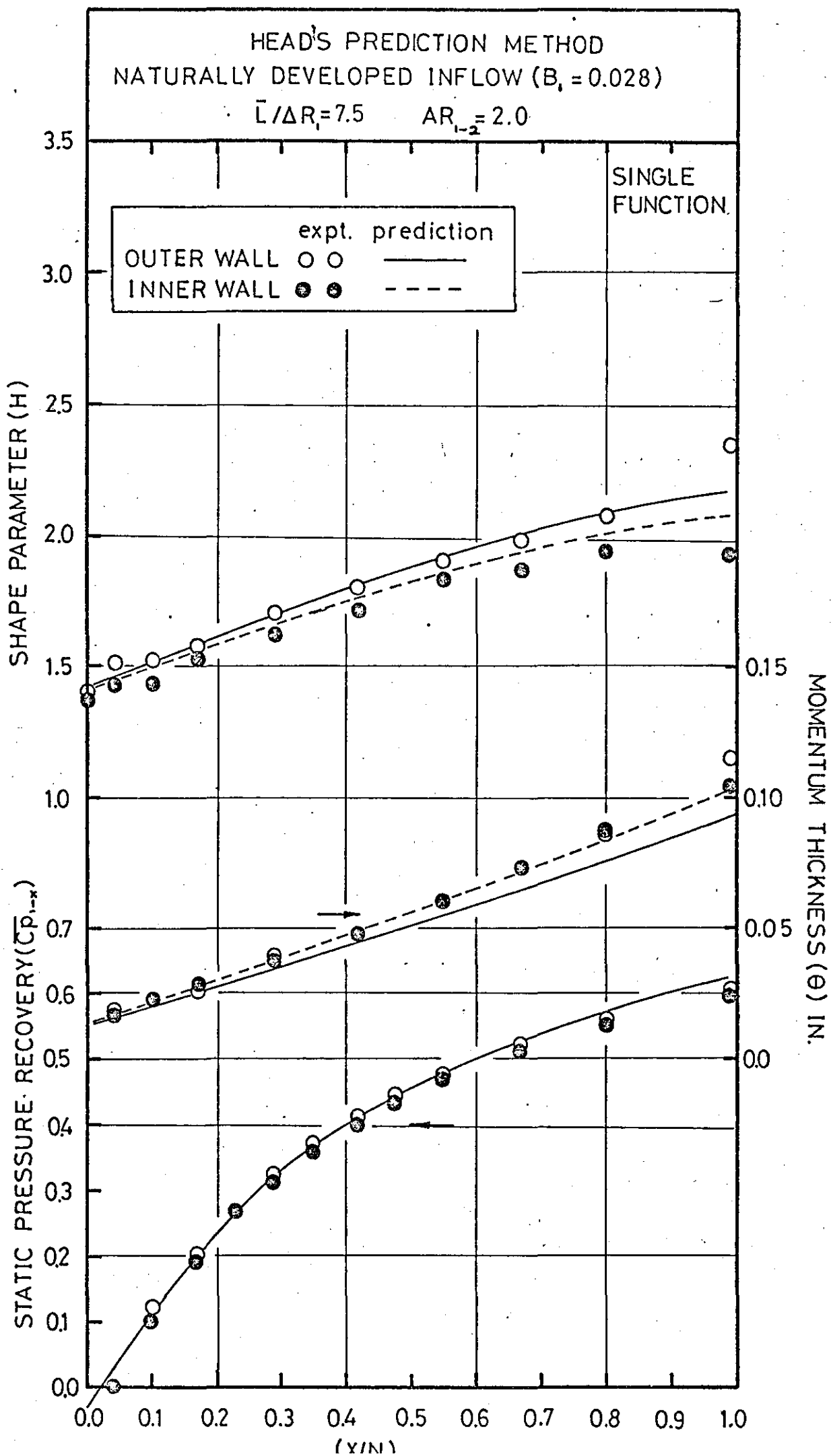


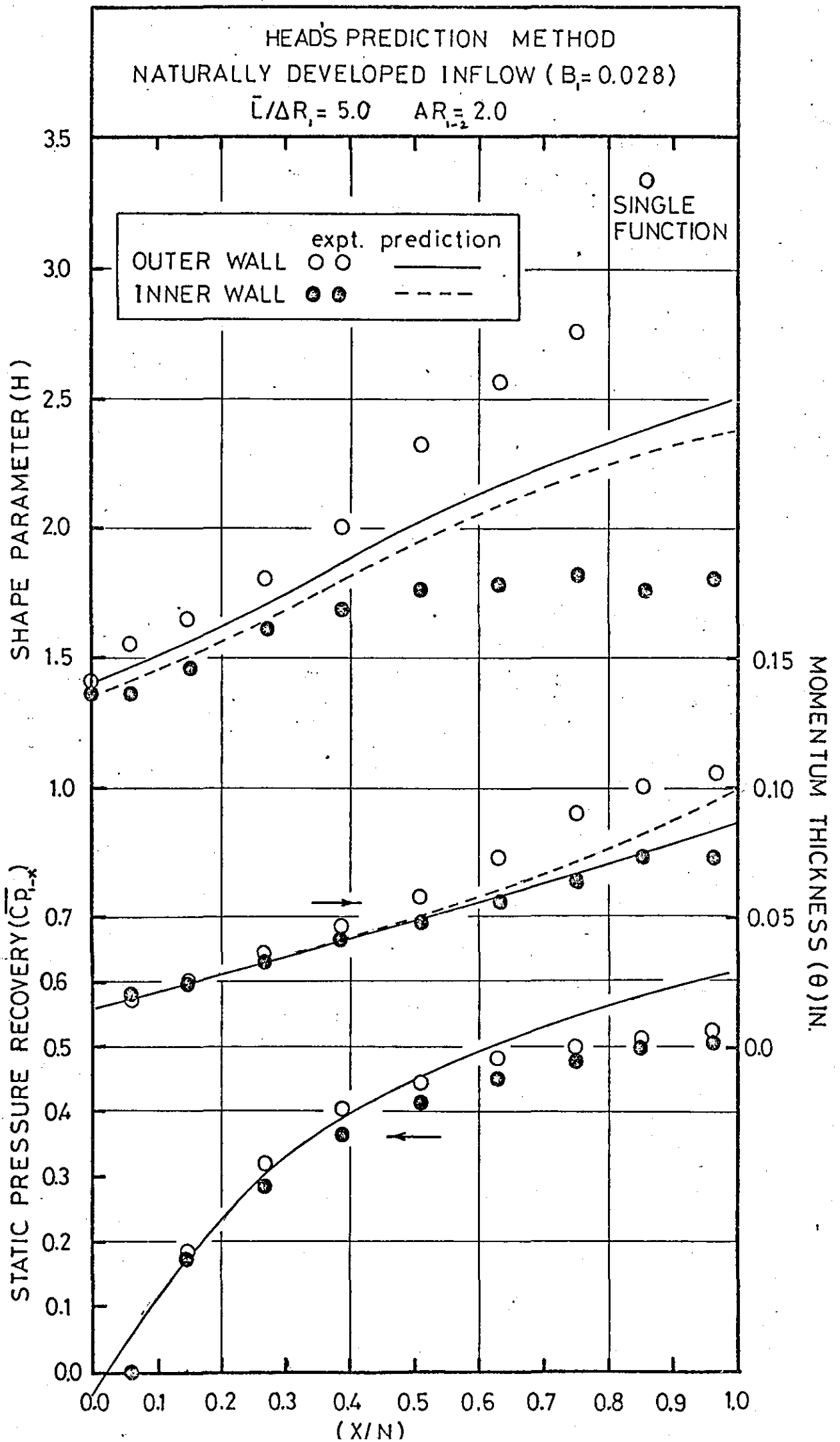
HEAD'S PREDICTION METHOD NATURALLY DEVELOPED INFLOW ($B_1 = 0.028$) $\bar{L}/\Delta R_1 = 7.5$ $AR_{1-2} = 2.0$

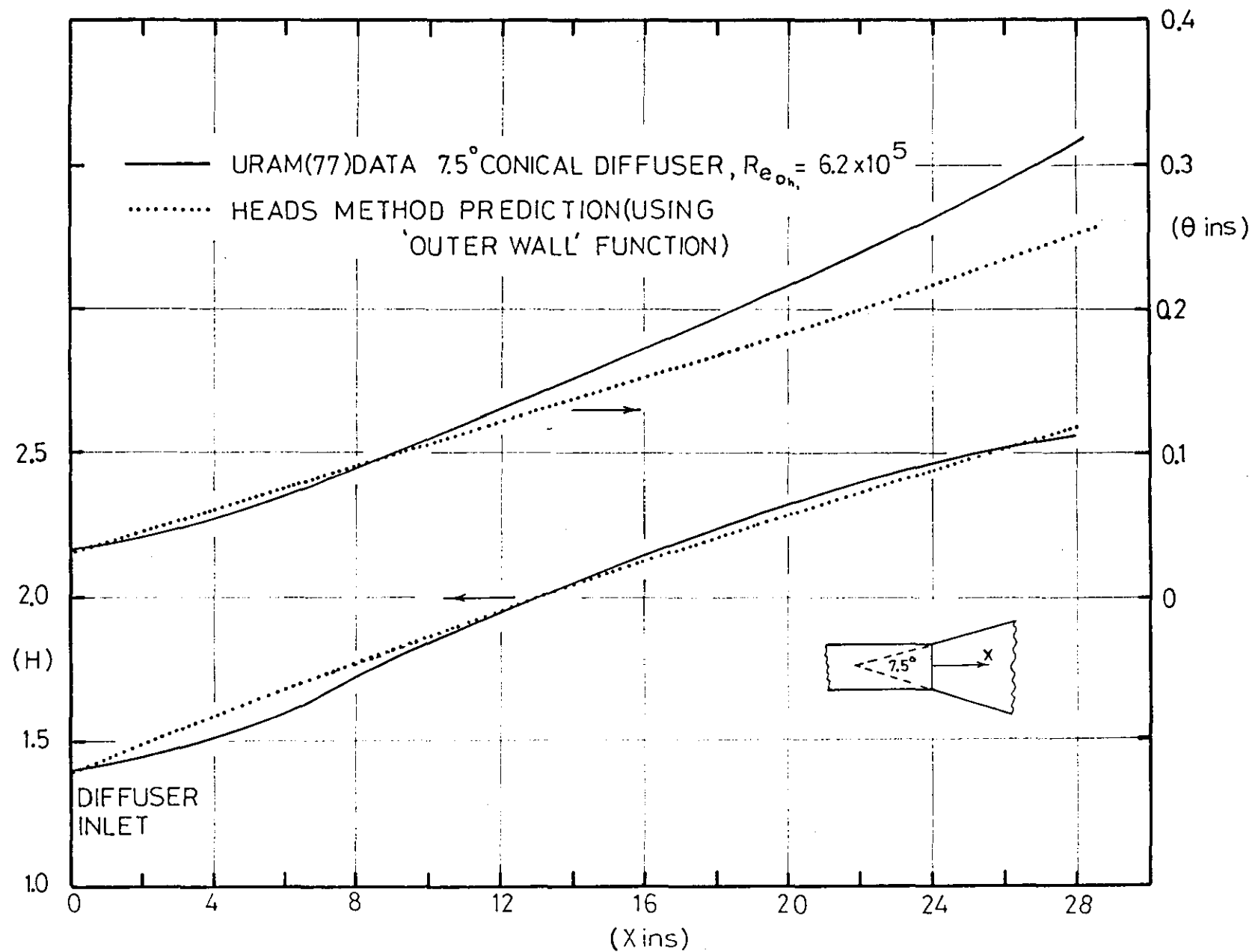






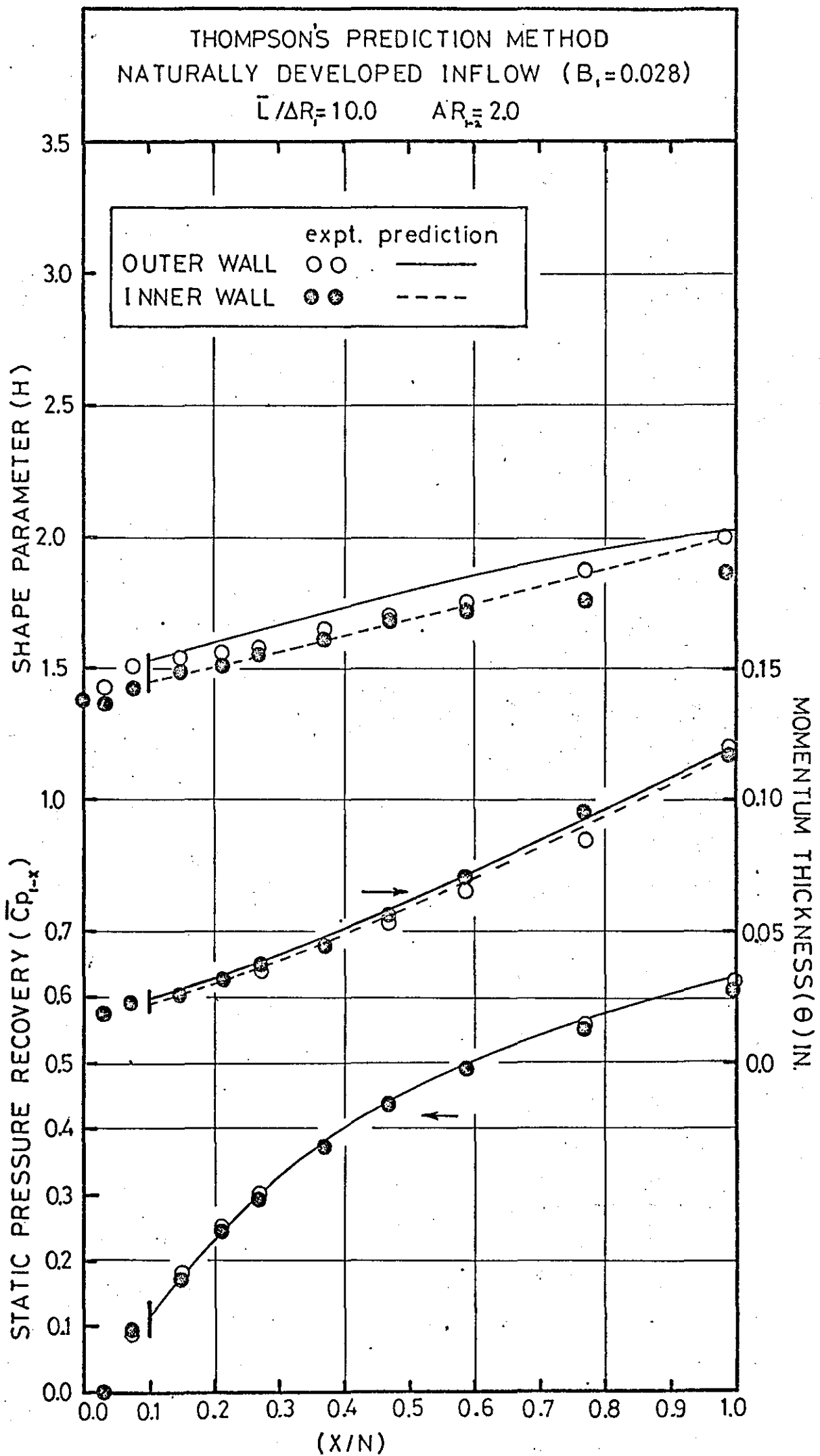






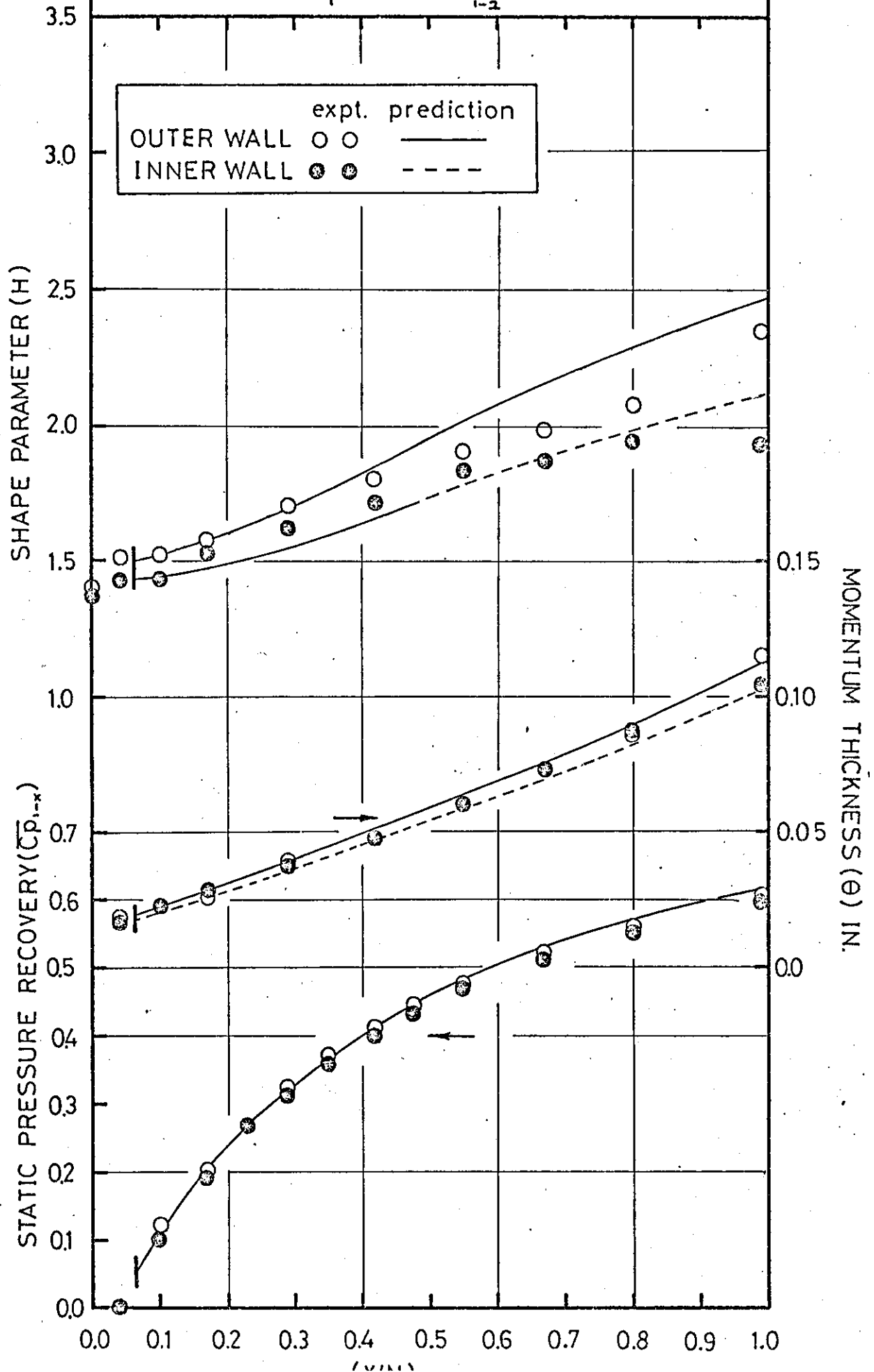
HEADS METHOD—COMPARISON WITH CONICAL DIFFUSER DATA

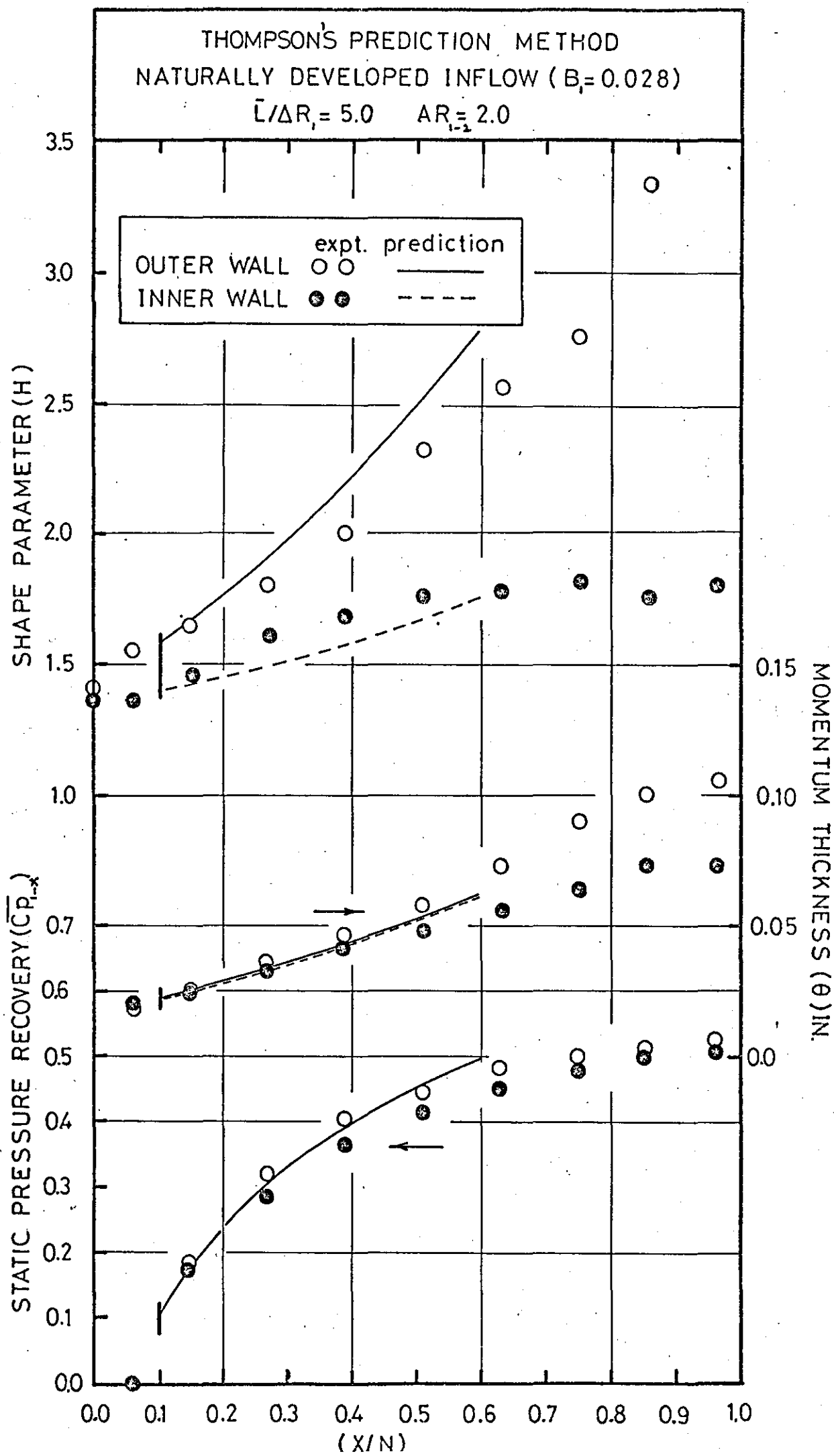
FIGURE 6.13

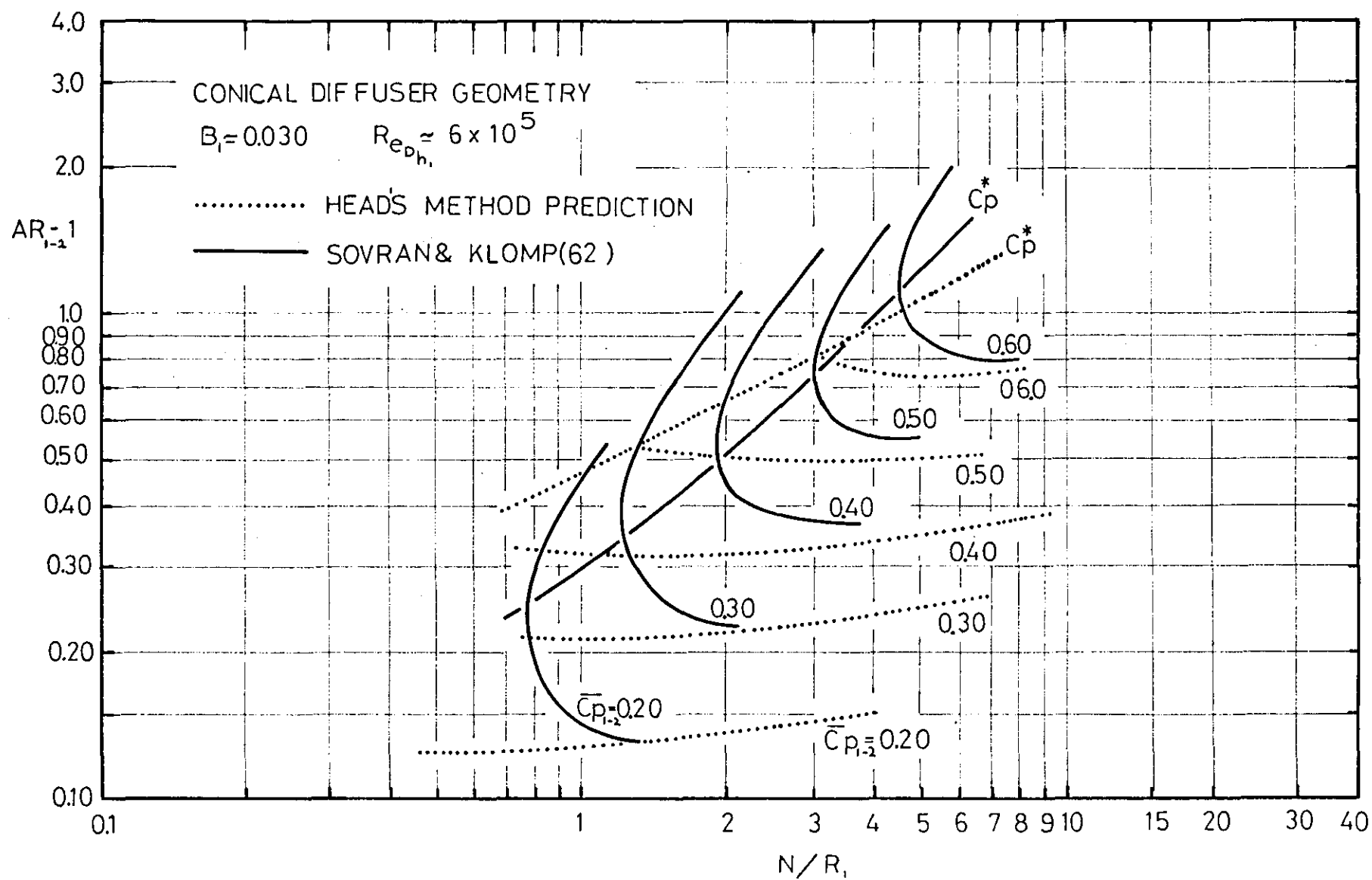


THOMPSON'S PREDICTION METHOD NATURALLY DEVELOPED INFLOW ($B_1 = 0.028$)

$\bar{L}/\Delta R_1 = 7.5$ $AR_{1-2} = 2.0$

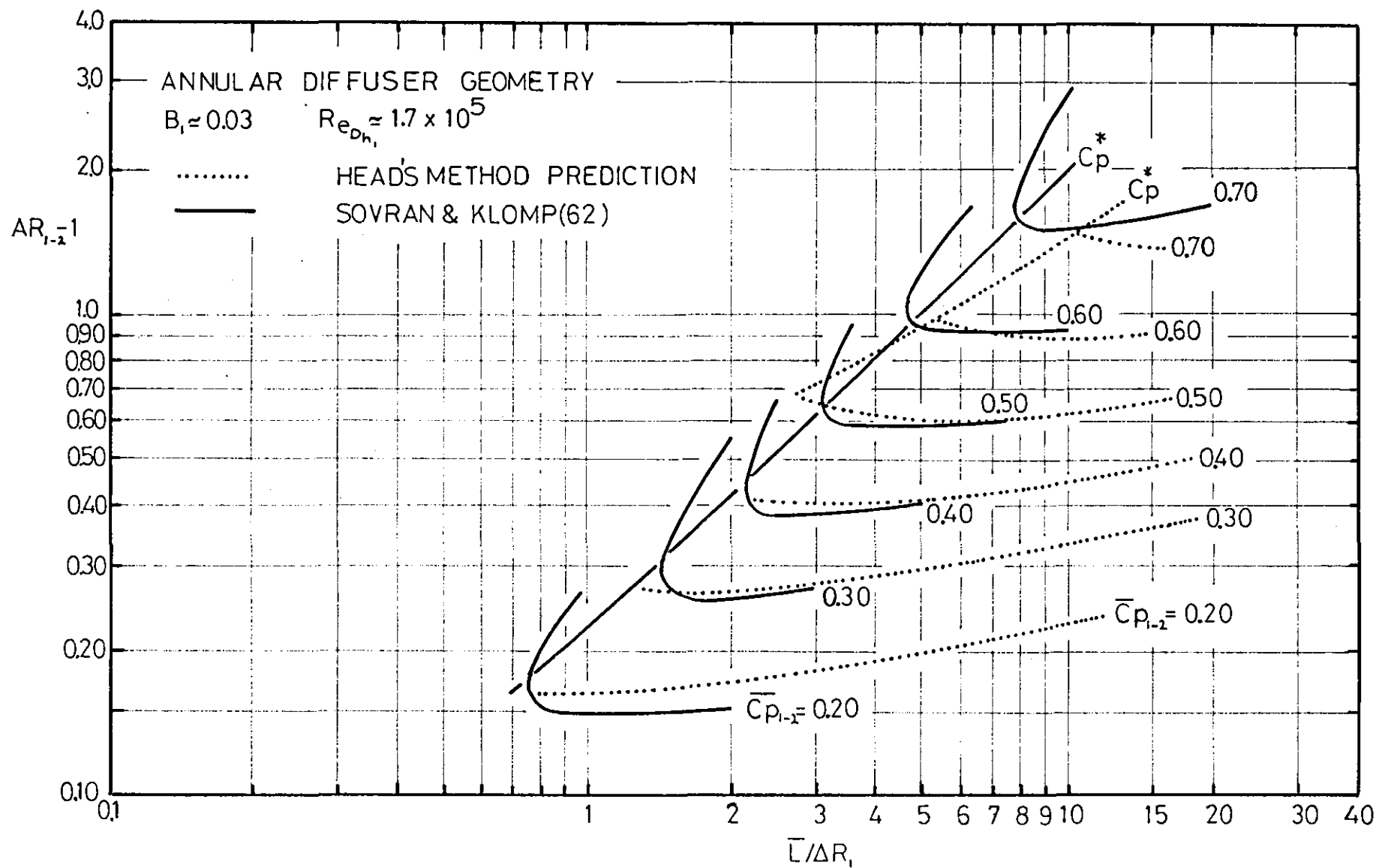






CONICAL DIFFUSER PERFORMANCE MAP

FIGURE 6.17



ANNULAR DIFFUSER PERFORMANCE MAP

FIGURE 6.18

7.0 CONCLUSIONS AND RECOMMENDATION FOR FUTURE WORK

The major points of interest which arose from the research program are summarised in this chapter.

7.1 Experimental Tests

A detailed investigation of a range of straight-core annular diffusers was undertaken. The diffuser geometries were chosen with reference to the optimum lines given by the work of Sovran and Klomp (62) and gave pressure gradients representative of industrial flows.

7.1.1 Naturally Developed Inflow

In the first part of the research program the diffusers were tested with a range of naturally developed inlet velocity profiles from near uniform flow to fully developed flow. The following points are noted:

- (i) The levels of diffuser performance, in terms of \overline{Cp}_{1-2} , compare well with the measured data of Sovran and Klomp (62). However the diffuser stability limits given by their work are not verified and the general applicability of these limits is open to question.
- (ii) For the test diffusers the value of \overline{Cp}_{1-2} fell with initial thickening of the inlet boundary layers with subsequent recovery as the inflow became fully developed.
- (iii) Downstream of diffuser exit, pressure recovery continued in the settling length due to momentum transfer; this was substantially complete within two hydraulic diameters.

Detailed investigation of the boundary layer growth in the test diffusers suggested that:

- (i) The disturbance associated with the flow curvature around the outer wall inlet bend presents the diffuser with a locally distorted inlet velocity profile which is accentuated by the

pressure gradient.

- (ii) The flow development is dominated by the pressure forces, especially in the early stages of diffusion.
- (iii) The turbulent shear stress distributions exhibit a maximum which moves away from the wall, the gradient of shear stress at the wall $\left[\frac{d\tau}{dR} \right]_{R=R_0}$ being approximately equal to the local axial pressure gradient $\frac{dp}{dx}$. The indications are that in the initial stages of diffusion the turbulent shear stress structure lags behind the development of the mean velocity profile.
- (iv) The non-dimensional mixing length distributions agree reasonably well with the form of a ramp function near the wall and a constant level in the outer part of the layer. However the magnitude of this constant level varies slightly.
- (v) Due to the large shear stress gradient in a direction normal to the wall the conventional form of the 'law of the wall' equation ceases to be valid; even at y^+ values as low as 100 deviation is observed.
- (vi) The excellent momentum balance plots confirm the utility of the experimental data and indicate that it may be used with confidence in the checking and generation of theoretical prediction methods.

7.1.2 Artificially Generated Inflow

In an attempt to separate the influences of 'turbulent mixing' and the local velocity profile a series of tests was carried out in which the turbulence levels were increased with minimal changes in the inlet velocity profile.

For mixing generated with a flow spoiler on the outer wall at inlet to

the $\bar{L}/AR_1 = 5.0$ diffuser, in the optimum case, the following effects were apparent:

- (i) A marked improvement in the stability of the diffuser exit flow was noted with an attendant improvement in \overline{Cp}_{1-2} of some 12% over the equivalent naturally developed inflow case, with no significant change in diffuser losses.
- (ii) The distortion of the boundary layer on the outer wall of the diffuser was reduced significantly.
- (iii) The shear stress distribution again exhibited a maximum which moves away from the wall; however in this case the gradient of shear stress normal to the wall is not equal to the local axial pressure gradient, $\left[\frac{d\tau}{dR} \right]_{R=R_0} < \frac{dp}{dx}$. The inclusion of the Reynolds normal stress terms from the mean flow equation partly accounts for this discrepancy indicating that in this case further terms from the mean flow equation must be taken into account. Similarly to the naturally developed inflow cases, the shear stress structure initially lags behind the development of the mean velocity profile.
- (iv) The absolute mixing length levels were considerably higher than those measured in the diffuser with naturally developed inflow. In non-dimensional form the ramp function of the mixing length distribution persisted over most of the boundary layer in the early stages of diffusion. In the latter stages of diffusion a constant level over most of the boundary layer was observed; however the value of the constant varied considerably along the diffuser.
- (v) The conventional form of the law of the wall ceases to be valid

due, as noted in the case of naturally developed inflow, to the large gradient of shear stress near the wall.

- (vi) The momentum balance, which includes all relevant terms, is excellent.

In the case of inlet flow mixing generated by a coarse gauze, which was applied to all three test diffusers, the following comments may be made:

- (i) The stability of the exit flow was markedly improved with the outer wall shape factor at diffuser exit (H_{o2}) being reduced from a value in excess of 3.0 to 1.8 in the $\bar{L}/\Delta R_1 = 5.0$ diffuser.
- (ii) Maximum improvements in pressure recovery ($\bar{L}/\Delta R_1 = 5.0$ diffuser) of approximately 20% in \overline{Cp}_{1-2} were noted, with small increases in diffuser energy losses.
- (iii) The high level of mixing near the wall contributed to such effect that the downstream settling length produced only slight additional pressure recovery.

The latter results serve to highlight the fact that inlet conditions can have far-reaching effects on diffuser performance. The practice of presenting diffuser performance in terms of gross geometry, while a useful design aid, has tended to minimise the importance of diffuser inlet conditions. It cannot be emphasised too strongly that the possible effects of inlet conditions should be equally well understood. It is within the author's experience that within industry serious problems have arisen which are directly attributable to the 'optimistic' application of the Sovran and Klomp performance/stability limit correlation.

7.2 Theoretical Methods

The flow development and overall performance, assuming naturally developed flow, in the test diffuser geometries was predicted for near-

uniform inflow using integral methods which had been modified for application to axi-symmetric flows and included entrainment based 'auxiliary equations'.

The method based on Head's entrainment model was very reliable and rapid in use and the predicted diffuser boundary layer growth and overall performance agreed well with experimental data. With the adoption of the separation correlation of Sandborn and Kline (56) this method was applied to a range of straight-core annular diffuser geometries and from these predictions it was possible to reproduce, to a fair degree of accuracy, the performance map of Sovran and Klomp (62).

The method based on Thompson's entrainment model, while potentially superior, proved unwieldy in use due mainly to its high graphical content. This method gave disappointing results in this particular application, and is not to be recommended where it is necessary to solve the flow using computer methods because of the prohibitive amount of running time required.

7.3 Future Work

The general solution of the flow in diffusers with arbitrary inlet flows must come from a theoretical approach since it is impossible to test all the possible diffuser geometries for all the possible inlet conditions. There is no doubt that the differential methods now being developed are moving in this direction but more experimental data is required before this can be achieved. These experiments must be carefully selected so as to give the maximum of useful data and a physical understanding of the problems of flow in diffusers.

